LYMAN ALPHA GALAXIES:

PHYSICAL PROPERTIES AND EFFECTS OF DUST AT HIGH REDSHIFT

by

Steven L. Finkelstein

A Dissertation Presented in Partial Fulfillment
of the Requirements for the Degree
Doctor of Philosophy

ARIZONA STATE UNIVERSITY

August 2008

LYMAN ALPHA GALAXIES:

PHYSICAL PROPERTIES AND EFFECTS OF DUST AT HIGH REDSHIFT

by

Steven L. Finkelstein

has been approved

July 2008

Graduate Supervisory Committee:

James E. Rhoads, Chair
Sangeeta Malhotra
Rogier Windhorst
Evan Scannapieco
John Shumway

ACCEPTED BY THE GRADUATE COLLEGE

ABSTRACT

This dissertation presents the results from five related studies of the nature of Lyman alpha emitting galaxies (LAEs) at high redshifts. These objects have long been predicted to be very young, and possibly the primordial first galaxies. Recent results have shown that these objects may in fact be more complicated. Three different studies at z $\sim$ 4.5 show that LAEs are mostly not primordial, as evidence was found for dust in most of our objects. These studies also show that not all LAEs are young, since two out of a sample of 15 LAEs appear to be much older ($\sim$ 500 Myr). These older objects are detected with large Lyman alpha equivalent widths (EWs) at an older age due to a clumpy interstellar medium (ISM) geometry. This geometry results in a higher escape fraction for Lyman alpha photons than for continuum photons, thus enhancing the EW to arbitrarily high values. This effect may be responsible for the large number of high EW LAEs detected in recent studies. Extrapolating these stellar population results to the far-infrared (FIR), it appears that nearly half of our sample of LAEs could be detected in their rest-frame FIR with a future observatory such as the Atacama Large Millimeter Array. Detection of the dust emission from these galaxies could confirm the earlier results that many of these objects contain a significant amount of dust. The final study is concerned with LAEs at a much lower redshift of z $\sim$ 0.3. These LAEs are older, more massive, and more metal rich than their high-redshift counterparts, indicating evolution in this type of galaxy. Studying LAEs at low redshift is the highest priority for the future, as one can perform far more detailed analyses then those done at high redshift.

I dedicate this thesis to my grandfather, Joseph Benezra, the inspiration behind my desire for higher learning.

ACKNOWLEDGMENTS

I would like to acknowledge funding support from the Arizona State University/NASA Space Grant, ASU Department of Physics and ASU School of Earth and Space Exploration. Support for this work was also provided by NASA through grant numbers HST-AR-11249, HST-GO-10240 and HST-GO-10530 from the Space Telescope Science Institute, which is operated by the Association of Universities for Research in Astronomy, Inc., under NASA contract NAS5-26555.

I would first like to thank my advisor, James Rhoads, for all the help he has given me over the last three years. I am deeply indebted to him for agreeing to take me on as a student before he even set foot at ASU, and for helping me through that first year, where I was knocking on his door nearly every day with some new data reduction problem. I think that the biggest reason for my success is that I always knew that James would take the time to listen to my problem, and offer advice, even when he was busy. Alongside James I would also like to thank Sangeeta Malhotra for all of the great advice, on astronomy and on life, that she has given me.

Along with both James and Sangeeta's help, I think the other big reason for my success is that they never stopped pushing me. Be it writing observing proposals, writing grants, or writing an extra chapter for this thesis, I was always urged to do more. While I was not always extremely receptive to these "suggestions," in the end I now see that it was for the best, and I thank you both. I also thank my other three committee members, Rogier Windhorst, Evan Scannapieco and John Shumway,

as well as David Smith, for taking the time to read through this thesis and offer valuable suggestions for its improvement.

One of the aspects that makes graduate school worthwhile (and tolerable!) are the people you meet, some who just have a passing role in your life, but others who become lifelong friends. Although these people are too many to name here, I would like to especially thank Russell Ryan, Todd Veach, Brian Frank, Allison Loll, Seth Cohen, Nimish Hathi, Amber Straughn, Norman Grogin and Nor Pirzkal for the help you've given me over the past few years.

I would like to thank my parents for their unwavering support. You have been helpful over the years in so many ways, be it listening to me complain about my first year physics courses, to trying to follow along when I explain my research. I don't think I could have finished without your support. To my sisters, Cherie and Elissa, I thank you for at least pretending to be interested when I talk about my research. I also want to thank Jasmine and Bella, for always making me smile.

Most importantly, I want to thank my (soon-to-be) wife, Keely. More than anyone else, you have kept me going. This has never been more difficult than over the last year, as we have both been under extreme pressure to finish our schooling. It takes a truly remarkable person to support me in the way that you have, and I am extremely lucky to have you. Very few people have the pleasure of spending their life with someone who shares their same passion, and I feel truly lucky to spend my life with you.

TABLE OF CONTENTS

Page

LIST OF FIGURES xii

LIST OF TABLES xv

CHAPTER

1 INTRODUCTION 1

1.1 Present Day Galaxies 1

1.2 The First Galaxies 2

1.3 Early Detections of Lyman Alpha Galaxies 6

1.4 Scientific Results 8

1.5 Reasons for Large Lyα EWs 9

1.6 Modeling the Stellar Populations of LAEs 12

2 THE AGES AND MASSES OF Lyα GALAXIES AT z $\sim$ 4.5 15

2.1 Abstract 15

2.2 Introduction 15

2.3 Data Handling 19

2.3.1 Observations 19

2.3.2 Data Reduction 20

2.3.3 Lyα Galaxy Selection 22

2.3.4 Stellar Population Models 24

2.4 Results 26

2.4.1 Lyα Galaxy Candidates 26

CHAPTER Page

2.4.2 Equivalent Width Distribution 26
2.4.3 Stacking Analysis 28
2.4.4 Age and Mass Estimates 30
2.5 Discussion 33
2.5.1 Age and Mass Estimates 33
2.5.2 Dusty Scenario 39
2.6 Conclusions 41
3 EFFECTS OF DUST GEOMETRY IN Lyα GALAXIES AT z = 4.4 . . . 43
3.1 Abstract 43
3.2 Introduction 44
3.3 Data Handling 46
3.3.1 Observations 46
3.3.2 Data Reduction 47
3.3.3 Object Extraction 48
3.3.4 Lyα Galaxy Selection 50
3.3.5 Spectroscopic Confirmations 53
3.3.6 Broadband Photometry 58
3.4 Modeling 59
3.4.1 Stellar Population Models 59
3.4.2 Dust Effects on the Lyα EW 61
3.4.3 IGM Inhomogeneities 64

CHAPTER Page

3.4.4 Equivalent Widths 65
3.5 Results 69
3.5.1 Fitting to Models 69
3.5.2 Object 1 72
3.5.3 Object 2 73
3.5.4 Object 4 73
3.5.5 Object 6 74
3.5.6 Best-Fit Models Without Dust 74
3.5.7 Monte Carlo Analysis 75
3.6 Discussion 80
3.6.1 Lyα Detection Fraction 80
3.6.2 Hα Equivalent Widths 80
3.6.3 Comparison to Other Work 84
3.7 Conclusions 86
4 Lyα GALAXIES: PRIMITIVE OBJECTS, DUSTY STAR-FORMERS OR EVOLVED GALAXIES? 88
4.1 Abstract 88
4.2 Introduction 89
4.3 Data Handling 92
4.3.1 Observations 92
4.3.2 Object Extraction 93

CHAPTER Page

4.3.3 Lyα Galaxy Selection 95
4.3.4 Candidate Redshifts 98
4.4 Stellar Population Modeling 100
4.5 Results 104
4.5.1 Model Fitting 107
4.5.2 NB656 Detected Objects 110
4.5.3 NB665 Detected Objects 114
4.5.4 NB673 Detected Objects 115
4.6 Discussion 127
4.6.1 Equivalent Width Distribution 127
4.6.2 Model Parameter Distribution 129
4.6.3 Causes of Model Uncertainties 137
4.7 Conclusions 141
5 THE EXPECTED DETECTION RATE OF DUST EMISSION IN HIGH-REDSHIFT Lyα GALAXIES 147
5.1 Abstract 147
5.2 Introduction 148
5.3 Method 153
5.3.1 Lyα Galaxy Sample 153
5.3.2 Dust Emission 154
5.4 Results 157

CHAPTER Page

5.4.1 Lyman Alpha Galaxies 159
5.4.2 Lyman Break Galaxies 161
5.4.3 Robustness of Results 162
5.5 Conclusions 171
6 STELLAR POPULATIONS OF Lyα GALAXIES AT z $\sim$ 0.3 173
6.1 Abstract 173
6.2 Introduction 173
6.3 Lyα Galaxy Sample 175
6.3.1 Stellar Population Modeling 177
6.4 Results 179
6.4.1 Stellar Population Age and Mass 180
6.4.2 Metallicity, Dust and ISM Clumpiness 193
6.4.3 Stellar Evolution Uncertainties 197
6.5 Conclusions 198
7 CONCLUSIONS 200
REFERENCES 208

LIST OF FIGURES

Figure		Page
1.	Distribution of rest-frame Lyman alpha equivalent widths in the LALA Cetus Field.	29
2.	Comparison of Cetus Field LAE object stacks to models.	32
3.	Comparison of Cetus Field LAE individual detections to models.	38
4.	CDF–S LAE candidate selection plane.	52
5.	Tests for CDF–S candidate validity.	54
6.	Cut-out stamps of four CDF–S LAE candidates.	55
7.	Model equivalent width distribution versus stellar population age.	68
8.	Best-fit models to four CDF–S LAEs.	76
9.	Best-fit dust-free models to four CDF–S LAEs.	78
10.	(a) Results from Monte Carlo simulations for four CDF–S LAEs.	81
10.	(b) Results from Monte Carlo simulations (continued).	82
11.	Flux selection planes for second CDF–S study.	97
12.	(a) Cut-out stamps of the new CDF–S LAEs.	101
12.	(b) Cut-out stamps of the new CDF–S LAEs (continued).	102
13.	(a) Best-fit results for all 15 CDF–S LAEs.	117
13.	(b) Best-fit results for all 15 CDF–S LAEs. (continued).	118
13.	(c) Best-fit results for all 15 CDF–S LAEs (continued).	122
13.	(d) Best-fit results for all 15 CDF–S LAEs (continued).	123
13.	(e) Best-fit results for all 15 CDF–S LAEs (continued).	124

Figure Page

14. Object and best-fit model equivalent width distributions for all 15 CDF–S LAEs. 128
15. Histograms of best-fit results for all CDF–S LAEs. 131
16. Histograms of most-likely results for all CDF–S LAEs. 134
17. Combined age probability curve averaged over all candidate CDF–S LAEs. 136
18. Color-color plane highlighting differences in Lyα and Hα EWs for CDF–S LAEs. 142
19. Comparison of LAE and LBG SEDs with ALMA sensitivities. 160
20. Dependence of FIR SED on temperature 163
21. Color-magnitude diagram for comparing LAEs and LBGs to ALMA sensitivity for z $\lesssim$ 4.5. 166
22. Color-magnitude diagram for comparing LAEs and LBGs to ALMA sensitivity for z $\gtrsim$ 4.5. 167
23. Predictions for a z=4.547 millimeter detected starburst galaxy. 170
24. Matching between *GALEX* positions and broadband images for z $\sim$ 0.3 LAEs 178
25. (a) Best-fit results for z $\sim$ 0.3 LAEs. 182
25. (b) Best-fit results for z $\sim$ 0.3 LAEs (continued). 183
25. (c) Best-fit results for z $\sim$ 0.3 LAEs (continued). 184
25. (d) Best-fit results for z $\sim$ 0.3 LAEs (continued). 185

Figure Page

25. (e) Best-fit results for z $\sim$ 0.3 LAEs (continued). 186

25. (f) Best-fit results for z $\sim$ 0.3 LAEs (continued). 187

25. (g) Best-fit results for z $\sim$ 0.3 LAEs (continued). 188

25. (h) Best-fit results for z $\sim$ 0.3 LAEs (continued). 189

25. (i) Best-fit results for z $\sim$ 0.3 LAEs (continued). 190

25. (j) Best-fit results for z $\sim$ 0.3 LAEs (continued). 191

26. Age distribution for z $\sim$ 0.3 LAEs. 194

27. Mass distribution for z $\sim$ 0.3 LAEs. 195

LIST OF TABLES

Table		Page
1.	Best-Fit Ages and Masses for a Constant SFH for Cetus Field LAEs .	36
2.	Best-Fit Ages and Masses for an Exponentially Decaying SFH for Cetus Field LAEs	37
3.	CDF–S Lyα Galaxy Candidates.	56
4.	Magnitudes of CDF–S Lyα Galaxy Candidates.	57
5.	Maximum Age for a Stellar Population with EW $>$ 200 Å.	71
6.	CDF–S Best-Fit Physical Parameters.	77
7.	Optical Magnitudes of 11 New Lyα Galaxy Candidates.	105
8.	NIR and IR Magnitudes of 11 New Lyα Galaxy Candidates.	106
9.	Best-Fit Single Population Models for CDF–S Lyα Galaxy Candidates.	125
10.	Best-Fit Two-Burst Models for CDF–S Lyα Galaxy Candidates.	126
11.	Derived FIR Properties of LAEs.	158
12.	Best-Fit Single Population Models of z $\sim$ 0.3 LAEs.	181

1. INTRODUCTION

1.1. Present Day Galaxies

Studying the formation and evolution of galaxies is currently one of the most active fields in astronomy, vastly helped by the great technological advances over the past few decades. Both large telescopes with multi-CCD cameras as well as big advances in computing power now allow observations and predictions of galaxies in unprecedented detail. In the early 20th century, extra-galactic astronomy focused on the study of nearby objects, as the technology did not exist to probe deeply into the Universe. Initial studies examined the morphology of nearby galaxies, finding that they fell into three main categories which together form the Hubble sequence (Hubble 1936): ellipticals, spirals and irregulars. From their colors, we know that the redder ellipticals are usually passively evolving, with no ongoing star formation (Eggen *et al.* 1962; Larson & Tinsley 1978). Recent studies suggest that most of these objects are the end result of major galaxy mergers (i.e. Kauffmann & White 1993; Kauffmann *et al.* 1993). When two galaxies of comparable size collide, it stimulates copious amounts of star formation, using up much of the available star-forming fuel (gas). After a period of time, the galaxy has relaxed into an elliptical shape, and as it is no longer forming stars, its color is redder, reflecting the number of older stars present.

Spiral galaxies, on the other hand, contain older stars in a central "bulge", with regions of active star formation in a number of outwardly extending spiral arms (e.g., Larson & Tinsley 1978). Gas and dust in these arms get compressed due to spiral density waves, stimulating star formation. Our own Milky Way is a galaxy of this type, and on a dark night one can see the gas and dust fueling this star formation

as a dark stripe in the Milky Way across the sky. Irregulars come in a variety of shapes, but they are usually less massive than spirals and ellipticals, although they too typically show large amounts of ongoing star formation activity.

The vast differences between present day galaxies leads to the natural curiosity of what galaxies looked like in the past. Peering into the history of the universe is possible due to the limitations imposed by the finite speed of light. As we look at more and more distant objects, we are not only looking farther away, but we are also looking back in time, as the photons from these galaxies take time to reach our eyes (or telescopes) at their speed of 300,000 km s^{-1}. This speed is incredibly fast, but it pales in comparison to the vast distances between galaxies. The nearest large spiral to our own is the Andromeda Galaxy (or M31), which at 2.4×10^{19} km distant, results in a travel time of 2.5 Myr for its photons to reach the Milky Way. Thus, we are seeing the Andromeda Galaxy as it was 2.5 Myr ago. This technique can be applied to look as far back in time as our current observatories allow. The farther back one wishes to look, the more observing time (or larger telescope) one will need, as flux falls off inversely proportional to the distance squared.

1.2. The First Galaxies

Countless studies have been done over the last century peering into the past to examine the history of the Universe. One extremely interesting line of questioning involved the idea of the first galaxies. What did they look like? What kind of stars did they contain? Can we observe them? When did they form? Knowing the redshift of formation was crucial to knowing whether or not these objects could be observed.

Estimates for the redshift of the first galaxies ranged from $2 \leq z \leq 30$ (Djorgovski & Thompson 1992). At these distances, any object would be difficult to observe as the light from objects is spread over an extremely large area. However, Partridge & Peebles (1967) published a study claiming that extremely distant galaxies could be detected. They state that if we are seeing these galaxies during formation, we should expect large bursts of star formation to be occurring, which would create objects with very strong ultraviolet (UV) continua. Nearby, this is difficult to observe from the ground, due to the atmospheric cut-off of UV light. However, in very distant objects, thanks to the expansion of the Universe, the UV light will be redshifted into the optical, which can be observed from the ground. Partridge & Peebles go one step further, stating that as much as 7% of the total radiation could be emitted in a single emission line: Lyman alpha (Lyα). A Lyα photon is emitted when a hydrogen atom transitions from its first excited state into its ground state ($2 - 1$). This transition results in the emission of a photon with energy of 10.2 eV, corresponding to a wavelength of 1215.67 Å. Thus, a galaxy with a redshift of $\gtrsim 2$ will have its Lyα flux detectable from the ground ($\lambda \gtrsim 3700$ Å).

Strong Lyα emission can be expected from star forming regions. Stars typically form in over-dense regions regions embedded in clouds of molecular hydrogen. When the first massive stars turn on, they will ionize the hydrogen gas out to a certain distance (creating a Strömgren sphere; Strömgren 1939), followed by a region of atomic hydrogen (in what is called the photo-dissociation region), all surrounded by molecular hydrogen. The most massive stars create large numbers of ionizing pho-

tons, which are photons containing enough energy to ionize a hydrogen atom (E > 13.6 eV; $\lambda < 912$ Å). When these photons reach the atomic hydrogen surrounding the star formation region, they will ionize the hydrogen, separating it into component electrons and protons. After a period of time, dependent on the density and temperature, some electrons will recombine with protons, re-forming hydrogen atoms. When they recombine, the electron needs to shed itself of the energy it gained when it was first ionized, and it does this by emitting photons. There are infinite numbers of energy levels which it can transition to in order to rid itself of the unwanted energy, but hydrogen atoms typically follow a few de-excitation paths, many of which involve the emission of a Lyα photon at the end. In fact, using case B recombination assumptions (which assumes that every Lyman-line photon undergoes many scatterings, also known as the large optical depth approximation), when a hydrogen atom recombines, there is a 2/3 chance that it will emit a Lyα photon to move it into the ground state. Thus, strong star formation begets many ionizing photons, which beget many Lyα photons, which explains the prediction of Partridge & Peebles.

This prediction spawned a plethora of studies to find the first galaxies (e.g., Meier & Terlevich 1981; Koo & Kron 1980; Djorgovski & Thompson 1992; De Propris *et al.* 1993; Cowie & Hu 1998; Rhoads *et al.* 2000). Standard theories predicted that they would be primeval in nature. That is, their metallicities would be extremely low, as metals require previous generations of stars. We could also expect there to be no dust present, assuming that the observations take place before the first stars begin to die. They could also contain the not-yet-detected metal-free stars, known as

"Population III" stars. Most of these first studies met with failure, as, though they used a wide variety of methods to detect redshifted Lyα emission lines, they were unable to confirm detection of the expected population of primeval galaxies (e.g., Koo & Kron 1980; Djorgovski & Thompson 1992; De Propris *et al.* 1993). Djorgovski & Thompson (1992) predicted that these objects should have an expected Lyα line flux of 10^{-16} erg s^{-1} cm^{-2}, which they claimed to be observable with their present day technology. When no candidate primeval galaxies (or Lyα galaxies as we shall call them from here on) were found, numerous ideas were presented to explain their scarcity. Perhaps their fluxes were less than predicted, possibly due to dust (Meier & Terlevich 1981). Lyα photons are resonantly scattered by neutral hydrogen, meaning that they effectively bounce off as they are absorbed and re-emitted, although they can be re-emitted in any direction. Thus, in a homogeneous medium, Lyα photons have much longer path lengths than continuum photons, strongly increasing their chance of encountering a dust grain if dust is present. Add that to the fact that Lyα photons have a much greater chance of absorption than redder continuum photons, and one can begin to see how a small amount of dust could vastly extinguish Lyα flux. This idea had its flaws, as Lyα galaxies (or Lyα emitting galaxies; LAEs) were *supposed* to be primitive, containing no dust. Nonetheless, this issue remained unresolved until the late 1990's, when two groups (Cowie & Hu 1998 & Rhoads *et al.* 2000) detected the first large samples of field LAEs.

1.3. Early Detections of Lyman Alpha Galaxies

There are three popular techniques for locating high-redshift galaxies. The first is called the Lyman break technique, pioneered by Steidel *et al.* (1996). This method involves observing a patch of sky in two adjacent broadband filters, such that the Lyα line falls roughly in the filter overlap region. Flux blueward of the Lyα line suffers attenuation due to clumps of neutral hydrogen in the intergalactic medium (IGM), thus even an object with a flat intrinsic continuum will show a red color between these filters. A color criterion can thus be determined to select galaxies at the chosen redshift with a Δz range of ~ 1. Follow-up spectroscopy can then confirm the redshift estimate, as well as measure a Lyα emission line if one is present (e.g., Shapley 2001, 2003). This method has the benefit of finding large numbers of high-redshift galaxies, but the detriment that follow-up spectroscopy is needed to further confirm the redshift and to measure the Lyα flux.

The second technique involves using a random mask of slits to perform a blind spectroscopic search for LAEs in a typically "blank" field (e.g., Martin *et al.* 2008). This has an advantage over the Lyman break technique in that one obtains the redshift and Lyα line flux in one (usually deeper) observation, but this technique necessitates serendipitous slit placement, and thus the number of objects detected is much less. The third method, narrowband selection, is one of the most popular techniques. One observes a blank field in a narrowband and a broadband filter, with the narrowband residing approximately in the middle of the broadband wavelength coverage. One then compares sources in the two images, and if a source is brighter in the narrowband

than in the broadband, it is an emission line galaxy candidate. This method covers the same angular area as the Lyman break technique, but samples a much thinner slice of redshift space, with a typical $\Delta z \leq 0.1$. While this reduces the total number of objects selected, it gives one a much better estimate of the object's redshift (although typically follow-up spectroscopy is desired to pinpoint the redshift, and confirm that the object is indeed a LAE).

Cowie and Hu (1998) used the narrowband selection technique to locate a sample of 10 LAEs at $z \sim 3.4$ down to a Lyα line flux of 2×10^{-17} erg s^{-1} cm^{-2} over 46 arcmin^2. Rhoads *et al.* (2000) started the Large Area Lyman Alpha survey (LALA), which in this first paper published the finding of 174 LAEs at $z \sim 4.5$ in two adjacent narrowband filters over ~ 0.3 deg^2, with narrowband fluxes from 2.6 to 5.2×10^{-17} erg s^{-1} cm^{-2}. Why did these two surveys succeed when surveys not five years earlier failed? The answers are different, but the underlying cause is the same: technological advancement. Cowie and Hu made use of the Keck telescopes for their observations, which with 10m diameter mirrors, are the largest telescopes in the world (at the time of this writing). Keck came online in the mid-1990's, thus it was not available for the earlier studies. Cowie and Hu were able to probe fainter line fluxes, close to 10^{-17} erg s^{-1} cm^{-2}, resulting in their discovery of numerous LAEs, even though their instrument (LRIS) had a field-of-view comparable to that used by Djorgovski & Thompson (~ 5 arcmin^2; 1992).

While the LALA survey used the 4 m Mayall telescope at the Kitt Peak National Observatory, which had been around for decades, they made use of the very new

MOSAIC camera, which allowed observations over a wide field by pasting together eight 2048x4096 CCDs, for a field-of-view of 1296 arcmin^2 (or 0.36 deg^2). This field of view is over 200 times larger than that used by Djorgovski & Thompson (1992), thus Rhoads *et al.* were able to detect large numbers of candidate LAEs in only 6 hours of imaging per filter. We can thus see that Lyα galaxies were fainter and sparser than originally predicted, as Cowie & Hu and Rhoads *et al.* have shown that an increase in depth and/or field-of-view results in the successful discovery of large numbers of LAEs.

1.4. Scientific Results

In the few years following these first detections there were numerous topics for study, as including the Lyα equivalent widths (e.g., Malhotra & Rhoads 2002, hereafter MR02; Dawson *et al.* 2007) and the Lyα luminosity functions (e.g., Malhotra & Rhoads 2004; Dawson *et al.* 2004, 2007; Gronwall *et al.* 2007; Ouchi *et al.* 2008; Deharveng *et al.* 2008). The luminosity function studies primarily looked into the evolution of the luminosity function with redshift to search for changes in LAE number density. Finding evidence that the LAE number density decreases at higher redshift could indicate that the IGM is becoming predominantly more neutral, and as thus is evidence for the onset of reionization. The results from these studies are still ambiguous, although both Malhotra & Rhoads (2004) and Ouchi *et al.* (2008) found results consistent with no evolution out to z $\sim$ 6.5, implying that their observations have not yet located the epoch of reionization. Deharveng *et al.* (2008) published a luminosity function for LAEs at z $\sim$ 0.3, identified using the *Galaxy Evolution Explorer*

(*GALEX*), finding that the number densities of LAEs at z $\sim$ 0.3 is much less than that at z $\sim$ 3.1 (Gronwall *et al.* 2007), implying significant evolution towards lower redshifts, perhaps consistent with hierarchical clustering theories of galaxy evolution.

In a spectroscopic study, Dawson *et al.* (2007) found that a non-negligible fraction of their confirmed Lyα lines had rest-frame equivalent widths (EWs) exceeding theoretical predictions from normal stellar populations. A stellar population with solar metallicity, a Salpeter (1955) initial mass function (IMF) and a constant star formation history will have a maximum Lyα EW of 260 Å at 1 Myr, dropping rapidly to a constant value of 95 Å by 100 Myr (dropping to zero in any kind of decaying star formation history). Dawson *et al.* found that 12 – 27% of their LAEs showed rest-frame EWs $>$ 240 Å. They were not the first to see this, as both Kudritzki *et al.* (2000) and MR02 also found a large number of LAEs with strong EWs. While it is certainly possible for a single LAE to have an EW near 250 Å, the sheer number of high EW objects indicates that either a large fraction of LAEs are $\sim$ 1 Myr, or that our initial assumptions are wrong. It is exceedingly unlikely that a large fraction of LAEs are only 1 Myr old, and even if they were, the chance that we would observe them during that 1 Myr is small.

1.5. Reasons for Large Lyα EWs

There are a few possibilities which could explain the large EWs seen in LAEs. The first possibility is that these objects are creating more ionizing photons than we know of, which in turn creates more Lyα photons. This could happen if the metallicity was extremely low, which would create hot stars. If the metallicity was zero, Popula-

tion III stars could be created. These zero metallicity objects would be expected to produce regions with very large Lyα EWs (Scannapeico *et al.* 2003; Venkatesan *et al.* 2003). Due to their hard spectra, these objects produce many photons which are capable of ionizing He II, thus He II recombination lines, such as λ1640, λ3202 and λ4686, could be possible signatures of Population III stars (i.e., Tumlinson & Shull 2000; Tumlinson *et al.* 2001). However, these signatures (specifically the 1640 Å line, which is expected to be the strongest; Tumlinson *et al.* 2001) have yet to be definitively detected (e.g., Dawson *et al.* 2004; Nagao *et al.* 2008), casting doubt upon the existence of Population III stars in these objects. Even a near zero metallicity will result in some increase in the Lyα line strength through hotter photospheres and/or top-heavy IMFs (e.g., Schaerer 2002; Schneider *et al.* 2006), although whether it is enough to explain the observations is doubtful.

Active galactic nuclei (AGN) are extremely bright regions near the centers of many galaxies which are fueled by the central black holes in these galaxies. AGN typically show an assortment of high ionization state emission lines, as well as a very strong Lyα line. These Lyα photons are not produced by star formation, and thus there is no fiducial limit on the EW. Thus, to be sure that known LAEs are not AGN, we have to screen against them. This is typically done in two ways. First, AGN frequently emit in X-rays, thus if a LAE is X-ray detected, it is a sign that it is a possible AGN. Wang *et al.* (2004) and Malhotra *et al.* (2003) surveyed *Chandra* X-ray data of the LALA fields, and concluded that less than 4.8% of the LAEs they studied could be possible AGN. However, in some cases it is possible that the X-rays

can be obscured, and thus it is also prudent to obtain spectra and check for the typical high ionization state lines seen in AGN. Dawson *et al.* (2004) found no detection of these lines in LAEs from the LALA survey, providing further proof that the majority of narrowband selected LAEs are not AGN, thus an active galactic nucleus is an unlikely source for the stronger than expected EWs observed.

Another possible cause of large Lyα EWs in high-redshift LAEs involves dust. According to Meier and Terlevich (1981), dust should severely attenuate Lyα, even more than continuum light, resulting in lower EWs. However, this involves an assumption that the interstellar medium (ISM) is roughly uniform, meaning that the Lyα will see dust in every direction. However, what if the ISM was clumpy? Neufeld (1991) argued (and Haiman & Spaans 1999 and Hansen & Oh 2006 theoretically confirmed) that if the ISM was sufficiently clumpy, the opposite effect could actually occur. Imagine an ISM consisting of clumps of evenly mixed dust and neutral hydrogen, with the inter-clump medium only containing ionized hydrogen. A Lyα photon will move freely throughout this ISM until it encounters a clump. When it does encounter a clump, it will be resonantly scattered by a hydrogen atom at the surface. At this point, it will be re-emitted in any direction, meaning that 50% of the time, it will move back out into the inter-clump medium. Even if it is sent directly into the clump, it will be absorbed immediately by the next hydrogen atom it encounters, thus it is extremely difficult for Lyα photons to penetrate deeply into these clumps.

Continuum photons suffer no such restrictions. They are not resonantly scattered by hydrogen, and thus they will make their way deeper into a clump, until they

are eventually absorbed or scattered by a dust grain, resulting in extinction and/or reddening of the continuum light. Thus, this ISM geometry results in (most of) the Lyα photons being screened from ever encountering a dust grain. Since the EW is a measure of the Lyα to continuum ratio, the EW we would measure is increased relative to the intrinsic value coming out of the star formation regions. While this scenario posed a definite possible explanation for the observed EW distribution, we had no way to study its existence until recently.

1.6. Modeling the Stellar Populations of LAEs

The technique of learning about distant galaxies by comparing their observed spectral energy distributions (SEDs) to theoretical models has gained popularity in recent years. The most widely used models are those of Bruzual & Charlot (2003; BC03). Essentially, these models take as input a stellar population metallicity, star formation history and age, and output the combined spectrum of all of the stars. One then fits a grid of models to their observations in order to see which model best explains the observed SED. Over the past five years, a few groups have used this technique to learn about Lyα galaxies (Chary *et al.* 2005; Gawiser *et al.* 2006; Pirzkal *et al.* 2007; Lai *et al.* 2007, 2008; Nilsson *et al.* 2007). Most of these studies find that LAEs are in general young and low mass, consistent with earlier predictions.

One thing these studies lack is a detailed examination of the contribution of the Lyα line to the SED. The motivation behind this thesis is to improve upon these earlier studies in order to investigate the cause of the large number of high EW LAEs seen. To do this we compare observations to models which include the effect of not

only a Lyα emission line, but also the effect of dust geometry (or clumpiness) on the Lyα EW. While the BC03 models do not tabulate emission line strengths, they do give the number of ionizing photons present in a given stellar population, which (using case B recombination assumptions) one can convert into a Lyα flux.

In Chapter 2 we discuss our first study, where we obtained continuum measurements of LAEs via broadband imaging. These ground-based observations were not deep enough to constrain the dusty scenario, but we were able to confirm that those LAEs with the largest Lyα EWs were (on average) some of the youngest and lowest mass objects in the Universe known to date. In Chapter 3, we improve upon our previous work by obtaining narrowband observations in the Great Observatories Origins Deep Survey (GOODS) Chandra Deep Field – South (CDF – S), which allowed the discovery of four new LAEs in a field with very deep public space-based broadband data. These deeper data allowed us to fit stellar population models to individual LAEs. Chapter 4 continues the work of Chapter 3 with a much larger sample of LAEs. In Chapter 5, we discuss different ways of constraining the dust in these objects by studying the likelihood of detecting dust emission from high-redshift LAEs. In Chapter 6, we finish with an analysis of low-redshift LAEs, and discuss the differences from their high-redshift counterparts. In Chapter 7, we present our conclusions, drawing upon the results of each study. Chapters 2 and 3 are published in the Astrophysical Journal, volume 660, page 1023 and volume 678, page 655 respectively. At the time of this writing, Chapter 4 is undergoing peer review at the Astrophysical Journal, Chapter 5 is undergoing peer review at the Monthly Notices

of the Royal Astronomical Society, and Chapter 6 is in preparation for submission to the Astrophysical Journal.

2. THE AGES AND MASSES OF Lyα GALAXIES AT z $\sim$ 4.5

2.1. Abstract

We examine the stellar populations of a sample of 98 z $\sim$ 4.5 Lyα emitting galaxies using their broadband colors derived from deep photometry at the Multiple Mirror Telescope (MMT). These galaxies were selected by narrowband excess from the Large Area Lyman Alpha survey. Twenty-two galaxies are detected in two or more of our MMT filters (g', r', i' and z'), with calculated rest-frame equivalent widths (EWs) from 5 to 800 Å. By comparing broad and narrowband colors of these galaxies to synthetic colors from stellar population models, we determine their ages and stellar masses. The highest EW objects have an average age of 4 Myr, consistent with ongoing star formation. The lowest EW objects show an age of 40 - 200 Myr, consistent with the expectation that larger numbers of older stars are causing low EWs. We found stellar masses ranging from 2×10^7 $M_\odot$ for the youngest objects in the sample to 2×10^9 $M_\odot$ for the oldest. It is possible that dust effects could produce large EWs even in older populations by allowing the Lyα photons to escape, even while the continuum is extinguished, and we also present models for this scenario.

2.2. Introduction

There are two popular techniques for locating galaxies at high redshift: the Lyman break technique (Steidel *et al.* 1996) and narrowband selection. The latter entails observing a galaxy in a narrowband filter containing a redshifted emission line. This method is useful to select high-redshift galaxies with strong Lyman alpha (Lyα) emission lines. While the line emission properties of Lyman break galaxies (LBGs) are known, little is known about the continuum properties of Lyα galaxies because they are so faint. Studying the continuum properties of these Lyα galaxies at high

redshift can tell us about their age, stellar mass, dust content and star formation history.

We have used the narrowband selection technique to locate and study Lyα emitting galaxies (LAEs) in the Large Area Lyman Alpha (LALA; Rhoads *et al.* 2000) survey Cetus Field at z $\sim$ 4.5. Similar studies have been done both in this field and in other fields (e.g., Rhoads *et al.* 2000, 2004; Rhoads & Malhotra 2001; Malhotra & Rhoads 2002; Cowie & Hu 1998; Hu *et al.* 1998, 2002, 2004; Kudritzki et al 2000; Fynbo, Möller, & Thomsen 2001; Pentericci *et al.* 2000; Stiavelli *et al.* 2001; Ouchi et al. 2001, 2003, 2004; Fujita et al. 2003; Shimasaku *et al.* 2003, 2006; Kodaira et al. 2003; Ajiki et al. 2004; Taniguchi *et al.* 2005; Venemans *et al.* 2002, 2004; Pascarelle *et al.* 1996ab). In many of these studies, the strength of the Lyα line has been found to be much greater than that of a normal stellar population (Kudritzki et al. 2000; Dawson *et al.* 2004). Malhotra & Rhoads (2002, hereafter MR02) found numerous LAEs with rest-frame equivalent widths (EWs) $>$ 200 Å. Assuming a constant star formation history, the EW of a normal stellar population will asymptote toward 80 Å by 10^8 yr, down from a maximum value of $\sim$ 240 Å. These galaxies are of interest, because it is believed that this strong Lyα emission is a sign of ongoing star formation activity in these galaxies (Partridge & Peebles 1967), and it could mean that these are some of the youngest galaxies in the early universe.

There are a few possible scenarios that could be creating these large EWs. Strong Lyα emission could be produced via star formation if the stellar photospheres are hotter than normal, which could happen in low-metallicity galaxies. It could also

mean that these galaxies have their stellar mass distributed via a top-heavy initial mass function (IMF). Both of these scenarios are possible in primitive galaxies, which are thought to contain young stars and little dust.

Active galactic nuclei (AGNs) can also produce large Lyα EWs. In an optical spectroscopic survey of z $\sim$ 4.5 Lyα galaxies, Dawson et al. (2004) found large Lyα EWs, but narrow physical widths (Δv $<$ 500 km s^{-1}). They placed tight upper limits on the flux of accompanying high-ionization state emission lines (e.g., N v λ1240, Si iv λ1398, C iv λ1549 and He ii λ1640), suggesting that the large Lyα EWs are powered by star formation rather than AGNs. Type I (broad-lined) AGNs are also ruled out as the Lyα line width is greater than the width of the used narrowband filters. While Type II AGN lines are narrower than our filters, they remain broader than the typical line width of our Lyα sample as determined by follow-up spectroscopy (e.g., Rhoads *et al.* 2003). Malhotra *et al.* (2003) and Wang *et al.* (2004) searched for a correlation between LAEs and Type II AGNs using deep *Chandra X-Ray Observatory* images. None of the 101 Lyα emitters known to lie in the two fields observed with *Chandra* were detected at the 3 σ level ($L_{2-8keV} = 2.8 \times 10^{42}$ erg s^{-1}). The sources remained undetected when they were stacked, and they concluded that less than 4.8% of the Lyα emitters they studied could be possible AGNs. Therefore, we are confident that there are at most a few AGNs in our Lyα galaxy sample.

Another possible scenario involves enhancement of the Lyα EW in a clumpy medium. In this scenario, the continuum light is attenuated by dust, whereas the Lyα line is not, resulting in a greatly enhanced observed Lyα EW (Neufeld 1991;

Hansen & Oh 2006). This can happen if the dust is primarily in cold, neutral clouds, whereas the inter-cloud medium is hot and mainly ionized. Because Lyα photons are resonantly scattered, they are preferentially absorbed at the surface. Thus, it is highly unlikely that a Lyα photon will penetrate deep into one of these clouds. They will be absorbed and re-emitted right at the surface, effectively scattering off of the clouds and spending the majority of their time in the inter-cloud medium. However, continuum photons are not resonantly scattered, and if the covering factor of clouds is large, they will in general pass through the interior of one. Thus the continuum photons will suffer greater attenuation than the Lyα photons, effectively enhancing the Lyα EW.

These Lyα galaxies are so faint compared to other high-z objects that have been studied, that not a lot is known about their continuum properties. Our primary goal is to better constrain the ages and stellar masses of these objects from their continuum light in order to better understand the driving force behind the strength of the Lyα line. We have obtained deep broadband imaging in the g', r', i' and z' bands for this purpose. Using the colors of these galaxies, we can study continuum properties of individual Lyα emitting galaxies at this redshift for the first time, allowing us to estimate their age, mass, star formation history and dust content. The next phase of our project will be to look into the likelihood of dust causing the large Lyα EW, which we will begin to do in this paper, as the colors of these galaxies might distinguish the cause of the large EW. Blue colors would indicate young stars with hot photospheres, while red colors would indicate dust quenching of the continuum,

enhancing the Lyα EW. Observations, data reduction technique and sample selection are reported in § 2.3; results are presented in § 2.4, and they are discussed in § 2.5. Conclusions are presented in § 2.6.

2.3. Data Handling

2.3.1. *Observations*

The LALA survey began in 1998 using the 4m Mayall telescope at the Kitt Peak National Observatory (KPNO). The final area of this survey was 0.72 deg^2 in two fields, Boötes and Cetus, centered at 14:25:57, +35:32:00 (J2000.0) and 02:05:20, -04:55:00 (J2000.0), respectively (Rhoads *et al.* 2000). The LALA survey found large samples of Lyα emitting galaxies at z = 4.5, 5.7, and 6.5, with a spectroscopic success rate of up to 70%. We observed the LALA Cetus Field for three full nights in November 2005, and again for four $\frac{1}{4}$ nights in January 2006, using the Megacam instrument (McLeod *et al.* 1998) at the Multiple Mirror Telescope (MMT). Megacam is a large mosaic charge-coupled device (CCD) camera with a 24' × 24' field of view, made up of 36 2048 × 4608 pixel CCDs. Each pixel is 0.08″on the sky. We acquired deep broadband images in four Sloan Digital Sky Survey (SDSS) filters: $g'(\lambda_c \sim$ 4750 Å), r' ($\sim$ 6250 Å), i' ($\sim$ 7750 Å) and z' ($\sim$ 9100 Å). The total exposure time in the g', r', i', and z' filters were 4.33, 3.50, 4.78 and 5.33 hr, respectively. Given that the seeing during the run was rarely below 0.8″, we chose to bin the pixels 2 × 2 to reduce data volume, resulting in a final pixel scale of $\sim 0.16''$pixel^{-1} in our individual images.

2.3.2. *Data Reduction*

The data were reduced in IRAF[1] (Tody 1986, 1993), using the MSCRED (Valdes & Tody 1998; Valdes 1998) and MEGARED (McLeod *et al.* 2006) reduction packages. The data were first processed using the standard CCD reduction steps done by the task ccdproc (overscan correction, trim, bias subtraction and flat fielding). Bad pixels were flagged using the Megacam bad pixel masks included with the MEGARED package.

Fringing was present in the i'- and z'-band data, and needed to be removed. For this, we made object masks using the task objmasks.[2] We then took a set of science frames in each filter, and combined them to make a skyflat using sflatcombine (using the object masks to exclude any objects from the resulting image). This skyflat was then median smoothed on a scale of 150 $\times$ 150 pixels (i') and 200 $\times$ 200 pixels (z'). The smoothed images were subtracted from the unsmoothed images, and the result was a fringe frame for each band. The fringing was then removed from the science images using the task rmfringe, which scales and subtracts the fringe frame. To make the illumination correction, skyflats were made, median smoothed 5$\times$5 pixels, normalized, and divided out of the science images.

The amplifiers in the reduced images were merged (from 72 to 36 extensions) using the MEGARED task megamerge. The World Coordinate System (WCS) writ-

[1]IRAF is distributed by the National Optical Astronomy Observatory (NOAO), which is operated by the Association of Universities for Research in Astronomy, Inc. (AURA), under cooperative agreement with the National Science Foundation.

[2]In order to prevent fringing from making it onto the object masks, we first made a skyflat without object masks, and divided this skyflat out of the science data. We then got the object masks from these quasi-fringe removed images. The rest of the procedure used the untouched science frames.

ten in the image header at the telescope is systematically off by 0.5° in rotation, so we used the task fixmosaic to adjust the rotation angle so that the WCS solution works better. The WCS was then determined using megawcs, and the WCS distortion terms were installed in the header using the task zpn.

The 36 chips were combined into a single extension using the program SWarp[3]. We ran SWarp on each input image, using a corresponding weight map that gave zero weight to known bad pixels and cosmic-ray hits. We located the cosmic rays using the method of Rhoads (2000). We specified the center of the output images to be the average center of the five dither positions we used (02:04:56, -05:01:01 [J2000.0]), which corresponded to an image size of 11988 × 10881 pixels and a pixel scale of $0.1587''\text{pixel}^{-1}$. During this process, each image was resampled (using the Lanczos-3 6-tap filter) and interpolated onto the new pixel grid. While this was done, SWarp determined and subtracted the background value in each extension.

An initial stack for each filter was made using SWarp to average together the individual images. To make the final version of the stack, we needed to remove the satellite trails that littered our images. To do this, we created a difference image between each individual input image and the initial stack. Using a thresholding technique, we flagged the satellite trails in this image, and combined those flags with the existing weight maps. We ran SWarp a final time with this as the input weight map, creating the final stack. We did this process for each band, giving us four images, one final stack in each of the g', r', i' and z' bands. In an attempt to increase

[3]SWarp is a program that resamples and co-adds together FITS images, authored by Emmanuel Bertin. It is distributed by Terapix at http://terapix.iap.fr/soft/swarp.

the signal of our objects, we tried co-adding R- and I-band images from the NOAO Deep Wide-Field Survey (NDWFS; Jannuzi & Dey 1999) to our r' and i' images; however, the additional signal did not make a significant difference in the results. The median FWHM in the final stacks were: g'=1.29″, r'=1.08″, i'=1.25″and z'=1.32″.

To calculate the photometric zero point for our observations we took images of the standard stars SA95 190 and SA95 193 during our run, where the zeropoint is defined as the magnitude of an object with one count in the image (for an integration time of 400 s). These standard stars are from Landolt (1992), and we used the transforms from Johnson-Morgan-Cousins to SDSS magnitudes from Fukugita et al. (1996). Averaging the results from the two stars for each band, we obtained these zero points: g'=33.13, r'=33.00, i'=32.58 and z'=31.43 mag. Using these zero points with our data, all of our results are in AB magnitudes.

2.3.3. *Lyα Galaxy Selection*

To extract the objects from each stack, we used the SExtractor package (Bertin & Arnouts, 1996). For SExtractor to accurately estimate the errors in the flux, it needed to know the gain in the input images. To calculate this, we needed the mean and standard deviation of the background of the images. Because the background was subtracted out in SWarp, we obtained the average background value in each band by averaging the values obtained from the pre-SWarped images, and adding this value onto the final stacks. We then ran SExtractor in the two-image mode using a 9 pixel aperture (2.32″) with the narrowband images from the LALA survey, giving us catalogs of objects that were detected in both images.

To calculate the errors on our photometry, we measured aperture fluxes at a few million randomly placed locations throughout the image. We performed the aperture photometry using SExtractor in two-image mode, with our stacked images as the photometry image and an artificial image containing randomly placed points as the detection image. We then measured σ empirically from the distribution of counts in these random apertures. The 5σ limiting magnitudes of our final stacks, measured in 2.32″diameter (9 pixel) apertures, were g'=26.38, r'=25.64, i'=25.13 and z'=24.31 mag.

The method we have used to locate Lyα galaxies involves taking an image using a narrowband filter containing the wavelength for Lyα at a certain redshift. We used the catalog from MR02, which was based on LALA narrowband images and broadband B_w, R, and I data from the NDWFS (Jannuzi & Dey 1999). The narrowband data consist of five overlapping narrowband filters, each with a FWHM $\sim$ 80 Å. The central wavelengths are $\lambda\lambda$6559 (H0), 6611 (H4), 6650 (H8), 6692 (H12), and 6730 (H16), giving a total redshift coverage $4.37 < z < 4.57$. To ensure that there was no overlap, we only used objects selected from the H0, H8 and H16 filters in our analysis. In order to compare the two data sets, the Megacam data were registered and remapped onto the same scale as the narrowband data using the IRAF tasks wcsmap and geotran.

Selection criteria for the MR02 catalog, following Rhoads & Malhotra (2001), were as follows: (1) 5 σ significance detection in the narrowband. This is calculated using an SExtractor aperture flux with the associated flux error; flux/error $\geq$ 5. (2)

4 σ significant excess of narrowband flux. This was calculated by taking narrowband flux – broadband flux, both calibrated in physical units, and the associated error [sqrt(error$^2_{broad}$ + error$^2_{narrow}$)] and demanding that flux difference / error $\geq$ 4. (3) Factor of $\geq$ 2 ratio between broad and narrowband fluxes, calibrated to the same units. (4) No more than 2 σ significant flux in the bluest filter observed (B_w).

2.3.4. *Stellar Population Models*

In order to study the properties of the galaxies in our sample we compare them to stellar population models, using the stellar population modeling software of Bruzual & Charlot (2003). With these models, we were able to choose a range of ages, metallicities and star formation histories for comparison with our sample. We chose ages ranging from 10^6 to 10^9 yr, metallicities from 0.02 $Z_\odot$ to $Z_\odot$ and exponentially decaying star formation histories with a characteristic timescale of $\tau = 10^3$ - 2×10^9 yr. We included dust via the Calzetti dust extinction law (Calzetti et al. 1994), which is applicable to starburst galaxies, in the range $A_{1200} = 0$ - 2 mag. Finally, we included intergalactic medium (IGM) absorption via the prescription of Madau (1995).

The Bruzual & Charlot (2003, hereafter BC03) code output the flux of a given stellar population in units of $L_\odot$ Å^{-1}. In order to go from flux in these units to bandpass averaged fluxes, we used the method outlined by Papovich *et al.* (2001). In short, we took the output from BC03, and converted it from L_λ into L_ν, and then from L_ν into F_ν (in units of ergs s^{-1} cm^{-2} Hz^{-1}) using $F_\nu = (1 + z)\ L_\nu\ /\ (4\pi d^2_L)$. This flux was then multiplied by the transmission function for a given bandpass, and integrated over all frequency. The bandpass averaged flux $\langle f_\nu \rangle$ is this result normalized to the

integral of the transmission function. AB magnitudes (Oke & Gunn, 1983) for the candidates were then computed.

In order to calculate colors that we could directly compare to our observations, it was necessary to add in emission-line flux from the Lyα line, which appears in the r' filter at z $\sim$ 4.5. While the BC03 software does not calculate emission-line strengths, we were able to use one of its many other output quantities: the number of ionizing photons. We calculated the Lyα emission-line strength[4] (in units of $L_{\odot}$Å^{-1} to match the model output) by using

$$Ly\alpha\ Linestrength = \frac{hc}{\lambda_{Ly\alpha} L_{\odot} \Delta\lambda}\ \frac{2}{3}\ n_{ion} \tag{1}$$

where n_{ion} is the number of ionizing photons, $\Delta\lambda$ is the bin size of the wavelength array (1 Å), and the factor of 2/3 represents the fraction of ionizing photons that will produce Lyα photons when interacting with the local interstellar medium (ISM) under case B recombination. In effect, this spreads the line flux over a finite wavelength interval, so that the conversion from L_{ν} to F_{ν} properly redshifts both the line and continuum emission. In order to model the clumpy dust scenario, we needed to ensure that the Lyα line did not suffer dust attenuation. To do this, the continuum flux was multiplied by the Calzetti dust law before we added in the Lyα flux to the spectrum at the correct wavelength bin. In this case, the continuum suffers dust attenuation, while the Lyα line does not.

[4]This calculation follows the simple assumptions that no ionizing photons escape, and that all Lyα photons escape.

2.4 Results

2.4.1. *Lyα Galaxy Candidates*

Using the catalog described above, we have identified 98 objects as Lyα galaxy candidates within the $24' \times 24'$ Megacam field of view, in a total comoving volume of 3.3×10^6 Mpc^3 (using the three non-overlapping LALA narrowband filters). We have classified 22 of these objects as continuum detections on the basis that they have at least 2σ detections in two of the r', i', or z' bands (the other 76 objects were undetected at this level in the broadband data, but we later stacked their fluxes for analysis).

We have in our possession Inamori Magellan Areal Camera and Spectrograph (IMACS) spectra of objects in the LALA Cetus Field (Wang *et al.* 2007). These spectra have been used to identify the redshift of the Lyα line in these galaxies. Out of the 98 total Lyα galaxy candidates, 28 have been spectroscopically confirmed as being Lyα emitters at z $\sim$ 4.5. Seven of these confirmations are among the 22 Megacam detections. Another seven of the Megacam detections have IMACS spectra but had no strong Lyα line identified. However, some of these may show a line with deeper spectra.

2.4.2. *Equivalent Width Distribution*

We calculated the rest-frame equivalent widths of our 22 detections using the ratio of the line flux to the continuum flux via

$$EW = \left(\frac{1 - \eta}{\frac{\eta}{\Delta\lambda_{BB}} - \frac{1}{\Delta\lambda_{NB}}} \right) \; (1 + z)^{-1} \tag{2}$$

where η is the ratio of narrowband to broadband flux (in units of f_ν), and $\Delta\lambda$ are the filter widths (80 and 1220 Å for the narrow and broad filters, respectively). The narrowband fluxes are measured from the LALA narrowband data discussed above, and the broadband fluxes are measured from our MMT r' data.

Figure 1 shows the calculated rest-frame EWs of our 22 continuum-detected galaxies. The range of EWs is 5 – 800 Å.[5] While the range of our EW distribution peaks at the low end of previous studies (i.e. most of our objects have rest-frame EW $\lesssim$ 200 Å), we recognize that the 76 undetected objects would all lie at the high EW end of this plot (in fact, they peak at EW well over 200 Å). Because they are undetected, this means that their broadband fluxes were too faint to be detected in our survey. However, they still have very bright narrowband fluxes, indicating strong Lyα emission. This strong emission, coupled with faint broadband r' magnitudes, results in a high Lyα EW.

From models of normal stellar populations (those with a near-solar metallicity and a Salpeter (1955) IMF), it was found that the maximum EW a galaxy could have is $\sim$ 240 Å at t $\sim 10^6$ yr, with the EW approaching a steady value of 80 Å at t $\sim 10^8$ yr (MR02; Charlot & Fall 1993). Our data show many objects with a rest-frame EW greater than 100 Å. While individual galaxies with EWs this high are possible from normal stellar populations, the ratio of high-low EWs is much greater than it ought to be when we account for the 76 objects without MMT detections. This implies that something is causing the EWs to be higher than normal. MR02 consider several

[5]However, the object with an EW of 5 Å is likely an interloper. It has a $\sim 10\ \sigma$ detection in g', and $> 30\ \sigma$ detections in r', $i'$and z'. We exclude this object from the rest of our analysis, giving us 21 detections.

possible explanations for this observation. Hot photospheres and/or the radiative transfer effects discussed above are sufficient explanations. Another possibility is that galaxies above a certain age, around 10^8 yr, are removed from the sample by some mechanism. For example, the first generations of stars might form (uniformly distributed) dust that further suppresses the Lyα EW, removing a large proportion of intermediate-EW objects from the sample. One of our goals in this study is to investigate whether the cause is massive stars creating more Lyα photons, or dust suppressing the continuum and thus enhancing the Lyα EW.

We note that four objects among our MMT detections show rest-frame EWs in excess of 230 Å. Such high EWs might be explained by a combination of extreme youth and/or low metallicity (e.g. Malhotra & Rhoads 2004), or might be produced by radiative transfer effects (Neufeld 1991; Hansen & Oh 2006). However, two of these objects are consistent with 200 Å EW at the 1 σ level, and the other two at the 2 σ level, so such mechanisms are not strictly required to explain these objects. Stronger evidence for such effects may be found among the 76 sources whose continuum emission was too faint for our MMT data.

2.4.3. *Stacking Analysis*

Our goal has been to be able to compare our objects to the models to obtain estimates of physical parameters such as age and stellar mass, along with dust content. We divided our objects into six groups that we then stacked (in order to increase the signal–to–noise) to get composite fluxes that we could compare to the models. The groups are: non-detections, which consists of the 76 selected objects which did not

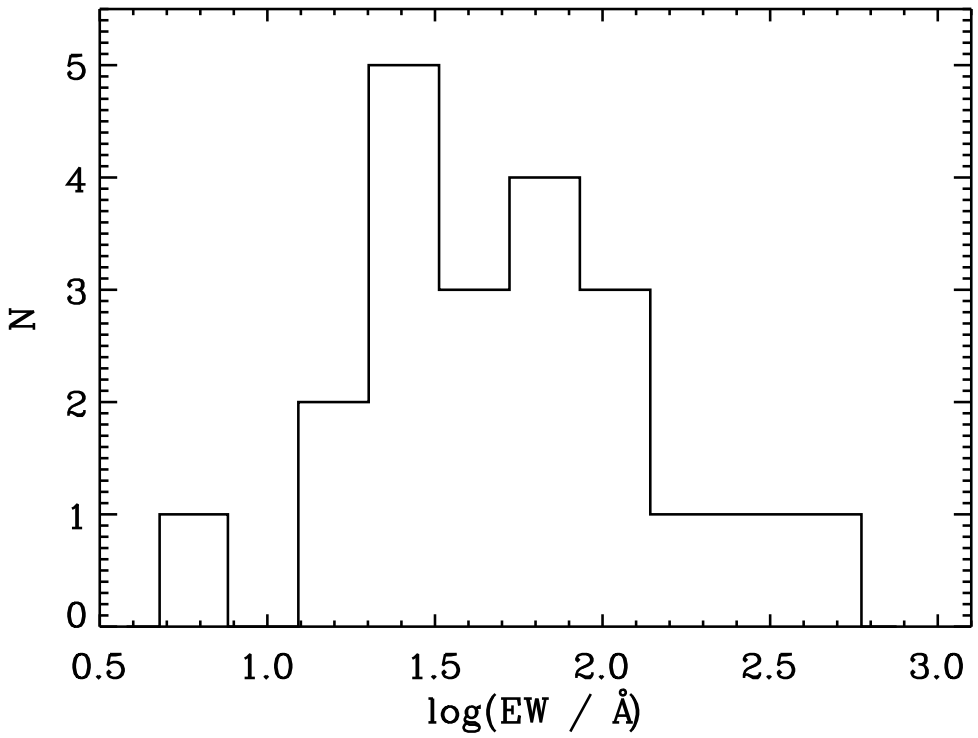

FIG. 1.—Distribution of rest-frame Lyα EWs from our 22 detections. The EWs range from 5 to 800 Å. The single object with EW < 20 Å is likely an interloper that has managed to satisfy our selection criteria. A normal stellar population has an EW that asymptotes to ~ 80 Å as its age goes to 10^8 yr, so something is causing the Lyα EW of many of these objects to be higher.

have a 2 σ detection in at least two bands (out of r', i', and z'); low EW, which consists of the seven detected objects with EW of 20 – 40 Å; middle EW, which consists of the seven detected objects with EW of 45 – 100 Å; high EW, which consists of the seven detected objects with EW $\geq$ 110 Å; detections, which consists of the 21 objects that were detected in the Megacam data; spectroscopically confirmed, which consists of the 28 objects (seven detected) that were confirmed to be Lyα emitters at z $\sim$ 4.5. These stacks are shown in Figure 2.

2.4.4. *Age and Mass Estimates*

In order to study these galaxies, we have created numerous synthetic stellar population models that we compare to our observed galaxies. The most illuminating way in which we can study the observed vs. model galaxies are in color-color plots (Figure 2 and Figure 3). We have plotted the r' - nb color vs. the r' - i' color of our objects, and then overplotted various model curves. Because changing the metallicity did not much change the position of the model curves in the plane we are studying, we have elected to only use models with Z = .02 $Z_{\odot}$. The differing line styles represent the two different star formation histories we used, with the solid lines representing continuous star formation, and the dashed lines representing exponentially decaying star formation with a decay time of $\tau = 10^7$ yr.

We ran the models at 24 different ages ranging from 1 Myr to 2 Gyr,[6] and in the figure we show the five ages that best surround the data, represented by different colors. We included dust in the models, ranging from $A_{1200} = 0$ to 2. The extent of

[6]At 1 Myr, the two different star formation histories have identical colors, so their model tracks overlap, that is why it appears as if there is no curve for an exponentially decaying galaxy at 1 Myr.

the model tracks represents the different dust optical depths. As we discussed above, this dust does not affect the strength of the model Lyα line. We have connected the zero-dust end of the model tracks with the dotted black line in order to show where galaxies with no dust should lie.

With significant flux in only three broadband points (r', i', and z'), it would be hard to fit each stack to models with a full range of every parameter. However, given what we have learned from studying these objects in the color-color plane, it is relatively straightforward to fit an age to each of these stacks (assuming a star formation history and no dust). In order to fit the age, we considered 20 different ages ranging from 1 to 200 Myr (including the five ages shown in Figure 2). By finding the model point (we used the $A_{1200} = 0$ point for each model; see discussion for details) closest to each stack, we have effectively found the average age of an object in the stack. Because we did not want to limit ourselves to one star formation history, we have found two ages for each object: one from the closest model with a constant star formation history (SFH), and one from the closest model with an exponential SFH. These ages are reported in Table 1 and Table 2 for constant and exponentially decaying SFHs, respectively. For a constant SFH, the ages ranged from 1 to 200 Myr, while for an exponentially decaying SFH, they ranged from 1 to 40 Myr.

In order to find the stellar mass, we wanted to only use the best fit model for each stack. We took that to be the model with the best-fit age found above, and we calculated a mass for each SFH. The mass was found by a simple weighted ratio of object flux to model flux. We derived the weighting by minimizing the ratio of the

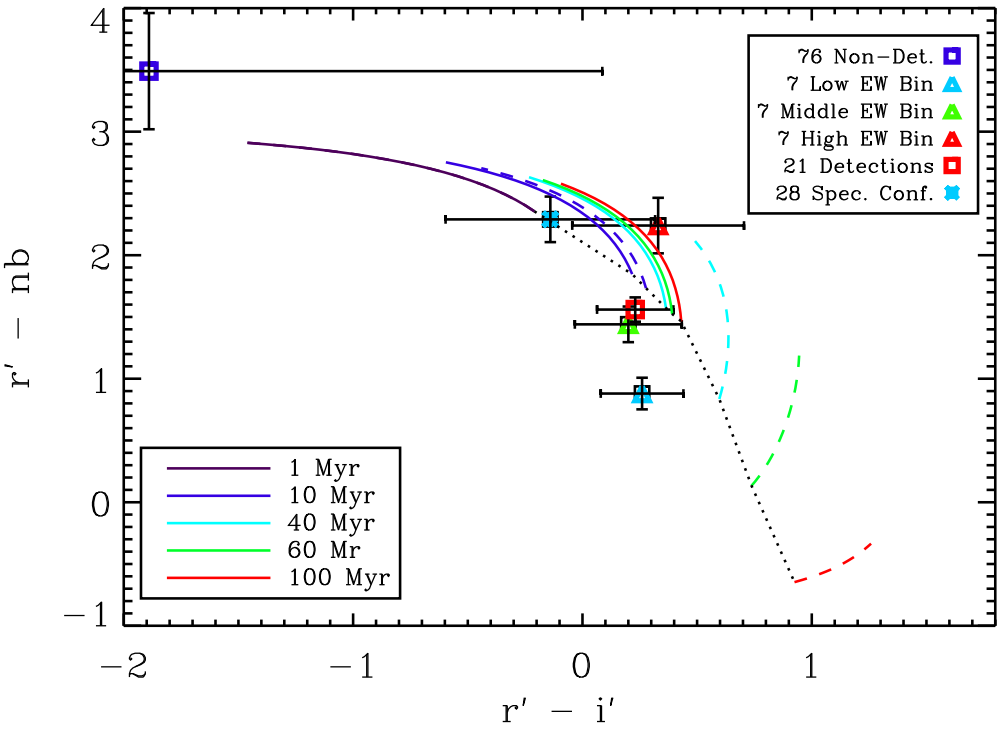

FIG. 2.—Color-color plot showing the six stacked points along with stellar population model tracks. The vertical axis is the r' - narrowband (H0) color, and the horizontal axis is the r' - i' color. The model tracks shown represent the colors of models in this plane. All models are for 0.02 $Z_{\odot}$. The solid tracks denote continuous star formation, while the dashed tracks denote exponentially decaying star formation, with a decay time of $\tau = 10^7$ yr. The different colors of the model curves represent the ages of the models. The length of the model curves represent the model colors with differing amounts of dust. Models were run with $A_{1200} = 0 - 2$, with the A_{1200} point lying at the smallest r' - nb color. The dotted black line connects the bottom of the model curves, and as such is the "zero-dust" line. Ages were found for each stack by minimizing the distance from the stack to the nearest $A_{1200} = 0$ model point (i.e. nearest point on the zero-dust line) for each star formation history (20 different possible ages were used).

mass error to the mass. The mass error was calculated via a Monte Carlo simulation using the flux errors from each band for each stack. These mass estimates are reported in Table 1 and Table 2. The masses of the objects from both types of star formation histories range from $\sim 2 \times 10^7$ to 2×10^9 $M_\odot$. These masses are indicative of an average object of the stack, and likewise the reported error is the error in the mean of the object mass in each stack, rather than the error in the measurement.

In Figure 3 we have plotted the 21 individually detected galaxies (plus the one outlier), along with their 1σ error bars. We have distinguished between the individual galaxies in order to show those that were spectroscopically confirmed. By their position in this plot, we hope to find out whether they have an intrinsically strong Lyα line, or one that is enhanced due to dust effects.

2.5. Discussion

2.5.1. *Age and Mass Estimates*

We fitted the ages of our stacked points using dust-free models. Objects in the stack of the 76 non-detections have the lowest age by far of all of the stacks (1 Myr), and thus the lowest mass (1.9×10^7 $M_\odot$). This is not surprising, however, because these objects are selected based on their Lyα line strength. In these galaxies, the line is strong enough to be seen clearly but the continuum is not, so they are intrinsically faint galaxies, implying a low stellar mass. Their colors are best fit by a low age, which also points to a low mass; the galaxy has simply not had that much time to form stars.

The three EW bins show a logical trend in age and mass. The lowest EW bin has the highest age at 200 (40) Myr, and thus the highest mass at 2.35 (1.62) $\times$ 10^9 $M_\odot$ for a continuous (exponentially decaying) SFH. This age is consistent with the fact that the EWs in this bin were not higher than normal, and thus, this EW bin is best fit by an older stellar population. The middle EW bin has a younger age and a smaller mass, and the highest EW bin has the youngest age out of the three bins at 4 (4) Myr, with the smallest mass at 9.5 (9.4) $\times$ 10^7 $M_\odot$. This would indicate that the objects with the highest EW are truly the most young and primitive galaxies in our sample (that were detected). The results for the stack of all 21 MMT-detected objects are intermediate among the results grouped by EW, as expected. The ages for this stack were 40 (10) Myr, and masses were 4.6 (2.0) $\times$ 10^8 $M_\odot$. The stack of spectroscopically confirmed objects should lie somewhere between the detected and non-detected stacks, and indeed this is the case, with ages of 3 (2) Myr, and masses of 6.2 (6.8) $\times$ 10^7 $M_\odot$.

The overall mass range we found of $\sim$ 2 $\times$ 10^7 – 2 $\times$ 10^9 $M_\odot$ is comparable to other studies of similar objects. Due to the fact that our observed magnitudes are brighter than the majority of surveys that we can compare to, we point to the trend between apparent magnitude and mass: that is, that the fainter an object is, the less massive it ought to be (assuming they are at similar redshifts). Ellis *et al.* (2001) discovered a very faint (I $\sim$ 30) LAE at z = 5.576 that was able to be detected because it was lensed by a foreground galaxy. Due to its faint magnitude, this object was determined to have a mass of around 10^6 $M_\odot$, implying a very young age ($\sim$

2 Myr). This object is consistent with our results, in that it is both much fainter and much less massive than the objects we are studying in this paper. Gawiser *et al.* (2006a) studied numerous LAEs that they detected at z $\sim$ 3.1, with a median R magnitude of $\sim$ 27. In order to take advantage of the full spectral range available to them, they stacked their sources before performing SED fitting. When this was done, they found an average mass per object of $\sim 5 \times 10^8\ M_\odot$. All of our stacks (except the stack of undetected objects) have an average individual object r' magnitude of less than 27, so even given the differences in photometric systems, they are likely brighter (much brighter, in fact, due to their increased distance). While (depending on the SFH) not all of these stacks have masses higher than $5 \times 10^8\ M_\odot$, they are of the same order.

Perhaps the best comparison to our results comes from the study by Pirzkal *et al.* (2007), where they study the properties of z $\sim$ 5 LAEs detected in the Grism ACS Program for Extragalactic Science (GRAPES) survey (Pirzkal *et al.* 2004). Using models with an exponentially decaying SFH, they found a mass range of 3 $\times$ 10^6 – 3 $\times$ 10^8 $M_\odot$ in objects with an i' range of 25.52 – 29.35 (the i' range of an average object in our stacks is from 25.12 to 29.90). While the majority of our objects have i' brighter than 26 (all except objects from the undetected stack and the spectroscopically confirmed stack), all of the GRAPES objects except one have i' fainter than 26 mag. This explains well the fact that our derived masses are in general greater than those derived for the GRAPES LAEs. We are studying

TABLE 1
BEST-FIT AGES AND MASSES FOR A CONSTANT SFH

Stack	r' magnitude of stack	Average r' mag. of one object	Age (Myr)	χ^2	Mass ($10^8 M_\odot$) per object
7 Low EW Objects	23.27 ± 0.10	25.38	200	18.48	23.54 ± 1.66
7 Mid EW Objects	23.49 ± 0.12	25.60	80	0.93	8.52 ± 0.74
7 High EW Objects	24.08 ± 0.21	26.19	4	0.94	0.95 ± 0.15
21 Det. Objects	22.39 ± 0.09	25.70	40	0.62	4.60 ± 0.29
76 Undet. Objects	23.31 ± 0.47	28.01	1	6.59	0.19 ± 0.07
28 Spec. Confirmed Objects	22.96 ± 0.18	26.58	3	0.05	0.62 ± 0.09

NOTES.—Each model has a metallicity of 0.02 $Z_\odot$. The low EW bin is from 20 to 40 Å; the middle bin is from 45 to 100 Å; the highest bin has objects with EW $\geq$ 110 Å. The bin with 21 detected objects consists of the 21 galaxies that were detected at the 2 σ level in at least two of the r', i' or z' bands. The last bin consists of the 28 objects that were spectroscopically confirmed to have a Lyα line at z $\sim$ 4.5. The χ^2 is defined as the square of the distance in sigma units to the best-fit age point (see Figure 2).

TABLE 2
BEST-FIT AGES AND MASSES FOR AN EXPONENTIALLY DECAYING SFH

Stack	Age (Myr)	χ^2	Mass ($10^8 M_\odot$) per object
7 Lowest EW Objects	40	4.05	16.15 ± 1.14
7 Middle EW Objects	20	1.05	4.24 ± 0.37
7 Highest EW Objects	4	0.97	0.94 ± 0.14
21 Detected Objects	10	3.43	1.97 ± 0.13
76 Undetected Objects	1	6.59	0.19 ± 0.07
28 Spec. Confirmed Objects	2	0.09	0.68 ± 0.10

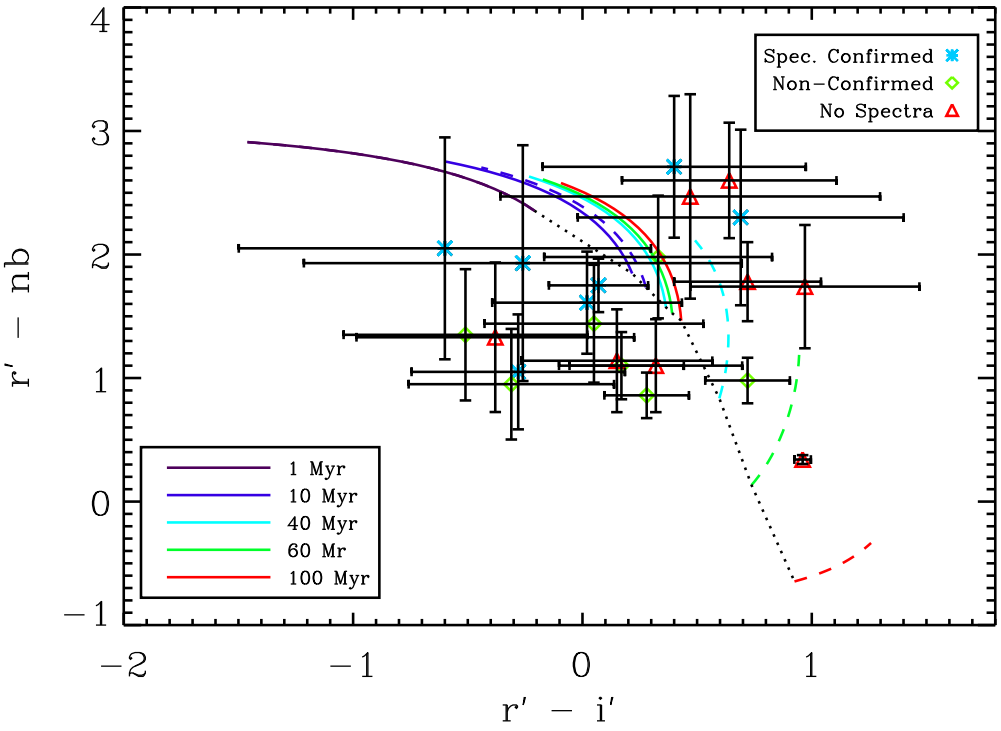

FIG. 3.—Color-color plot showing the location of the 21 individual detections (with the outlier), along with stellar population model tracks. The individual galaxies are plotted with different colored symbols to denote whether they have been spectroscopically confirmed to be at z $\sim$ 4.5. The axes and model tracks are the same as in Figure 2. In general, objects above the zero-dust line would have their EW enhanced due to dust effects, while objects below this line would have intrinsically high EWs, or have their whole spectrum attenuated by a geometrically homogeneous dust distribution (for the low EW subsample).

intrinsically brighter, and thus more massive objects. While our wavelength baseline is not very large, we are able to estimate the mass of stars producing UV and Lyα light.

2.5.2. *Dusty Scenario*

In studying Figure 3 we have identified three distinct regions in the color-color plane: one region that would house intrinsically blue objects, one region of red objects with high EW, and one of red objects with low EW. The region that lies below the zero-dust line and blueward of r' - $i' = 0$ would appear to house objects that have moderate-to-high EWs with blue colors, indicating that they are intrinsically blue, containing young stars. The lower EW/redder r' - i' color sub-area of this region would contain objects that may have some dust, but it is affecting both the continuum and Lyα line, lowering the EW and reddening the color.

The second region consists of the area above the zero-dust line with an r' - nb color $\gtrsim 2$. This region would house objects that lie in the dusty regime of the models, yet they would still have "red" r' - nb colors, indicating a large EW. Objects such as these could be explained by dust quenching of the continuum (causing the "red" r' - i' color), while the Lyα line would not be affected by the dust, making it appear to be strong (causing the red r' - nb color). The last region consists of the area above the zero-dust line, but with a smaller r' - nb color (r' - i' ~ 1, r' - $nb = 1 - 1.5$). Objects in this area would have a redder r' - i' color, with a smaller r' - nb color (smaller EW), indicating that they are perhaps older galaxies with some dust effects present.

In the above paragraphs, we have outlined different regions in our color-color plane that would house objects from the different scenarios we are examining. We planned to use this to determine the likelihood of dust quenching of the continuum resulting in a large Lyα EW. However, the current error bars on individual objects are large compared to their distance from the zero-dust line. In order to quantify this, we calculated the distance of each object from the zero-dust line in units of σ. The mean distance of the 21 objects we are studying is 1.10 ± 0.48 σ. While it is possible that the dust enhancement of the Lyα line is present in our sample, due to the large error bars we cannot rule out the possibility that all of these objects lie on the zero-dust line at a level of ~ 1 σ.

Performing the same exercise with the six stacked points with their smaller error bars, the mean distance from the zero-dust line is 1.17 ± 0.81 σ. However, the smaller error bars do allow us to make more of a characterization of a few of the stacks. We can most likely rule out clumpy dust enhancement of the Lyα line for the low and middle EW stacks, mainly because they lie below the zero-dust line, and far from the region in our color-color plane where we would expect to find the enhanced line. Also, in the EW enhancement scenario, one would expect to find extremely high EW Lyα lines, and these two stacks do not contain the highest 33% EW objects in our sample. There still may be dust present in these objects, but it would be in a uniform distribution, quenching both the continuum and the Lyα line.

2.6. Conclusions

We have used MMT/Megacam broadband photometry in order to study the continuum properties of Lyα emitting galaxies at z$\sim$ 4.5. By dividing our objects into six different categories and stacking them, we were able to derive age and stellar mass estimates for an average galaxy in each stack (ignoring dust effects). In all cases, the best-fit ages were young, with the oldest age coming from objects with the lowest EW. Even those objects had an age of only 200 Myr (40 Myr) for a continuous (exponentially decaying) star formation history. As would be expected, the bin with the highest EW had the youngest age out of the continuum detected objects at 4 Myr (from both SFHs). The youngest age from both SFHs came from objects whose continuum flux was undetected, mostly because these were detected in the narrowband image, and not in the continuum images.

The derived stellar masses ranged from $\sim 2 \times 10^7$ $M_\odot$ for the undetected objects to $\sim 2 \times 10^9$ for the lowest EW objects. Our derived masses are consistent with other mass estimates of similar objects. In the majority of cases, the masses of our objects were greater than those from other studies (Ellis *et al.* 2001; Gawiser *et al.* 2006a; Pirzkal *et al.* 2007). However, the magnitudes of our individual objects were brighter than those of the comparison studies, implying that our objects are larger, more massive galaxies than those from the other studies. In conclusion, while we have not yet been able to definitively determine the likelihood of dust enhancement of the Lyα line, we have been able to shed some light on the physical properties of these high-z objects. The Lyα galaxies in this survey, especially those with the largest

Lyα EWs, are some of the youngest and least massive objects in the early universe known to date.

3. EFFECTS OF DUST GEOMETRY IN Lyα GALAXIES AT z = 4.4

3.1. Abstract

Equivalent widths (EWs) observed in high-redshift Lyα galaxies could be stronger than the EW intrinsic to the stellar population if dust is present, residing in clumps in the inter-stellar medium (ISM). In this scenario, continuum photons could be extinguished, while the Lyα photons would be resonantly scattered by the clumps, eventually escaping the galaxy. We investigate this radiative transfer scenario with a new sample of six Lyα galaxy candidates in the GOODS CDF–S, selected at z = 4.4 with ground-based narrowband imaging obtained at CTIO. Grism spectra from the *HST* PEARS survey confirm that three objects are at z = 4.4, and that another object contains an active galactic nucleus (AGN). If we assume the other five (non-AGN) objects are at z = 4.4, they have rest-frame EWs from 47 to 190 Å. We present results of stellar population studies of these objects, constraining their rest-frame UV with *HST* and their rest-frame optical with *Spitzer*. Out of the four objects which we analyzed, three were best fit to contain stellar populations with ages on the order of 1 Myr and stellar masses from 3 – 10 $\times$ 10^8 $M_\odot$, with dust in the amount of A_{1200} = 0.9 – 1.8 residing in a quasi-homogeneous distribution. However, one object (with a rest EW $\sim$ 150 Å) was best fit by an 800 Myr, 6.6 $\times$ 10^9 $M_\odot$ stellar population with a smaller amount of dust (A_{1200} = 0.4) attenuating the continuum only. In this object, the EW was enhanced $\sim$ 50% due to this dust. This suggests that large EW Lyα galaxies are a diverse population. Preferential extinction of the continuum in a clumpy ISM deserves further investigation as a possible cause of the overabundance of large-EW objects that have been seen in narrowband surveys in recent years.

3.2. Introduction

Over the last decade, numerous surveys have been conducted searching for galaxies with strong Lyman alpha emission (Lyα galaxies) at high redshift (e.g., Rhoads *et al.* 2000, 2004; Rhoads & Malhotra 2001; Malhotra & Rhoads 2002; Cowie & Hu 1998; Hu *et al.* 1998, 2002, 2004; Kudritzki *et al.* 2000; Fynbo, Möller, & Thomsen 2001; Pentericci et al 2000; Ouchi *et al.* 2001, 2003, 2004; Fujita *et al.* 2003; Shimasaku et al 2003, 2006; Kodaira et al. 2003; Ajiki *et al.* 2004; Taniguchi et al 2005; Venemans *et al.* 2002, 2004; Pascarelle *et al.* 1996ab; Nilsson *et al.* 2007). Many of these studies have discovered Lyα galaxies with large rest-frame Lyα equivalent widths (EWs; Kudritzki et al. 2000; Malhotra & Rhoads 2002; Dawson *et al.* 2004, 2007; Shimasaku *et al.* 2006). Since it was first suggested 40 years ago (Partridge & Peebles 1967) that Lyα emission would be an indicator of star formation in the first galaxies during formation, it has been thought that strong Lyα emission would be indicative of copious star formation. However, the ratio of high to low EWs found in many of these surveys is too high to be explained by a so-called normal stellar population with a Salpeter (1955) initial mass function (IMF) and a constant star formation history (SFH). This normal stellar population has a maximum EW of 260 Å at 10^6 yr, settling towards 95 Å by 10^8yr. Thus something is causing the EWs in many of the observed Lyα galaxies to be higher than normal.

We examine three possible causes for the stronger than expected Lyα EWs seen in these high-redshift objects. Strong Lyα emission could be produced via star formation if the stellar photospheres were hotter than normal. This could happen in ex-

tremely low metallicity galaxies, or galaxies which have their stellar mass distributed via a top-heavy IMF, forming more high-mass stars than normal. More high-mass stars would result in more ionizing photons, which would thus create more Lyα photons when they interact with the local interstellar medium (ISM). Low-metallicity or top–heavy IMFs are possible in primitive galaxies, which are thought to contain young stars and little dust (Ellis et al. 2001; Venemans et al. 2005; Gawiser *et al.* 2006a, Pirzkal *et al.* 2007; Finkelstein *et al.* 2007).

Active galactic nuclei (AGNs) can also produce large Lyα EWs. However, the lines in Type I AGNs are much broader than the width of the narrowband filter, and none of the accompanying high ionization state emission lines have been detected in many Lyα galaxies (Dawson *et al.* 2004). While the lines in Type II AGN are narrower, a deep *Chandra* exposure in the LALA fields showed no significant X-ray flux, even when individual galaxies were stacked (Malhotra *et al.* 2003; Wang *et al.* 2004). Wang *et al.* determined that less than 4.8% of their sample could be possible AGNs. Thus while one could never entirely rule out AGNs from their sample, if one uses well thought out selection criteria, one could be confident that there are at most a small number of AGN interlopers. In general, narrowband selection techniques usually result in a low AGN fraction.

While Lyα galaxies are historically thought to be primitive and dust free, there is a scenario involving dust which could cause an older stellar population to exhibit a strong Lyα EW. If the dust is primarily in cold, neutral clouds with a hot, ionized inter-cloud medium the Lyα EW would be enhanced because Lyα photons

are resonantly scattered (Neufeld 1991; Hansen & Oh 2006). Assuming the clouds are thoroughly mixed with neutral hydrogen, Lyα would be preferentially absorbed by the hydrogen at the surface of these clouds, while continuum photons would be more likely to penetrate these clouds more deeply before they get absorbed by dust. The Lyα photons would likely be re-emitted quickly, proceeding to effectively "bounce" around the ISM by being absorbed and re-emitted right on the surface of these clouds. Thus Lyα photons would have a much greater chance of escaping the galaxy than continuum photons, which would suffer a much greater chance of extinction. In this scenario a strong Lyα EW could be observed in a galaxy with an older stellar population and a clumpy dusty interstellar medium. Our goal in this chapter is to research the likelihood that this scenario is occurring in a sample of Lyα galaxies.

In this paper we assume a Benchmark Model cosmology, where $\Omega_m = 0.3$, $\Omega_\Lambda = 0.7$ and $H_0 = 0.7$ (c.f. Spergel et al. 2007). All magnitudes in this paper are listed in AB magnitudes (Oke & Gunn 1983). In §3.3 we discuss our data reduction and sample. In §3.4 we discuss our stellar population models. In §3.5 we detail our results, and they are discussed in §3.6. We present our conclusions in §3.7.

3.3. Data Handling

3.3.1. *Observations*

In order to study Lyα galaxies at z = 4.4, we obtained a 2.75 hr exposure in the 6563 Å (Hα) narrowband filter (NB656) in October 2006 using the MOSAIC II CCD imager on the Blanco 4m telescope at Cerro Tololo Inter-American Observatory (CTIO). MOSAIC II has eight CCDs over a $36' \times 36'$ field of view, with each pixel

covering 0.27″on the sky. In our previous study (Finkelstein et al. 2007; Chapter 2), we obtained ground-based broadband data of regions with preexisting narrowband data. However, the broadband data were not nearly deep enough to constrain the dusty scenario.

We observed the Great Observatories Origins Deep Survey (GOODS; Giavalisco *et al.* 2004) Chandra Deep Field – South (CDF–S; RA 03:31:54.02, Dec -27:48:31.5 [J2000]) to take advantage of the publicly available extremely deep *Hubble Space Telescope* (*HST*) Advanced Camera for Surveys (ACS; Ford *et al.* 1998) and *Spitzer* Infrared Array Camera (IRAC; Fazio *et al.* 2004) broadband data. In addition, the photometry and astrometry of these broadband data have been extremely well determined, further reducing errors in our results. These data consist of the following broadband filters: F435W (B), F606W (V), F775W (i'), F850LP (z'), 3.6 μm (channel 1), 4.5 μm (channel 2), 5.8 μm (channel 3) and 8.0 μm (channel 4). The comoving volume probed by the NB656 filter in the CDF-S region is $\sim 2.85 \times 10^5$ Mpc^3.

3.3.2. *Data Reduction*

The CTIO data were reduced with IRAF (Tody 1986, 1993), using the MSCRED (Valdes & Tody 1998; Valdes 1998) reduction package, following the method set forth in Rhoads et al. (2000, 2004). First, we performed the standard image reduction steps of overscan subtraction, bias subtraction and flat–fielding. Cross-talk was also removed between chip pairs sharing readout electronics. We derived a supersky flat from the science data, and used this to remove the residual large–scale imperfections in the sky. The world coordinate systems (WCS) of individual frames were

adjusted by comparing the frames to the astrometry from the USNO–A2.0 catalog. Cosmic rays were rejected using the algorithm of Rhoads (2000), and satellite trails were manually flagged and excluded from the final stacked image. Weights for image stacking were determined using the ATTWEIGHT algorithm (Fischer & Kochanski 1994), with the task mscstack being used to make the final stack. See Rhoads et al. (2000) and Wang et al. (2005) for further details on data reduction.

3.3.3. *Object Extraction*

In order to select Lyα galaxies in our field, we used the GOODS CDF–S ACS version 1.0 catalogs, obtained from the GOODS website. Because the GOODS ACS data are much deeper and have a higher resolution than our narrowband data, we chose to extract sources from our narrowband data using point-spread function (PSF) fitting routines rather than aperture photometry. We were able to do this because typical high-z Lyα galaxies are not resolved from the ground (Pirzkal *et al.* 2007). We performed PSF fitting using the routines in the IRAF port of DAOPHOT (Stetson 1987).

We chose the positions to fit the PSF based on the positions of sources in the GOODS catalogs. The objects we were looking for were z $\approx$ 4.4 Lyα galaxies, so they should be B-band dropouts with a narrowband excess. We used the B-dropout color criteria from Giavalisco *et al.* (2004)

$$(B-V) \geq 1.2 + 1.4 \times (V-z') \;\&\; (B-V) \geq 1.2 \;\&\; (V-z') \leq 1.2 \qquad (3)$$

with the magnitudes from the GOODS catalogs in order to find out which objects were Lyman break galaxies (LBGs) at z $\sim$ 4.4. The number counts of the V magnitudes of

all objects in the catalog turned over just brighter than 27th magnitude, so we chose to only fit the PSF to objects with $V \leq 27$ mag, in order to avoid selecting objects beyond the completeness limit of the GOODS dataset.

The input list to the PSF-fitting routine consisted of the x and y positions in the narrowband image, corresponding to the right ascention and declination coordinates of the objects we wanted to fit from the GOODS catalog. To be sure the coordinates matched up correctly, we performed a transformation to correct for any WCS distortion between the WCS of the narrowband image and the GOODS catalog. The PSF-fitting routine was then given this corrected list of x and y coordinates along with the PSF image computed from the narrowband image. The outputs were a file of the object magnitudes along with a subtraction image (an image showing the residuals left when the fitted PSFs were subtracted out). On inspecting this image, we found that with the exception of extremely bright stars or extended objects, this method of PSF fitting extracted the objects very well.

In order to calculate the zero point of the Hα image, we plotted a color-magnitude diagram of Hα - V versus V. The Hα filter is contained entirely within the V filter, so that the mean colors of these objects should be zero. We fit the zero point using only unsaturated stars, and find a zero point of 27.55 mag for 1 count in the final image. The DAOPHOT photometry errors imply a 5 σ limiting magnitude of 24.90 for the narrowband image.

3.3.4. *Lyα Galaxy Selection*

We find z ≈ 4.4 galaxy candidates by seeing which B-band dropouts exhibit a narrowband excess. Figure 4 shows the color-magnitude diagram for all of the objects we extracted, highlighting the B-band dropouts, along with the initial galaxy candidates. There were 11 initial candidates, and six of them we eventually determined to be true candidates after visual inspection showed that they were real, uncontaminated objects. The five objects which were rejected at this stage were either contaminated by a nearby star or were not visible above the noise in the NB656 image.

We performed a number of tests to check the validity of our six candidates. First, we looked for other B-dropouts with similar V-band magnitudes to each of the six candidates, and then checked to see whether these somewhat randomly selected objects showed any narrowband excess, which none of them did. We then looked at the subtraction image. With a perfect PSF extraction, we should see nothing at the location of our candidates. Indeed, when inspecting these subtracted areas, nothing stands out from the noise. Finally, we took a mosaicked image of the GOODS V-band tile and convolved it to the seeing of the ground-based Hα image ($\sim 0.9''$). We then subtracted this image from the Hα image, and checked to insure that the six candidates showed a narrowband excess, which five out of the six did. The object that did not show an excess on visual inspection is near a bright object (object 5), and also has the smallest computed excess, which could explain why it does not stand out above the noise in the Hα - V image. Figure 5 shows stamps of each of the six candidates, along with the results of some of the methods listed above. Figure 6 shows

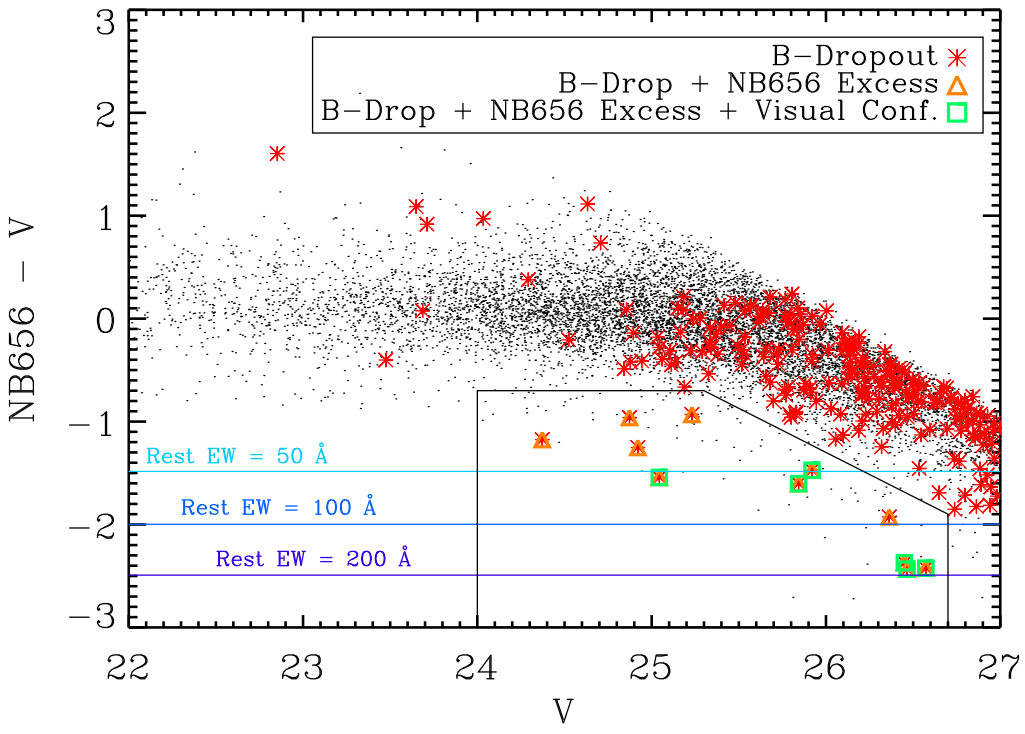

FIG. 4. —Color-magnitude diagram of all objects extracted from the narrowband (NB656) image via PSF fitting. The 11 objects showing a narrowband excess that were also B-dropouts were selected as z = 4.4 Lyα galaxy candidates. Six of these 11 initial candidates were confirmed following a visual inspection of the image, with the other five being either too close to a neighboring bright star or visually undetected in the image. Also shown in this plot are lines of constant rest-frame equivalent width for three values of EW.

stamps of each candidate in each of the Hα, B, V, i', z', 3.6 μm and 4.5 μm bands. Table 3 details the EWs of each object, while Table 4 lists the magnitudes of each object for each filter we used.

3.3.5. *Spectroscopic Confirmations*

While we have assumed that our narrowband filter has selected Lyα galaxies at z $\approx$ 4.4, it could also pick up [O III] emitters at z $\sim$ 0.3 and [O II] emitters at z $\sim$ 0.75. Ideally, we would like to be able to see a Lyα line in a given spectrum to make a confirmation, but lacking that we can still confirm a redshift based off of a Lyman break. The Probing Evolution and Reionization Spectroscopically (PEARS; PI S. Malhotra) *HST* Treasury Program (#10530) has obtained ACS grism spectroscopy of approximately a third of the solid angle of the CDF–S via 5 ACS pointings. Four of our candidates were observed in PEARS.

Based on the positions of emission lines and breaks in the observed spectra, we have been able to spectroscopically confirm objects 1, 2 and 6 to be at z $\approx$ 4.4. While object 4 is not in any of the PEARS fields, it is covered by GOODS–MUSIC (Grazian et al. 2006), and it was calculated to have a photometric redshift of 4.42. For completeness, we list the photometric redshifts for objects 1, 2 and 6, which are 4.24, 4.44 and 4.36, respectively.

In order to search for AGNs in our sample, we checked the CDF–S data set (Giacconi *et al.* 2001), which consists of a deep *Chandra X-ray Observatory* exposure in the GOODS CDF–S. One object was detected in the Chandra data (Object 3),

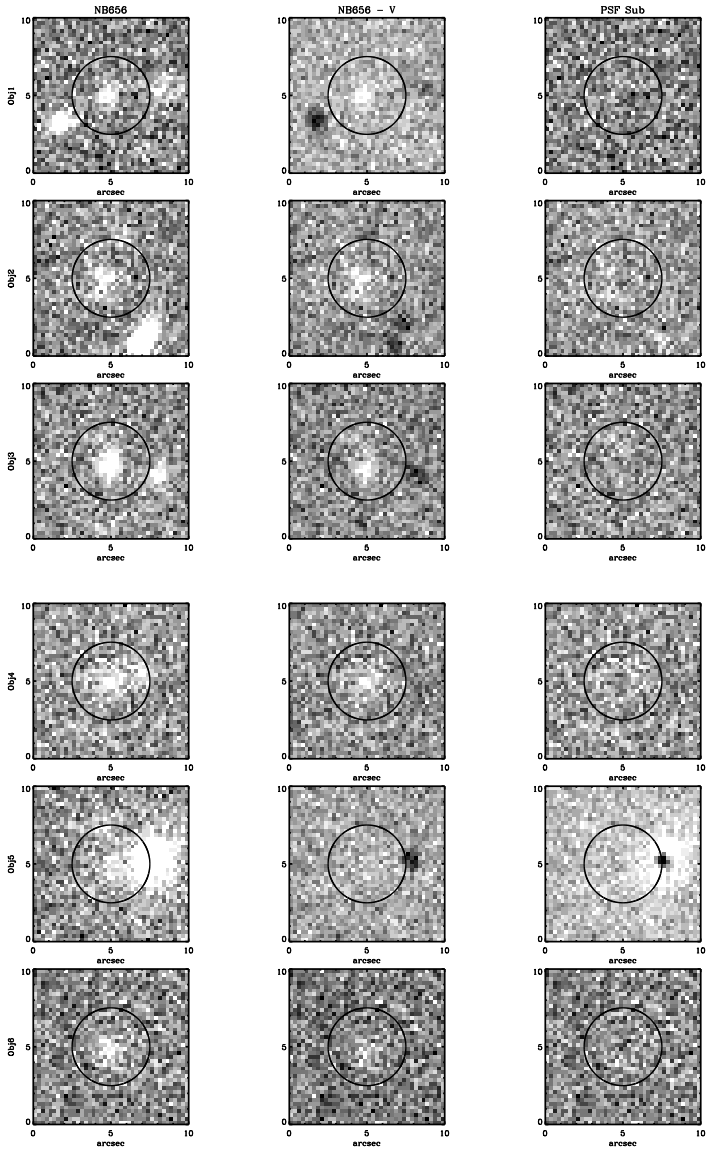

FIG. 5.—Results from our tests to check the validity of our candidates. The first column shows a 10″ stamp of each candidate in the NB656 image. The second column shows each candidate in a narrowband excess (NB656 - V) image. We see flux in five out of the six objects, visually confirming that they exhibit a narrowband excess. The one object that doesn't definitively show a narrowband excess is very near a bright star, which could affect this observation. Regardless, this object is thrown out of our analysis as the nearby star contaminates its *Spitzer* fluxes. The third column shows each candidate's position in the subtraction (PSF-residual) image. The lack of any flux above the noise proves that the PSF extraction was satisfactory.

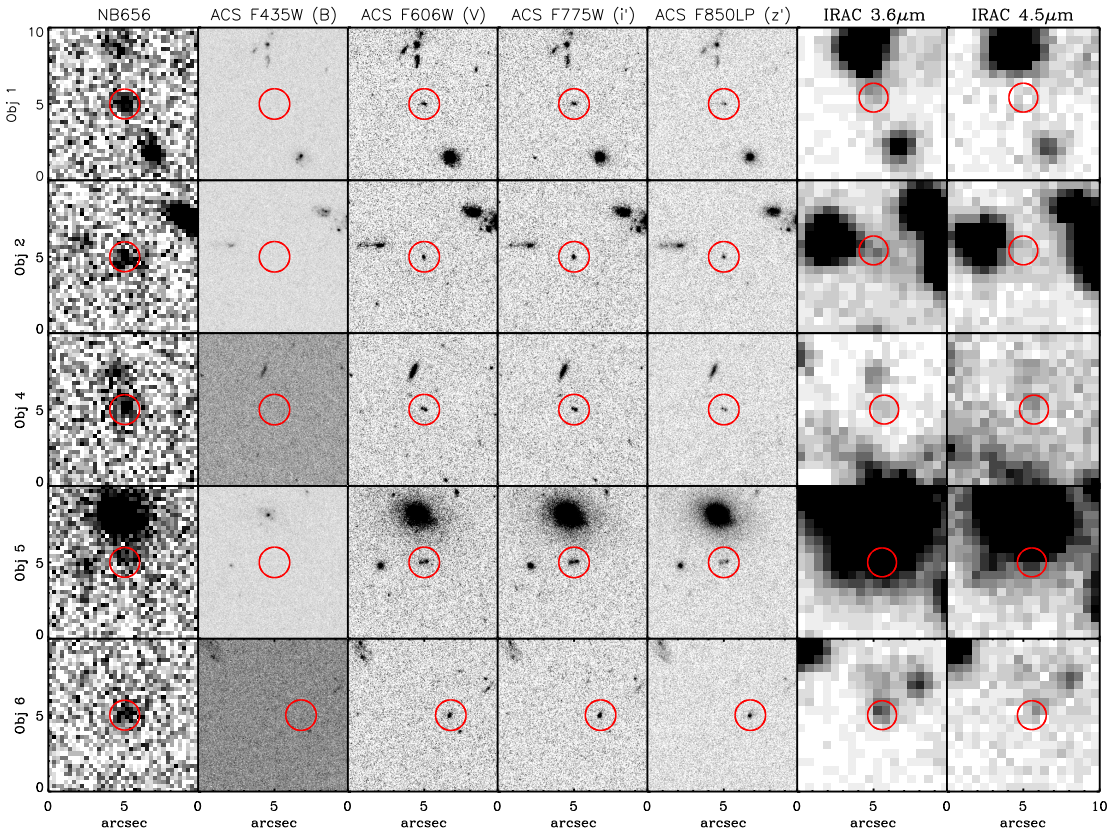

FIG. 6.—10″ stamps of each candidate in the narrowband, the four *HST*/ACS bands, and two *Spitzer*/IRAC bands. The circles are 2″ in diameter, and are drawn to highlight the objects.

TABLE 3
CDF–S LYα GALAXY CANDIDATES

Name	m_{AB} (NB656)	m_{AB} (F606W)	Rest EW (Å)	Spectroscopic Conf.
Object 1	24.03	26.49	189.7 ± 46.8	∼4.4
Object 2	24.15	26.52	166.6 ± 42.9	∼4.4
Object 3	23.50	24.84	52.8 ± 5.9*	AGN @ z=3.19
Object 4	24.08	26.37	149.1 ± 36.4	No Spectra
Object 5	24.48	25.89	46.9 ± 13.0	No Spectra
Object 6	24.24	25.81	56.3 ± 11.0	∼4.4

NOTES.—*Object 3 is a known AGN at z = 3.19, and the line we detected in the narrowband filter is [C IV], thus the EW for object 3 is the [C IV] rest-frame EW for an object at z = 3.19. The calculated rest-frame EWs for the other objects assume a redshift equal to that of Lyα at the center of the Hα filter, which is 4.399. Objects 1, 2, 3 and 6 had grism spectra from the PEARS survey, thus we were able to spectroscopically confirm objects 1, 2 and 6 to be at z $\approx$ 4.4.

TABLE 4
MAGNITUDES OF CDF–S LYα GALAXY CANDIDATES

Name	IAU Format Name	m_{NB656}	m_B	m_V	$m_{i'}$	$m_{z'}$	m_{Ch1}	m_{Ch2}
Obj 1	J033215.991-274231.57	24.03	29.54	26.49	25.70	25.95	25.20	$\geq 25.64^*$
Obj 2	J033239.771-275114.95	24.15	$\geq 29.11^*$	26.52	25.52	25.61	25.24	$\geq 25.92^*$
Obj 4	J033258.380-275339.58	24.08	30.40	26.37	25.54	25.70	24.89	24.92
Obj 5	J033224.227-274129.48	24.45	$\geq 29.11^*$	25.89	25.10	24.84	23.09	24.23
Obj 6	J033248.244-275136.90	24.24	$\geq 29.11^*$	25.81	24.96	24.82	24.16	24.93

NOTES.—$^*3\sigma$ upper limits. Coordinates and magnitudes for each of our candidate Lyα galaxies. Each magnitude has been corrected to represent the total magnitude for the object.

and we found in the literature that it is a known [C IV] λ1549 emitter at z = 3.19 (Szokoly *et al.* 2004; Xu *et al.* 2007). This object was not included in our analysis.

3.3.6. *Broadband Photometry*

For our analysis, we used the updated version of the GOODS CDF–S catalog (ver. 1.9; M. Giavalisco *et al.* 2008 in preparation) which has deeper observations in i' and z', resulting in lower error bars for those two bands. As an external check on the photometry errors in the GOODS catalog, we used the Hubble Ultra Deep Field (HUDF; Beckwith et al. 2006) catalog. The HUDF is much deeper than the version 1.9 data in the same regions, thus any errors would be dominated by the v1.9 data. We matched the HUDF and v1.9 catalogs, then plotted the magnitude difference between the two versus the version 1.9 data for each of the four bands (B, V, i' and z'). We characterized this error as being 1σ of the spread in the magnitude difference in a certain magnitude slice. This error was small (< 0.1 mag in our magnitude regime), but in the cases where it was larger than the version 1.9 photometry error[7], we used this error in its place.

When comparing data from different telescopes to models, we needed to be sure that the magnitudes we were using from our narrowband, ACS and IRAC data were defined the same way. In the narrowband, we obtained fluxes from PSF fitting, so then the magnitudes from these fluxes were total magnitudes. For the GOODS ACS data, we used the MAG_AUTO magnitudes, which are known to be 5% fainter

[7]The 1σ spread in the v1.9 photometry errors was 0.020, 0.027 and 0.023 mag for the V, i' and z' bands, respectively, at 26th magnitude.

than the total magnitude (Bertin 2006). Thus, we corrected the GOODS ACS data, adding on a factor of 5% to the flux to make them total magnitudes.

The GOODS *Spitzer* IRAC data do not yet have a public catalog, but a catalog has been created using the TFIT software package (Laidler et al. 2007). TFIT uses *a priori* knowledge of spatial positions and morphologies from a higher resolution image (in this case the GOODS ACS z' image) to construct object templates and fit them to the lower resolution image. However, this used the ACS catalog's MAG_ISO parameter as a guideline for the radius of the galaxy, so in order to find the total magnitude, we added to the IRAC magnitudes the difference between MAG_ISO and MAG_AUTO for our objects in the ACS z' catalog. We then added an additional factor of 5% to correct the IRAC magnitudes to be total magnitudes. We now had total magnitudes for our objects in nine bands, from B to 8.0 μm.

3.4. Modeling

3.4.1. *Stellar Population Models*

We have derived the physical properties of our candidate Lyα galaxies by comparing them to stellar population models, using the modeling software of Bruzual & Charlot (2003; hereafter BC03). Comparing to models allows one to choose a variety of physical parameters to see which matches the observations the best. We attempted to fit the following parameters for each galaxy: age, metallicity, SFH, mass and dust content. We used a grid of 24 ages ranging from 1 Myr to 1.35 Gyr (the age of the Universe at z = 4.4). We fit the objects to the full range of metallicity available with BC03, from 0.005 to 2.5 $Z_{\odot}$. We modeled exponentially

decaying SFHs with characteristic decay times (τ) of 10^6, 10^7 and 10^8 yr. We also approximated an instantaneous burst/simple stellar population (SSP) by using an exponentially decaying SFH with $\tau = 10^3$ yr, and a constant SFH with $\tau = 4 \times 10^9$ yr. We included dust via the Calzetti dust extinction law (Calzetti *et al.* 1994), which is applicable to starburst galaxies, using the range $0 \leq A_{1200} \leq 2$. Galactic dust was included from the method of Schlegel *et al.* (1998) with a value of E(B - V) = 0.009 mag. We include intergalactic medium (IGM) absorption via the prescription of Madau (1995).

The BC03 models do not tabulate any emission lines, but in order to model the dusty scenario we needed to include the Lyα emission line. We derived the Lyα line flux from the number of ionizing photons output for each model, assuming case B recombination (see Finkelstein et al. 2007; Chapter 2 for details). Some of our objects showed a stronger 3.6 μm flux than would have otherwise been expected. At z = 4.4, the Hα emission line would fall in this filter, so we also included an Hα emission line in the models (assuming case B recombination, the Hα line strength is 0.112 times the Lyα line strength; Kennicutt 1983).

In order to model the clumpy dust scenario, we needed to ensure that the Lyα line did not suffer dust attenuation. To do this, the continuum flux (and Hα flux) was multiplied by the Calzetti dust law before we added in the Lyα flux to the spectrum at the correct wavelength bin. In this case, the continuum suffers dust attenuation while the Lyα line does not. Lyα sits right at a step function in the Madau IGM treatment, so the amount of attenuation applied to Lyα depends strongly on the exact wavelength

position of the Lyα line. The accepted interpretation is that the internal kinematics of a given galaxy will result in half of the Lyα flux coming out slightly blue of the rest wavelength, and half slightly red. This results in the characteristic asymmetric profile of the Lyα observed in many spectra, where the blue side is truncated. We approximate this interpretation by attenuating the Lyα line to be approximately one half of its original (post-dust where applicable) flux.

In order to go from the BC03 output flux to bandpass-averaged fluxes, we used the method outlined by Papovich *et al.* (2001). In short, we took the output from BC03, and converted it from L_λ into L_ν, and then from L_ν into F_ν (units of erg s^{-1} cm^{-2} Hz^{-1}) using $F_\nu = (1 + z)\ L_\nu\ /\ (4\pi d^2{}_L)$ to do the conversion and redshift the spectrum. This flux was then multiplied by the transmission function for a given bandpass (including the filter transmission and the quantum efficiency of the detector), and integrated over all frequencies. The bandpass averaged flux $\langle f_\nu \rangle$ is this result normalized to the integral of the transmission function. AB magnitudes (Oke & Gunn 1983) for the models were then computed.

3.4.2. *Dust Effects on the Lyα EW*

The scenario we are probing observationally is whether or not dust could enhance the Lyα EW. Traditionally, it has been thought that Lyα galaxies could possibly be too primitive to have formed dust yet. However, some evidence does exist that would enable a galaxy to form dust quickly. Massive stars evolve on a very short timescale, so after a few Myr, a galaxy could begin to have some heavier elements in its ISM. Also, supersolar metallicities and CO emission have been seen in quasars at

$z \sim 6$ (Pentericci *et al.* 2002; Bertoldi *et al.* 2003), and Lyα emission has been seen in submillimeter-selected galaxies (Chapman *et al.* 2004).

However, even if Lyα galaxies did have dust, it has been thought that it would vastly attenuate the Lyα flux (Meier & Terlevich 1981). Lyα photons have long scattering path-lengths, making them extremely vulnerable to dust attenuation, assuming a uniform distribution of dust. It is possible that dust could be geometrically distributed such that the Lyα photons are attenuated less than the continuum. The most likely of these scenarios involves an ISM with clumpy dust clouds thoroughly mixed with neutral hydrogen within an inter-cloud medium which is tenuous and ionized (Neufeld 1991; Hansen & Oh 2006). Evidence for the possible existence of this scenario also comes from Giavalisco *et al.* (1996), who find a lack of correlation between UV slope and Lyα EW, meaning that a UV slope indicative of dust does not necessarily mean a low Lyα EW. They conclude that the ISM in their sample of galaxies is highly inhomogeneous, and that the transport of Lyα photons is primarily governed by the geometry of the ISM rather than the amount of dust.

This is intriguing, because if Lyα galaxies had a dusty, inhomogeneous ISM then it is possible that the continuum photons were attenuated and the Lyα photons were not. Then the observed EW would be greater than the EW intrinsic to the underlying stellar population by a factor relating to the amount of dust present. To better understand this, we will follow the journey of a photon through an ISM, starting from the point when it is emitted from a massive star. This star will emit numerous ionizing photons, 2/3 of which will become Lyα photons assuming case B

recombination. When a Lyα photon encounters a region of dust mixed with neutral hydrogen, it has a very high probability of being absorbed by the first hydrogen atom it encounters. It will then be reemitted in a random direction, with an equal chance of being sent back the way it came as being sent forward in its original direction of travel. If the ISM is uniformly distributed, the Lyα photon will only move a short distance before it is absorbed again, requiring a very long time for a given Lyα photon to escape the galaxy. If the ISM is composed of clouds in a nearly empty inter-cloud medium, then when a Lyα photon is emitted back out of the clump,[8] it will travel a long distance before it encounters another clump, vastly increasing the probability that it will escape the galaxy. Even if it is re-emitted in the direction further into the clump, it will still be scattered close to the surface, so it still has a chance to escape.

However, continuum photons in a homogeneously distributed ISM will be absorbed by dust as they travel through the ISM. Since their wavelengths are continuously distributed, they will essentially be unaffected by the presence of neutral hydrogen. The same holds true in a clumpy ISM. A continuum photon will be able to "bypass" the hydrogen in the clump until it encounters a dust grain, at which point it could either get scattered or absorbed. If the continuum photon is absorbed, it will eventually be reemitted, but its wavelength will have changed to the far-IR. The net effect of this is to lower the amount of continuum flux escaping the galaxy (as well as to redden the flux due to those photons which are scattered rather then absorbed).

[8]The probability of a Lyα photon being absorbed in a clump is $\sim 2\sqrt{\epsilon}$, where ϵ is the single scattering albedo (Hansen & Oh 2006). This is valid for $\epsilon \ll 1$, where $\epsilon = 0$ signifies complete reflectance)

Thus, a clumpy ISM could result in a higher Lyα EW than the underlying stellar population.

It has been generally believed that Lyα galaxies are very young, primitive objects. If we find proof that an object shows dust enhancement of the Lyα EW, it could turn out that some fraction of Lyα galaxies known to exist could in fact be older, more evolved stellar populations, changing our view of where Lyα galaxies belong in the galaxian zoo.

3.4.3. *IGM Inhomogeneities*

Although differences in the IGM can affect the models in the V band, we chose to include this band in our fits. The V-band is complicated, as at z = 4.4 it contains the entire Lyα forest region from the Lyman limit out to Lyα. To account for inhomogeneities in the IGM, we chose to include a flux variance for the model V-band flux (this results in a second parameter in the denominator for the V-band χ^2 term; see §3.5.1). To account for IGM absorption in our models, we have attenuated the cumulative flux which comes out of BC03 by a factor of exp(-τ_{IGM}), such that the bandpass averaged flux in the V-band is given by

$$\langle f_V \rangle = \int_{\lambda_1}^{\lambda_2} f_{BC03,\lambda} e^{-(\tau_\lambda + \delta\tau_\lambda)} d\lambda \tag{4}$$

where $f_{BC03,\lambda}$ is the initial output of the models and $\delta\tau_\lambda$ is the 1σ error in the IGM optical depth due to inhomogeneities among different lines of sight. We can then break this up into a sum over discrete intervals, and calculate the variance, which for a small $\delta\tau_\lambda$ is

$$\sigma^2_{\langle f_V \rangle} = \sum_{n=1}^{N} f^2_{BC03,\lambda} \left(e^{-\tau_\lambda}\right)^2 (\delta\tau_\lambda)^2 \Delta\lambda^2 \tag{5}$$

where N is the number of bins we chose to break the V-band into. We approximate this as

$$\sigma^2_{\langle f_V \rangle} = N \left(\delta\tau_\lambda\right)^2 \frac{F_V^2}{N^2} \left(e^{-\tau_\lambda}\right)^2 \tag{6}$$

where $F_V{}^2$ is the total flux in the bandpass. The rms flux in the V-band due to the IGM inhomogeneities is then

$$\sigma = F_{BC03,V} e^{-\tau} \delta\tau N^{-\frac{1}{2}} \tag{7}$$

Thus the fractional error in the model flux which needs to be added in is $\delta\tau \times \mathrm{N}^{-\frac{1}{2}}$. To make this physically correct, the bin size should be equal to a typical clustering length for Lyα forest clouds, such that the Lyα forest optical depth variations in adjacent bins are essentially uncorrelated. Penton et al. (2000) calculated the two-point correlation function for Lyα forest clouds. They found that the correlation drops to zero at a separation of $\sim$ 11 Mpc. For z = 4.4, the co-moving distance between the front and back of the V-band filter is 1205 Mpc. Thus, we chose to use 110 bins. The uncertainty in the IGM absorption ($\delta\tau$) was found from Madau (1995). Extrapolating from his example of a z $\sim$ 3.5 galaxy, we found an uncertainty in exp(-τ) of $\sim$ 0.35, which corresponds to $\delta\tau \sim = 1.05$. Plugging these values into the above equations, we find that we need to include an error of $\sim$ 0.1 mag for the V-band model fluxes to account for inhomogeneities in the IGM.

3.4.4. *Equivalent Widths*

Model Lyα equivalent widths were calculated using the ratio of the model flux in the Lyα wavelength bin to the average continuum value on either side of that bin ($\times$ $\Delta\lambda$). We compare our model EW distribution to previous studies (i.e. Charlot & Fall

1993; Malhotra & Rhoads 2002; hereafter MR02). We also quantify the multiplicative effect adding clumpy dust to the models has on the Lyα EW.

Figure 7 shows the EWs of our models plotted versus stellar population age for Z=.02$Z_{\odot}$ and three different star formation histories: SSP (single burst), $\tau = 10^7$ (exponentially decaying) and a constant star formation history. We first discuss the results from the left-hand vertical axis, which shows the EWs from dust-free models. All of the models start at some value ($\sim$ 400 Å) at 10^6 yr and then decay from there. The EWs from the SSP and τ models fall all the way to zero at approximately 30 and 100 Myr, respectively. Models which are constantly forming stars asymptotically reach a constant value of EW at $\sim$ 120 Å due to the constant replenishment of massive stars. The upturn at later ages for the SSP and τ models are due to either hot horizontal branch stars and/or planetary nebula nuclei, which will start to dominate the UV flux after $\sim 10^8$ yr. While technically their Lyα EWs will be high, the actual UV continuum flux is tiny compared to what it was at earlier ages, and thus objects in this stage will likely not appear in Lyα galaxy samples. We calculate that at 400 Myr (the age at which the UV-upturn causes the EW to surpass 50 Å) a mass in excess of 10^{12} $M_{\odot}$ would be required in order for a given stellar population to be detected in our narrowband image. This mass is extremely high even in local universe terms (e.g., Tremonti et al. 2004), and thus is not likely to exist at high redshift. In order to distinguish EWs due to young stars from EWs due to faint UV continuum flux, the solid lines in these plots change to dashed lines when the continuum (V-band) flux falls to 10% of its value at 10^6 yr.

Charlot & Fall (1993) computed the Lyα EW from stellar population models using an earlier version of the Bruzual & Charlot software (1993). Their models assumed solar metallicity and case B recombination. They computed the Lyα EW for multiple IMF slopes, upper-mass cut-offs and star formation histories, with their youngest age being 5 Myr. For a SSP with a near-Salpeter IMF (x = 1.5; $x_{Salpeter}$ = 1.35) their maximum EW was calculated to be 210 (240) Å for an upper-mass cut-off of 80 (120) $M_{\odot}$, falling to zero at 40 Myr. The EWs from our SSP model have a maximum value of 400 Å (only $\sim$ 100 Å at t = 5 Myr), falling to zero by $\sim$ 20 – 30 Myr. However, their definition of SSP differs from ours. We defined ours as having a characteristic decay rate of 10^3 yr, while their burst model had a timescale of 10^7 yr. We can thus compare their results to our τ model (which has $\tau = 10^7$ yr). This model has a maximum EW of 400 Å ($\sim$ 200 Å at 5 Myr), much closer to the results of Charlot & Fall. For a constant SFH, Charlot & Fall find a maximum Lyα EW of 150 (250) Å falling to a constant value of 90 (100) Å by 10^8 yr for an upper-mass cut-off of 80 (120) $M_{\odot}$ (our upper-mass cut-off was 100 $M_{\odot}$). Our continuously star-forming models start at a maximum EW of $\sim$ 400 Å ($\sim$ 220 Å at 5 Myr), falling to 120 Å by 10^8 yr. Taking into account the differences between IMF slopes, metallicities and upper-mass cut-offs, we feel our constant SFH models are consistent with those of Charlot & Fall. In a more recent study, MR02 did a similar analysis using Starburst99 models (Leitherer *et al.* 1999). Their Salpeter IMF model has a constant SFH, upper-mass cut-off of 120 $M_{\odot}$ and Z = 0.05 $Z_{\odot}$. The EW from

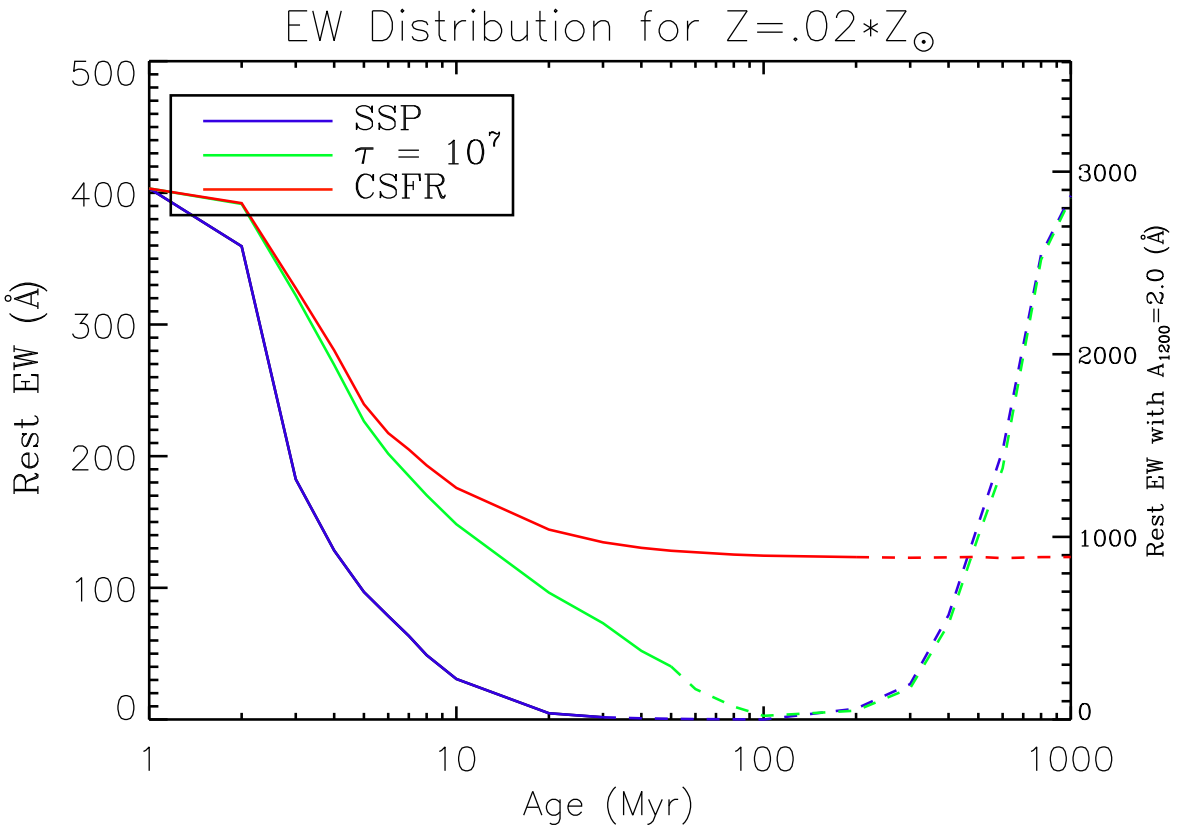

FIG. 7.—Equivalent width distribution from the models for Z = .02 $Z_{\odot}$. The upturn in EW at late age is caused by either hot horizontal branch stars and/or planetary nebulae nuclei, either of which will dominate the UV flux at later ages. However, at this point the total UV flux is much less that it was at early ages, such that a stellar population this old would likely not be picked up in a narrowband selected survey. Due to this, the line-style changes to dashed at the point where the V-band flux drops below 10% of its value at 10^6 years. The left-hand axis shows the rest-frame EW with no dust, and the right-hand axis shows the rest-frame EW with $A_{1200} = 2.0$. In order to observe a galaxy with an EW > 200 Å, it either needs to be only a few Myr old with no dust, or with dust it can be older than 10 Myr. Comparison to previous studies (Charlot & Fall 1993; Malhotra and Rhoads 2002) shows that our model EWs are consistent with previous results.

this model had a maximum value of 300 Å at an age of 1 Myr, asymptoting to a value of 100 Å by 100 Myr, both of which are consistent with our models.

When clumpy dust comes into the models, things can change dramatically. As we discussed above, in our models the dust is not attenuating the Lyα line, which results in the Lyα EW being enhanced as the continuum is suppressed. Consequently, given an amount of dust extinction, the Lyα EW will be enhanced by a multiplicative factor. For dust amounts of $A_{1200} = 0.5$, 1.0, 1.5 and 2.0 mag, this factor is 1.64, 2.68, 4.40 and 7.21, respectively. The right-hand vertical axis in Figure 7 shows what the EWs from the models are with 2.0 mag of clumpy dust extinction. This shows that for a given model, one can have an older age while still keeping a high EW. For example, for a SSP with Z = 0.02 $Z_{\odot}$, the EW drops below 200 Å by 3 Myr, while with 2.0 mag of clumpy dust, this does not happen until after 10 Myr, over a factor of three times longer, making it much more likely that this object would be observed with a high EW in a narrowband selected survey. Table 5 shows the maximum possible age allowed for a stellar population with EW $<$ 200 Å for a variety of models.

3.5. Results

3.5.1. *Fitting to Models*

Using our bandpass averaged fluxes, we were able to fit our objects to the BC03 models. We have nine possible bands to choose from for fitting: CTIO-MOSAIC Hα, *HST*/ACS F435W (B), F606W (V), F775W (i'), F850LP (z'), *Spitzer*/IRAC channel 1 (3.6 μm), channel 2 (4.5 μm), channel 3 (5.8 μm) and channel 4 (8.0 μm). In order to separate the model-dependent parameters from other factors, we elected to fit flux

ratios to the models, and then fit the mass to the best-fit model at the end. We computed a flux ratio to the i' band for each band, with a corresponding flux ratio error propagated through.

The χ^2 was then computed for each model – object combination using:

$$\chi^2 = \sum_i \frac{\left[f^i_{obj} - f^i_{mod}(t, \tau, A_{1200}, Z)\right]^2}{\sigma^2(f^i_{obj})} \tag{8}$$

where i denotes the bandpass, f_{obj} is the object flux ratio, f_{mod} is the model flux ratio and $\sigma(f_{obj})$ is the error in the flux ratio for a given bandpass, derived from the error in the flux for each bandpass and the error in the i'-band flux. All fluxes were in units of f_ν (ergs s^{-1} cm^{-2} Hz^{-1}).

Out of our five Lyα galaxy candidates, we only fit stellar population models to four of them. While we have no reason to suspect object 5 is not a real Lyα emitter, its proximity to a very bright object makes its *Spitzer* fluxes inaccurate. With only the ACS and narrowband data to go on, there are not enough available passbands to fit this object. Thus the four objects which we fit were: 1, 2, 4 and 6. While we did have data in all nine bands listed above, not all were used in our fitting. Both the IRAC 5.8 and 8.0 μm were undetected in the four objects we fit, and thus were not used. Because the entire B-band is blue-ward of the Lyman break, we can be highly confident that on any line of sight there will be no significant flux transmitted through the B-band. If redshift were a free parameter in our models, then we would definitely use the B-band, as the absence of flux would be a helpful redshift indicator. However, given that three of our four objects were spectroscopically confirmed (and the fourth has a photo-z) to be at z = 4.4, we did not feel it would be worthwhile

TABLE 5
MAXIMUM POSSIBLE AGE ALLOWED FOR A STELLAR POPULATION WITH EW > 200 Å

SFH	No Dust		$A_{1200} = 2.0$	
	Z = .02*$Z_\odot$	Z = $Z_\odot$	Z = .02*$Z_\odot$	Z = $Z_\odot$
SSP	3 Myr (182 Å)	1 Myr (193 Å)	10 – 20 Myr (222 – 34 Å)	5 – 6 Myr (424 – 181 Å)
$\tau = 10^7$	7 Myr (184 Å)	3 Myr (186 Å)	50 – 60 Myr (291 – 167 Å)	50 – 60 Myr (300 – 193 Å)
Constant SFH	8 Myr (193 Å)	3 Myr (190 Å)	Never	Never

NOTES.—Values in parenthesis are the Lyα equivalent widths at the reported ages. Since the grid of model ages is not continuous, in some cases there is a large amount of time around when the EW drops below 200 Å in the models. In these cases we report the ages and EWs on either side of 200 Å. Depending on the star formation history and metallicity, two magnitudes of clumpy dust extinction can keep the Lyα EW above 200 Å up to 3 – 20 times longer than just young stars alone (indefintiely for a population which suffers no drop in star formation activity). Models with dust have q = 0 (see §3.5.1).

to introduce redshift as a free parameter. Thus we have left the B-band out of the fitting.

As a final step, we introduced a parameter, q, which we called the clumpiness parameter because its value simulates the effects of different dust geometries. Previously, when we applied dust to the models, we added in the Lyα flux after the dust was added, so that the Lyα flux was not attenuated. This had a very "cartoon" effect on the models, meaning that Lyα was either attenuated by all of the dust or by none of the dust. We still proceed in the same order as before, only now we multiplied the Lyα flux by $e^{-q\tau}$, with q ranging from 0 to 10. A q value of zero represents exactly what our original models had been doing, by not attenuating Lyα by dust. This models the dust geometry of clumpy clouds in an empty inter-cloud medium, i.e., Neufeld (1991) and Hansen & Oh (2006). A q value of 10 attenuates Lyα 10 times more than the continuum. Thus, $q \geq 10$ models the effects of a uniform dust distribution, attenuating Lyα much more than the continuum due to the fact that it is resonantly scattered. Values between 0 and 10 model differing geometries, with the case of $q = 1$ modeling a geometry where Lyα and the continuum are attenuated at the same rate (possibly a scenario with dust in clouds, but in which the inter-cloud medium is not entirely empty). Introducing this parameter vastly increased the quality of the best fits, but it did come at a cost. Since we had no additional data, we could not add another free parameter without taking away one. We decided to remove metallicity as a free parameter, as the effects of changing metallicity had the least effect on the models. We decided to fix a value of Z = .02 $Z_\odot$ for all models.

3.5.2. *Object 1*

Object 1 is best fit by a 5 Myr stellar population with a mass of $3.0 \times 10^8\ M_\odot$, a continuous star formation history, and 1.1 mag of dust extinction (A_{1200}) which attenuates Lyα 50% more than the continuum ($q = 1.5$). The quality of this fit was high, with $\chi_r^2 = 2.00$. This object is thus very young, but its red color (specifically, z' - 3.6 μm) indicates a significant amount of dust. However, an object this young, especially with a continuous SFH, already has a pretty high Lyα EW. Thus, even though it is best fit by a significant amount of dust, it does not require this dust to enhance its EW, as evidenced by its value of $q > 1$. This object fits the mold of a "typical" Lyα galaxy, as it is young and low mass. This being said, its dust content is intriguing as it indicates that this object is definitely not primitive.

3.5.3. *Object 2*

Object 2 is also best fit by a young, low-mass stellar population (3 Myr; $3.2 \times 10^8\ M_\odot$), however it has a fast-decaying SFH, with $\tau = 10^6$ yr. It has less dust than object 1 ($A_{1200} = 0.9$ mag), but a larger value of q, with $q = 2$ indicating that Lyα is being extinguished at twice the value of the continuum. However, we should be somewhat skeptical about these results, as this object has the worst fit out of our sample, with $\chi_r^2 = 5.269$. That being said, these results are not astonishing, as they indicate that this object is possibly very similar to object 1.

3.5.4. *Object 4*

Object 4 is the most intriguing object in our sample. It has the highest quality fit of the whole sample, with $\chi_r^2 = 1.326$, lending the most credibility to its results.

It is best fit by an 800 Myr, 6.5×10^9 $M_\odot$ stellar population with a continuous SFH. While the amount of dust extinction is lower than the other objects ($A_{1200} = 0.4$ mag) it has a value of $q = 0$, the only object with $q < 1.5$. While 0.4 mag of dust is not a lot, if it is not attenuating Lyα, as $q = 0$ attests to, it will increase the EW by $\sim 50\%$, making this object a candidate for dust enhancement of the Lyα EW. This object definitely does not fit the mold of a typical Lyα galaxy with its old age and larger mass. Although we only have one object like this in our small sample, its existence means that Lyα galaxies may not all be uniformly young.

3.5.5. *Object 6*

Similar to objects 1 and 2, object 6 is also best fit by a young (3 Myr) and low-mass (9.9×10^8) stellar population. It has an exponentially decaying SFH with $\tau = 10^6$ yr and 1.8 mag of dust attenuating Lyα 50% more than the continuum. The best-fit model ($\chi^2_r = 2.121$) has a low EW of ~ 61 Å, which is very comparable to the measured EW of the object, which was ~ 56 Å. Although this object has a young age, its fast-decaying SFH and large amount of dust which *is* attenuating Lyα are keeping the Lyα EW down. Figure 8 shows the best-fit models for each object, and Table 6 details the best-fit parameters.

3.5.6. *Best-Fit Models Without Dust*

As an exercise, we wanted to see what the best-fit models to these objects would be if we forced the amount of dust to be zero while keeping everything else the same. In doing this, the number of degrees of freedom became three, because both dust and q were dropped as free parameters, thus the reduced χ^2 reported is

$\chi^2/3$. Figure 9 shows the results of this analysis. With no dust, all of the objects were forced to have an older age to explain the red colors. In all cases, the best-fit model with no dust had a significantly higher χ^2_r than the best-fit model allowing dust, thus we can be reasonably sure that these objects have some dust, and that we have treated it correctly in the models.

3.5.7. *Monte Carlo Analysis*

To determine confidence regions for our model parameters, we ran 10^4 Monte Carlo simulations. In each simulation, we add or subtract flux to each band for each object equal to a Gaussian random deviate multiplied by the object's flux error in a given band. Each band had its own random number in each simulation, which was computed by the IDL function RANDOMN, which generates Gaussian–distributed random numbers. For each possible model (25200 possible models; 5 SFHs, 24 ages, 21 dust optical depths and 10 values of q), the χ^2 was computed for each simulated object flux. The result was that for each object, we now had 10,000 best-fit models. In an ideal case, these models would be distributed around the best-fit parameters to the actual observations.

In order to see if this was true, we plotted contours showing the density of best-fit parameters for each object in three planes: dust versus age, dust versus q and age versus q (Figure 10).[9] The blue, green and red contours show the 1 σ (68%), 2 σ (95%) and 3 σ (99.5%) confidence levels, respectively. For object 1, it appears as if

[9]We acknowledge that we are prevented from observing part of the dust vs. q plane due to selection effects. A galaxy with $A_{1200} = 2.0$ and $q = 10$ would have its Lyα much too supressed to be selected via the narrowband. Similarly, a galaxy with $A_{1200} = 2.0$ and $q = 0$ would be bright in the narrowband, but its continuum flux would be vastly attenuated, thus an object such as this may not have enough data to be used in a stellar population study.

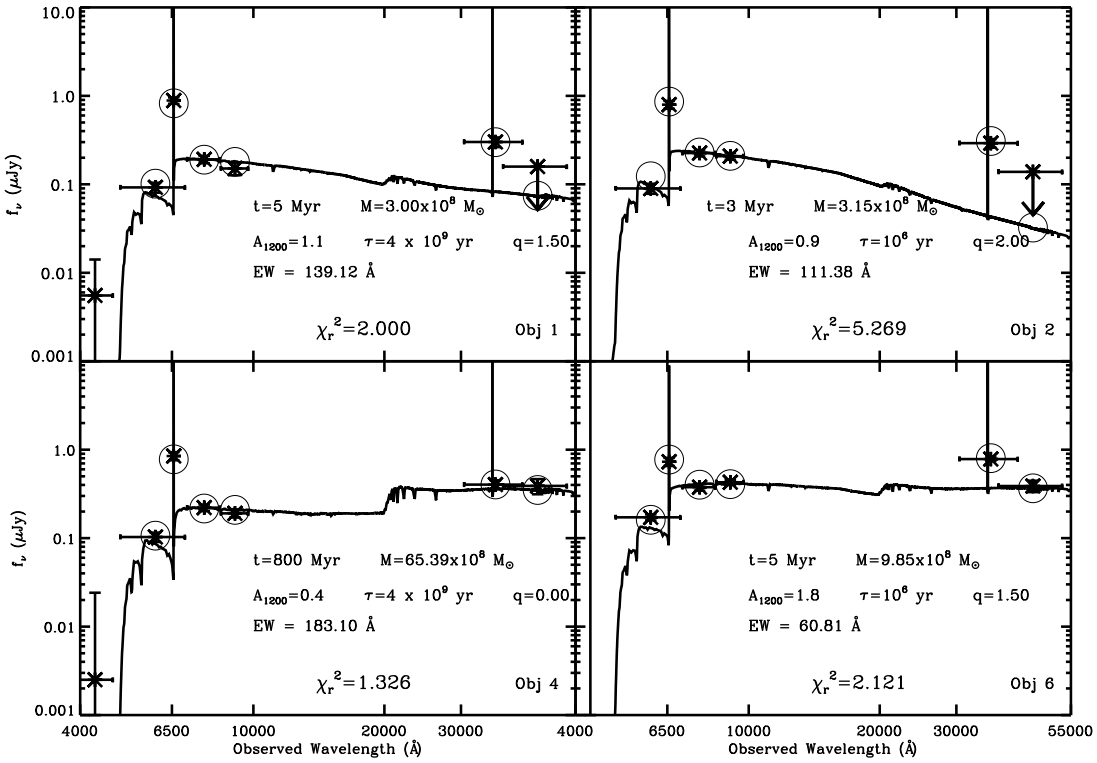

FIG. 8.— The open circles are centered on the positions of the bandpass averaged fluxes of the best-fit models. Object 1 is best fit with a young, low-mass stellar population with a continuous SFH. The best-fit model contains over a magnitude of dust, but its geometry is such that it is extinguishing Lyα 50% more than the continuum. Object 2 is best fit by a young, low-mass stellar population with an exponentially decaying SFH with $\tau = 10^6$ yr. There is a little less than a magnitude of dust, but it is extinguishing Lyα at twice the amount of the continuum. Object 4 is by far the most interesting object in our sample. It is best fit by a much older, higher-mass stellar population with a continuous SFH. It has less dust that the other models, but this dust is not attenuating Lyα at all, enhancing the observed Lyα EW. The combination of dust and a continuous SFH is allowing this object to have a high EW at an age of 800 Myr. Object 6 is best fit by a young, low-mass model similar to objects 1 and 2. However, the best-fit model has nearly 2 mag of dust attenuating Lyα twice as much as the continuum, resulting in a lower EW.

TABLE 6
CDF–S BEST-FIT PHYSICAL PARAMETERS

Name	χ^2_r	Age (Myr)	Mass ($M_\odot$)	A_{1200} (mag)	SFH	q
Object 1	2.000	5	3.00×10^8	1.1	Continuous	1.50
Object 2	5.269	3	3.15×10^8	0.9	$\tau = 10^6$	2.00
Object 4	1.326	800	65.39×10^8	0.4	Continuous	0.00
Object 6	2.121	5	9.85×10^8	1.8	$\tau = 10^6$	1.50

NOTES.—The best-fit parameters for each of our objects. These were found by minimizing the reduced χ^2 between each object and a grid of models.

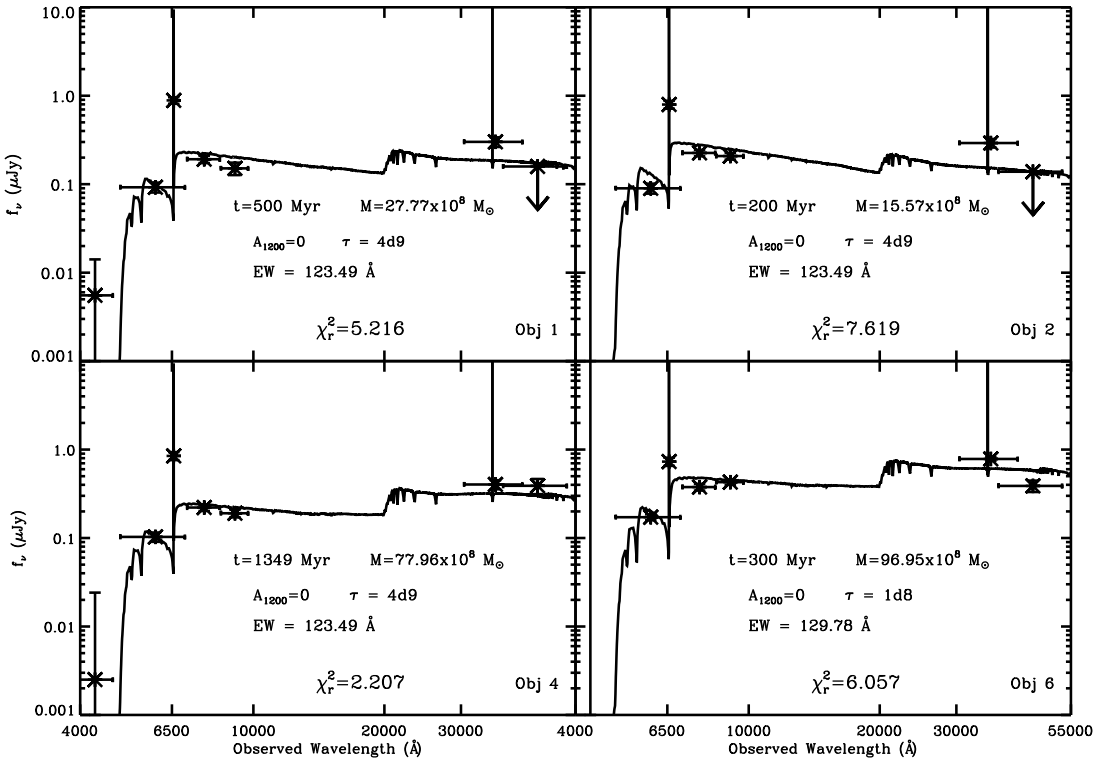

FIG. 9.—Best-fit stellar populations forcing the models to have no dust. All objects are best fit by older, more massive stellar populations, but the quality of these fits are of much lower quality (higher χ^2) than the best-fit models with dust.

the age is well constrained to be very young, as the 1 σ contour is fairly thin along the age axis. The same is true for q, constraining it to be between 1 and 3, ruling out dust enhancement of the Lyα EW for this object. The only parameter that may be degenerate is dust, as the 1 σ contour is very long along the dust axis. However, in no case is any model best fit with zero dust, and the 1 σ contour is roughly centered on the best-fit value of $A_{1200} = 1.1$.

Object 2 is very similar to object 1 in that its age is well constrained to be young, and its q value is well constrained to be greater than 1. Similarly, the dust in object 2 is slightly degenerate, but it is well constrained to have some dust, with the best-fit value being the most likely value. The age of object 6 is also well constrained to be young, although there is a slight 1 σ blip at t = 100 Myr. The q value is even better constrained than in objects 1 or 2, being very centered on the best-fit value of 1.5. Dust is still degenerate, although less so than in objects 1 or 2, with 1 σ values ranging from 1.5 to 2.0 mag.

Object 4 is the only object in our sample which shows evidence of dust enhancement of the Lyα EW. The age is mostly constrained to be $>$ 100 Myr, with a large 1 σ area centered around the best-fit model at 800 Myr, and a smaller 1 σ area around 200 Myr (and an even smaller one at 30 Myr). A range of dust values are permitted, but generally lie in the range from 0.1 to 0.9 mag. The q parameter is definitely constrained to be < 1, with the 1 σ area centered around the best fit, with no part of it being greater than $q = 0.25$. Thus this object is well constrained to have an old age and a small amount of dust with a dust geometry which is enhanc-

ing the Lyα EW. It should be noted that the effect of dust is not enormous. Dust extinction of 0.4 mag will increase the Lyα EW by $\sim$ 50%, meaning that the EW of this object was not negligible beforehand, mainly due to a constant SFH. However, the dust pushes this object's best-fit model EW from a value of $\sim$ 120 up to $\sim$ 180 Å. Given the model EW curves we saw earlier, if one ignored the possible effects of dust one would expect to see many more 120 Å EW objects than 180 Å. While this effect is only seen in one object, it shows that we cannot afford to ignore the effect dust could have on Lyα EWs, as we have shown it can help explain the perceived over-abundance of high-EW sources.

3.6. Discussion

3.6.1. *Lyα Detection Fraction*

Out of the whole GOODS CDF–S catalog, we found that there were 229 B-band dropouts. The dropout criteria selects galaxies with a Δz range of $\sim$ 1.0. The width of our narrowband filter is 80 Å around a central wavelength of 6563 Å, corresponding to a Δz range of 0.07 for Lyα. Thus, about $0.07 \times 229 = 16$ B-dropouts lie in the redshift range where we could detect Lyα. Among these, only five show a narrowband excess. This corresponds to a Lyα detection fraction of 31%, comparable with previous studies (e.g., Shapley *et al.* 2003; 25%).

3.6.2. *Hα Equivalent Widths*

When comparing the best-fit models to the data points, it is obvious that the model Hα flux is dominating the model 3.6 μm flux, as is evident from the fact that the 3.6 μm data point is far above the model continuum level. The model rest-frame

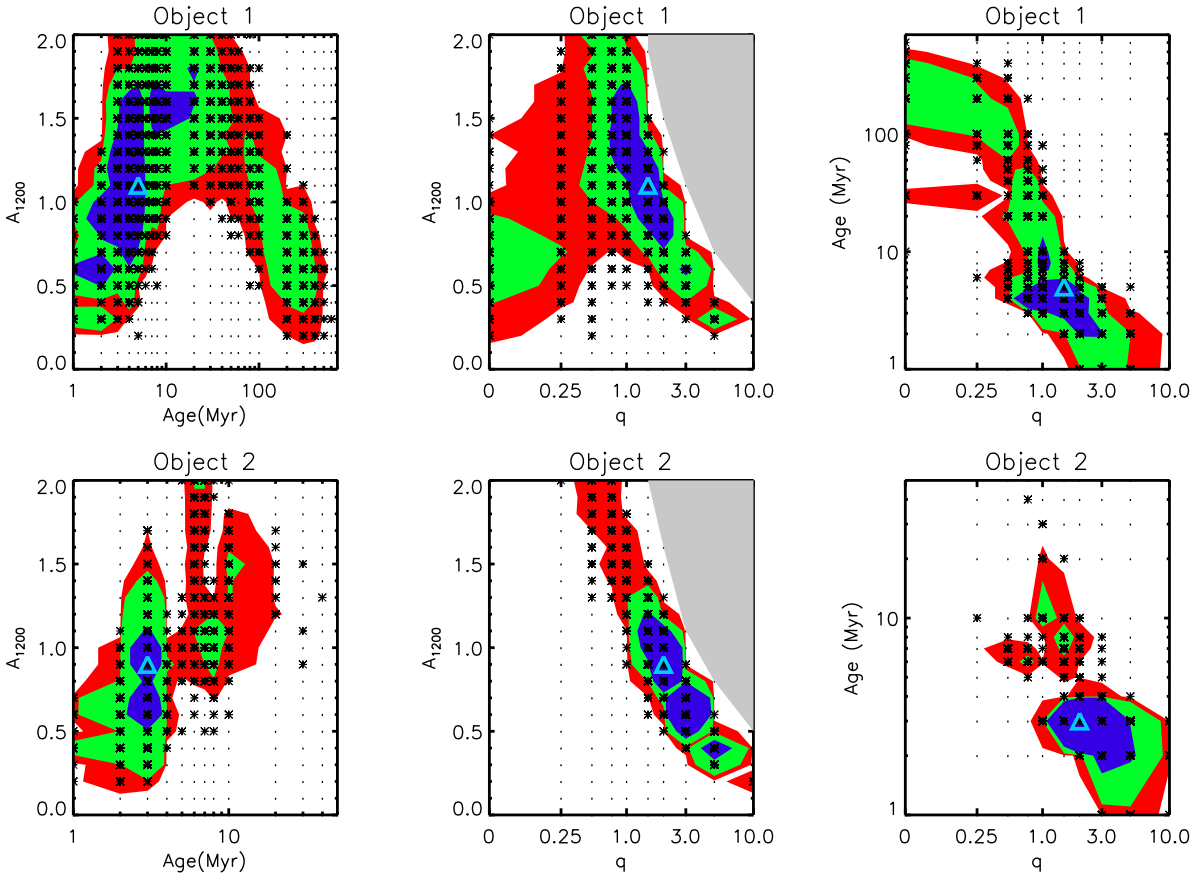

(a)

FIG. 10.—(a) Contours showing the density of results from our Monte Carlo simulations. Each asterisk represents the best fit of one Monte Carlo run (most of the asterisks are really multiple points). The rest of the model grid which did not have a best fit are denoted by dots. The best-fit model from the actual object is denoted by a blue triangle. The objects are in separate rows, and the columns represent three different planes: dust vs. age, dust vs. q and age vs. q (note that the range of the age axis is different for some of the objects). Continued on next page...

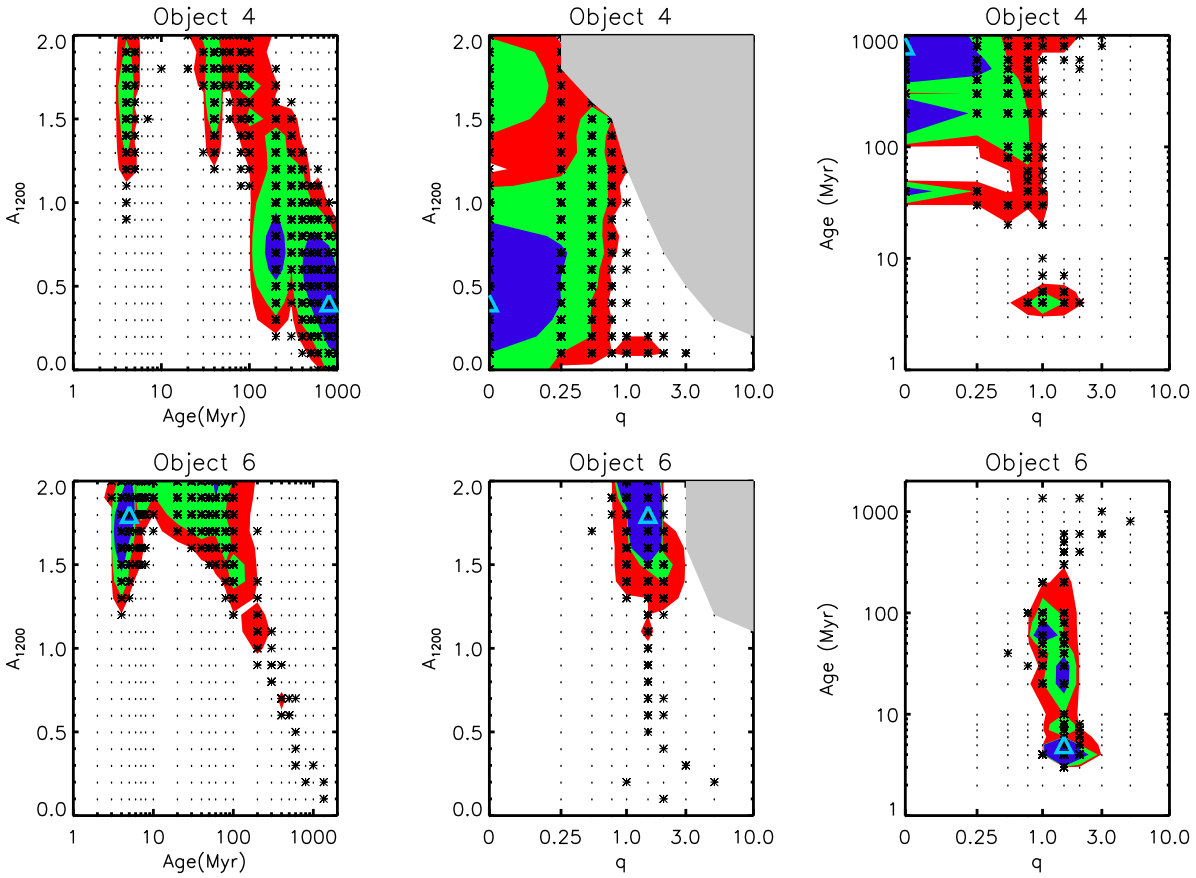

(b)

FIG. 10.—(b) Sixty-eight percent of the best fits from the simulations fall in the blue contour, and as such this is the 1 σ contour. Likewise, the green is the 2 σ contour and the red is the 3σ contour. The cross-hatched region represents the area of parameter space where we would not expect to detect an object due to dust extinction. Models falling in this region had their V or NB656 band flux reduced to less than a third of that of the best-fit model. Studying these figures, we were satisfied that our best-fit models accurately represented the most-likely best fit for each object.

Hα EWs are 3800, 8500, 200 and 1700 Å for objects 1, 2, 4 and 6, respectively. At first glance, these seem large, but one needs to remember that with the exception of object 4, these objects have been found to be extremely young, low-mass, star-forming galaxies. Keeping that in mind, these values of Hα EW are quite reasonable.

In a survey of H II regions in a nearby galaxy, Cedres *et al.* (2005) found that the Hα EW distribution peaked at $\sim$ 1000 Å, with a few H II regions with EWs as high as 10000 Å. In an analysis of a z = 6.56 Lyα galaxy, Chary et al. (2005) derived an Hα EW of 2000 Å, concluding that the Hα line dominated the 4.5 μm flux in their object. While computing the synthetic properties of starburst galaxies, Leitherer and Heckman (1995) computed a Hα EW of $\sim$ 3200 Å for a population with 0.1 $Z_{\odot}$ and a constant star formation history. Taking into account model differences (including a difference of 5 times in metallicity) we find our values of Hα EWs to be consistent with those previously found in the literature for star-forming galaxies.

The addition of Hα flux to the model spectra led to an interesting result. In a young star-forming galaxy both Lyα and Hα photons will be produced in large quantities, producing the large Lyα and Hα EWs seen in objects 1, 2 and 6. However, if the Lyα EW is only observed as being large due to dust enhancement, than the Hα EW should not be large (as Hα photons are not resonantly scattered). This is seen in our sample, as object 4 has a best-fit Hα EW of only 200 Å, much less than the other three objects. Thus, obtaining data about $H\alpha$ lines in Lyα galaxies could be an important diagnostic for deciphering the underlying stellar population, as the Lyα/ $H\alpha$ ratios should indicate whether dust enhancement is playing a role. This

tool will be a prime candidate for study on future observatories such as the *James Webb Space Telescope* or the Stratospheric Observatory for Infrared Astronomy.

3.6.3. *Comparison to Other Work*

It is useful to compare our results to those of other studies done using *HST* and *Spitzer* data together, as the IR data (which corresponds to the rest-frame optical at z = 4.4) better constrains the stellar masses as it is less attenuated by dust than the rest-frame UV. Two recent studies have been published studying Lyα emitting galaxies (LAEs) at z $\sim$ 5 and 5.7 by Pirzkal *et al.* (2007) and Lai *et al.* (2007), respectively. Pirzkal *et al.* studies the stellar populations of nine LAEs in the HUDF detected on the basis of their Lyα emission lines in the Grism ACS Program for Extragalactic Science (GRAPES; Pirzkal et al. 2004; Xu *et al.* 2007; Rhoads *et al.* 2008) survey. Using stellar population models similar to ours, they found very young ages ($\sim 10^6$ yr) and low masses ($\sim$ few $\times\ 10^7\ M_\odot$), with some dust in a good fraction of their objects. Lai et al. studied three narrowband-selected LAEs spectroscopically confirmed to lie at z $\sim$ 5.7 in the GOODS HDF-N field. Also using BC03 models, with an instantaneous burst SFH they found ages from 5 to 100 Myr (up to 700 Myr with a constant SFH), and masses from 10^9 to $10^{10}\ M_\odot$. Their objects were also best fit by dust, with E(B - V) $\sim$ 0.3 – 0.4 ($A_V \approx 1$ – 1.2).

Three of our four objects have ages consistent with those from Pirzkal *et al.* (2004) and Lai *et al.* (2007), who find ages from $\sim$ 1 to 100 Myr. Our fourth object has an age much larger than those found in these papers, at 800 Myr. Eight out of the nine Pirzkal *et al.* objects have M $< 10^8\ M_\odot$, whereas the Lai *et al.* objects

have masses 2 orders of magnitude higher. The masses of our objects reside in the middle, from 10^8 to 10^9 $M_\odot$. The likely reason that our masses are higher than those of Pirzkal *et al.* is because they reach fainter luminosities, detecting objects with emission lines as faint as 5×10^{-18} erg s^{-1} cm^{-2}. On the flipside, the larger masses from Lai et al. are likely due to their selection criteria. They found 12 LAEs in the GOODS-N field, but they only analyzed the three objects with significant 3.6 and 4.5 μm flux. They acknowledge that their masses are high, and that this may be due to selecting objects from the high-mass end of the mass distribution.

Another difference is how each study treated Lyα in their model fitting. Pirzkal *et al.* chose to exclude the ACS i' band from their fitting, as at their redshifts the Lyα line would fall in this band, and they did not want to include the uncertainties that subtracting the line flux from the i' flux would create. Lai *et al.* chose to treat Lyα by estimating the amount of flux Lyα contributed to the i' flux, then adding this percentage as an i'-band error ($\sim 30\%$). As described in detail in earlier sections, we chose to add the Lyα emission to the models in order to investigate the effect dust had on the Lyα EW. While each of these methods has its merit, the method of Pirzkal *et al.* likely introduces the least amount of uncertainty by simply not including the broadband which contains the Lyα emission. They had the luxury that in addition to the ACS and IRAC data, they also had *HST* NICMOS and Very Large Telescope (VLT) ISAAC near-IR data, so cutting a band from the fitting did not force them to throw out a constraint.

One other interesting study is that done by Chary *et al.* (2005) by fitting stellar population models to a z = 6.56 Lyα galaxy with near-IR and IRAC data. As we mentioned above, they determined that their 4.5 μm flux was dominated by a Hα line, implying vigorous star formation. Taking this line into account, they found a best-fit stellar population of 5 Myr, 8.4×10^8 $M_\odot$ with $A_V = 1.0$ mag. This is even dustier than our objects, showing that not only is dust common at z = 4.4, it may exist in Lyα galaxies up to z $\sim$ 6.5.

By including Lyα in our models rather then attempting to subtract out its influence in the observed broadbands, we were able to investigate the effect dust geometry had on the Lyα EW. While the other two studies listed here did not do this analysis, they did include homogeneous dust in their models. They found that many/all of their objects were best fit by including at least a small amount of dust. This confirms our result that regardless of the effect of the dust geometry, one needs to include dust when analyzing LAEs, as it appears to be present in a majority of them. Failure to include dust in the models will result in a poorer fit, likely with an older or more massive stellar population than is really in place.

3.7. Conclusions

We have presented the results of our analysis of four narrowband selected Lyα galaxies in the GOODS CDF–S. By observing in such a well studied field, we were able to take advantage of the plethora of deep public broadband data (GOODS *HST* ACS, *Spitzer* IRAC and MUSIC), as well as previous spectroscopic studies (PEARS)

available in the region. Three out of our four objects were spectroscopically confirmed to lie at z = 4.4. The other object has a photometric redshift of 4.42.

Previously, it had been assumed that Lyα galaxies were young, low-mass galaxies with little to no dust. Even when dust has been found, it has been assumed to be homogeneously distributed, meaning that it would attenuate the Lyα flux much more than the continuum flux because Lyα photons are resonantly scattered. However, a scenario has been theoretically studied in which the geometry of a dusty ISM could actually enhance the Lyα EW rather than reduce it. This scenario consists of an ISM in which the dust resides in clouds, mixed in with neutral hydrogen, whereas the inter-cloud medium is hot and ionized. In this scenario, Lyα photons would effectively bounce off the surface of the clouds, finding it much easier to escape the galaxy than continuum photons. Thus, a galaxy could exhibit a much larger Lyα EW than that intrinsic to the underlying stellar population.

In order to investigate this, we have compared the fluxes of our objects to stellar population models. We have included Lyα emission in the models, as well as introducing a clumpiness parameter, q, which dictates how much Lyα is attenuated by a given dust amount. Three of our four objects were best fit by models with a very young age ($\sim$ few Myr) and low stellar masses ($\sim$ few $\times$ 10^8 $M_\odot$), with a significant amount of dust ($A_{1200} = 0.9 - 1.8$) attenuating the Lyα flux more than the continuum ($q = 1.5 - 2.0$). However, one object, object 4, is best fit by a vastly different model. This object is best fit by a much older, more massive stellar population, with an age of 800 Myr and M = 6.5 $\times$ 10^9 $M_\odot$. What is interesting about this object is that

its EW is among the highest in our sample. Even with a constant SFH, an 800 Myr stellar population would not be able to produce a Lyα EW above 120 Å, while this object has an observed rest-frame EW of $\sim$ 150 Å and a best-fit model EW of $\sim$ 180 Å. Thus something is causing the EW of this object to be enhanced, and the models tell us that it is due to dust. This object is best fit by $A_{1200} = 0.4$ mag of dust, and while this is less than any of the other objects, the clumpiness parameter is best fit to be $q = 0.0$. This means that the 0.4 mag of dust are attenuating the continuum, but not the Lyα flux, enhancing the EW by 50%.

Comparing our results to those from other studies, we find that our age and mass results are consistent when data and selection differences are accounted for. However, no other observational studies have yet tried to model the effect dust could have on Lyα for differing geometries. While our sample size is small, analysis of a larger sample could indicate that there are really two classes of Lyα galaxies: a young, low-mass Lyα galaxy with an intrinsically high Lyα EW and an older, higher-mass galaxy with a lower intrinsic EW which has been enhanced due to dust.

4. Lyα GALAXIES: PRIMITIVE OBJECTS, DUSTY STAR-FORMERS OR EVOLVED GALAXIES?

4.1. Abstract

We present stellar population modeling results for 11 newly discovered Lyman alpha emitting galaxies (LAEs), as well as four previously known LAEs at z $\sim$ 4.5 in the Chandra Deep Field – South. We fit stellar population models to these objects in order to learn specifically if there exists more than one class of LAE. Past observational and theoretical evidence has shown that while many LAEs appear to be young, they may be much older, with Lyα EWs enhanced due to resonant scattering of Lyα photons in a clumpy interstellar medium (ISM). Our results show a large range of stellar population age (3 – 500 Myr), stellar mass (1.6×10^8 – 5.0×10^{10} $M_\odot$) and dust extinction (A_{1200} = 0.3 – 4.5 mag), broadly consistent with previous studies. With such a large number of individually analyzed objects, we have looked at the distribution of stellar population ages in LAEs for the first time, and we find a very interesting bimodality, in that our objects are either very young (< 15 Myr) or old (> 450 Myr). This bimodality may be caused by dust, and it could explain the Lyα duty cycle which has been proposed in the literature. We find that eight of the young objects have SEDs consistent with a clumpy ISM. We find that dust geometry appears to play a large role in shaping the SEDs that we observe, and that it may be a major factor in the observed Lyα equivalent width distribution in high redshift Lyα galaxies, although other factors (i.e. outflows) may be in play. We conclude that 13 out of our 15 LAEs are dusty star-formers, with the other two LAEs being evolved galaxies.

4.2. Introduction

While high-redshift galaxies can be hard to observe due to dimming with distance, narrowband selection of Lyα galaxies has proven a very efficient method to select high-redshift galaxies based on a strong emission line (e.g., Rhoads *et al.* 2000, 2004; Rhoads & Malhotra 2001; Malhotra & Rhoads 2002; Cowie & Hu 1998; Hu *et al.* 1998, 2002, 2004; Kudritzki *et al.* 2000; Fynbo, Möller, & Thomsen 2001; Pentericci *et al.* 2000; Ouchi *et al.* 2001, 2003, 2004; Fujita *et al.* 2003; Shimasaku *et al.* 2003, 2006; Kodaira et al. 2003; Ajiki *et al.* 2004; Taniguchi *et al.* 2005; Venemans *et al.* 2002, 2004; Pascarelle *et al.* 1996ab; Gawiser *et al.* 2006a; Lai *et al.* 2007, 2008; Nilsson *et al.* 2007; Finkelstein *et al.* 2008a). These objects are of interest, as over 40 years ago Partridge & Peebles (1967) proposed that they may be signs of primitive galaxies in formation. This was easy to understand, as Lyα photons are copiously produced in star formation regions, and we would expect the first galaxies to be undergoing periods of extreme star formation. However, not until recently have we had the data to verify this assumption.

The availability of stellar population modeling codes has allowed the derivation of physical parameters of galaxies from photometry alone. In the past few years (thanks to large surveys such as the Great Observatories Origins Deep Survey (GOODS)), broadband photometry of LAEs has become deep enough to compare objects to these models, learning about such parameters as stellar population age, stellar mass, and dust extinction. First results from these studies were unsurprising, as stacking analyses showed that an average LAE was young ($\sim 10 - 100$ Myr), low

mass (10^{7-8} $M_{\odot}$) and dust free (e.g., Gawiser *et al.* 2006a; Finkelstein *et al.* 2007, Chapter 2; Lai *et al.* 2008). Recently, deeper data has allowed the comparison of individual high-redshift LAEs to models for the first time, as chronicled in Chary *et al.* (2005), Pirzkal *et al.* (2007), Lai *et al.* (2007) and Finkelstein *et al.* (2008a, Chapter 3). These studies have shown a wide range of results, with LAE ages from 1 – 1000 Myr, masses from 10^{6-10} $M_{\odot}$ and, most surprisingly, dust extinction with A_V up to 1.3 mag. These results show that while some LAEs may be young and dust-free, many are dusty, and some are even evolved (i.e. old and high mass).

This raises an interesting question, as how can an evolved stellar population produce enough Lyα photons to be picked up by a narrowband selected survey? Many scenarios have been proposed (i.e. zero metallicity, top-heavy initial mass function etc.), but these are rather extreme, and given the amount of dust extinction we see, they would be unlikely to produce enough Lyα photons to explain the observed excesses. We have thus decided to observationally test a scenario developed theoretically by Neufeld (1991) and Hansen & Oh (2006), where the Lyα equivalent width (EW) actually gets *enhanced* due to a dusty interstellar medium (ISM). This is counter-intuitive, as dust will strongly suppress any ultraviolet (UV) photons. The news is even worse for Lyα photons, as they resonantly scatter off of neutral hydrogen atoms, thus their mean-free-paths are rather small, vastly increasing their chances of encountering a dust grain. However, as Neufeld and Hansen & Oh suggest, an ISM that is very clumpy could actually prevent the Lyα photons from seeing the dust at all. This can happen if the dust and neutral hydrogen lie in clumps, with a tenuous, ionized

medium separating the clumps. In this geometry, the Lyα photons stand a very high chance of being resonantly scattered at the surface of these clumps, spending most of their time in the inter-clump medium. In this manner, the Lyα photons are effectively screened from ever encountering a dust grain. The story is different for continuum photons, as they are not resonantly scattered, thus they will penetrate deeply into a clump, with a strong chance of being scattered or absorbed. As EW is a measure of line-to-continuum flux, this effectively enhances the observed EW over that due to the stars (or more accurately, the stars interaction with the interstellar hydrogen in their immediate surroundings). Note that the Lyα flux itself is not being increased, rather the Lyα-to-continuum ratio is being enhanced (see §3.4.2 for a detailed explanation of this scenario).

In Finkelstein *et al.* (2008a; hereafter F08a), we analyzed a sample of four LAEs, fitting model spectra to their SEDs, searching for proof that this type of ISM exists. Three of our objects were best fit by young (5 Myr) dusty ($A_{1200} \sim 1 - 2$ mag) stellar populations, similar to those seen by Pirzkal *et al.* (2007) at $z \sim 5$ and Chary *et al.* (2005) at $z \sim 6.5$. However, the fourth object was best fit by an old (800 Myr) stellar population, with 0.4 mag of dust arrayed in a clumpy ISM, showing evidence of dust enhancement of the Lyα EW. Also interesting was the age distribution, as these galaxies were either very young or very old, although this distribution was hard to quantify with such a small sample. Using our larger sample, we will now see if the absence of "teenage" LAEs is real, and see if most LAEs are primitive objects, dusty star-formers, or evolved galaxies. Further detection of dust enhancement of the

Lyα EW can help explain the larger than expected EWs seen in many LAEs (e.g., Kudritzki *et al.* 2000; Malhotra & Rhoads 2002; Finkelstein *et al.* 2007).

This paper is organized as follows. In §4.3 we present our observations, including our object selection and redshift information where applicable. In §4.4 we present our stellar population models. Our best-fit results for each object are presented in §4.5, and we discuss the implications of these results in §4.6, including suggestions for future improvement. We present our conclusions in §4.7. In this Chapter we assume Benchmark Model cosmology, where $\Omega_m = 0.3$, $\Omega_\Lambda = 0.7$ and $H_0 = 0.7$ (c.f. Spergel *et al.* 2007). All magnitudes in this paper are listed in AB magnitudes (Oke & Gunn 1983).

4.3. Data Handling

4.3.1. *Observations*

In F08a, we published a study based on narrowband imaging of the GOODS Chandra Deep Field – South (CDF–S; RA 03:31:54.02, Dec -27:48:31.5 [J2000]) obtained at the Blanco 4m telescope at Cerro Tololo InterAmerican Observatory (CTIO) with the MOSAIC II camera (MOSAIC II is a mosaic CCD camera, with eight 2k×4k CCDs spanning 36′×36′on the sky). These data were taken in the NB656 (Hα) filter, and resulted in the discovery of four LAEs at z = 4.4. In semester 2007B, we applied for, and were awarded, three nights at Blanco with MOSAIC II (two whole nights and two $\frac{1}{2}$ nights) to obtain observations in two 80 Å wide narrowband filters adjacent to NB656. We obtained five hours of observations in the NB665 (Hα + 80) filter, and 5.5 hours in the NB673 ([S II]) filter, which can be used to select LAEs at z = 4.47

and z = 4.52, respectively. Conditions were photometric over the whole run, with a typical seeing of 0.9″.

The CTIO data were reduced with IRAF (Tody 1986, 1993), using the MSCRED (Valdes & Tody 1998; Valdes 1998) reduction package, following the method set forth in Rhoads *et al.* (2000, 2004). First, we performed the standard image reduction steps of overscan subtraction and bias subtraction, followed by flat–fielding using dome flats obtained during our run. Cross-talk was also removed between chip pairs sharing readout electronics. We derived a supersky flat from the science data, and used this to remove the residual large–scale imperfections in the sky. The world coordinate systems (WCS) of individual frames were adjusted by comparing the frames to the astrometry from the USNO–B1.0 catalog. Cosmic rays were rejected using the algorithm of Rhoads (2000) and satellite trails were manually flagged and excluded from the final stacked image. The final stack for each filter was made using mscstack, using scaling from mscimatch. See Rhoads *et al.* (2000) and Wang *et al.* (2005) for further details on the data reduction process. The seeing and zeropoint of the final stack was 0.92″(0.91″) and 29.811 (29.847) mag for the NB665 (NB673) filter.

4.3.2. *Object Extraction*

To select LAEs in our field, we require broadband photometry encompassing the Lyα line to calculate a narrowband excess, as well as a broadband filter blueward of the line verifying that the flux is indeed extinguished due to intervening intergalactic medium (IGM) material. We used B and R broadband data from the ESO Imaging Survey (EIS; Arnouts *et al.* 2001), which obtained deep $U'UBVRI$ data

of 0.25 deg^2 surrounding the CDF–S. The 5 σ depth in our bands of interest are $B_{AB} = 26.4$ and $R_{AB} = 25.5$ mag. While there is deep, high-resolution *Hubble Space Telescope* (*HST*) data in this field, in order to do our selection we would have to smooth these data to the resolution of our ground-based data[10], and at that point, the EIS data is marginally deeper, and it has the benefit that we can select LAEs over a larger area. The EIS B and R-band images were registered separately to both narrowband images using the IRAF tasks wcsmap and geotran.

We extracted objects from our stacked images using the SExtractor software (Bertin & Arnouts 1996) in two-image mode. In this mode, the software first detects objects in the narrowband (detection) image, and then extracts the flux from those positions in the second image. Using both the NB665 and NB673 as the detection image, we extracted fluxes from the EIS B and R-bands, as well as all three narrowbands (including the NB656 image from F08a). In order to reduce the number of false positive detections, we first extracted objects using a set of SExtractor parameters used in the Large Area Lyman Alpha (LALA; Rhoads *et al.* 2000) Survey. We then selected LAE candidates (see §4.3.3) using these catalogs. We then iterated, changing the SExtractor detection parameters, reducing the number of objects detected while still detecting the previously identified candidates. This iterative step resulted in a $\geq$ 33% reduction in detected objects over the whole field, drastically reducing the number of spurious sources. Our final detection parameters were DETECT_MINAREA = 9 pixels ($\sim$ size of the seeing disk) and DETECT_THRESH = 0.50 (NB665) and 0.95

[10]If we run our selection with the full resolution *HST* data, we run into a problem with crowded sources, where two objects in the *HST* image are not resolved separately in the narrowband images. This results in a computed narrowband excess, where one may not exist.

(NB673). We then used these parameters to create our final catalogs for narrowband selected sources in the narrowband, B and R-band images.

4.3.3. *Lyα Galaxy Selection*

We use the selection criteria from Malhotra & Rhoads (2002; hereafter MR02) to select Lyα galaxy candidates from our catalogs. For an object to be considered as a candidate, we demand a 5 σ significance detection in the narrowband, a 4 σ significance narrowband flux excess over the R band, a factor of 2 ratio of narrow-broad flux, and no more then 2 σ significant flux in the B-band. The first three criteria ensure that it is a significant narrowband detection with a significant narrowband excess, while the last criterion checks that it is at z $\sim$ 4 (sources at z $\gtrsim$ 3.5 will have their B-band flux reduced due to IGM absorption). Application of these selection criteria in the LALA survey resulted in an AGN contamination fraction of $< 5\%$ (Wang *et al.* 2004), and a follow-up spectroscopic confirmation success rate of $> 70\%$ (Dawson *et al.* 2004).

Selecting objects in the overlap region between our narrowband data and the EIS data, we find 130 LAE candidates in the NB665 image and 126 in the NB673 image. While these objects all satisfied our selection criteria, it is possible that some of them could be noise spikes or other types of spurious sources (i.e. near the wings of bright stars). As a last check, we visually inspected the narrowband images at the positions of each of these 256 candidates, ensuring that a real object (i.e. detectable above the noise by eye) existed at these positions. Removing from our sample sources that did not appear to be real, we find a total of 42 good LAE candidates in the NB665

image, and 85 in NB673. Figure 11 shows our flux selection planes, highlighting the selection criteria and visually confirmed LAE candidates.

While the EIS data worked very well for our selection, we require the higher-resolution and broader wavelength coverage of the GOODS *HST* Advanced Camera for Surveys (ACS; Ford *et al.* 2000) and *Spitzer* Infrared Array Camera (IRAC; Fazio *et al.* 2004) data to be able to fit stellar population models to these objects. For our analysis, we used the updated version of the GOODS CDF–S catalog (ver. 1.9; Giavalisco *et al.* 2008 in prep) which has deeper observations in the i' and z'-bands, resulting in lower error bars for those two bands. The IRAC data do not yet have a public catalog, but a catalog has been created using the TFIT software package (Laidler *et al.* 2007). TFIT uses *a priori* knowledge of spatial positions and morphologies from a higher-resolution image (in this case the GOODS ACS z' image) to construct object templates and fit them to the lower resolution image, enabling one to extract reliable fluxes even in crowded regions. To find which of our LAE candidates resided in the smaller GOODS CDF–S area, we performed position matching between our candidates and the GOODS v1.9 catalog, using a matching radius of $0.6''$. We found that 17 total LAE candidates were covered by the GOODS data, 5 selected in NB665 and 12 in NB673. While each of these objects satisfied our B-band deficiency criteria, four of them had visible flux in the ACS B-band image, thus these four were thrown out of the sample as low-redshift interlopers, leaving us with 13 total LAE candidates (2 in NB665 and 11 in NB673).

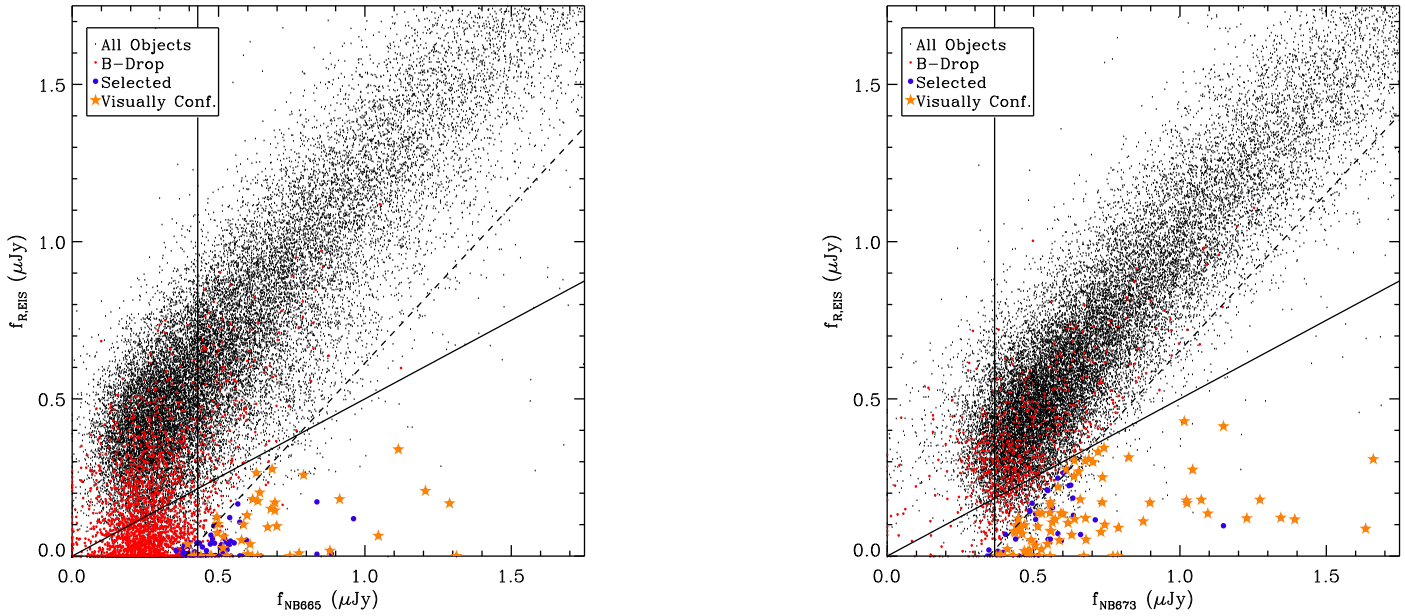

FIG. 11.—Flux selection planes for objects detected in NB665 (left) and NB673 (right), with broadband (EIS R) flux on the vertical axis and narrowband flux on the horizontal axis. The three lines represent three of the selection criteria. Any object to the right of the vertical line satisfies the 5 σ narrowband detection requirement (computed using the mean narrowband flux error from all objects). Objects below the solid diagonal line have a narrow-broad flux ratio of > 2, and objects below the dashed diagonal line satisfy the 4 σ narrowband excess criteria. Black dots represent all objects extracted from the image, while red dots represent those that satisfy the fourth selection criteria of a less than 2 σ significant B-band flux. Blue dots represent those objects which satisfy all four selection criteria, and gold stars are those candidates which were confirmed to be real upon visual inspection of the image. While there should be no blue dots above the selection lines, and likewise no red dots below, there are a few because the lines were computed using the mean errors from the entire sample, while the selection criteria were applied to each object using their individual uncertainties.

4.3.4. *Candidate Redshifts*

The *HST* Probing Evolution and Reionization Spectroscopically (PEARS; Rhoads *et al.* 2008) survey has obtained grism spectra over much of the CDF–S. However, none of the seven candidate LAEs which were covered by PEARS yielded any definitive information from their spectra, which were significantly noise dominated. We then searched through two public catalogs, MUSIC (Grazian *et al.* 2006) and FIREWORKS (Wuyts *et al.* 2008) for photometric (photo-z) and spectroscopic (spec-z) redshifts for our candidates. Six of our candidates had photo-z's from either MUSIC or FIREWORKS (when an object had a photo-z in both surveys, we use the value from FIREWORKS, as they published the 1 σ errors on each photo-z), and two of these six also had published spectroscopic redshifts.

The first of these two had a spec-z of 0.508 from the VIMOS VLT Deep Survey (VVDS; Le Fevre *et al.* 2004). This is an interesting redshift, as we would expect our two main interlopers to be [O II] and [O III] emitters, at redshifts ~ 0.8 and 0.3, respectively. However, Le Fevre *et al.* give this redshift a quality value of 2, meaning that it only has a 75% confidence level. Furthermore, the photo-z from FIREWORKS is slightly higher, at 0.68 ± 0.07, thus we believe that this object is consistent with an [O II] emitting interloper, and we exclude it from further analysis. The second of these objects has a spec-z of 4.00 from the FORS2 spectroscopic catalog (v3.0; Vanzella *et al.* 2008). This redshift was given a "C" quality, meaning that it is a "potential redshift." We were able to download and look at the 1D spectrum, and it does appear that there is a possible continuum break at ~ 6200 Å, with two emission

lines redward of the break. They identified the first line as Lyα, putting it at z = 4.0. The second of the emission lines is the one which fell in our narrow-band filter, and if this redshift is correct, then we detected CII emission (λ1335 Å). While this is possible, it is unlikely, thus we think that two scenarios are possible. This break could be due to the Lyα forest, and the first emission line is just a noise spike, meaning that we are indeed measuring Lyα emission at z $\sim$ 4.5 (this is tenuously verified by the photo-z of 4.16 $\pm$0.16, which is $\sim$ 2 σ from 4.5). Or, equally likely, this could be the 4000 Å continuum break, meaning that we are detecting Balmer line emission from Hβ (λ4861 Å), Hγ (λ4341 Å), or Hδ (λ4102 Å) at z = 0.4 to 0.6. We decided to keep this object in the sample, while keeping in mind its redshift ambiguity when we make our conclusions.

The four other candidate LAEs with redshifts had calculated photo-z's of 0.54, 3.82, 4.25 and 4.52. Of these, we exclude only the first from further analysis given its low photo-z. While its B-band flux does not appear upon visual inspection of the B-band image, it does appear somewhat detected in a plot of its spectral energy distribution (SED), meaning that this object could be either an [O II] or [O III] emitter.

Lastly, while narrow-band surveys typically result in a low fraction of active galactic nuclei (AGN), they are a possible contaminant as they frequently show strong Lyα emission. In order to check for AGN, we examined the *Chandra* 1 Ms X-ray catalog (Giaconni *et al.* 2001), performing position matching between our objects and this X-ray catalog. We found no matches out to a search radius of 5″, thus we believe

that none of our final sample of 11 candidate LAEs contain AGNs. Figure 12 shows cutout stamps of our 11 candidates at the relevant wavelengths.

4.4. Stellar Population Modeling

To learn about the physical properties of our objects, we computed model stellar population spectra using the software from Bruzual & Charlot (2003; hereafter BC03). We used a similar procedure as in F08a, computing model BC03 spectra from a grid of metallicities, star formation histories (SFHs), and stellar population ages. We used five different metallicities, ranging from Z = 0.005 – $0.02Z_{\odot}$. We used an exponentially decaying SFH, with the characteristic decay time, τ_{SFH}, ranging from 10^5 - 4×10^9 yr. The minimum value of τ_{SFH} is much shorter than our youngest possible model age, thus it is essentially a burst, or simple stellar population (SSP). The maximum τ_{SFH} is much older than the age of the Universe at z = 4.4, thus it is simulating a continuous SFH. The three intermediate values, 10^6, 10^7 and 10^8 yr represent true exponentially decaying SFHs. We used a grid of 48 stellar population ages (t_{pop}), ranging from 1 Myr - 1.434 Gyr (the closest age point to the age of the Universe at z = 4.5), with 30 of the ages being $\leq$ 100 Myr. In order to model the clumpy ISM scenario, we require our model spectra to contain Lyα emission lines. While the BC03 code does not compute line emission, it does compute the number of ionizing photons at each age, and from this we can derive the Lyα emission line flux using Case B recombination. We also included $H\alpha$ emission at a value of $\sim$ 11% of the Lyα strength (case B), as $H\alpha$ emission is typically strong in star forming galaxies, and at this redshift can dominate the 3.6 μm flux.

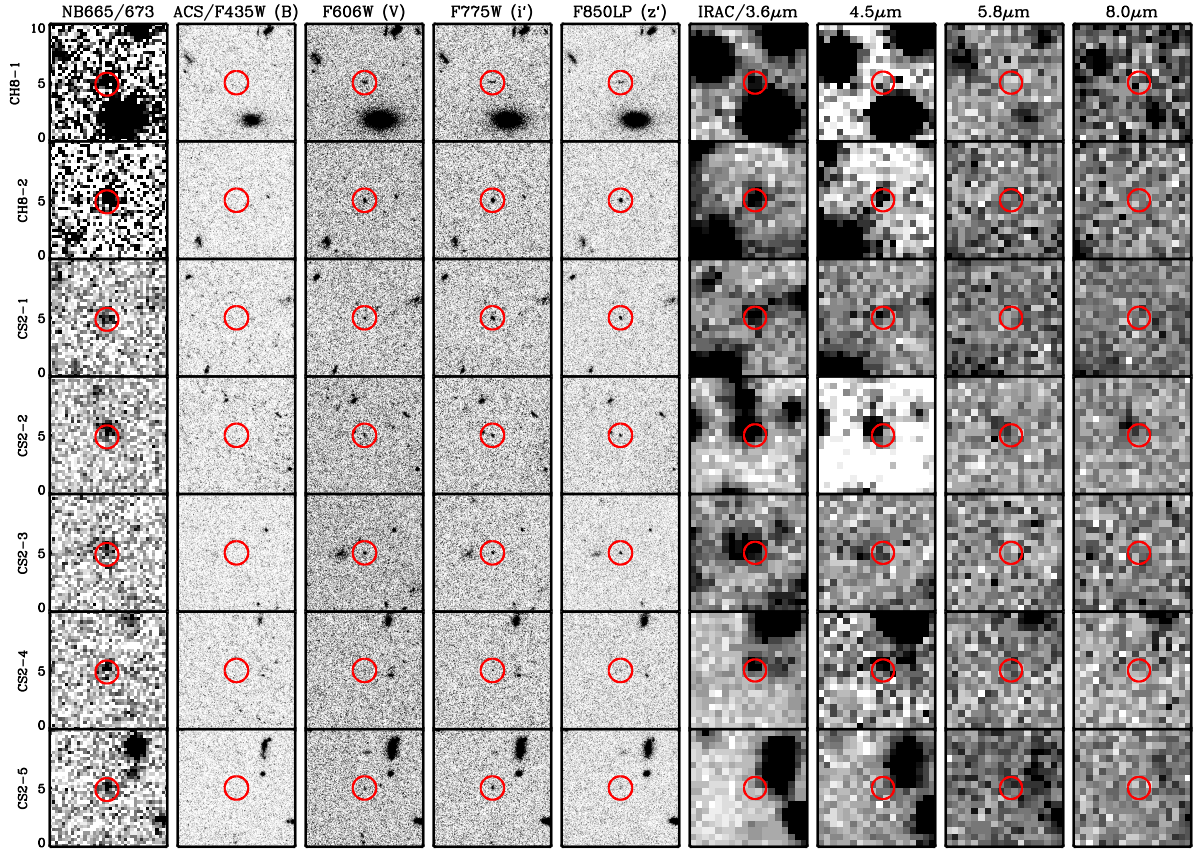

(a)

FIG. 12.—(a) 10″ cutouts of our 11 new objects (see F08a for a similar figure for the original four objects). The circles are 2" in diameter, and are drawn to highlight the object. The columns from left-to-right: narrowband image (NB665 or NB673 depending on the object); *HST*/ACS B, V, i' and z'; *Spitzer*/IRAC 3.6, 4.5, 5.8 and 8.0 μm. All objects are easily visible in the narrowband detection images, and all look to have a brighter narrowband than V-band image by eye. All objects, except CS2-7, are undetected in the IRAC 5.8 and 8.0 μm images. The lack of detectable B-band flux illustrates the high-redshift nature of these objects. While many objects are crowded in the IRAC 3.6 and 4.5 μm images, our use of the TFIT algorithm uses the ACS z' high resolution image as a template to extract the fluxes of our crowded sources.

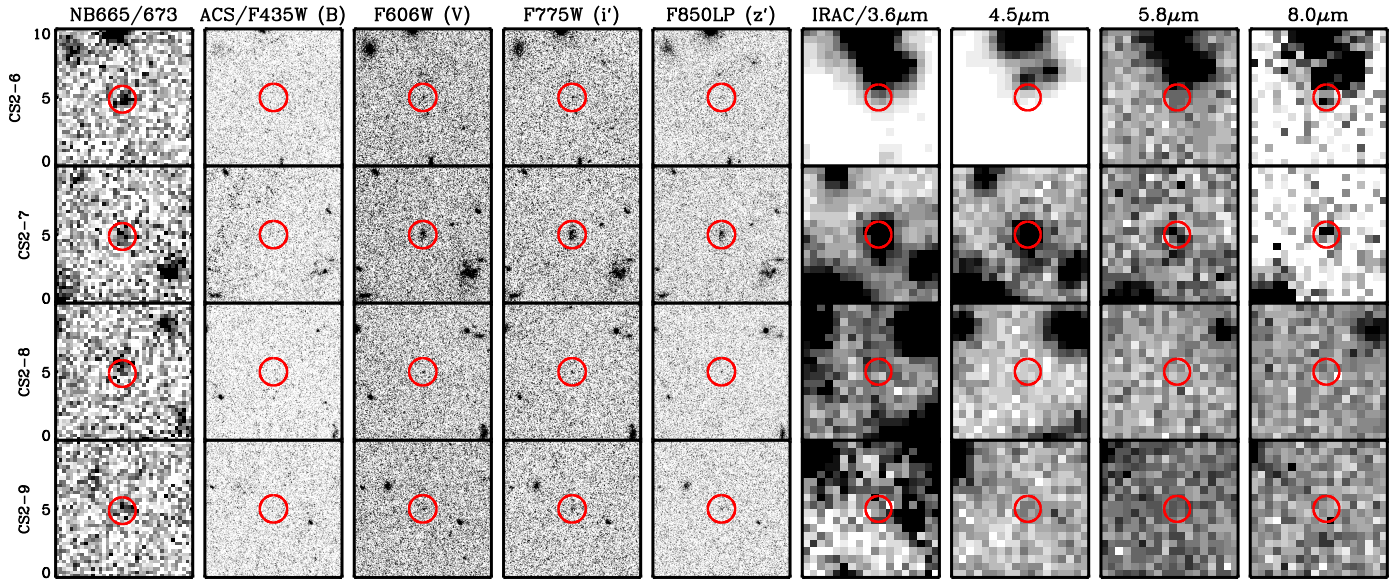

(b)

FIG. 12.—(b) Continued.

To apply dust attenuation to our spectra we used the dust law from Calzetti *et al.* (1994), which is applicable to starburst galaxies. We attenuated our model spectra by 21 different amounts of dust extinction at 1200 Å, from $A_{1200} = 0.0$ to 5.0. While we allowed all continuum wavelengths to be attenuated by dust, we wanted to be able to control the rate at which Lyα was attenuated with respect to the continuum, thus we applied a new free parameter, which we call the clumpiness parameter. When we apply dust of a given optical depth to a continuum wavelength element, we multiply the flux by $e^{-\tau}$. For the Lyα wavelength bin, we instead multiply by $e^{-q\tau}$, where q is the clumpiness parameter, which ranged from 0 – 10. When q is zero, Lyα photons are not attenuated by dust at all, and thus this represents the extreme clumpy ISM scenario. When q is 10, resonance scattering works against the Lyα photons, and they suffer much greater extinction than continuum photons, which is the case in a homogeneous ISM. Intermediate values of q represent intermediate geometries, but the important point is that for any value of $q < 1$, the Lyα EW is being enhanced over that intrinsic to the stars. We impress upon the reader that the dust is mixed in with the gas, thus it is the geometry of the gas which is dominating the Lyα radiative transfer, as Lyα photons are resonantly scattered.

We then took our model spectra, which were output by BC03 in units of L_λ, and converted them to f_ν, redshifting them and attenuating their far-UV (FUV) with Madau (1995) IGM absorption in the process (see F08a for further details). Although all of our Lyα flux is in one wavelength bin, it should not all be attenuated by the IGM, as in a real spectrum, about half of the flux would be on each side of the true

wavelength of Lyα. Thus, when we applied the IGM, we only allowed it to attenuate half of the Lyα flux. Lastly, we computed the bandpass averaged fluxes $\langle f_\nu \rangle$ of each spectra through all of our observed filters (NB656, NB665, NB673, B, V, i', z', 3.6, 4.5, 5.8 and 8.0 μm), which gave us fluxes which we could directly compare to our candidate LAEs.

4.5. Results

In the time since F08a, we have updated our model grid and fitting program, thus we include the objects from F08a in our analysis, computing updated best-fit models for the four objects. This gives us a total of 15 candidate LAEs, discovered in a total comoving volume of 8.5×10^5 Mpc^3 (the total volume from the three narrowband filters in the CDF–S overlap region). We have assigned the LAEs from F08a identifiers of CHa-1 through CHa-4, where "C" stands for CDF–S and "Ha" stands for the detection filter (NB656 or $H\alpha$ in this case). CHa-1 and 2 are objects 1 and 2 from F08a, CHa-3 is object 4, and CHa-4 is object 6. We also assign similar identifiers to our new objects, with CH8-1 and 2 representing the two candidate LAEs detected in NB665, and CS2-1 through CS2-9 representing the nine candidate LAEs detected in NB673. We will use these identifies hereafter to represent our 15 candidate LAEs. Table 7 & Table 8 list each candidate by name, with their multi-wavelength magnitudes and their spectroscopic information when available.

TABLE 7
OPTICAL MAGNITUDES OF LYα GALAXY CANDIDATES

Name	GOODS v1.9 ID	RA (J2000)	Dec (J2000)	Narrow-band	F435W B	F606W V	F775W i'	F850LP z'	Rest EW (Å)
CHa-1	7210	53.066629	-27.708769	24.03	29.54	26.49	25.70	25.95	$189.7^{+84.1}_{-52.5}$
CHa-2	24722	53.165712	-27.854153	24.15	$\geq 29.11^*$	26.52	25.52	25.60	$166.5^{+77.9}_{-48.9}$
CHa-3	33166	53.243251	-27.894329	24.08	30.40	26.37	25.54	25.70	$149.1^{+64.6}_{-42.4}$
CHa-4	29436	53.201016	-27.860250	24.24	$\geq 29.11^*$	25.81	24.96	24.82	$56.3^{+17.2}_{-13.8}$
CH8-1	29775	53.204198	-27.817216	24.44	29.43	26.85	26.45	26.15	$175.9^{+98.3}_{-59.2}$
CH8-2	31908	53.225148	-27.833556	24.39	$\geq 29.11^*$	25.93	24.95	25.07	$53.4^{+15.7}_{-13.7}$
CS2-1	3533	53.039731	-27.773229	23.58	$\geq 29.11^*$	27.10	25.76	25.79	$2798.8^{+\infty}_{-1935.2}$
CS2-2	7326	53.067369	-27.812334	23.49	$\geq 29.11^*$	27.60	26.79	26.53	$> 10000^{+\infty}_{-13279.3}$
CS2-3	13009	53.102239	-27.793217	24.12	$\geq 29.11^*$	27.29	26.63	26.01	$690.9^{+3648.2}_{-383.5}$
CS2-4	16270	53.119230	-27.932951	24.66	31.11	28.68	27.99	27.83	$> 10000^{+\infty}_{-8424.9}$
CS2-5	19333	53.135419	-27.729731	24.68	30.67	28.17	26.84	27.31	$2366.7^{+\infty}_{-1810.0}$
CS2-6	19934	53.138953	-27.695547	24.40	$\geq 29.11^*$	27.85	27.73	27.39	$1870.8^{+\infty}_{-1354.9}$
CS2-7	23979	53.161371	-27.737037	24.49	$\geq 29.11^*$	26.04	25.04	24.81	$53.2^{+29.4}_{-19.8}$
CS2-8	24214	53.162613	-27.803605	24.20	30.07	28.71	28.13	28.06	$> 10000^{+\infty}_{-11292.0}$
CS2-9	25038	53.167696	-27.886145	24.96	$\geq 29.11^*$	27.82	27.09	27.20	$356.3^{+676.9}_{-183.6}$

NOTES.—*3 σ upper limits. Optical AB magnitudes of our LAE candidates. The narrowband magnitudes come from our ground-based data, while the optical magnitudes come from the GOODS v1.9 catalog (all magnitudes are computed from the SExtractor MAG_AUTO parameter, and thus are a close approximation of the total flux). The calculated rest-frame EWs assume a redshift equal to that of Lyα at the center of their respective filters. In three of the objects, the computed EW comes out to be > 10000 Å due to the extremely faint continuum (F606W) fluxes. Likewise, these faint continuum fluxes can result in infinite upper limits on these EWs. Both CS2-2 and CS2-8 have EWs technically consistent with zero, but these errors are dominated by the faint continuum fluxes.

TABLE 8
NIR AND IR MAGNITUDES OF LYα GALAXY CANDIDATES

Name	J	H	Ks	3.6μm	4.5μm	5.8μm	8.0μm	Published Redshifts
CHa-1	$\geq$ 25.75*	$\geq$ 25.25*	$\geq$ 25.25*	25.26	$\geq$ 25.69*	$\geq$ 23.69*	$\geq$ 23.53*	4.24
CHa-2	$\geq$ 25.75*	$\geq$ 25.25*	$\geq$ 25.25*	25.29	$\geq$ 25.98*	$\geq$ 23.88*	$\geq$ 23.74*	4.44
CHa-3	$\geq$ 25.75*	$\geq$ 25.25*	$\geq$ 25.25*	24.94	24.98	$\geq$ 23.42*	$\geq$ 23.28*	4.42
CHa-4	$\geq$ 25.75*	$\geq$ 25.25*	$\geq$ 25.25*	24.22	24.98	$\geq$ 23.76*	$\geq$ 23.65*	4.36
CH8-1	$\geq$ 25.75*	$\geq$ 25.25*	$\geq$ 25.25*	25.61	$\geq$ 25.59*	$\geq$ 23.60*	$\geq$ 23.39*	3.82
CH8-2	$\geq$ 25.75*	$\geq$ 25.25*	$\geq$ 25.25*	24.99	25.60	$\geq$ 23.77*	$\geq$ 23.65*	-1.00
CS2-1	—	—	—	24.87	$\geq$ 25.71*	$\geq$ 23.72*	$\geq$ 23.57*	-1.00
CS2-2	$\geq$ 25.75*	$\geq$ 25.25*	$\geq$ 25.25*	26.14	$\geq$ 25.66*	$\geq$ 23.56*	$\geq$ 23.37*	4.52
CS2-3	$\geq$ 25.75*	$\geq$ 25.25*	$\geq$ 25.25*	25.32	$\geq$ 25.64*	$\geq$ 23.58*	$\geq$ 23.42*	4.25
CS2-4	$\geq$ 25.75*	$\geq$ 25.25*	$\geq$ 25.25*	23.87	24.59	$\geq$ 22.84*	$\geq$ 22.74*	-1.00
CS2-5	$\geq$ 25.75*	$\geq$ 25.25*	$\geq$ 25.25*	$\geq$ 25.94*	$\geq$ 25.32*	$\geq$ 23.28*	$\geq$ 23.15*	-1.00
CS2-6	$\geq$ 25.75*	$\geq$ 25.25*	$\geq$ 25.25*	25.08	24.44	$\geq$ 22.71*	$\geq$ 22.56*	-1.00
CS2-7	24.96	24.77	23.92	22.69	22.82	22.92	22.50	4.00/4.16
CS2-8	$\geq$ 25.75*	$\geq$ 25.25*	$\geq$ 25.25*	$\geq$ 26.48*	$\geq$ 25.88*	$\geq$ 23.87*	$\geq$ 23.72*	-1.00
CS2-9	$\geq$ 25.75*	$\geq$ 25.25*	$\geq$ 25.25*	$\geq$ 25.78*	$\geq$ 25.26*	$\geq$ 23.18*	$\geq$ 23.04*	-1.00

NOTES.—*3 σ upper limits. AB Magnitudes of our candidates in the near-infrared (NIR) and IR. All but one of our candidates were undetected in the VLT/ISAAC NIR data, thus we display the 3 σ upper limits (CS2-1 was not covered by VLT/ISAAC). When the *Spitzer*/IRAC observations had a less than 3 σ significance, we display the 3 σ upper limits. The redshift information comes from the MUSIC and FIREWORKS catalogs; see §2.4 for more details (-1.00 means that the object was not detected by either survey).

4.5.1. *Model Fitting*

4.5.1.1. *Computing the Best-Fit Model*

We derived the best-fit model to our observations via the method of χ^2 fitting, where the model with the lowest reduced χ^2 (χ^2_r) was assigned to be the best fit for a particular galaxy. χ^2_r is the χ^2 divided by the number of degrees of freedom (ν), which is defined as the number of constraints (data points) minus the number of free parameters. While each object has numerous data points, we do not fit all of them to the models for various reasons. First off, in order to separate model parameters from mass, we fit flux ratios (colors) rather than fluxes, computing the ratio of flux in each band to the i'-band. We then derive the mass by scaling the best-fit model up to match the observations (using the detected r', i', z', 3.6 μm and 4.5 μm bands). Thus, while this means that we do not count mass as a free parameter, we likewise do not count the i'-band as a constraint. Also, since our objects are narrow-band selected, we have a very good idea of their redshift, thus we do not include redshift as a free parameter. For objects detected in NB656, NB665 and NB673, we assign the models a redshift of 4.399, 4.470 and 4.532, respectively (corresponding to the redshift of a Lyα emission line at the center of each filter). As the B-band flux should remain undetected for our candidates if we have the redshift correct, the B-band data point does not add much physical information to our fits unless redshift is a free parameter, thus it is excluded.

The 5.8 and 8.0 μm fluxes of most candidates have a significantly less than 3 σ significance, thus adding them to the fitting produces a higher value of χ^2, while

not adding much physical information. We do not include these bands in the fitting, except for CS2-7, which is detected in both bands. CS2-7 also has published near-infrared (NIR) fluxes from VLT/ISAAC (J, H and Ks) in the FIREWORKS catalog, which we add to the fit for this object.

As the FIREWORKS catalog was Ks-selected, it only contained one of our objects. However, given the importance of fitting the SED between observed 1 and 3.6 μm (rest-frame 1800 - 6500 Å), we examined the positions in the ISAAC J, H and Ks-band mosaics of our other 14 candidates. In no cases were we able to definitively visually identify an object above the noise. However, any information in this wavelength regime will help the model fitting. The fluxes of our objects are high enough, and the images are deep enough, that including the upper limits should provide meaningful constraints. This is unlike IRAC 5.8 and 8.0 μm, where the upper limits are much higher than the expected object flux. We thus include 3 σ upper limits on the J, H and Ks bands during our model fitting. We treat these upper limits, as well as the 3.6 and 4.5 μm points when they are undetected, in a manner similar to that of Nilsson *et al.* (2007). Briefly, we set the flux of each object equal to its 3 σ upper limit (the 3 σ limiting magnitude of the images for the J, H and Ks bands, and the actual 3 σ flux from the TFIT errors for the IRAC bands), with the 1 σ flux error being equal to 33% of its upper limit flux. We then run our χ^2 fitting code like normal, except that when an upper limit is compared to the model, a χ^2 penalty is only assessed if the model flux is greater than the object (3 σ) flux. In this manner models which exceed the upper limits are strongly disfavored.

4.5.1.2. *Complicated Star Formation Histories*

While our range of star formation histories may accurately represent the SFHs of our objects, it may be more complicated. Specifically, we would like to see if any of our objects are better fit by two bursts of star formation. This could provide an alternate explanation to dust enhancement when an object has red colors, but a strong EW. In this scenario, the strong Lyα EW could be from a relatively small fraction of young stars, with a large fraction of old stars causing red optical colors (while not contributing much to the rest-frame UV). We follow the maximum age method of Papovich *et al.* (2001), where the young burst is allowed to vary in age, but the old burst is fixed to have occurred at $z \rightarrow \infty$, which at $z \sim 4.5$ corresponds to $t_{pop} \approx 1.4$ Gyr. We force both populations to have a burst SFH ($\tau_{SFH} = 10^5$), and for simplicity we also assume that they have the same metallicity, dust extinction, and dust clumpiness. Thus, the free parameters are: t_{pop} (young), Z, A_{1200}, q and fraction of mass in old stars. We chose a grid of allowable mass fractions, ranging from no mass in old stars, up to 99%.

4.5.1.3. *Range of Allowable Parameters*

The process we have described above allows us to accurately compute the best-fit model to a given object SED. While this may represent the true stellar population of the object, it is more critical to know the range of allowable parameter space, as in most cases there are many other models with χ^2_r near to the minimum value. We chose to investigate these possible degeneracies via Monte Carlo simulations. In each simulation, we vary the observed flux in each bandpass by a random amount

proportional to the flux errors, recomputing the best fit. We then run 7000 simulations, using different random numbers in each simulation, giving us 7000 best fits per object. These best fits show us how the uncertainties in our observations can lead to changes in the best-fit models. In cases where the best fits do not change much, we can assume that the original best-fit model well constrains the stellar population in the given object. However, in cases where the Monte Carlo results vary widely, our models are not able to constrain the objects very well.

4.5.2. *NB656 Detected Objects*

We will now go through a detailed discussion of the results for each object. These results are shown in Figure 13. In this figure, each row corresponds to one object. The first column displays the best-fit single population model to the data, listing out some of the best-fit parameters. The second column is similar, except that it displays the best-fit two-burst model. The third and fourth columns display the results of the Monte Carlo analysis for the single-population models, with the third column displaying t_{pop} vs. A_{1200}, and the fourth column displaying t_{pop} vs. q (clumpiness). We tabulate the best-fit single-population and two-burst models in Table 9 and Table 10, respectively.

4.5.2.1. *CHa-1*

The best-fit model for object CHa-1 (object 1 from F08a) is very young and relatively low mass, at 3 Myr and 2.8×10^8 $M_\odot$. This model has 1 magnitude of dust extinguishing Lyα somewhat more than the continuum (q = 2.0). The metallicity is best fit by 20% of Solar, higher than the fixed metallicity value from F08a, and the

SFH is best fit by continuous star formation. These parameters are very similar to those from F08a. We attribute the small differences in age, dust and q to the different treatment of the IRAC upper limits in the current work, as well as they ability of metallicity to vary. The best-fit model has a rest-frame EW of 81 Å, which is low for 3 Myr, but as q = 2, the Lyα flux is being attenuated by some of the dust. This is significantly less than the computed EW from the object's narrowband excess of 190 $\pm$ 47 Å. We attribute this difference to being due to the uncertainty in where the Lyα line falls in both the narrowband and the broadband filters, thus the F606W flux may not be indicative of the true continuum flux due to intervening IGM absorption. See §4.6.1 for further discussion on this matter. The best-fit two-burst model is also a good fit, containing 70% of its mass in old stars, for a mass-weighted age of 1005 Myr. This two-burst model is an example of an object which exhibits strong Lyα emission without the need for an extremely clumpy ISM, even though its mass is dominated by older stars. The results of the Monte Carlo simulations show that while the best-fit age is young, there are islands of allowable parameter space as old as several hundred Myr, implying that the best-fit model is not unique in explaining the observed SED of this object (also explaining why the two-burst model is a good fit). To fit this object, the older models have correspondingly less dust (as the older age will redden the colors, so dust is less necessary), and a smaller q (as the age goes up, q will have to go down to keep the Lyα flux constant). The 68% confidence intervals span a somewhat larger region of allowed parameter space than those for this object in

F08a, which we attribute again to the different treatment of the IRAC upper limits, and also the addition of the NIR upper limits.

4.5.2.2. *CHa-2*

CHa-2 (object 2 from F08a) is older than CHa-1, at 50 Myr, and more massive, at 1.4×10^9 $M_\odot$. It is best fit by $A_{1200} = 1.25$, although the clumpiness (q) value of 1 implies that the dust does not affect the value of the EW. The metallicity is 2% of Solar, consistent with the fixed value in F08a, and this object has an exponentially decaying SFH with $\tau_{SFH} = 10^8$ yr. The model EW of 76 Å is near what we would expect for 50 Myr, thus dust enhancement or extinction of the line is not necessary. This model is both older and higher mass than in F08a, and in this case the new treatment has resulted in a much better fit, with a higher A_{1200} and a lower q in the current work. The best-fit two-burst model is a slightly worse fit, but it is significantly different as it has 80% of its mass in old stars, and its total mass is a factor of 2.3X more. It still has q = 1, thus the age of its young component is very young in order to keep the Lyα flux up. The age of this object is better constrained than CHa-1, as nearly all of the Monte Carlo simulations result in $t_{pop} \lesssim 100$ Myr. However, large ranges of both dust and q are allowed, although some amount of dust and a value of $q \leq 3$ seems to be strongly favored.

4.5.2.3. *CHa-3*

We were very interested in the updated results for CHa-3 (object 4 in F08a), as it was by far the most interesting object in F08a, showing definitive signs of dust enhancement of the Lyα EW, with a best fit of 800 Myr, 6.5×10^9 $M_\odot$, A_{1200}= 0.4

and q = 0. The updated results for this object confirm those from F08a, as a large amount of dust enhancement appears to be occurring, allowing this object to exhibit a decently strong Lyα EW ($\sim$ 100 Å) at an old age. The updated best-fit age of 454 Myr is less than that from F08a (and it is less massive at 3.8 $\times$ 10^9 $M_\odot$), yet it is still best fit by q = 0 with A_{1200}= 0.3 mag. It is still fit by continuous star formation, but now that the metallicity is allowed to vary, the new, higher best-fit value of Z = $0.2Z_\odot$ also explains the younger age (the higher metallicity will result in redder colors, thus the best-fit age is lowered from 800 Myr to 454 Myr to cancel out this effect). The two-burst best fit is a slightly worse fit, but it can also explain this object's SED, with 99% of the mass in old stars, with the other 1% of the mass from a 4 Myr old burst giving a mass-weighted age of $\sim$ 1420 Myr. The q of 1 and A_{1200}= 0.4 mag show that while the line is not actually being enhanced, some amount of clumpiness is still required in order to keep the Lyα flux from being completely extinguished. The Monte Carlo results show that the age of this object is strongly favored to be $>$ 100 Myr, although there are a few small 68% confidence islands at younger ages. This object is well constrained to contain a very clumpy ISM, as nearly all of the simulations result in q $\leq$ 1 (with a small island at q $\sim$ 3). These results further confirm our previous interpretation that this object represents a new class of LAE: one that is old, yet still exhibits strong Lyα emission due to a clumpy ISM enhancing the escape fraction of Lyα photons over continuum photons (although the Monte Carlo results show that there is a slight chance that this object is younger, with dust heavily extinguishing the Lyα flux).

4.5.2.4. *CHa-4*

The last of the objects from F08a, CHa-4 (object 6), again shows similar results to F08a, with a young age (6 Myr) and low mass ($5.8 \times 10^8\ M_\odot$). The dust extinction is less, at A_{1200}= 1.0 mag (vs. 1.8 from F08a), yet the q value has increased to keep a similar extinction of the Lyα flux (this model has a low EW of only 27 Å, consistent with our measured value of 56 Å). However, this model is not well constrained, as evidenced by its relatively high χ^2_r value, and the violation of the J-band upper limit. The shape of the observed SED is interesting, as both the z' and 4.5 μm flux are higher than the NIR upper limits. This could mean that two-burst fit could produce a more consistent model, as the optical/NIR fluxes could be due to a young component, with the IRAC fluxes due to a significant old component. This is in fact what the best-fit two-burst model shows, with only 10% of the stellar mass in young (3 Myr) stars. However, the χ^2_r of this model is even higher, thus this object awaits deeper NIR data to fully analyze its SED.

4.5.3. *NB665 Detected Objects*

4.5.3.1. *CH8-1*

The first of our new sample, CH8-1, has a best-fit stellar population that is young and dusty, with its best-fit model of t_{pop} = 2.5 Myr, $2.9 \times 10^8\ M_\odot$, A_{1200} = 2.0 mag and q = 1. The best-fit Lyα EW is somewhat high, at $\sim$ 130 Å, and unaffected by dust. The two-burst model also shows a good fit, with only 20% of its mass in young stars, and a small amount of dust enhancement helping to keep the line strong (q = 0.75). This two-burst model has a mass three times greater than the single

population model, but it's metallicity is reduced by a factor of five. Nearly all of the simulations result in best-fit models with young ages, with q $<$ 1 and a good amount of dust, although there is a small island at very old age, with some dust and q = 0. This uncertainty likely derives from the undetected 4.5 μm flux, as the 3.6 - 4.5 μm color constraints the amount of $H\alpha$ emission, which should only be strong in a young, star forming galaxy. We will return to this issue in §4.6.3.1.

4.5.3.2. *CH8-1*

This object is best fit by a young (10 Myr) medium (for LAEs) mass (4.6 $\times$ 10^8 $M_\odot$) stellar population. Normally a galaxy this young would show very strong Lyα emission, however this object is best fit by A_{1200} = 0.5 mag with the highest value of the clumpiness parameter (meaning it has the most homogeneous ISM) in our sample of q = 5. The best-fit two burst model is actually a slightly better fit, with only 10% of its mass in a young (4 Myr) population, for a mass-weighted age of 1291 Myr, and six times more massive than the single population model. This model also shows significant attenuation of the Lyα flux, with q = 5. Both A_{1200} and q appear to be very well constrained to be low and high, respectively, however the age does have a few allowed regions, one around the best fit at 10 Myr, and a few more at higher age.

4.5.4. *NB673 Detected Objects*

4.5.4.1. *CS2-1*

CS2-1 has the lowest quality fit of our sample, which appears to mainly come from the inability of the model to account for both the V-band and narrowband flux.

The best-fit model is somewhat young, although higher mass, at 13.2 Myr and 1.3 × 10^9 $M_\odot$, with a lot of dust (2.5 mag) extinguishing the continuum slightly more than Lyα (q = 0.75), thus the Lyα EW is being slightly enhanced. The best-fit two-burst model is an even worse fit. The allowed parameter space is of moderate size, with the age constrained to be $<$ 100 Myr, some amount of dust, and q likely $\leq$ 2. However, given the poor quality of the best fit, we do not lend much weight to these results.

4.5.4.2. *CS2-2*

This object has a similar age as CS2-1, with a higher mass of 2.0 × 10^9 $M_\odot$. A stellar population of this age with this object's best-fit SFH ($\tau_{SFH} = 10^6$) will have a relatively low Lyα EW. However, the EW of this best-fit model is 400 Å, showing significant enhancement of the EW, coming from the 3.5 mag of dust extinction from a very clumpy (q = 0) ISM. This object has a very large narrowband excess, due mostly to the faintness of its V-band flux, which is why the best-fit model needs a high EW. However, the i' - z' color is very red, thus the object is better fit by a 13 Myr population with clumpy dust responsible for the red colors and high EW, rather than a very young population. The two-burst fit is also a good fit, with 30% of its mass in old stars. The two-burst model also shows dust enhancement, with the same A_{1200} and q as the single population model. The best-fit parameters are very well constrained to have an age $\sim$ 10 Myr, and a lot of clumpy dust. This is another object which we can add to our growing list of those that show evidence that dust enhancement may be occurring.

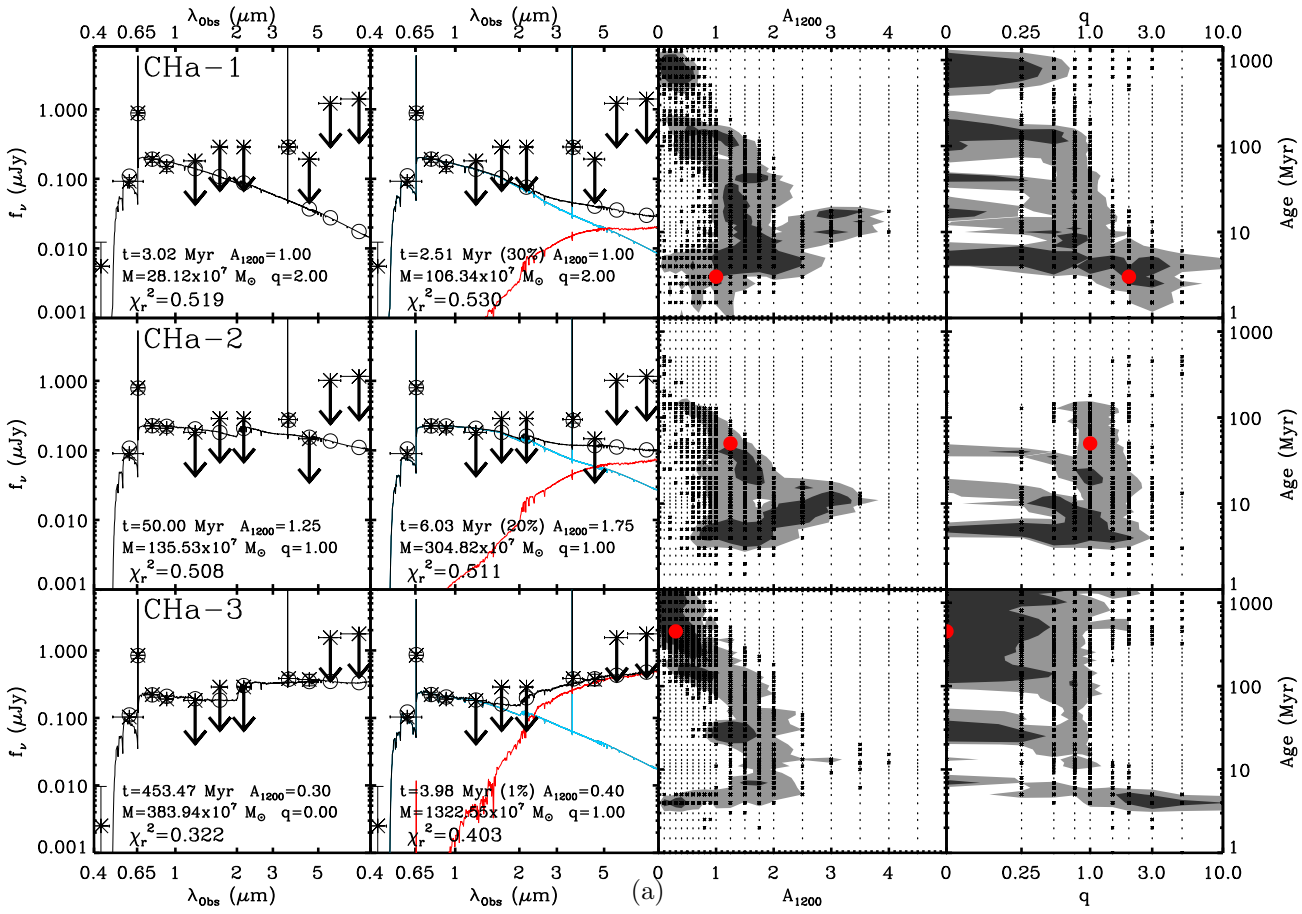

FIG. 13.—(a) The first column contains the best-fit single population models to the first six of our candidate LAEs, with their observed SEDs over-plotted. The open circles represent the bandpass-averaged fluxes of the models, highlighting the $H\alpha$ dominated 3.6 μm flux of the younger objects. The second column has the best-fit two-burst models to our objects. Objects with no mass in old stars can still have a worse fit than those in the first column, as they are forced to have a burst SFH. The third and fourth columns contain the Monte Carlo simulation results (for single-population models), with the best-fit point in red. The dark and grey shaded areas represent the 68% and 95% confidence intervals, respectively.

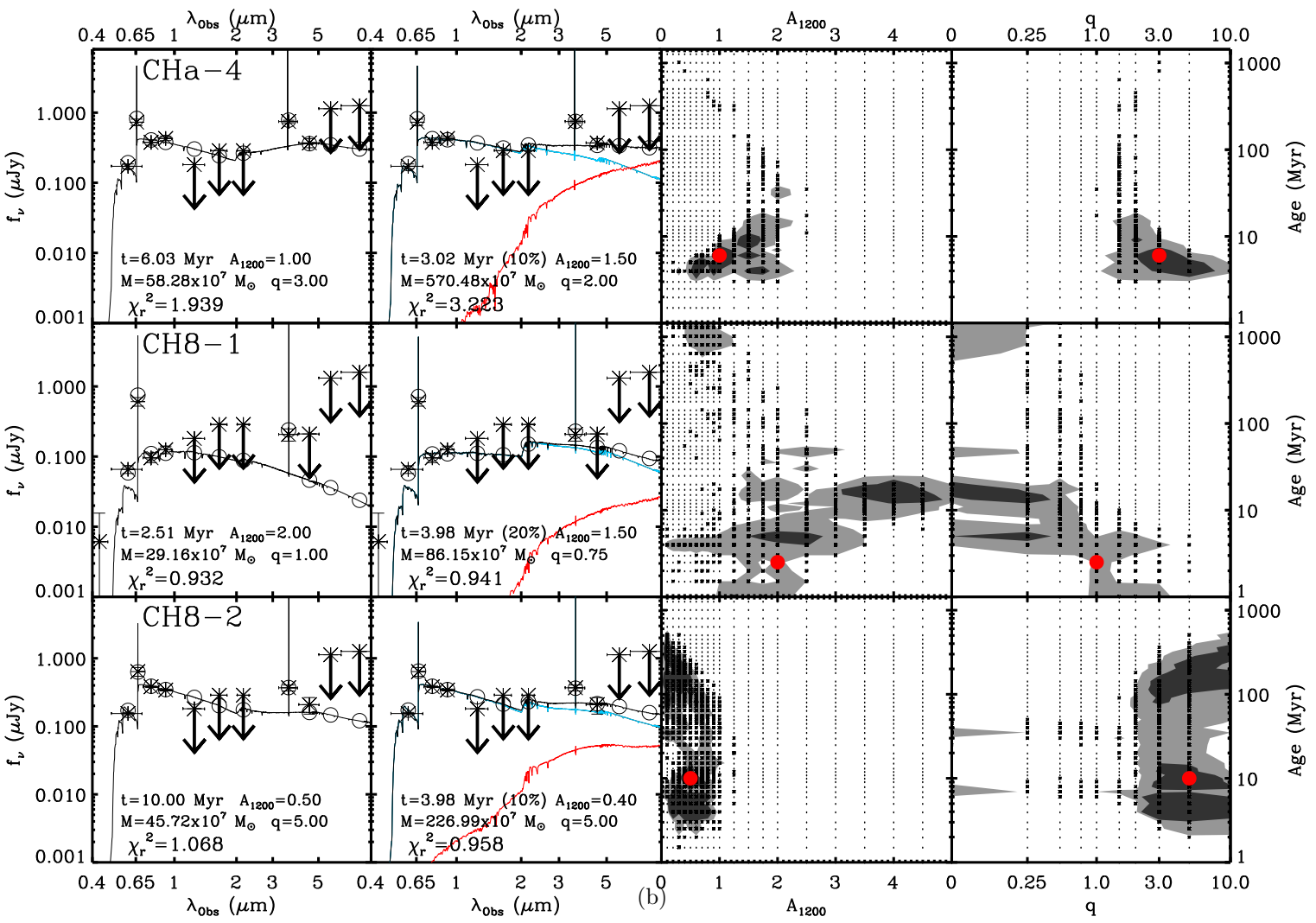

FIG. 13.—(b) Continued.

4.5.4.3. *CS2-3*

The best-fit model to CS2-3 has a very similar population to that of CS2-2, although this object has a substantially higher quality fit. Its best-fit parameters of 12 Myr, 6×10^9 $M_\odot$, $A_{1200} = 4.5$ mag and q = 0.25 show that a significant amount of dust enhancement may be responsible for its Lyα EW of 341 Å. The best-fit two-burst model shows a nearly identical population, with 10% of its slightly greater mass in old stars. The physical parameters of this object also appear to be very well constrained, as shown by the Monte Carlo simulation results.

4.5.4.4. *CS2-4*

The observed SED of CS2-4 is very red, yet the 3.6 - 4.5 μm color favors a young population with red colors due to dust extinction, thus this object is best fit by a 4 Myr old population, with a mass of 10^9 $M_\odot$, and 5 mag of dust extinction, with some amount of dust enhancement occurring (q = 0.75). The two-burst model has a slightly poorer fit, but it is a very different population with a mass-weighted age of 1420 Myr and a mass of $\sim 5 \times 10^{10}$ $M_\odot$, as well as significant dust enhancement. While both q and A_{1200} are relatively well constrained, the simulations fall into two different age ranges; one at the best-fit value of ~ 5 Myr, and another, larger region at ~ 500 Myr. This island of older best-fit models requires q = 0. Thus, we conclude that this object could be a young population with a small amount of dust enhancement, or a very old population with a large amount of dust enhancement.

4.5.4.5. *CS2-5*

This object has a best-fit age of 15 Myr, with a mass of 1.7×10^8 $M_\odot$. This object also shows dust enhancement in its best-fit model, with $A_{1200} = 1.0$ mag and q = 0. Both the best-fit single population and two-burst models have similar fit qualities, although both are relatively poor fits. While q is relatively well constrained to be small, both A_{1200} and t_{pop} span a wide region of allowed parameter space. This object is undetected in all *Spitzer* bands, thus these results may not be constraining.

4.5.4.6. *CS2-6*

CS2-6 has one of the highest quality fits in our sample, and it too exhibits signs of possible dust enhancement of the Lyα EW. The very red SED is best fit by a 40 Myr, 4.8×10^9 $M_\odot$ population, with all 4.0 mag of dust extinction affecting the continuum only, significantly enhancing the Lyα EW (1000 Å). The best-fit two-burst model has a worse fit quality, with a similar combined population. This is allowed as the undetected NIR fluxes do not constrain the amplitude of the 4000 Å continuum break (see §4.6.3.1). Both dust and q are relatively well constrained. The age is somewhat constrained to be $\leq$ 40 Myr, but there are a few small allowed regions at higher age.

4.5.4.7. *CS2-7*

CS2-7 is peculiar as it is the only object in our sample with detected J, H, Ks, 5.8 and 8.0 μm fluxes. In §4.3.4 we discussed that this object has both spectroscopic and photometric redshifts pointing to a likely redshift of ~ 4. Although this object's observed SED shows excesses at the positions of both Lyα and $H\alpha$, these excesses

are not very strong, and thus cannot definitively tell us the redshift of this object. Its best-fit model has a young age of 5 Myr, yet a high mass of $2.8 \times 10^9\ M_\odot$, with 3.0 mag of dust extinguishing Lyα more than the continuum (q = 1.5). The age of this model is very poorly constrained, as in our simulations nearly the entire range of possible ages was allowed. However, the two-burst model is a much better fit, with 99% of the mass in old stars, and the remaining 1% in a 2.5 Myr old burst. The derived mass of the two-burst model is $\sim 10^{11}\ M_\odot$, which is surprisingly high, thus the two-burst fit for this object is suspect. We caution the reader again that the results for this object may not be wholly accurate, as we cannot be certain that the redshift of the models truly represent the redshift of this object.

4.5.4.8. *CS2-8*

CS2-8 has a best-fit model of 5 Myr and $1.6 \times 10^8\ M_\odot$, with dust enhancing its already high EW ($A_{1200} = 3.0$; q = 0). Many values of dust appear to be allowed, with $A_{1200} = 3$ to 4 mag favored. Dust enhancement looks to be very favored in this object, as nearly all simulations fall at q $\leq$ 0.5. The best-fit two-burst model is identical to the single population model.

4.5.4.9. *CS2-9*

Lastly, while CS2-9 has the lowest χ_r^2 of all of our objects, this is partly due to the fact that we have no detections redward of the z'-band, thus while we report our results for this object, they only represent a possible population for this object; deeper NIR and IR data are needed to fully constrain this object's stellar population.

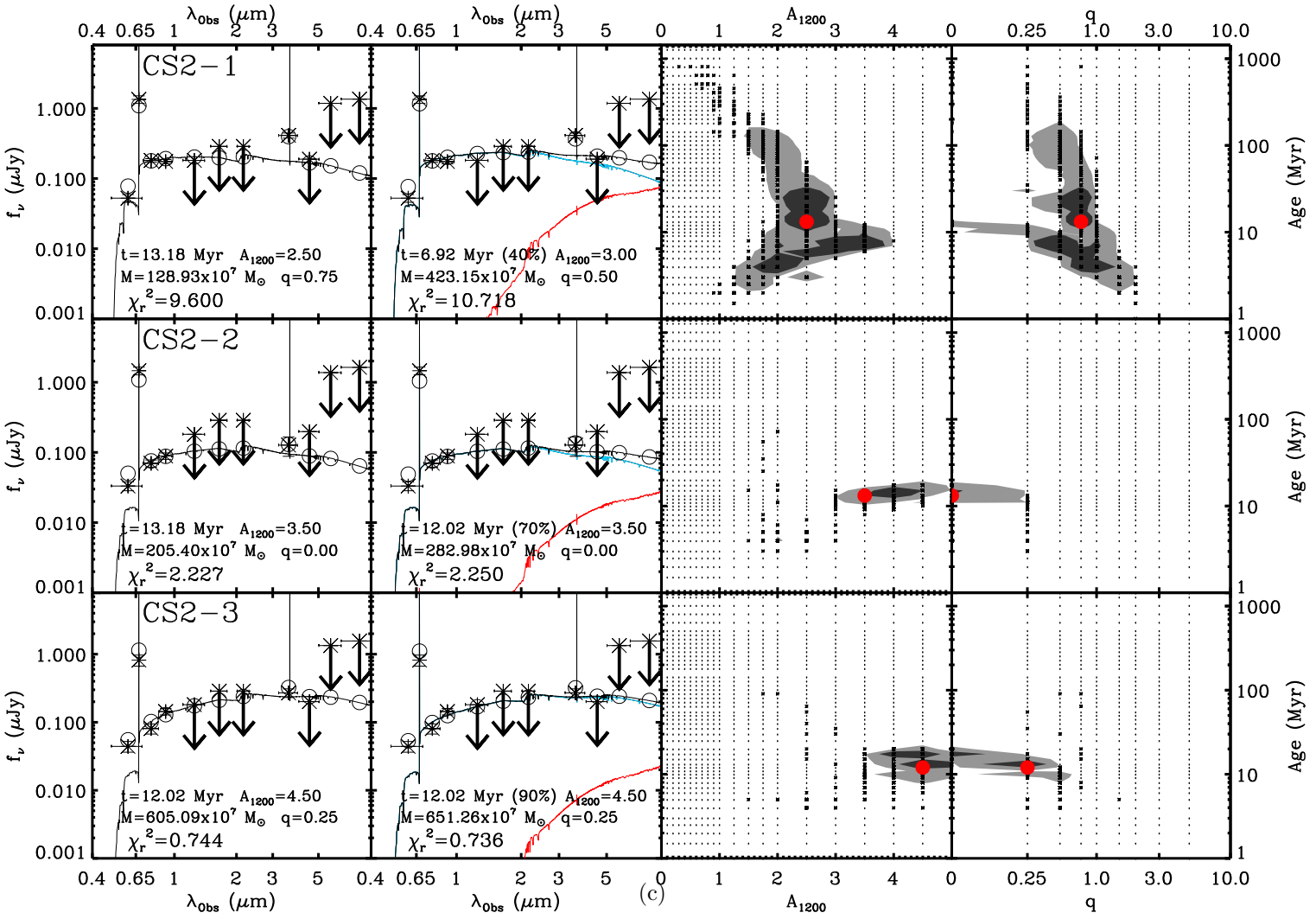

(c)

FIG. 13.—(c) Continued.

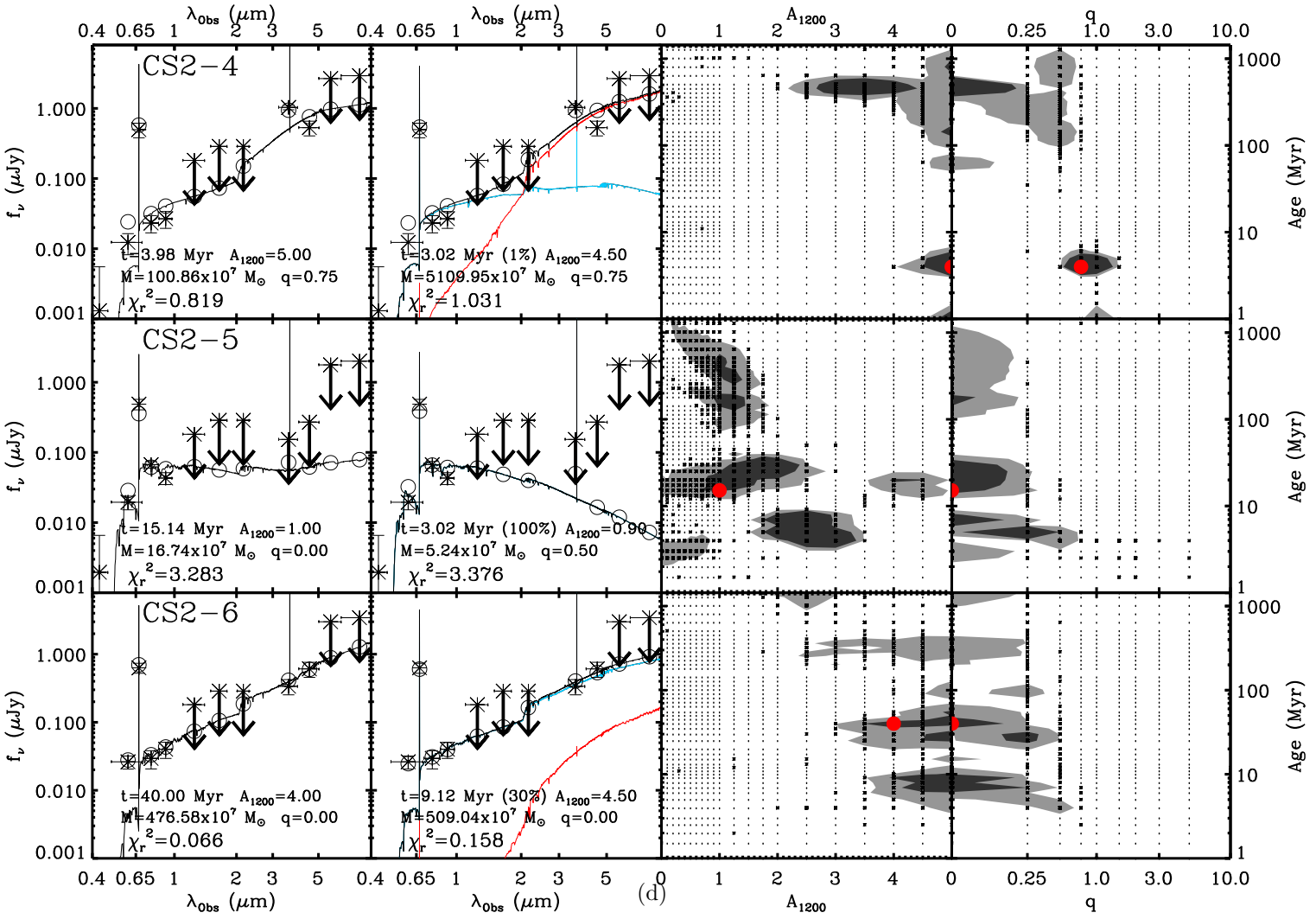

(d)

FIG. 13.—(d) Continued.

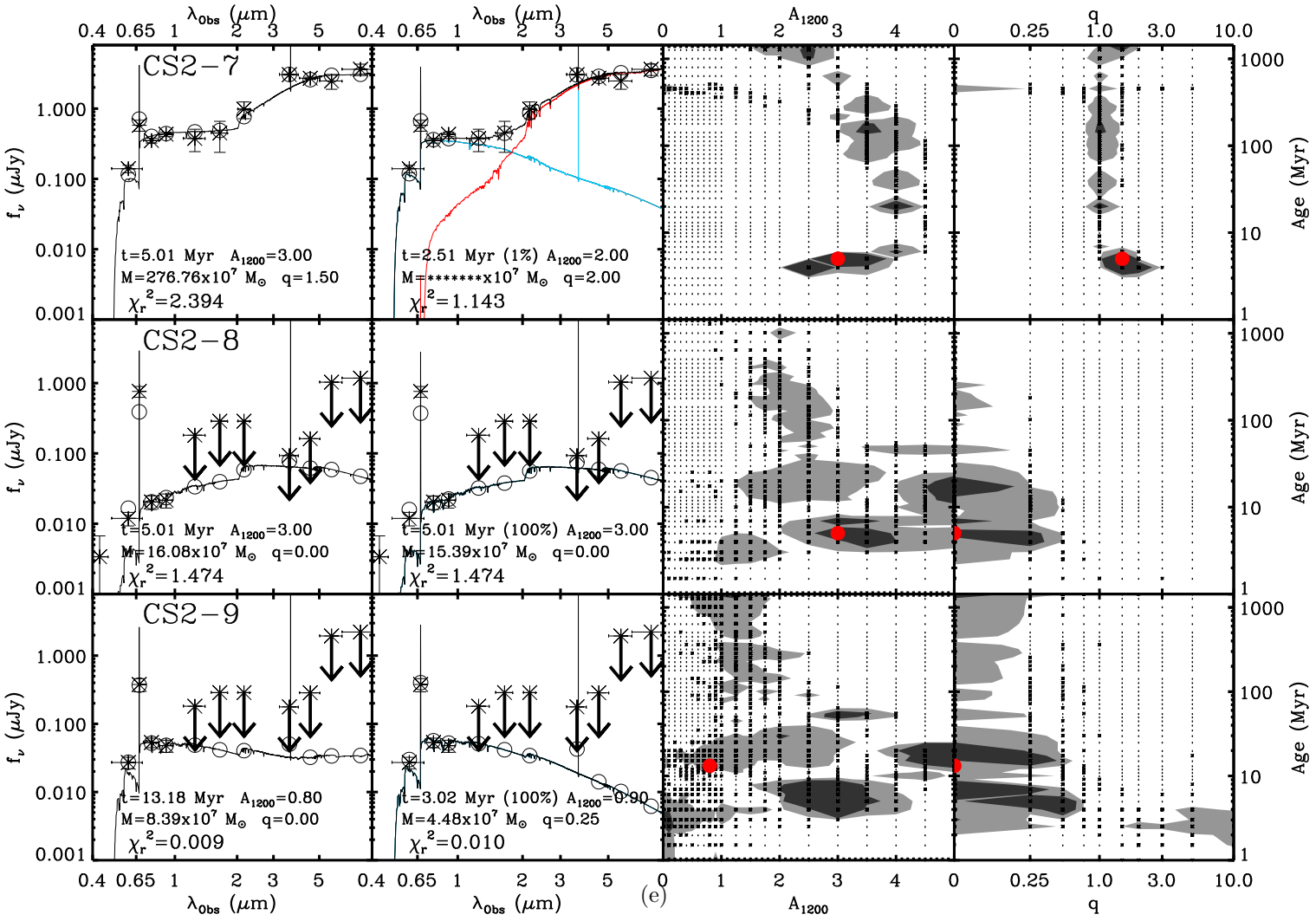

(e)

FIG. 13.—(e) Continued.

TABLE 9
BEST-FIT SINGLE POPULATION MODELS

Name	t_{pop} (Myr)	Mass (10^7 $M_\odot$)	Z ($Z_\odot$)	τ_{SFH} (yr)	A_{1200} (mag)	q	Model EW (Å)	χ^2_r
CHa-1	3.0	28.12	0.2	4x10^9	1.00	2.00	81.49	0.52
CHa-2	50.0 (4.0)	135.5 (52.84)	0.02	10^8	1.25 (2.00)	1.00 (1.00)	75.54	0.51
CHa-3	453.5	383.9	0.2	4x10^9	0.30	0.00	97.43	0.32
CHa-4	6.0	58.28	0.005	10^7	1.00	3.00	27.39	1.94
CH8-1	2.5 (12.0)	29.16 (157.1)	1.0	10^7	2.00 (4.00)	1.00 (0.25)	131.3	0.93
CH8-2	10.0	45.72	0.005	10^7	0.50	5.00	20.04	1.07
CS2-1	13.2	128.9	0.02	10^7	2.50	0.75	135.8	9.60
CS2-2	13.2	205.4	0.005	10^6	3.50	0.00	398.2	2.23
CS2-3	12.0	605.1	0.005	10^5	4.50	0.25	340.8	0.74
CS2-4	4.0 (500.0)	100.9 (4972)	0.005	10^6	5.00 (3.50)	0.75 (0.00)	478.3	0.82
CS2-5	15.1	16.74	1.0	10^7	1.00	0.00	122.9	3.28
CS2-6	40.0 (7.0)	476.6 (94.79)	1.0	10^7	4.00 (4.50)	0.00 (0.00)	999.6	0.07
CS2-7	5.0	276.8	0.005	10^6	3.00	1.50	30.6	2.39
CS2-8	5.0	16.08	1.0	10^5	3.00	0.00	533.3	1.47
CS2-9	13.2 (7.0)	8.39 (32.85)	1.0	4x10^9	0.80 (3.00)	0.00 (0.00)	140.8	0.01

NOTES.—The minimized χ^2 single population model for each object. Age, mass, metallicity, SFH timescale, A_{1200} and q (clumpiness) were allowed to vary during the fitting process. The model EWs are rest-frame (including the effects of IGM absorption), and computed from a ratio of Lyα flux to continuum flux redward of the line. Values in parenthesis show the most-likely model results (see §4.6.2).

TABLE 10
BEST-FIT TWO-BURST POPULATION MODELS

Name	t_{pop} (Myr)	Mass (10^7 $M_\odot$)	Z ($Z_\odot$)	A_{1200} (mag)	q	Mass Fraction in Old Stars	Model EW (Å)	χ^2_r
CHa-1	2.5	106.3	0.02	1.00	2.00	0.70	72.38	0.53
CHa-2	6.0	304.8	0.005	1.75	1.00	0.80	66.99	0.51
CHa-3	4.0	1323	0.4	0.40	1.00	0.99	66.12	0.40
CHa-4	3.0	570.5	0.2	1.50	2.00	0.90	27.77	3.22
CH8-1	4.0	86.15	0.2	1.50	0.75	0.80	138.2	0.94
CH8-2	4.0	227.0	0.02	0.40	5.00	0.90	21.04	0.96
CS2-1	6.9	423.2	0.02	3.00	0.50	0.60	154.4	10.72
CS2-2	12.0	283.0	0.005	3.50	0.00	0.30	382.3	2.25
CS2-3	12.0	651.3	0.005	4.50	0.25	0.10	340.8	0.74
CS2-4	3.0	5110	0.005	4.50	0.75	0.99	431.9	1.03
CS2-5	3.0	5.24	1.0	0.90	0.50	0.00	108.4	3.38
CS2-6	9.1	509.0	0.2	4.50	0.00	0.70	638.0	0.16
CS2-7	2.5	13408	0.02	2.00	2.00	0.99	29.2	1.14
CS2-8	5.0	15.39	1.0	3.00	0.00	0.00	533.3	1.47
CS2-9	3.0	4.48	1.0	0.90	0.25	0.00	132.8	0.01

NOTES.—Same as Table 9, only these models had two bursts of star formation; one maximally old burst at 1440 Myr, and a second burst at t_{pop}. We list the mass fraction in the old burst for each best-fit model.

Nonetheless, this object also shows dust enhancement of the Lyα EW, with A_{1200} = 0.8 mag and q = 0 in its best-fit 13.2 Myr, 8.4×10^7 $M_\odot$ population. However, with the exception of q, the best-fit parameters are very poorly constrained, as evidenced by the simulation results.

4.6. Discussion

4.6.1. Equivalent Width Distribution

In Figure 14 we plot both the distribution of EWs derived from the computed narrow-band excess of our objects (see Finkelstein *et al.* 2007 for this calculation), and the EWs from the best-fit models. While both distributions peak at a rest-frame EW of $\sim$ 100 Å, the object EWs show a larger number of high EWs, and vice versa for the model EWs. As we alluded to in §4.5, we believe that this is due to the inherent uncertainty in calculating EWs from the observed fluxes. This calculation relies on a measurement of the line-flux to continuum-flux ratio, and due to intervening IGM material we lack a true measurement of the continuum flux in the regime surrounding the line. Examining the V-band data points in Figure 13, one can see that the bandpass is nearly all blueward of the Lyα line, thus it does not contain a true measurement of the intrinsic continuum flux.

However, the EWs of our models are computed in a more accurate fashion, as we have the entire model spectrum at our disposal. Our model EWs are calculated using:

$$EW_{rest,model} = \frac{f(\lambda_{Ly\alpha})}{f(\lambda_{Ly\alpha+1})} * (\lambda_{Ly\alpha+1} - \lambda_{Ly\alpha}) * (1+z)^{-1} \quad (9)$$

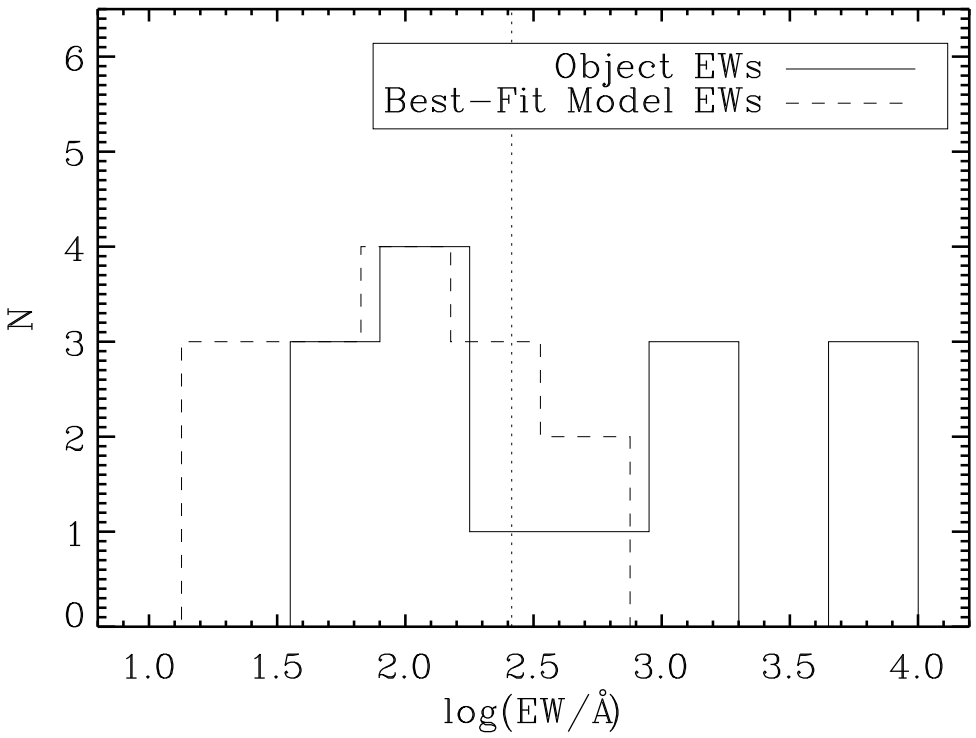

FIG. 14.—The rest-frame EWs as measured from our narrowband and continuum (F606W) observations are plotted in the solid histogram, with the rest-frame EWs from the best-fit models plotted in the dashed histogram. The dotted line denotes an EW of 255 Å, which is the maximum EW allowed by a Z = 0.02 $Z_{\odot}$ stellar population (at 1 Myr). Eight (five) objects (best-fit models) have computed EWs $>$ 255 Å, implying that other effects (i.e. dust enhancement etc.) are in play. We are inclined to trust the model EWs over the computed EWs of the objects, as the object EWs suffer from the uncertainty of where the line falls in the narrowband and F606W filters.

where $\lambda_{Ly\alpha}$ is the wavelength position of the Lyα line (1215 Å in the model; the entire line is concentrated in this bin), and $\lambda_{Ly\alpha+1}$ is the wavelength element immediately to the right of Lyα (1217 Å). In this fashion we obtain a true measurement of the stellar continuum near the line, and thus, at least when the quality of the fit is acceptable, we consider the EWs from the best-fit models as being more indicative of the true value.

For our purposes, we define a "normal" stellar population as one with a continuous SFH, Salpeter IMF, and Z = $.02Z_{\odot}$ (i.e., no dust or top-heavy IMF etc. causing high EWs). This population has a maximum Lyα EW of 255 Å at 1 Myr (including the effects of IGM), asymptoting to a constant value of 76 Å by 100 Myr. We can examine the importance of q in our sample by comparing our best-fit model EWs to this normal stellar population. We find that 11 of our best-fit model EWs are higher than 76 Å, meaning that they have to be younger than 100 Myr, which is consistent with our results. However, we also find that five of these 11 have best-fit model EWs $>$ 255 Å, which means that dust enhancement is likely to be occurring to explain their EWs. This is confirmed by our results, as four of these five have q = 0, with the other having q = 0.25, thus showing that a clumpy ISM is significantly enhancing their Lyα EW.

4.6.2. Model Parameter Distribution

4.6.2.1. Best-Fit Models

In Figure 15a we show the distribution of best-fit ages from our models. In F08a, out of four galaxies, we found that three had ages of near to 10^6 yr, with one

near 8×10^8 yr. In our current study, we see that most of our objects have best-fit ages $\lesssim 10$ Myr, with three out of the 15 objects showing ages ≥ 40 Myr. However, we still have a large age range where we find no objects, from 50 - 450 Myr. There are many scenarios one could think of to fit this distribution. Perhaps the distribution of ages is continuous, and we just need a larger sample to fill in the gaps. One intriguing possibility is that this distribution is true, i.e. we see Lyα galaxies when they are very young, and still see a few out to a few 10's of Myr, but then some physical mechanism is blocking the Lyα emission until much older age. Before the first generation of stars dies, Lyα photons may find it easier to escape, especially if the initial dust is clumpy. After a few 10's of Myr, stars will begin to die and these young galaxies will be actively forming dust. As the dust gets thicker, the amount of Lyα escaping will be reduced. However, after some period of time, the stars may begin to "punch holes" through the dust, resulting in a clumpy (or porous) ISM that can enhance the observed EW, creating an object like CHa-3. In Figure 15b we show the distribution of the best-fit clumpiness parameter. We find that 60% (9/15) of our objects show possible evidence that an ISM dominated by a clumpy geometry ($q < 1$) is enhancing their EWs. A few objects have $q \geq 3$, indicating a more homogeneous ISM, although both of these objects have interesting fits, mostly due to their SEDs with "red upturns".

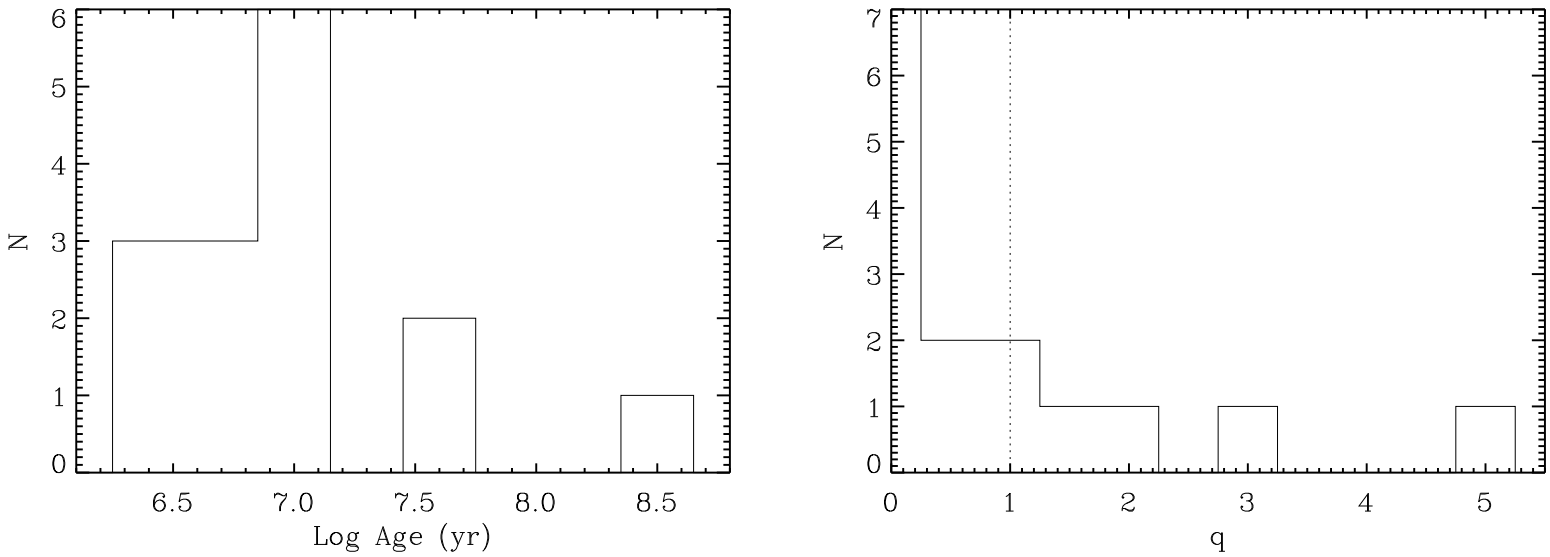

FIG. 15.—The distribution of best-fit stellar population ages and clumpiness parameters from our single component models. The majority of our objects have young ages, and a majority of our sample also requires clumpy dust to enhance their Lyα EWs.

From Table 9 we see that our derived masses span a large range, from 8.4 $\times$ 10^7 to 4.8 $\times$ 10^9 $M_\odot$, with half of our sample at or over 10^9 $M_\odot$. These results are similar to those seen in past studies. We (Finkelstein *et al.* 2007) have previously found a mass range of 10^8 to 2 $\times$ 10^9 $M_\odot$ in a sample of 21 LAEs from ground-based photometry at z $\sim$ 4.5, with an age range of 4 – 200 Myr. Pirzkal *et al.* (2007) found a mass range of 7 $\times$ 10^6 to 1.4 $\times$ 10^9 $M_\odot$, and an age range of 1 – 20 Myr at z $\sim$ 5. These objects likely show a smaller maximum age and mass since they were detected via grism spectroscopy in the *Hubble* Ultra Deep Field, thus these authors probed deeper into the continuum luminosity function. Gawiser *et al.* (2006a) stacked a large number of LAEs at z $\sim$ 3.1, and found an average age of 90 Myr, with a mass of 5 $\times$ 10^8 $M_\odot$. Lai et al (2007, 2008) performed two studies, one at z $\sim$ 5.7, and one at 3.1. At z $\sim$ 5.7, they found a mass range of 1.4 $\times$ 10^9 to 1.4 $\times$ 10^{10} $M_\odot$. This higher upper mass is likely due to these authors sampling the high end of the mass function, as they reported results from IRAC detected objects only. These objects had an age range of 5 - 700 Myr. At z $\sim$ 3.1, they separated their samples into IRAC undetected and IRAC detected stacks, and found an average stellar population of 200 Myr and 3 $\times$ 10^8 $M_\odot$ for the undetected stack, and 1 Gyr and 10^{10} $M_\odot$ for the IRAC detected stack. Chary *et al.* (2005) found one LAE at z = 6.56, with a best-fit stellar population of 5 Myr and 8.4 $\times$ 10^8 $M_\odot$. Overall, we have found a broad range of ages and masses, but they appear consistent with these previous results.

While our detection of dust is very interesting, many of these other studies have found evidence for dust extinction as well. While Lai *et al.* (2008) and Gawiser

et al. (2006a) do not find dust in their stacking analyses, Chary *et al.* (2005), Pirzkal *et al.* (2007) and Lai *et al.* (2007) do find dust in their analyses of individual objects, with A_V as high as 1.3 (A_{1200} is roughly a factor of 4 greater than A_V). This shows an interesting trend, in that studies which analyze objects separately seem to detect dust extinction, while those that stack fluxes do not. To see if our objects followed this trend, we did a quick test by averaging the fluxes in each band from our best-fit models, and then re-fitting this "stack" of our objects. We found that our sample has an average stellar population with t_{pop} = 6 Myr, 8.0×10^8 $M_\odot$, A_{1200} = 2.5, q = 1 and EW $\sim$ 90 Å, with a 99% confidence level of containing some measure of dust. This average population appears to be indicative of the average properties of our sample, including the detection of dust.

4.6.2.2. Most-Likely Models

Although we find many objects with q < 1, which allows Lyα emission at older age, we find that still only one object is best fit by an old (> 100 Myr) stellar population. However, taking the Monte Carlo results into account, we can assign some objects more likely ages, A_{1200}'s and q's, as the Monte Carlo simulations illuminate the likelihood range of these parameters. For those objects where their best fit lies in the largest 68% confidence region, we leave their parameters fixed. However, if this is not true, we assign them the age, A_{1200} and q from the center of the largest 68% confidence region from the Monte Carlo contour plots. We do this for: CHa-2, CH8-1, CS2-4, CS2-6 and CS2-9. Figure 16a and Figure 16b show updated histograms using the new ages and q's for these five objects.

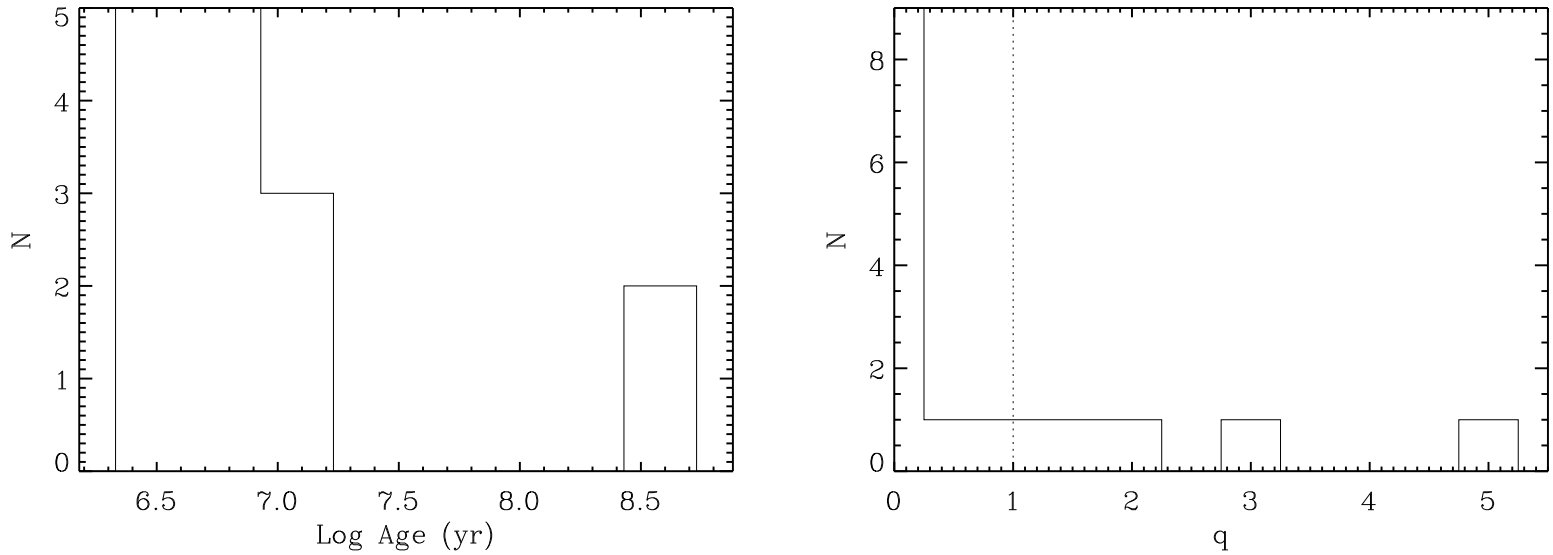

FIG. 16.—The distribution of most-likely stellar population ages from our single component models. These were derived from the Monte Carlo simulation results. In cases where the best-fit model did not lie in the largest 68% confidence region, we set the best-fit age and q value to that derived from the center of the largest 68% confidence region, computing these new histograms. The age distribution is interesting, as it implies that some mechanism is preventing us from seeing LAEs at "moderate" ages.

While the q distribution is mostly unchanged (although now 67% of objects have q < 1), the slight change in the distribution of ages has important consequences. First, both CHa-2 and CS2-6, which had ages of 40 and 50 Myr, respectively, are much more likely to have ages of < 10 Myr. Secondly, CS2-4, which had a best-fit age of 6 Myr with only a little dust enhancement, has a most likely age of 500 Myr with lots of dust enhancement. Thus, our distribution has significantly changed, with 13 of our objects at ≤ 15 Myr, and 2 objects at ≥ 450 Myr, both best-fit with significant amounts of dust enhancement. As the Monte Carlo results highlight how the observational errors can lead to uncertainties in the model fitting, we regard these most-likely models as the true results of our work. These new results show an even greater bimodality than the best-fit results, suggesting a possible recurrence of the Lyα emitting phase in these galaxies (e.g., Shapley *et al.* 2001; Malhotra & Rhoads 2002; Lai *et al.* 2008).

As another test, we took the Monte Carlo results and computed the probability of each object being fit by each age in our age grid, normalized to the number of simulations (i.e. so that the total probability is normalized to 1). We could then look at probability curves for each object. In order to see the probability distribution of age across our whole sample, we averaged all of these curves for each object, creating Figure 17. This figure verifies the by-eye results of Figure 16a, in that we see two distinct peaks in age for our LAEs, at 4 Myr and 400 Myr, showing definite bimodality.

We also examined these most-likely models in order to see how much the mass changed for these objects vs. their best-fit results. As one would expect, the difference

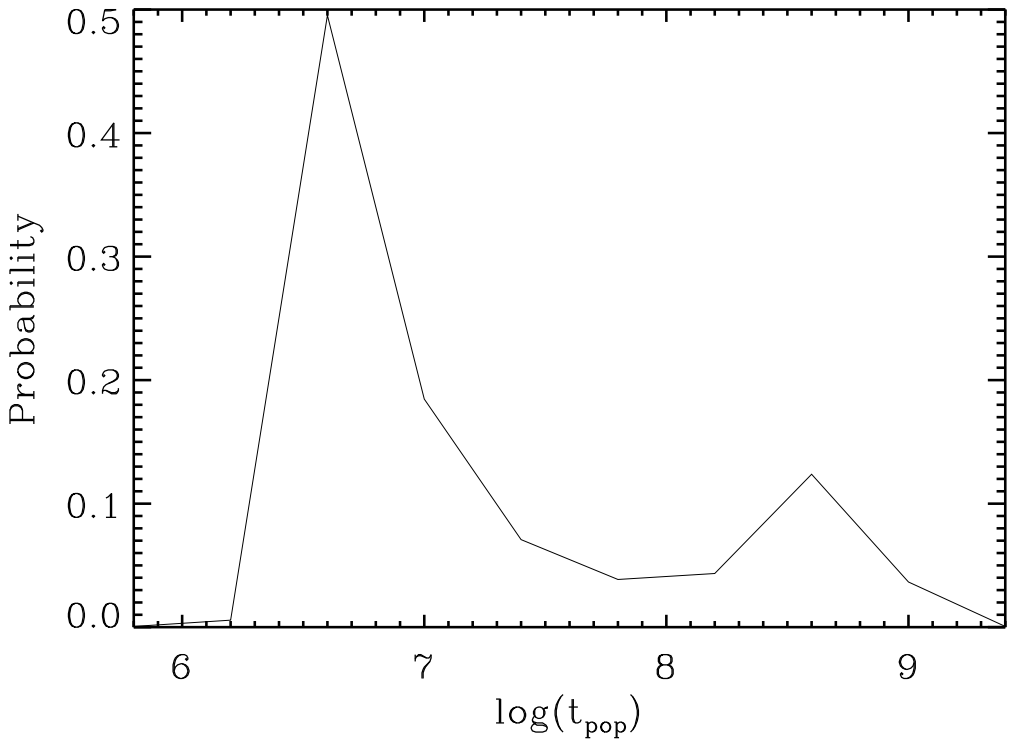

FIG. 17.—The composite age probability curve of all of our LAEs, made by averaging the probability curve for each object derived from the Monte Carlo simulation results. This age probability distribution backs up our by-eye results from Figure 16a, showing a double peaked distribution, at $\sim$ 4 and 400 Myr.

was large for CS2-4, which has a most-likely mass of 5.0×10^{10} $M_{\odot}$, 50 times larger than the mass derived for this object from the best-fit young stellar population. The differences in mass for CHa-2, CH8-1, CS2-6 and CS2-9 were smaller, with their most-likely masses being 5.3×10^{8}, 1.6×10^{9}, 9.5×10^{8} and 3.3×10^{8} $M_{\odot}$, respectively. This brings our upper end up to 5.0×10^{10} $M_{\odot}$, consistent with the upper mass end from Lai *et al.* (2007, 2008). We tabulate these most-likely results in parenthesis in Table 9.

4.6.3. Causes of Model Uncertainties

4.6.3.1. Importance of NIR

We spent a lot of effort to try to get meaningful NIR fluxes for our objects. Although the ISAAC observations ended up not being deep enough, we were still able to put upper-limit constraints in this regime, which did somewhat constrain the models. However, our results would be much improved with NIR detections. The reason for this is that the best indicator of age is the spectral break near 4000 Å. Objects dominated by older stellar populations will show a significant break here, while young objects will not. At z $\sim$ 4.5, the NIR brackets this break, with the J and H-band blueward, and the Ks-band just redward. The wavelength distance between Ks and 3.6 μm is too large for the IRAC band to constrain the break, and it is further complicated by $H\alpha$ emission at this redshift. Likewise, if dust is involved, the z'-band is too far away to constrain the continuum on the blue-side. Thus NIR is crucial to constraining the ages of these objects.

One good example is shown in the best-fit model spectrum for CS2-7, which is the only object where we have NIR detections. Its H - Ks color ($\simeq$ 0.85 mag) constrains the 4000 Å break to be relatively small, thus the red Ks - 4.5 μm color ($\simeq$ 1.1 mag) is caused by dust, with A_{1200} = 3.0 mag in this object. We have no such constraints for CS2-4, which has an extremely red z' - 4.5 μm color ($\simeq$ 3.24 mag). With the absence of intervening information, this color is equally likely to be fit by either a lot of dust, or old stars causing the break. The best-fit model fits the data with young stars with A_{1200} = 5.0 mag. However, as shown by the Monte Carlo results, a much older age appears more likely, with the break causing the red color. Future observing time constraining the physical properties of Lyα galaxies will need to include NIR observations at the highest priority.

4.6.3.2. $H\alpha$ Emission

As we discussed in F08a, the amount of $H\alpha$ emission relative to the amount of Lyα emission we observe can be a crucial constraint on the cause of the Lyα EW. If the Lyα EW is high due to young stars, the $H\alpha$ EW will also be high, as both types of photons are created in large numbers in star forming regions. However, if the Lyα EW is high due to clumpy dust, the $H\alpha$ EW will not be high, as $H\alpha$ photons are not resonantly scattered. Thus, a high Lyα to $H\alpha$ ratio implies clumpy dust enhancement of the Lyα EW. We can obtain a handle on this by examining the 3.6 - 4.5 μm colors. Figure 18 plots the narrowband excess (F606W - NB) vs. the 3.6 - 4.5 μm color, which is proportional to the $H\alpha$ EW. We can use this color-color plane to examine whether comparing the two EWs provides new physical insight.

To do this, we plot both the positions of our objects in this plane, as well as a few representative model tracks. The extent of these model tracks represents the amount of dust extinction, from A_{1200} 0 - 5 mag. The line-style represents the age, with the solid line being a 5 Myr old population, dotted 20 Myr, and dashed 800 Myr. The line colors represent the clumpiness, with blue being q = 0, green q = 1, and red q = 10. We then consider the best-fit age, A_{1200}, and q for each object, and see whether we find any trends that are consistent with the models.

Considering age first, we see that the tracks move to the right with age, representing $H\alpha$ emission being reduced and the optical continuum becoming redder at older ages. We should thus see our younger objects towards the left, and older towards the right. However, we do not see this trend, as the oldest three objects, CHa-3, CS2-4 and CS2-6, lie across the whole range of 3.6 - 4.5 μm color, thus it does not appear as if these two colors alone are enough to constrain the age in practice.

As for the clumpiness, the models show that low q results in a higher narrowband excess, and vice versa, as we would intuitively expect. Looking at our objects, we do see this trend, as our three objects with the highest q values have the lowest narrowband excess, and nearly all of the q = 0 objects lie towards the top of this plane. Lastly, we look at the dust extinction. If q is near zero, the points should move upward with dust. If q is near 1, they should move to the right, and if q is very high, they should move directly down. We do see some trends, although not as strong as those seen with q. If we take all points with q = 0, we do see a trend of

less dust with decreasing narrowband excess, with the exception of CS2-6. Only two objects have q = 0.75, but we see the same trend with these two.

The increasing trend towards lower-redshift science opens up the door to use the $H\alpha$ line as a diagnostic tool to understand LAEs. We have shown that even at high redshift, the derived Lyα-to-$H\alpha$ ratio can put some constraints on the dust extinction and geometry in LAEs. Future studies with a broader wavelength coverage and more data points (i.e. including the NIR) will allow for better fits to the data. This will remove some of the uncertainty coming from the model fitting, perhaps allowing the EW comparison to constrain the age.

4.6.3.3. Other Scenarios for Preferential Lyα Escape

While we have shown that clumpy dust can enhance the Lyα EWs in some of our objects, other mechanisms might also explain their observed SEDs. First, Lyα could appear brighter relative to the continuum if an external gas shell around the star formation region preferentially allowed the escape of Lyα in some directions. This would result in Lyα being "beamed" in some direction, and if we were to observe the galaxy from this direction, we would detect a large Lyα EW. This mechanism could result in the Lyα EW being enhanced by a factor of a few, in a modest fraction of galaxies.

A second possibility for Lyα escape involves the presence of large outflows. These would work in favor of Lyα escape in two ways. First, if the Lyα photons were to back-scatter off the far side of the expanding shell, they would appear redshifted to the static part of the galaxy during their trek back though the galaxy (i.e. moving

mirror effect), and thus would not be scattered by any HI atoms. Likewise, imagine if the Lyα photons were emitted in our direction from some stationary point in the galaxy, but the near side of the galaxy had an expanding outflow, the Lyα photon would again appear redshifted to the hydrogen in the ISM, and thus would pass out of the galaxy unobscured. Velocity shifts in the Lyα line relative to interstellar lines have been seen locally by Kunth *et al.* (1998). Using a stack of 811 z $\sim$ 3 Lyman break galaxy spectra, Shapley *et al.* (2003) detected a mean Lyα redshift of 360 km s^{-1} relative to the systemic redshift of the galaxy. However, Lyα galaxies are intrinsically fainter, and thus it is difficult to detect their continua in individual spectra (i.e., Dawson *et al.* 2004), let alone interstellar absorption lines. This remains a top priority for the next generation of extremely large telescopes.

4.7. Conclusions

We have presented the results from our analysis of 11 newly discovered, and four previously known, narrowband selected Lyα galaxies in the CDF–S. We compared the SEDs of these objects to stellar population models in order to determine their physical properties such as age, mass, and dust extinction. More specifically, we are interested in finding out whether enhancement of the Lyα EW due to a clumpy, dusty ISM can be responsible for some of the large Lyα EWs which we have observed.

We first computed the best-fit stellar population model to each object allowing one SFH. For the four objects which we previously analyzed in F08a, we confirmed our earlier results, which had three of the objects being fairly young, and one being very old. The old object (CHa-3) still appears to have a strong Lyα line due to dust

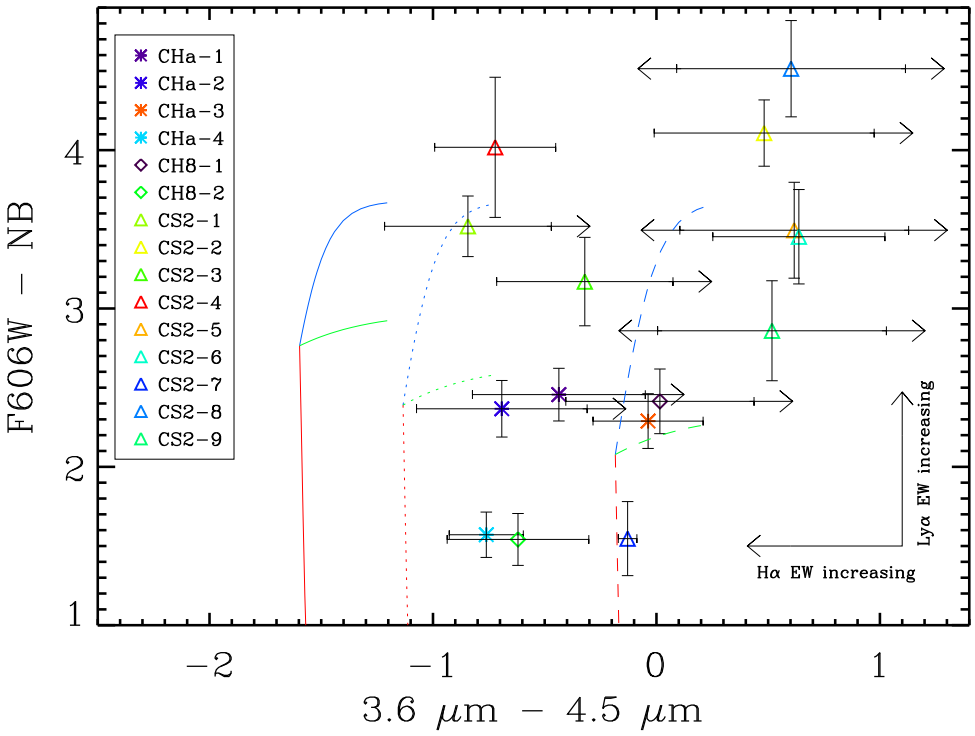

FIG. 18.—Color-color plot of our objects, with the narrow-band excess (F606W - NB) on the vertical axis, and the 3.6 - 4.5 μm color on the horizontal axis, which is a measure of the $H\alpha$ line strength. Each of our objects are plotted with a different color-symbol combination for identification. The colors follow the age, with purple being the youngest, and red being the oldest (using the most-likely ages). We plot arrows showing the direction in the plane that both the Lyα and $H\alpha$ EWs increase. The colored lines show how our models change with age, dust and q. All models are $0.02Z_{\odot}$ and have a continuous SFH. The colors represent different q values, with blue representing q = 0, green q = 1 and red q = 10. The line-styles represent different ages, with solid being 5 Myr, dotted 20 Myr and dashed 800 Myr. The extent of the lines represents the amount of dust extinction, with the crossing of all three colors representing zero dust, and the end of the line representing A_{1200} = 5.0 mag. While we do see best-fit q and A_{1200} trends matching up with the model tracks, these colors do not appear to well-constrain the age, although this may be due to the uncertainty in our model results.

enhancement, shown by its value of the clumpiness parameter (q) of zero. Although none of the rest of our sample was best fit by an age over 50 Myr, the majority of our best-fit models did require some amount of clumpy dust enhancement of the Lyα EW, with 9/15 objects having q < 1, thus dust enhancement is widespread.

As a test, we also allowed objects to be fit by two bursts of star formation: One at a maximally old age of 1.4 Gyr, and one at any time. Many of our objects showed significantly worse fits with two bursts, with only one (CS2-7) being significantly better fit by two bursts (although the redshift ambiguity of this object leaves this result in question). However, we do feel as if it was a necessary exercise to fit all objects to this model, as a two-burst population could be a viable alternative explanation to those objects which appear old due to dust enhancement.

To assess the validity of our results, we ran 7000 Monte Carlo simulations, obtaining a best fit for each object from each simulation. In the resulting contour plots, we can examine whether the best-fit model truly represents the most likely model by seeing if the best fit lies in the largest 68% confidence region. If it does not, we assign the object a new age, A_{1200} and q based on the largest 68% confidence region. Figure 16a and Figure 16b plot histograms of the most likely ages and q's for our sample. The distribution of ages is interesting, in that it implies that LAEs are either very young (< 15 Myr), or very old (> 450 Myr).

There could be many explanations for this, but we propose that this "bimodality" in LAE stellar population ages may be due to dust. At the beginning of this work, we asked the question of whether LAEs were primitive objects, dusty star-formers,

or evolved galaxies. This work, among others, has shown that while many LAEs are young, they are not primitive. Using our most likely results, we find a range of A_{1200} of 0.3 to 4.5 mag, thus all of our objects have some amount of dust extinction in them. As dust comes primarily from evolved stars and stellar deaths, the existence of dust is strong evidence that LAEs are not primitive, as the dust has been produced by a previous generation of stars. We find that out of our 15 candidate LAEs, 13 of them appear to be dusty star-forming galaxies, with ages from 3 - 15 Myr, and A_{1200} from 0.4 to 4.5 mag. The remaining two objects appear to be evolved galaxies, with ages of 450 and 500 Myr, and A_{1200} of 0.3 and 3.5 mag, respectively, exhibiting Lyα emission due to dust enhancement of the EW.

The young galaxies in our sample, although they are dusty due to a previous generation of stars, still manage to emit Lyα, mainly due to dust enhancement (8/13 have $q < 1$). After a few 10's of Myr, enough massive stars have exploded to further saturate the ISM with dust, and this could explain the drop-off in numbers (Figure 16a), and why we don't see any LAEs from 13 - 450 Myr. After some period of time, the stars have changed the ISM geometry enough so that Lyα can escape again. This ISM is now very patchy, which is why both of our old LAEs show dust enhancement of the Lyα EW in their model spectra. While this scenario is intriguing, a much larger sample is needed before we can see if this age bimodality is statistically significant.

Although we have tried to ensure that our stellar population fits are valid, there are still some concerns with a few objects. Objects CS2-3, CS2-4 and CS2-6 have

Spitzer fluxes which are blended in with near-neighbors. While we have used fluxes from TFIT to combat this problem, there is still some uncertainty in the results from these objects. As we mention in §4.4, objects CS2-5, CS2-8 and CS2-9 are undetected in all *Spitzer* bands, thus their stellar populations are being derived from the ACS and narrowband fluxes alone (with the NIR and IR upper limits adding some constraints). Lastly, the redshift for CS2-7 is uncertain, thus attempting to fit a z = 4.52 model to an object at z = 4.00 can result in incorrect conclusions. To see how these uncertainties affect our conclusions, we look at the results from the other eight objects, which we consider a "conservative" sub-sample. Using the most-likely results from this sub-sample, we find a median q value of 1.00, with $q < 1$ in 50% of our objects, close to what we found with the whole sample (67%). The median dust extinction in this conservative sub-sample is 2.0 mag, which is less than the sample as a whole. We still find dust in all objects, but many of those objects with the highest extinction levels have been cut from this sample, thus it is possible that those high values of A_{1200} may not be accurate. However, the presence of dust in all objects still implies that these objects are not primitive.

While we inferred many properties about LAEs in this work, we have also learned that more data is needed before we can truly match our objects to the models. For most of our objects, we are missing data in a crucial area of the SED, constraining the 4000 Å break. Without these data points, objects are allowed to be either old or dusty to explain the red colors, a degeneracy which can be fixed with better NIR data. Future observatories such as the *James Webb Space Telescope* will be sensitive

in this regime, and will provide the data needed to better constrain these objects. Nonetheless, with the data in hand, we can now say that dust enhancement of the Lyα EW is occurring in the majority of our sample, and needs to be accounted for in future stellar population studies.

5. THE EXPECTED DETECTION RATE OF DUST EMISSION IN HIGH-REDSHIFT Lyα GALAXIES

5.1. Abstract

Recent results have shown that a substantial fraction of high-redshift Lyman alpha galaxies contain considerable amounts of dust. This implies that Lyman alpha galaxies are not primordial, as has been thought in the past. However, this dust has not been directly detected in emission. Rather, it has been inferred based on extinction estimates from rest-frame ultraviolet (UV) and optical observations. This can be tricky, as both dust and old stars redden galactic spectra at the wavelengths used to infer dust. Measuring dust emission directly from these galaxies is thus a more accurate way to calculate not only the amount of dust extinction present, but also the total dust mass, giving us real physical information on the stellar populations and interstellar medium (ISM) enrichment. However, these observations are difficult given current facilities, as continuum photons absorbed by dust will be re-emitted in the far-infrared, which at high redshift will be observed at sub-millimeter and millimeter wavelengths. New generation instruments, such as the Atacama Large Millimeter Array (ALMA) being constructed in the Chilean Andes, and the Sub-Millimeter Array (SMA) on Mauna Kea, should be able to detect dust emission from some of these galaxies. Using measurements of the UV spectral slopes, we derive far-infrared flux predictions for a sample of 24 $z \geq 4$ Lyman alpha galaxies. We find that in only a few hours, we can detect dust emission from $42 \pm 21\%$ of our Lyman alpha galaxies with ALMA. Comparing these results to those found from a sample of 21 Lyman break galaxies (LBGs), we find that LBGs are on average 50% more likely to be detected than Lyα galaxies, implying that they are more dusty, and thus indicating an evolutionary difference between these objects. These observations

will provide better constraints on dust in these early galaxies to those derived from their UV and optical fluxes alone. Current stellar population studies show a large range in allowable population parameters. Directly detecting the dust emission will pin down the amount of dust, providing better constraints on the remaining physical properties. Undeniable proof of dust in these galaxies could explain the larger than expected Lyα equivalent widths seen in many Lyα galaxies today.

5.2. Introduction

Lyman alpha (Lyα) galaxies have been studied in detail for nearly a decade now, and we are only just beginning to learn about the properties of individual objects. Most initial narrowband studies (e.g., Hu *et al.* 1998; Rhoads *et al.* 2000) observed blank fields with two filters: a narrowband filter (to capture the Lyα emission line), and a broadband filter encompassing this narrowband (used to measure a narrowband excess). Learning the detailed properties of individual Lyα galaxies would be difficult with these data. However, these early studies were able to measure the equivalent widths (EWs) of their objects, calculated from the ratio of narrowband flux to broadband flux (Malhotra & Rhoads 2002).

Some of these initial results were surprising, as in many cases the Lyα EW distribution was higher than one might have expected from stellar population models, as many objects exhibited rest-frame Lyα EWs over 200 Å (e.g., Kudritzki *et al.* 2000; Malhotra & Rhoads 2002; Dawson *et al.* 2004, 2007; Shimasaku *et al.* 2006; Finkelstein *et al.* 2007). A normal stellar population (defined as having a Salpeter (1955) initial mass function (IMF), solar metallicity, and a constant star formation

history) has a maximum Lyα EW of 260 Å at 1 Myr, falling to a constant value of 95 Å at 100 Myr. Thus, while objects with EWs $\geq$ 200 Å are possible with a normal stellar population, they would all have to be extremely young. Looking at a random sample of Lyα galaxies, it would be extraordinarily rare if they all had ages of only a few Myr, thus something is likely happening to skew the EWs higher than they should be.

There are many possible reasons why this could be occurring, and the easiest area to examine is the assumption of a normal stellar population. For example, if a stellar population had sub-solar metallicity, it would form stars with hotter stellar photospheres. These stars would then pour out more ionizing photons, which, after interacting with the local interstellar medium (ISM), would in turn create more Lyα photons. Another possibility exists, whereby if a galaxy had a top-heavy initial mass function, it would create more massive stars than a Salpeter IMF, again resulting in more ionizing photons, and thus more Lyα photons. Both of these scenarios are possible in primitive, dust-free galaxies. Strong Lyα lines also come from the active galactic nuclei (AGN) components of some galaxies, but previous work has shown that most Lyα galaxies detected via narrowband selection are not AGN (Malhotra *et al.* 2003; Wang *et al.* 2004). In practice, if we do discover that a Lyα galaxy in our sample is an AGN, we throw it out of the sample.

Traditional belief holds that if a stellar population has dust present, it will strongly attenuate any Lyα photons. Lyα photons are resonantly scattered by any neutral hydrogen present, thus in a homogeneous ISM, they will have to travel much

further to escape the galaxy, dramatically increasing the chance of absorption by dust (Meier & Terlevich 1981). However, if the dust is in an inhomogeneous distribution, it is possible that a galaxy could appear to have a strong Lyα EW at later ages.

In this scenario, Lyα can escape unaffected by dust if it is somehow screened from interacting with the dust grains. This can happen if the dust resides in cold, neutral clumps embedded in an ionized inter-clump medium. This scenario was first proposed by Neufeld (1991) and examined in detail more recently by Hansen & Oh (2006). In this ISM geometry, the Lyα photons get scattered by neutral hydrogen at the surface of these clumps, and thus never see the dust which is embedded deeper inside. However, the continuum photons suffer no such restriction, so they pass un-obstructed into the interior of the clump, with many continuum photons being absorbed (extincted) and scattered (resulting in reddening of the continuum color). The Lyα photons proceed to bounce around from clump to clump, eventually escaping the galaxy. The net result of this is an increase in the Lyα – continuum flux ratio over that intrinsic to the stellar population. We would thus detect this galaxy with a higher EW, irrespective of its stellar population characteristics.

We believe that this scenario may be responsible for some of the high-EW objects seen in narrowband studies, and in our previous work (Chapter 4; Finkelstein *et al.* 2008b; hereafter F08b), we found ten objects out of a sample of 15 LAEs where this scenario appears to be in effect (one of which was also studied in Chapter 3; Finkelstein *et al.* 2008a). Two of these objects are evolved galaxies with large Lyα EWs due to this dust enhancement scenario (the other eight are still young, but

have their Lyα EWs enhanced to be larger than their already large value due to dust). The first of these two evolved galaxies was best fit by a 450 Myr, 3.8 x 10^9 $M_\odot$ stellar population with a rest-frame EW of $\sim$ 100 Å. This relatively high EW at old age was due to dust, as the best-fit model had 0.3 magnitudes of dust extinction at 1200 Å, but this dust was in a geometry such that it did not attenuate Lyα measurably. This resulted in a $\sim$ 35% increase in the Lyα EW over a similar stellar population with no dust. The second of these objects had a most likely age (see Chapter 4 for derivation of most likely age) of 500 Myr, a mass of 5×10^{10} $M_\odot$, and 3.5 mag of dust extinction in a very clumpy geometry, greatly enhancing the Lyα EW.

While these two objects are very interesting, and could go a long way towards explaining the apparent discrepancy in EW distributions, the rest of the objects in the sample had their own surprises. They were all young and lower-mass, with ages from 3 – 15 Myr, and masses from 1.6×10^8 – 5.0×10^{10} $M_\odot$. These ages and masses are indicative of the traditional belief of Lyα galaxies, where they are very young, and possibly primordial in nature. However, all of these thirteen LAEs were best fit by stellar populations with considerably non-primordial amounts of dust, with A_{1200} = 0.5 – 4.50, with many galaxies showing indications of a clumpy ISM.

Many other recent studies have detected dust in their Lyα galaxies (e.g., Chary *et al.* 2005; Pirzkal *et al.* 2007; Lai *et al.* 2007). These studies have arrived at this conclusion based off of a similar analysis as we did in Chapter 4, by fitting the observations to stellar population models. However, these model parameters can be degenerate, as at rest-frame UV and optical wavelengths the reddening of the

continuum color could be due to both dust *and* old stars. While observing these objects in the rest-frame optical with the *Spitzer Space Telescope* helps reduce this degeneracy, data at longer wavelengths could provide much tighter constraints.

When UV and optical photons are absorbed by dust, they are re-emitted in the far-infrared (FIR), resulting in a second observed peak in the spectral energy distribution (SED). Observing these galaxies in the sub-millimeter and millimeter (mm) regimes would detect this dust emission directly, which could resolve this red-color degeneracy. The Atacama Large Millimeter Array (ALMA) will be a uniquely sensitive tool to detect these high-redshift galaxies if they have dust, given its excellent observing conditions and large baseline. Thus, obtaining ALMA observations (even non-detections), will provide a much tighter constraint on the amount of dust in these objects than rest-frame UV-optical observations alone. We use ALMA as a measure of future observatory capabilities of detecting dust emission from LAEs. If we can confirm that many Lyα galaxies do in fact have dust, then it will help confirm that they are not the primitive galaxies that they were once thought to be. On the other hand, if we do not find evidence for dust, it may indicate that a top-heavy IMF or Population III stars are responsible for the strong Lyα EWs.

Where applicable, we assume Benchmark Model cosmology, where $\Omega_m = 0.3$, $\Omega_\Lambda = 0.7$ and $H_0 = 0.7$ (c.f. Spergel *et al.* 2007). All magnitudes are listed in AB magnitudes (Oke & Gunn 1983). In §5.3 we discuss our sample of Lyα galaxies which we use to make predictions. In §5.4 we present our results, and in §5.5 we make conclusions about the implications of these results.

5.3. Method

5.3.1. *Lyα Galaxy Sample*

We examine samples of LAEs from two recent studies: Finkelstein *et al.* 2008b (Chapter 4) and Pirzkal *et al.* 2007. The sample from Chapter 4 consists of 15 Lyα galaxies in the Great Observatories Origins Deep Survey (GOODS) *Chandra* Deep Field – South (CDF–S) narrowband selected to be at z $\approx$ 4.5. We will use the identifiers from Chapter 4, which are based on their detection filters: CHa-1 to 4 (detected in NB656, or $H\alpha$), CH8-1 and 2 (detected in NB665, or $H\alpha$ + 80), and CS2-1 to 9 (detected in NB673, or [S II]). See Chapter 4 for further details on the data reduction and selection process. Eight of the 15 objects have published photometric redshifts putting them near z $\sim$ 4 – 4.5 (MUSIC, Grazian *et al.* 2006; FIREWORKS, Wuyts *et al.* 2008). As mentioned in the introduction, 13 of these objects were best fit by young (3 – 15 Myr), low mass (1.6 – 60 $\times$ 10^8 $M_\odot$) stellar populations with a good amount of dust (A_{1200} = 0.5 – 4.5), with the dust in some cases enhancing the Lyα EW. Two objects (CHa-3 and CS2-4) were determined to contain older (450 – 500 Myr), more evolved populations, with dust extinction attenuating the continuum only due to a clumpy ISM, thus enhancing the Lyα EW.

The sample from Pirzkal *et al.* (2007; hereafter P07) consists of nine Lyα galaxies selected in the *Hubble* Ultra-Deep Field (HUDF; Beckwith *et al.* 2006), identified by their emission lines with spectra from the GRAPES (Grism ACS Program for Extragalactic Science; Pirzkal *et al.* 2004; Malhotra *et al.* 2005; Xu *et al.* 2007; Rhoads *et al.* 2008) survey. These objects were selected based on a detectable Lyα emission

line in the GRAPES grism data, and broadband ACS photometry consistent with a Lyman break galaxy (P07). In this paper, we will use the object IDs from P07: 631, 712, 4442, 5183, 5225, 6139, 9040, 9340 and 9487. These objects lie in the redshift range $4.00 \leq z \leq 5.76$, with Lyα line fluxes ranging from 17 – 60 $\times$ 10^{-18} erg s^{-1} cm^{-2} and z' magnitudes from 25.66 – 28.36. Using an exponentially decaying star formation history (SFH), P07 found best-fit ages of 1 – 20 Myr and stellar masses from 7 $\times$ 10^6 – 1.8 $\times$ 10^9 $M_\odot$. Three of the objects were best fit by dust, with 0.05 – 0.6 magnitudes of extinction in the V-band (four objects were best fit with dust using a single-burst SFH, and five objects were best fit with dust using a two-burst SFH).

For comparison with our LAEs, we also use the catalog of spectroscopically confirmed HUDF Lyman Break Galaxies (LBGs) from Hathi, Malhotra & Rhoads (2008; hereafter HMR08; Malhotra *et al.* 2005; Rhoads *et al.* 2008). There are 49 LBGs in the catalog, but for objects at redshifts greater than 4.5, we require J and H band measurements to derive their FIR fluxes, thus we were restricted to using only 21 of the 49 LBGs.

5.3.2. *Dust Emission*

While we know that photons absorbed by dust are re-emitted in the far-infrared, the stellar population models used in both Chapters 3 & 4 and P07 (Bruzual & Charlot 2003), while computing fluxes as red as 160 μm rest-frame, do not compute dust emission. In order to predict the FIR dust emission from the objects in our sample, we exploit a relation between the UV spectral slope (β; defined as $f_\lambda \propto$

λ^{β} by Calzetti *et al.* 1994) and the infrared excess (defined as the ratio of FIR flux to UV flux) detailed in Meurer *et al.* (1997; hereafter M97). This relation is shown in Figure 1 of M97, with the infrared excess increasing exponentially with the spectral slope. This relation is due to dust reddening of the spectral slope (β becoming less negative). Larger quantities of dust will increase the amount of UV extinction, increasing the amount of flux re-emitted in the FIR.

Since we have obtained estimates of dust in our previous studies, we could use our derived extinction values to estimate the FIR flux. However, not all objects are able to be detected in the observed IR, especially at higher redshift. These IR data are necessary to break the aforementioned degeneracy of red colors due to dust or old stars. We aim to predict FIR fluxes independent of stellar population modeling results, with the goal that our method can be applied to objects which only have detections in the optical or NIR.

To use the M97 relation, we first require the UV spectral slope for all objects in our sample, which usually requires spectra. However, in M97, the authors detail a method of obtaining β from the broadband V and R magnitudes. Unfortunately, this relation is only valid for z $\sim$ 3, but HMR08 compute similar relations for z $\sim$ 4 and z $\sim$ 5 – 6. For objects in our sample with z $\leq$ 4.5, we computed β via:

$$\beta = 5.65 \times (i' - z') - 2 \tag{10}$$

and for objects with z $>$ 4.5, we computed β via:

$$\beta = 2.56 \times (J - H) - 2 \tag{11}$$

14 of the 24 objects in our sample were calculated to have $\beta \geq$ -2.5, indicating that the dust in these galaxies is contributing significantly to their FIR fluxes. Table 11 details the relevant parameters for each object in our sample, including the UV spectral slopes calculated with the above method.

Once β is calculated, we use the relation from M97 to compute the FIR flux from the UV flux (defined in M97 as the flux at 2320 Å). First, we used the continuum slope calculated in equation 5.1 or 5.2, and then from the definition of continuum slope (see above), we calculated the UV flux via:

$$F_{UV} = f_{\lambda,z} \cdot \left(\frac{[2320 \cdot (1+z)]^{\beta+1}}{9200^{\beta}} \right) \tag{12}$$

where $f_{\lambda,z}$ is the z' flux density in units of f_λ and 9200 Å is the central wavelength of the z' filter. To find F_{FIR}/F_{UV}, we fit an exponential function to the dashed line in Figure 1 of M97. The equation of this line was:

$$\frac{F_{FIR}}{F_{UV}} = 66.3 \cdot e^{1.41 \cdot \beta} - 1.92 \tag{13}$$

This equation accurately matched M97's Fig. 1 over the range of -2.5 $< \beta <$ 4. While some objects in our sample did have $\beta <$ -2.5, these objects will have a very small F_{FIR}/F_{UV} ratio, and thus the emission from their small amount of dust will very likely not be detectable.

In order to obtain the FIR flux densities at a few representative wavelengths, we used equation 10 from M97, which details how the FIR flux is composed of the flux densities at 60 μm and 100 μm (in Jy):

$$F_{FIR} = 1.26 \times 10^{-11} (2.56 f_{60} + f_{100}) \text{ erg s}^{-1} \text{ cm}^{-2} \tag{14}$$

To independently calculate f_{60} and f_{100}, we require a second equation relating these two parameters. We used a template SED from Bendo *et al.* (2006), who computed the best-fit modified blackbody curve to NGC 4631, an edge-on Sd galaxy (a reasonable local analog to LAEs). They found that a simple blackbody modified by a $\lambda^{-1.2}$ term[11] (Eqn. 5.6), with a dust temperature of 28 K, fit their observed data points from ~ 10 – 1000 μm.

$$B_\nu(T) \propto \frac{2h\nu^3}{c^2} \frac{1}{e^{h\nu/kT} - 1} \left(\frac{c}{\nu}\right)^{-1.2} \tag{15}$$

Adopting an SED of this form and T = 28 K, we calculated a ratio of f_{100}/f_{60} of 3.64. Using this in combination with Eqn. 5.5, we found:

$$f_{60} = \frac{F_{FIR}}{1.26 \times 10^{-11}(2.58 + 3.64)} \text{ Jy} \tag{16}$$

5.4. Results

While we know the rest-frame 60 μm flux for the objects in our sample, we also would like to know how their FIR flux changes with wavelength. To do this, we scaled the Bendo *et al.* modified blackbody function up to the value of the 60 μm flux for each object (redshifted to the redshift of the object), so that we could see how their fluxes behaved at all wavelengths in the range of interest. We can then compare the flux densities of these objects at any FIR wavelength to the sensitivities of sub-mm instruments to see if an object will be detected.

With the ALMA sensitivity calculator[12], we computed ALMA sensitivity curves using the default set of parameters for an integration time of four hours in bands 8

[11] This modification is an emissivity law, which comes from physical models for the FIR absorption by small particles (e.g., Draine 2004).

[12] Available online at: http://www.eso.org/projects/alma/science/bin/sensitivity.html

TABLE 11
PROPERTIES OF LAES IN THE SAMPLE

Name	Redshift	β	f_{UV} (10^{-20} erg s^{-1} cm^{-2})	f_{60} (μJy)	f_{100} (μJy)	Dust Detectable? (Y/N)
CHa-1	4.40	-3.46 ± 1.14	1.84	—	—	N
CHa-2	4.40	-2.50 ± 0.75	3.41	0.178	0.648	N
CHa-3	4.40	-2.90 ± 0.81	2.76	—	—	N
CHa-4	4.40	-1.21 ± 0.68	10.46	169.1	615.4	Y
CH8-1	4.47	-0.35 ± 1.18	3.97	248.1	903.2	Y
CH8-2	4.47	-2.67 ± 0.25	5.13	—	—	N
CS2-1	4.53	-2.22 ± 0.57	2.96	4.733	17.23	N
CS2-2	4.53	-0.52 ± 0.97	2.65	129.7	472.2	Y
CS2-3	4.53	1.52 ± 1.23	8.44	7784	28333	Y
CS2-4	4.53	-1.14 ± 2.37	0.65	12.05	43.87	Y
CS2-5	4.53	-4.70 ± 1.37	0.32	—	—	N
CS2-6	4.53	-0.10 ± 2.46	1.37	125.3	456.1	Y
CS2-7	4.53	-0.74 ± 0.65	11.95	419.3	1526	Y
CS2-8	4.53	-1.65 ± 1.94	0.44	3.296	12.00	N
CS2-9	4.53	-2.66 ± 1.58	0.70	—	—	N
631	4.00	-2.34 ± 0.18	2.28	1.779	6.477	N
712	5.20	N/A	0.747	—	—	N
4442	5.76	-4.94 ± 5.39	0.145	—	—	N
5183	4.78	-0.75 ± 0.88	0.327	11.80	42.97	Y
5225	5.42	-3.61 ± 0.45	3.422	—	—	N
6139	4.88	-2.03 ± 0.49	4.191	13.63	49.61	Y
9040	4.90	-1.87 ± 0.67	3.093	15.27	55.58	Y
9340	4.71	N/A	0.521	—	—	N
9487	4.10	-2.62 ± 0.33	0.822	—	—	N

NOTES.—Objects with $\beta <$ -2.5 were not able to have their FIR excess derived via the Meurer relation, and thus we do not tabulate their fluxes at 60 and 100 μm (with such a steep slope, they likely would not have detectable dust emission).

(385 – 500 GHz) and 9 (602 – 720 GHz). Continuum measurements are possible with ALMA in 8 GHz instantaneous bandpasses, corresponding to a bandpass width of 14 μm at 730 μm (Wilson 2007). We thus chose three windows in which to compare our objects to the ALMA sensitivity curves: 450, 610 and 730 μm. The average sensitivity in an 8 GHz band-width across these three bandpasses are plotted as thick black lines in Figure 19. From the relative positions of these sensitivities to the SED curves from our objects in this figure, we can see which objects will have their dust emission detected with ALMA.

5.4.1. *Lyman Alpha Galaxies*

Out of the fifteen objects in the CDF-S sample, Figure 19 shows that seven of them appear to contain enough dust to be detected in the observed sub-mm. These seven objects, CHa-4, CH8-1, CS2-2, CS2-3, CS2-4, CS2-6, and CS2-7, contain dust in a range A_{1200} = 1.0 – 4.5 mag. One of these, CS2-3, which was best fit by A_{1200} = 4.5 mag, has the brightest f_{100} data point (28333 μJy) in the whole sample, further proof that our derivation of FIR fluxes is consistent with our model fitting. Objects CHa-1, CHa-3, CH8-2, CS2-5 and CS2-9 have $\beta <$ -2.5, thus we did not calculate their FIR fluxes. Objects CHa-2, CS2-1 and CS2-8 do have measurable 60 μm fluxes (0.2 – 4.7 μJy), but these are likely too faint to be detectable. It is of note that CS2-4 is only detectable in the 730 μm band.

Three of the GRAPES LAEs which we analyzed appear to be bright enough in the FIR to be seen with ALMA, although only in the 730 μm band. These objects

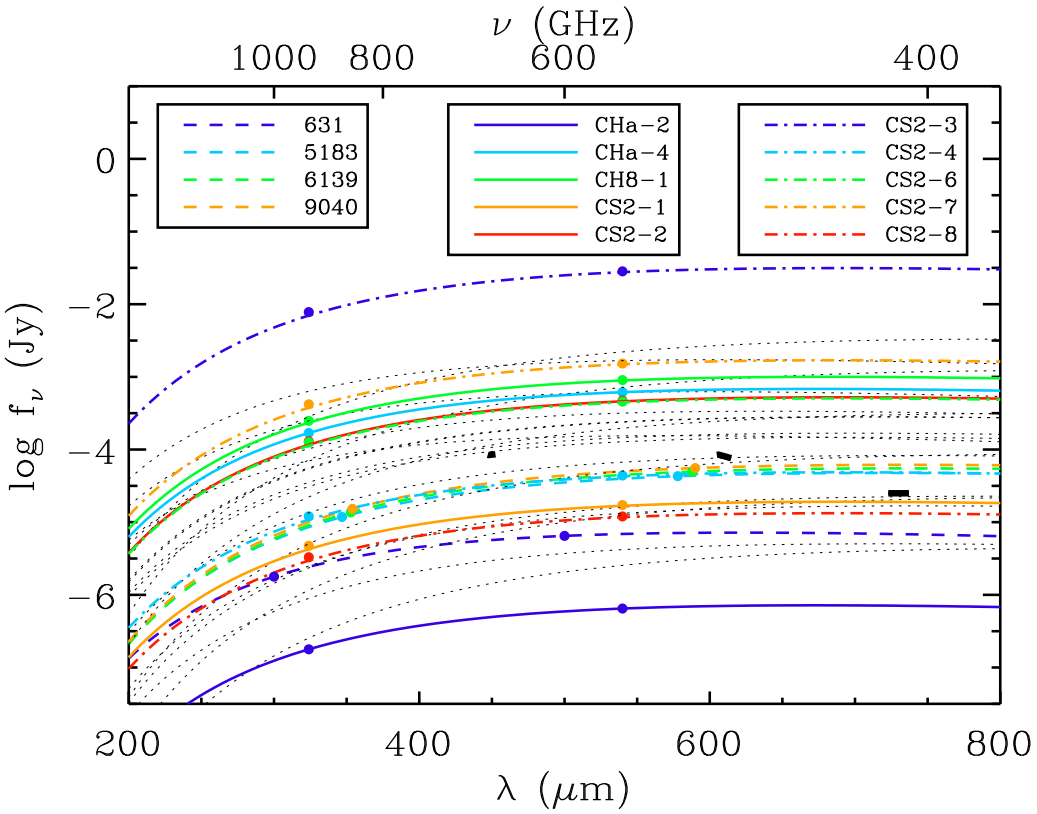

FIG. 19.—Derived FIR SEDs versus observed wavelength of our objects, with six LAEs being shown in the plotted range. The different colored lines show the LAEs, while the dashed gray lines show the SEDs of the sample of LBGs. The curves were derived by scaling the computed 60 μm flux point to a modified blackbody curve (Bendo *et al.* 2006). The FIR fluxes of these objects were computed via the relation between the UV spectral slope and FIR excess from Meurer *et al.* (1997). The thick black lines show the ALMA sensitivities in a four hour integration, in three windows at 450, 610 and 730 μm. Out of the whole sample, ten LAEs (13 LBGs) would have their dust emission detected in a 4 hour ALMA integration.

are 5183, 6139 and 9040. In Pirzkal *et al.* (2007), object 5183 has a maximum dust extinction[13] of $A_V = 0.6$ magnitudes (equivalent to $A_{1200} \sim 2.4$), and object 6139 is best fit by 0.4 magnitudes of dust extinction. This is consistent with our results, which imply that the UV light absorbed by this dust is being re-radiated in the FIR. While object 9040 was not best fit by any dust, the authors do acknowledge that its best-fit model was still a poor fit, although they are confident that it is a LAE at its measured redshift.

5.4.2. *Lyman Break Galaxies*

Figure 19 also plots the derived FIR SEDs of the sample of 21 LBGs. Dust emission from 11 of the LBGs is detectable at 450, 610 μm and 730 μm, with two additional LBGs being detectable at only 730 μm. In a rough comparison between LBGs and LAEs, we calculate that 42% of our 24 LAEs are detectable with ALMA, compared with 62% for LBGs. While these numbers may be consistent given the relatively small sample sizes, it could be indicative of a larger difference between the types of objects. Traditionally, LBGs are thought to harbor more evolved and more massive stellar populations than those in LAEs. From this result, we also see that LBGs may also have a higher dust content than LAEs. This is confirmed by the average β of the two samples, which indicates that LBGs have a redder UV slope with $\langle\beta_{LBG}\rangle$ = -1.62, compared with $\langle\beta_{LAE}\rangle$ = -1.97. A similar effect was seen in Vanzella *et al.* (2006), who found $\langle\beta_{LBG}\rangle$ = -1.7 and $\langle\beta_{LAE}\rangle$ = -2.1, as well as in Pentericci *et al.* (2007), who found that LBGs were dustier than LAEs. This is interesting, given

[13]This value of dust extinction is the maximum amount of extinction present in this object, because the models were fit to this object using upper limit constraints on the rest-frame optical fluxes.

that in Chapter 4 we found that our sample of LAEs had much higher dust extinction rates than we would have thought. Thus, while LAEs appear to have some amount of processed ISM, the ISM of LBGs appears to be much more enriched, resulting in higher dust emission in the FIR.

5.4.3. *Robustness of Results*

We have chosen a value of $f_{100}/f_{60} = 3.64$ from Bendo *et al.* (2006), which corresponds to a dust temperature of 28 K. However, there is a large uncertainty in the FIR color which we have chosen. Larger values of f_{100}/f_{60} imply a cooler ISM (thus a cooler dust temperature), while smaller values imply a warm ISM, more consistent with compact star formation (Dale *et al.* 2001). Dale *et al.* (2001) and Dale and Helou (2002) compute model FIR SEDs assuming a large range in FIR color, from $0.8 < f_{100}/f_{60} < 3.3$, with the smaller values corresponding to warmer ISMs. Since LAEs are expected to be undergoing significant bouts of star formation, and they are quite compact (e.g., Pirzkal *et al.* 2007), it is interesting to see how our derived FIR SEDs would change if we assume a warmer value of f_{100}/f_{60}. The observations presented in Dale & Helou (2002) show that the number of objects drops off considerably below $f_{100}/f_{60} = 1$, so we assumed $f_{100} = f_{60}$, and redid our calculations. Figure 20 shows these results for CS2-2, which was one of the fainter LAES which was detected in all ALMA bands. Since warmer FIR SEDs will result in fainter fluxes in the ALMA observable range, this plot can give us an idea of the limits on our predicted fluxes.

We find that although the shape of the SED has changed as expected, it does not affect the results for this particular object. However, since the peak of the dust

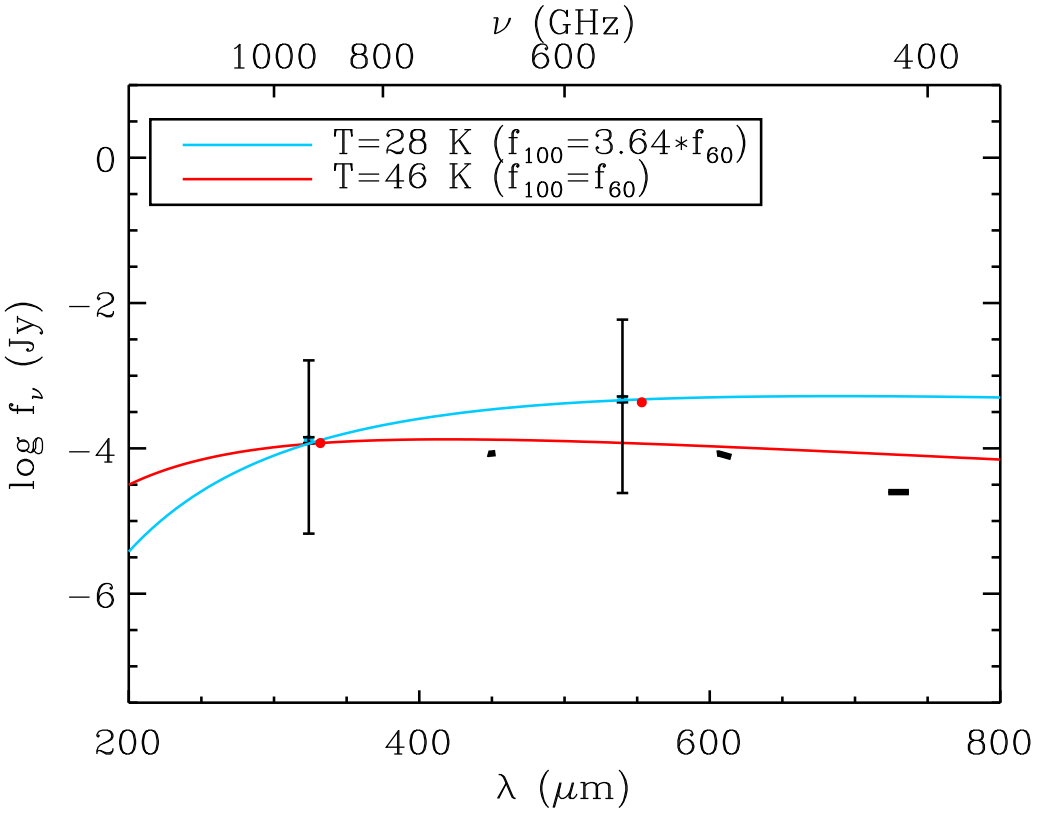

FIG. 20.—Same plane as Figure 19. The blue line plots the predicted rest-frame FIR SED for CS2-2. The literature shows that the temperature of the SED depends on whether the star formation proceeds in compact or widespread environments. We thus show (in red) our predictions if we assumed a warmer SED, with T = 46K. The change in temperature does not radically alter our results, although it does move the peak of the dust emission towards lower wavelengths. This can affect our results when an object is only detected in the reddest ALMA band. We also show the derived errors on our original SED, obtained from the i' and z' photometric errors. The tiny error bars inside the photometric errors are the errors derived from the scatter in the M97 relation (Meurer *et al.* 1999).

emission has moved toward shorter wavelengths, objects which were only detected in the 730 μm band may be less likely to be detected if they have a warmer SED. As another illustration of our uncertainties, we have plotted the 1 σ errors on our original predicted 60 and 100 μm fluxes, obtained from the photometric i' and z' errors. We also plot error bars derived from the uncertainty in the M97 relation, as described in Meurer *et al.* (1999; 0.04 dex uncertainty in $\log(F_{FIR}/F_{UV})$). These errors are much smaller than the photometric errors, although the photometric errors do show moderate uncertainty, thus it is worth deeper investigation into the extent which the photometric errors can alter our results.

Using equations 5.1 – 5.7, we can calculate the dust emission from any object given a z' magnitude and a color ($i' - z'$ for redshifts less than 4.5, and $J - H$ for redshifts greater than 4.5). Figure 21 and Figure 22 show these results at 730 μm, with contours showing the flux levels for any color-magnitude combination, and one contour specifically showing the ALMA 4 hour sensitivity at 730 μm. Figure 21 plots all objects in our whole LAE+LBG sample with z $\leq$ 4.53. The mean redshift of this subsample is 4.33, so the flux curves were derived for this redshift. Figure 22 plots all objects with z $>$ 4.53, with the flux curves derived for the mean redshift of this subsample, which was 5.26.

The different colored circles represent the three different samples (CDF-S LAEs, HUDF LAEs, and HUDF LBGs), with filled circles representing objects we found that would be detectable with ALMA via Figure 19. All filled circles lie above the ALMA 4 hour sensitivity contour (black line), showing that Figure 19, Figure 21 &

Figure 22 are mutually consistent, although the three detectable HUDF LAEs do lie less than 1 σ above the ALMA 4 hour sensitivity contour. Using these figures, one could then take the color, magnitude and rough redshift of any object, and determine if the dust emission could be detected depending on whether the points lie above the ALMA sensitivity contour.

Figure 21 & Figure 22 also allow us to examine the robustness of our results, since we have included the 1 σ errors on our objects fluxes. We can thus see how close our objects are to the ALMA sensitivity limit as a function of their photometric errors. While 42% of the LAEs will have their dust emission detectable, only 21% (5/24) of them lie more than 1 σ from the ALMA sensitivity contour. Likewise, for LBGs, only 33% lie more than 1 σ from the ALMA 4 hour sensitivity contour. However, some objects which lie below the ALMA contour are less than 1 σ away. Thus, we can define a maximum percentage of objects with detectable dust emission, including not only those above the line, but those that are below but within 1 σ. We find this to be 63% for LAEs and 81% for LBGs. This allows us to put an error bar on our LAE ALMA detection fraction, of 42 $\pm$ 21 % (likewise 62 $^{+19}_{-29}$ % for LBGs).

While the FIR – β relation was derived at low redshift, both Seibert, Heckman & Meurer (2002) and Reddy & Steidel (2004) find that it also applies at high redshift. In addition, Teplitz *et al.* (2006) found that when they compared far-UV to *Spitzer* observations, the results were in general agreement with the FIR – β relation. Chapman *et al.* (2005) have investigated this relation using a sample of sub-millimeter selected galaxies at z $\sim$ 2. The authors conclude that the bolometric luminosity of

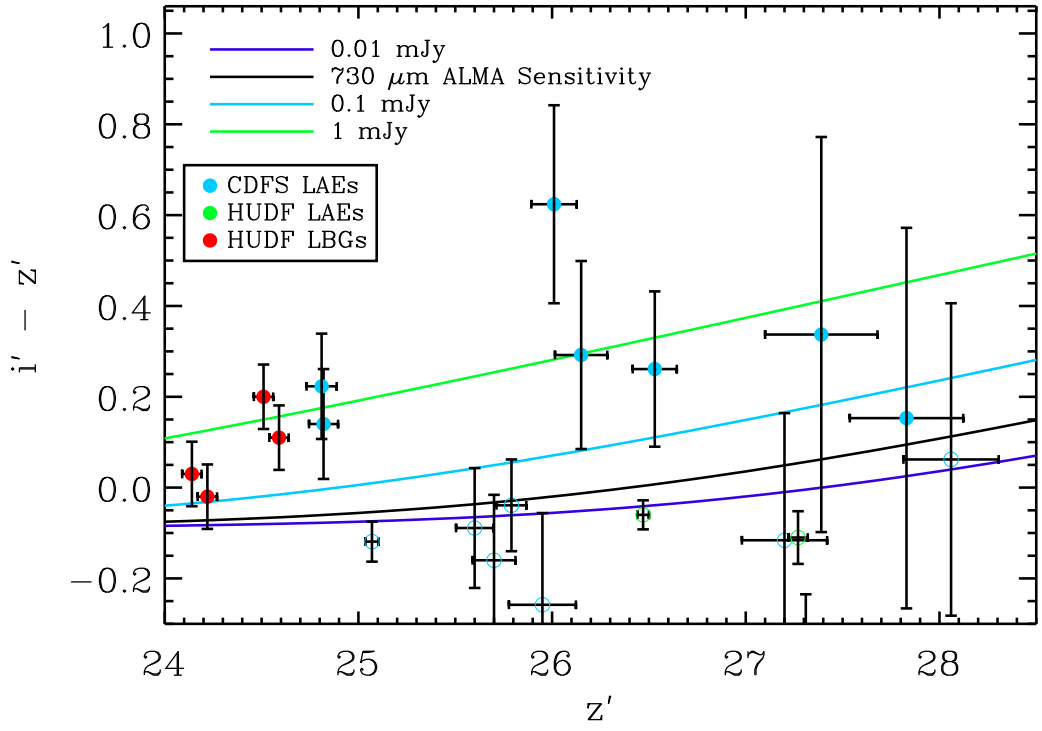

FIG. 21.—A color-magnitude diagram, depicting the position of all objects with z $\leq$ 4.5. Filled circles represent objects which would be detected with ALMA at 730 μm (and possibly also at 450 and 610 μm), with open circles representing those objects which would be undetected (based on Figure 19). Blue circles represent the CDFS LAEs, while green denotes the HUDF LAEs and red the HUDF LBGs. The contours show the observed fluxes at 730 μm for a computed grid of magnitudes and colors ($i' - z'$). The black contour shows the 4 hour ALMA 730 μm sensitivity limit. The contours were all computed for z = 4.33, which is the mean redshift of all objects in our sample at z $\leq$ 4.5. The error bars on the data points are the 1 σ errors.

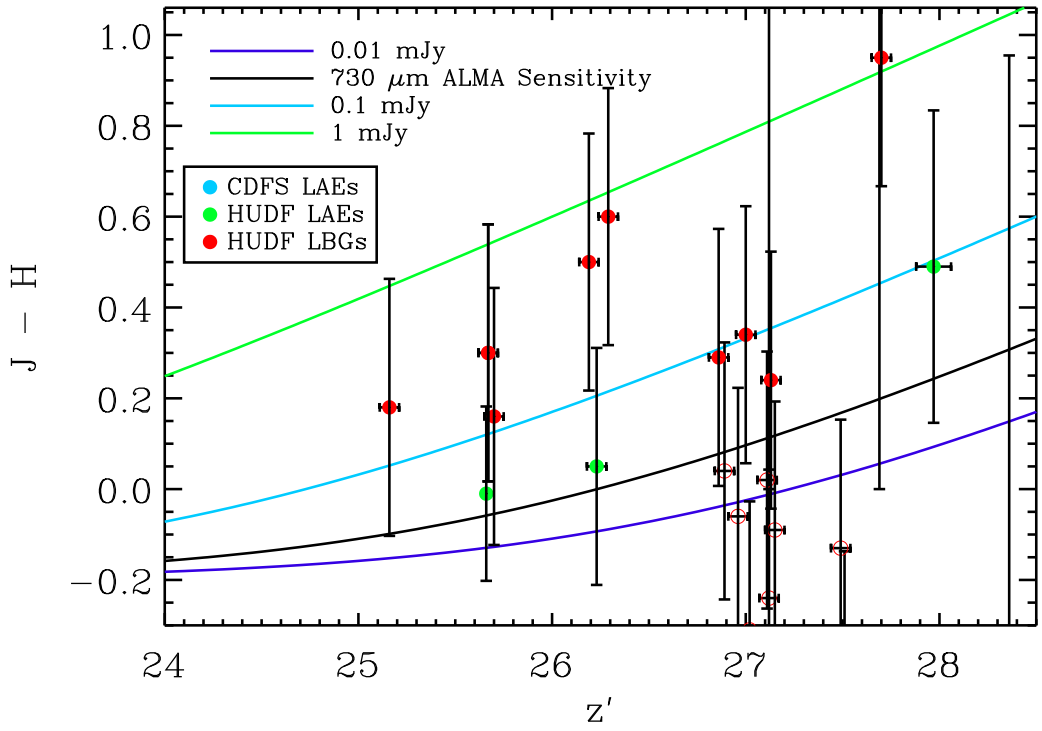

FIG. 22.—The same as Figure 21, for all objects with z > 4.5, thus the color is J - H. The contours were all computed for z = 5.26, which is the mean redshift of all objects in our sample at z > 4.5.

sub-millimeter galaxies are underestimated by 2 orders of magnitude when derived from their UV properties. This indicates that our derived FIR fluxes may be lower limits, implying that we could be underestimating the detection fraction.

However, Reddy *et al.* (2006) found that the M97 relation may not apply to all star-forming galaxies at z $\sim$ 2. They find that galaxies with derived ages $<$ 100 Myr exhibit a smaller FIR excess than that predicted by the M97 relation, indicating that these young galaxies have redder UV colors for a given amount of dust extinction that older galaxies. This is of concern as most of our LAEs have very young derived stellar population ages. In addition, Baker *et al.* (2006) find that the M97 relation also over-predicts the FIR flux for the gravitationally lensed LBG cB58. However, there are differences between these objects and LAEs, as they are at a lower redshift, and they are continuum selected. We thus cannot know if the same age dependence will apply to LAEs until we obtain a statistical sample of rest-frame FIR detections of LAEs. In addition, the Reddy *et al.* figure which illustrates the age discrepancy does not have error estimates on their young object points, thus it is hard to discern how significant this effect is. Baker *et al.* do show error bars, and these errors imply that their observations are only off the M97 relation by $\sim 1\ \sigma$.

If young objects do have systematically lower F_{FIR}/F_{UV} ratios, it would be worrying, as it could imply that we are over-predicting the FIR fluxes of our LAEs by as much as an order of magnitude. It is thus prudent to apply our results to any relevant observations to see if our FIR flux predictions are accurate. Although very few galaxies with Lyα emission have been detected in their rest-frame FIR, Capak *et*

al. (2008) have recently published a study of a spectroscopically confirmed millimeter starburst galaxy, which does exhibit Lyα emission. They publish the observed SED of this galaxy from X-rays to radio wavelengths. Using the published optical magnitudes, we can compute β, and predict the FIR flux. Doing this, we calculate a predicted 554 (rest 100) μm flux of 2637^{+5049}_{-1875} μJy. The closest point in the observed SED is at 1.1mm, at 4800 ± 1500 μJy. These observations are consistent with our calculations. Although this is an admittedly small sample size, it does give evidence that despite claims in the literature about over- or under-predicting FIR fluxes, our predictions do match observations. We show the SED from Capak *et al.* along with our predictions for this object in Figure 23.

While we believe that our calculations are consistent with the true FIR flux, it is still worth investigating the dependence of our results on these derived FIR fluxes. To do this, we reduced our FIR flux to be 50% of its derived value, and computed the ALMA detection fraction of both types of objects. We calculated a detection fraction of 25% for LAEs and 62% for LBGs (54% and 76% for LAEs and LBGs respectively within 1σ of the ALMA contour). Thus, while we believe that the M97 relation is applicable to our objects, we find that our conclusions are robust to a factor of two variation in their true FIR flux.

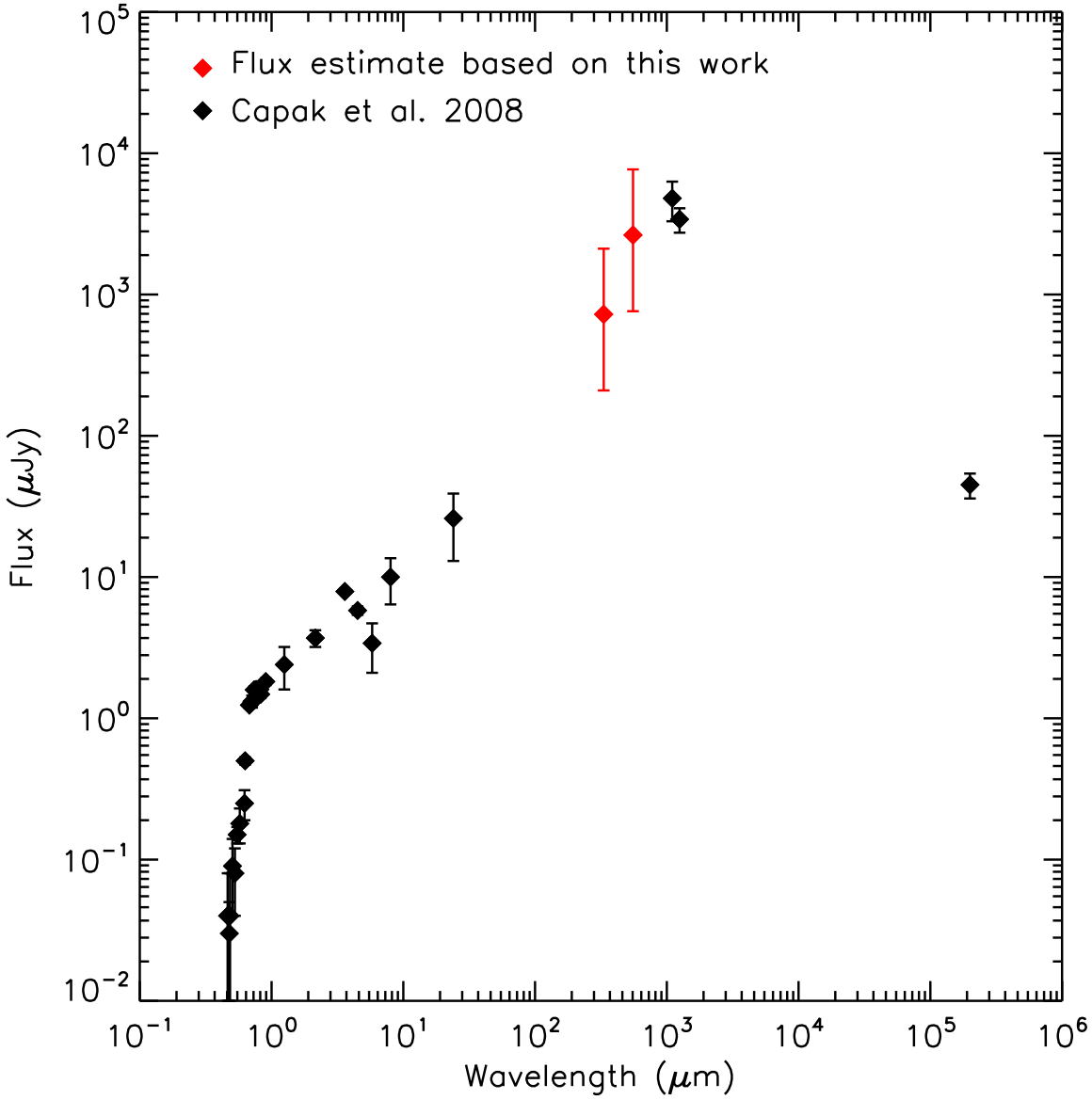

FIG. 23.—In this figure we plot the SED from Capak *et al.* (2008) for a millimeter detected Lyα emitting starburst galaxy, spectroscopically confirmed to lie at z=4.547. Our predicted FIR fluxes match up well with the observed SED, providing further evidence that the Meurer relation is applicable at high redshift.

5.5. Conclusions

Directly observing dust emission from Lyα galaxies will provide undeniable proof that these earliest of galaxies have undergone some enrichment of their ISM. While these observations are currently difficult, we have been able to predict whether a sample of 24 LAEs would be detected with a future sub-mm observatory such as ALMA based on their optical and NIR fluxes. Exploiting a relation from Meurer *et al.* (1997), which relates the far-infrared excess to the UV continuum slope, we have derived the FIR fluxes from these LAEs, which will be primarily due to dust emission. By comparing these fluxes to the projected sensitivity of ALMA at 450, 610 and 730 μm, we conclude that 42% (10/24) of our sample of LAEs should be detectable with ALMA, based on their dust emission.

We perform the same analysis on a sample of 21 Lyman Break Galaxies, finding that 62% (13/21) of the LBGs are detectable with ALMA, or about 50% higher than the detection fraction of LAEs. This may be a function of our small sample size, or it may be the result of a true dichotomy in the dust contents of LAEs and LBGs, likely arising because LBGs are a more evolved class of high-redshift galaxies. In order to generalize our results, we computed the FIR fluxes for a wide range of continuum magnitudes and colors, comparing these fluxes to the ALMA 4 hour sensitivity limit. Thus, knowing the continuum magnitude and color of any object, one can then predict whether its dust emission will be detectable.

While stellar population modeling gives some insight on the amount of dust in high-redshift galaxies, future sub-mm instruments will allow us to directly observe the

dust emission from these objects, providing a more complete census of dust. From our analysis of LAEs and LBGs in the HUDF, we calculate a number density of ALMA detectable LAEs and LBGs of 0.26 arcmin^{-2}, and 1.13 arcmin^{-2}, respectively. Thus, even in a small ALMA survey area, one could expect to detect a number of high-redshift objects with ALMA in a reasonable amount of time. In our previous analysis of LAEs, the addition of the clumpiness parameter allows strong Lyα flux to come from an arbitrarily old and dusty galaxy, thus these ALMA observations will help to constrain the amount of dust, and thus the level of clumpiness.

These results will have considerable impact on several areas of galaxy evolution, specifically on the star formation history (e.g., Giavalisco *et al.* 1996), which, since it is derived from UV observations, is critically dependent on accurate measurements of the dust content. Combining ALMA with UV observations, we will have a complete map of star formation in high-redshift galaxies (i.e. Gao 2008). Studying the sub-millimeter emission of these objects will also allow calculation of the total dust mass, which is something one cannot calculate from UV-optical data alone. Along with learning about the total amount of dust in these objects, ALMA will give us the opportunity to investigate the distribution of dust due to its excellent resolution. At 730 GHz, ALMA can achieve resolutions down to 0.01″pix^{-1}. Combining ALMA observations with high resolution *HST* data will allow us to investigate dust on local scales at high redshift for the first time. Strong sub-millimeter detections combined with strong Lyα emission could indicate that dust enhancement of the Lyα EW is widespread.

6. STELLAR POPULATIONS OF Lyα GALAXIES AT z $\sim$ 0.3

6.1. Abstract

We present the results of a stellar population analysis of 30 Lyman alpha emitting galaxies (LAEs) at z $\sim$ 0.3, previously discovered with the *Galaxy Evolution Explorer* (*GALEX*). With a few exceptions, we can accurately fit model spectral energy distributions to these objects. We find an overall age and mass range of 4 Myr – 10 Gyr and 1.6×10^7 – 1.5×10^{11} $M_\odot$, respectively. These narrow to a range of 200 Myr – 8 Gyr and 9.3×10^8 – 1.5×10^{11} $M_\odot$ when we restrict ourselves to the 22 LAEs with $\chi^2_r < 10$. These results suggest that low-redshift LAEs are significantly different that those found at high redshift. We also find that these LAEs show a trend towards higher metallicity than those at high redshift, as well as a much tighter range of dust attenuation and dust geometry. These results represent the first time that the physical properties of non-local LAEs have been studied at z < 3, spanning a giant leap in cosmic time.

6.2. Introduction

Over the past decade thousands of Lyman alpha emitting galaxies (LAEs) have been discovered from $2.4 <$ z < 6.96. The discovery of these objects was highly anticipated, as it was predicted that strong Lyα emission would be a signpost of primitive galaxies in formation, and thus these objects could represent some of the first galaxies in the Universe (Partridge & Peebles 1967). Initial results were promising, as these objects appeared to be faint, compact, and exhibiting very large Lyα equivalent widths (EWs). In fact, the observed EW distribution had so many large EWs that it appeared that something other than a normal stellar population was producing this distribution (Kudritzki *et al.* 2000; Malhotra & Rhoads 2002; Finkelstein *et al.* 2007;

Dawson *et al.* 2007). This appeared to indicate that these objects were extremely primitive, as either a near-zero metallicity, or very top heavy initial mass function would be required to explain the sheer number of large EW LAEs.

However, with the new results coming from stellar population modeling, the identification of LAEs as primitive galaxies came into doubt. Numerous studies began to detect dust in LAEs, which is an indicator that a prior generation of stars has lived and died, thus making these objects not primitive (Chary *et al.* 2005; Lai *et al.* 2007; Pirzkal *et al.* 2007; Finkelstein *et al.* 2008ab). If they were not primordial, then another explanation was required to explain the large EWs observed, and this came in the form of dust. If the interstellar medium (ISM) in LAEs primarily consists of clumps of neutral hydrogen and dust in an otherwise empty medium, then it is possible that the Lyα EW will be enhanced over the value intrinsic to the star forming regions (Neufeld *et al.* 1991; Hansen & Oh 2006).

In Chapters 3 & 4 (Finkelstein *et al.* 2008ab), we demonstrated that dust enhancement from a clumpy ISM can help explain the SEDs of a sample of z $\sim$ 4.5 LAEs, with clumpy dust appearing to exist in 10 out of a sample of 15 LAEs. We also found plausible evidence for dust in every object in our sample, again suggesting that these objects are not primordial, although their derived metallicities were rather low (with half of the sample having Z $< 0.2\ Z_{\odot}$).

With these results, it then becomes interesting to study the evolution of LAEs as one goes to lower redshift. However, large samples of LAEs have only been detected down to z $\sim$ 3.1 (Gawiser *et al.* 2006a; McLinden *et al.* 2008 in prep), with a few

individual LAEs found as low as z $\sim$ 2.4 (Pascarelle *et al.* 1996ab; van Breukelen, Jarvis & Venemans 2005). Given the atmospheric ultraviolet (UV) cut-off at $\sim$ 3700 Å (as well as the loss of CCD quantum efficiency), detection of LAEs at z $\lesssim$ 2 is not possible from the ground. However, LAEs could be detected using the space-based UV telescope, *Galaxy Evolution Explorer* (*GALEX*), at z $\lesssim$ 1. Deharveng *et al.* (2008) recently published the discovery of 96 LAEs at $0.2 < z < 0.35$ via *GALEX* spectroscopy, using data from the publicly available *GALEX* GR2 data release. We present the results from a stellar population modeling analysis of 30 of these objects, with an emphasis on their differences from high-redshift LAEs.

In this paper we assume Benchmark Model cosmology, where $\Omega_m = 0.3$, $\Omega_\Lambda = 0.7$ and $H_0 = 0.7$ (c.f. Spergel *et al.* 2007). All magnitudes in this paper are listed in AB magnitudes (Oke & Gunn 1983).

6.3. Lyα Galaxy Sample

Deharveng *et al.* (2008; hereafter D08) recently published the results of a *GALEX* search for low-redshift Lyα emitting galaxies, which consisted of, among others, their positions, spectroscopic redshifts, Lyα line fluxes and EWs, and *GALEX* far-UV (FUV) and near-UV (NUV) broadband magnitudes. In order to compare these objects to stellar population models, we require optical broadband fluxes. We thus chose to take a sub-sample of the D08 objects, including only those that have extensive ancillary data. Specifically, we looked at objects in the Extended Groth Strip (EGS) and the Chandra Deep Field – South (CDF–S), both of which have extensive multi-wavelength public datasets.

The All-Wavelength Extended Groth Strip International Survey (AEGIS; Davis *et al.* 2007) covers the EGS from radio to X-ray wavelengths. We focused on optical data from the Canada-France-Hawaii Telescope Legacy Survey[14] (CFHTLS), which consists of broadband data covering one square deg. of sky (with seeing $\lesssim 1''$). The 5 σ limiting AB magnitudes of these data are: u' (27.2), g' (27.5), r' (27.2), i' (27.0) and z' (26.0). D08 publish the positions of 39 Lyα galaxies in the EGS, and we find that 30 of them fall in the CFHTLS survey area. We then use simple positional matching to locate the optical counterparts to the remaining 30 objects. One object had no nearby optical counterpart, so we exclude it from further analysis, leaving us with 29 objects. One would normally do this by picking a reasonable matching radius ($\sim 1''$), and selecting the closest object within that radius as the counterpart. However, this is difficult given that *GALEX* has a system spatial resolution of $4''$ and $5.6''$ FWHM in the FUV and NUV channels, respectively, and thus the *GALEX* positions can have high uncertainties (relative to typical ground-based seeing). To account for this, we use a much larger search radius ($7''$), and then visually inspect the results to be sure that we are selecting the correct optical counterpart. Figure 24 shows the results of this exercise, showing the CFHTLS i'-band image, with red circles denoting the *GALEX* positions (with a $5''$ diameter), green circles denoting all objects from the CFHTLS i'-band selected catalog ($2''$ diameter), and orange circles encompassing the

[14]Based on observations obtained with MegaPrime/MegaCam, a joint project of CFHT and CEA/DAPNIA, at the Canada-France-Hawaii Telescope (CFHT) which is operated by the National Research Council (NRC) of Canada, the Institut National des Science de l'Univers of the Centre National de la Recherche Scientifique (CNRS) of France, and the University of Hawaii. This work is based in part on data products produced at the Canadian Astronomy Data Centre as part of the Canada-France-Hawaii Telescope Legacy Survey, a collaborative project of NRC and CNRS.

green circle which we selected as the optical counterpart. In most cases, we see both red and orange circles centered around an object, however, in some cases the *GALEX* position is between two or more sources (object IDs 2682 and 17005), and in these latter cases we removed these objects from further consideration, leaving us with 27 EGS LAEs.

We performed a similar procedure in the CDF-S, this time using data from the Multiwavelength Survey by Yale-Chile (MUSYC; Gawiser *et al.* 2006b), which cover the Extended CDF-S to a 5 σ depth of 26.0, 26.9, 26.4, 26.4, 24.6 and 23.6 AB mag in the U, B, V, R, I and z' filters, respectively. Out of the 15 *GALEX* selected LAEs, we find that four are covered by the MUSYC data. Two of these have unambiguous optical counterparts, while a third has one bright object at the center of the *GALEX* beam, with another faint object near the edge of the beam. The fourth object has nothing at the center of the *GALEX* beam, with two objects at the edge. We thus kept the first three objects, while excluding the fourth one. Thus our final sample consists of 30 LAEs, 27 in the EGS and 3 in the CDF-S.

6.3.1. *Stellar Population Modeling*

Our motivation for this study was to learn about the stellar population ages and masses of low-redshift LAEs. To do this, we use the stellar population modeling code of Bruzual & Charlot (2003; BC03), combined with the method from Chapters 3 & 4 (Finkelstein *et al.* 2008ab). Briefly, we compute a grid of models, varying the metallicity, star formation history, stellar population age, and dust extinction (using the dust law of Calzetti *et al.* 1994). Lyα and $H\alpha$ emission are included using the

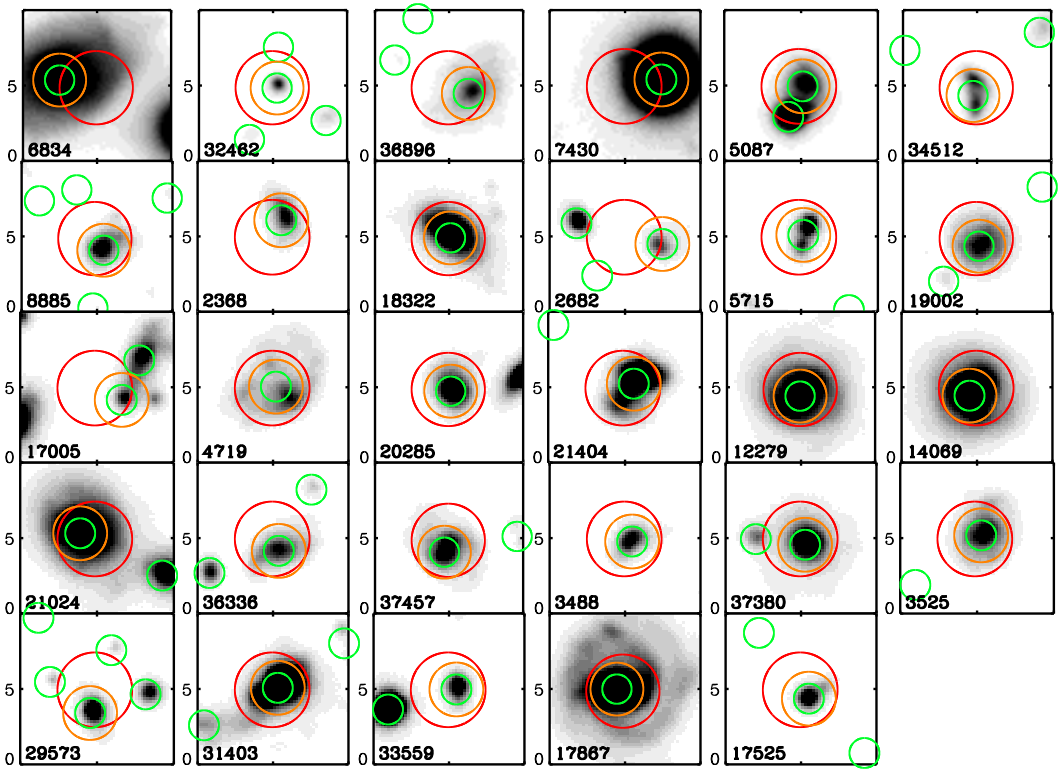

FIG. 24.—i'-band cutouts of the positions of the 29 LAEs in the EGS covered by the CFHTLS. Red circles are centered on the *GALEX* positions of these objects as published in Deharveng *et al.* (2008), with radii of 2.5″, comparable to the FWHM of the *GALEX* beam. Green circles denote all objects in the CFHTLS i'-band selected catalog. Orange circles are centered on the object selected by our matching code to be the optical counterpart. In the majority of cases, the red, orange and green circles form a bulls-eye, meaning that the *GALEX* beam is centered on the optical counterpart. In a few cases (2682 and 17005) the *GALEX* beam is near, but not encompassing, two or more objects. We remove these objects from our sample. This leaves us with 27 LAEs with matching optical counterparts in the EGS. We find another three LAEs with optical counterparts in the CDF-S from the MUSYC survey.

number of ionizing photons (output by BC03) and case B recombination. Various levels of interstellar medium clumpiness (i.e. Neufeld 1991; Hansen & Oh 2006; Finkelstein *et al.* 2008ab) are allowed by lowering the amount of dust attenuating Lyα relative to the continuum. The model spectra are then redshifted to the *GALEX* spectroscopic redshift of a given object (in redshift bins of 0.02), and attenuated by intergalactic medium (IGM) absorption via the Madau (1995) prescription. The best-fit model is then found via χ^2 minimization. See Chapters 3 & 4 for more extensive details on this process. We used the *GALEX* Lyα line fluxes, FUV and NUV fluxes for all objects[15], along with the optical broadband data discussed above.

6.4. Results

Table 12 tabulates and Figure 25 displays the best-fit models for each of our objects. Each page of Figure 25 shows the results for three objects. We gave our objects new identifiers, with CDFS1–3 representing the three LAEs in the CDF–S, and EGS1-27 the 27 LAEs in the EGS. The top row displays the best-fit single population model, while the bottom row displays the best-fit model allowing two separate bursts of star formation; one at 10 Gyr ago, and one at any time (see Chapter 4 for details). While the two burst model does allow for additional flexibility in the model fitting, it was ruled out by a large margin in most cases, only providing a vastly better fit to one object (EGS1).

During our initial model fitting, the lowest reduced χ^2 (χ^2_r) was still much greater than one, even though many of the best-fit models appeared to match the

[15]We used a standard error of 4×10^{-16} erg s^{-1} cm^{-2} for the line fluxes (from D08), and assumed a 20% error on the FUV and NUV broadband fluxes.

observations. We found that our flux errors were likely underestimated, as these objects are so bright, that their flux errors are rather small. To correct for this, we added a 5% systematic error into the χ_r^2 denominator, which allowed for the objects with the best fits to have χ_r^2 near to unity (Papovich et al. 2001). We attempted to rule out the possibility that any of these objects were AGN by examining X-ray data, where available (AEGIS *Chandra* data), to see if any of our objects were detected (none were). However, it is worth noting that EGS4 shows possible signs of AGN in its spectra with its very steep spectral slope. Also, the inability of the model to fit the *GALEX* NUV flux could indicate a possible emission line at that wavelength.

6.4.1. *Stellar Population Age and Mass*

From the single population fits, we find an age range of 4 Myr – 10 Gyr, with a median age of 1.4 Gyr. Correspondingly, we derive stellar masses from 1.6×10^7 – 1.5×10^{11} $M_\odot$, with the lowest masses corresponding to the youngest ages, as we would expect. The best fits of the two youngest objects, EGS2 and EGS25, are both of poor quality. This coupled with the fact that the next youngest object is 200 Myr old, lends doubt as to the conclusions which can be drawn from these two objects. In fact, even with our systematic error included, eight of the 30 objects still have χ_r^2 > 10. Excluding these objects, we find age and mass ranges of 203 Myr – 8 Gyr and 9.3×10^8 $M_\odot$ – 1.5×10^{11} $M_\odot$, respectively.

TABLE 12
BEST-FIT SINGLE POPULATION MODELS

Name	t_{pop} (Myr)	Mass (10^7 $M_\odot$)	Z ($Z_\odot$)	τ_{SFH} (yr)	A_{1200} (mag)	q	EW (Å)	χ^2_r	z
CDFS1	2000	454.2	0.005	10^8	0.60	0.25	200.3	5.61	0.22
CDFS2	227.3	608.9	2.5	10^7	0.50	0.50	87.74	7.57	0.37
CDFS3	2000	7691	0.2	10^8	2.50	1.50	37.94	2.37	0.22
EGS1	1800	7357	0.2	10^8	4.50	1.00	114.1	20.75	0.20
EGS2	4.0	1.6	0.2	10^5	0.30	0.00	202.2	75.47	0.21
EGS3	2000	320.0	0.2	10^8	0.90	1.00	114.7	8.48	0.21
EGS4	3000	14978	0.02	10^8	3.50	0.75	259.2	21.85	0.21
EGS5	1800	296.6	0.2	10^8	0.30	1.50	100.3	3.05	0.22
EGS6	286.1	93.9	0.2	10^7	0.80	0.50	148.2	3.10	0.24
EGS7	255.0	144.6	0.4	10^7	0.60	1.00	95.42	2.04	0.25
EGS8	360.2	128.5	0.2	10^7	0.40	0.25	135.6	2.91	0.24
EGS9	8000	4615	0.2	$4x10^9$	0.80	1.50	81.26	4.73	0.25
EGS10	227.3	120.3	0.4	10^7	0.60	1.00	95.50	0.78	0.25
EGS11	321.0	343.9	0.2	10^7	1.50	1.00	103.4	1.35	0.26
EGS12	360.2	365.3	0.2	10^7	0.80	0.75	123.8	1.79	0.26
EGS13	2000	636.9	0.02	$4x10^9$	1.25	1.50	67.56	2.80	0.26
EGS14	5000	4696	0.2	$4x10^9$	3.00	1.00	115.0	7.93	0.26
EGS15	10000	11348	0.4	$4x10^9$	1.50	1.50	53.99	10.75	0.27
EGS16	4500	6551	0.2	$4x10^9$	3.00	1.00	114.9	6.47	0.27
EGS17	3000	13670	0.4	10^8	2.50	1.00	103.9	15.10	0.27
EGS18	360.2	233.7	0.2	10^7	0.30	2.00	79.31	2.25	0.27
EGS19	2000	913.0	0.02	10^8	0.60	2.00	68.78	3.29	0.27
EGS20	321.0	167.9	0.02	10^7	0.50	1.00	103.0	0.90	0.27
EGS21	1800	1478	0.2	10^8	1.25	1.50	65.60	2.78	0.29
EGS22	1015.2	612.3	0.2	10^8	1.50	1.50	58.47	1.87	0.29
EGS23	202.6	130.9	0.2	10^7	0.90	1.00	104.1	1.58	0.29
EGS24	404.2	4344	0.02	10^7	4.00	0.50	617.9	10.45	0.31
EGS25	4.0	32.0	1.0	10^5	3.50	0.75	146.6	22.61	0.33
EGS26	1434	14506	1.0	10^8	3.00	1.00	92.29	5.60	0.35
EGS27	1278	513.2	0.4	$4x10^9$	0.00	0.00	103.4	234.12	0.46

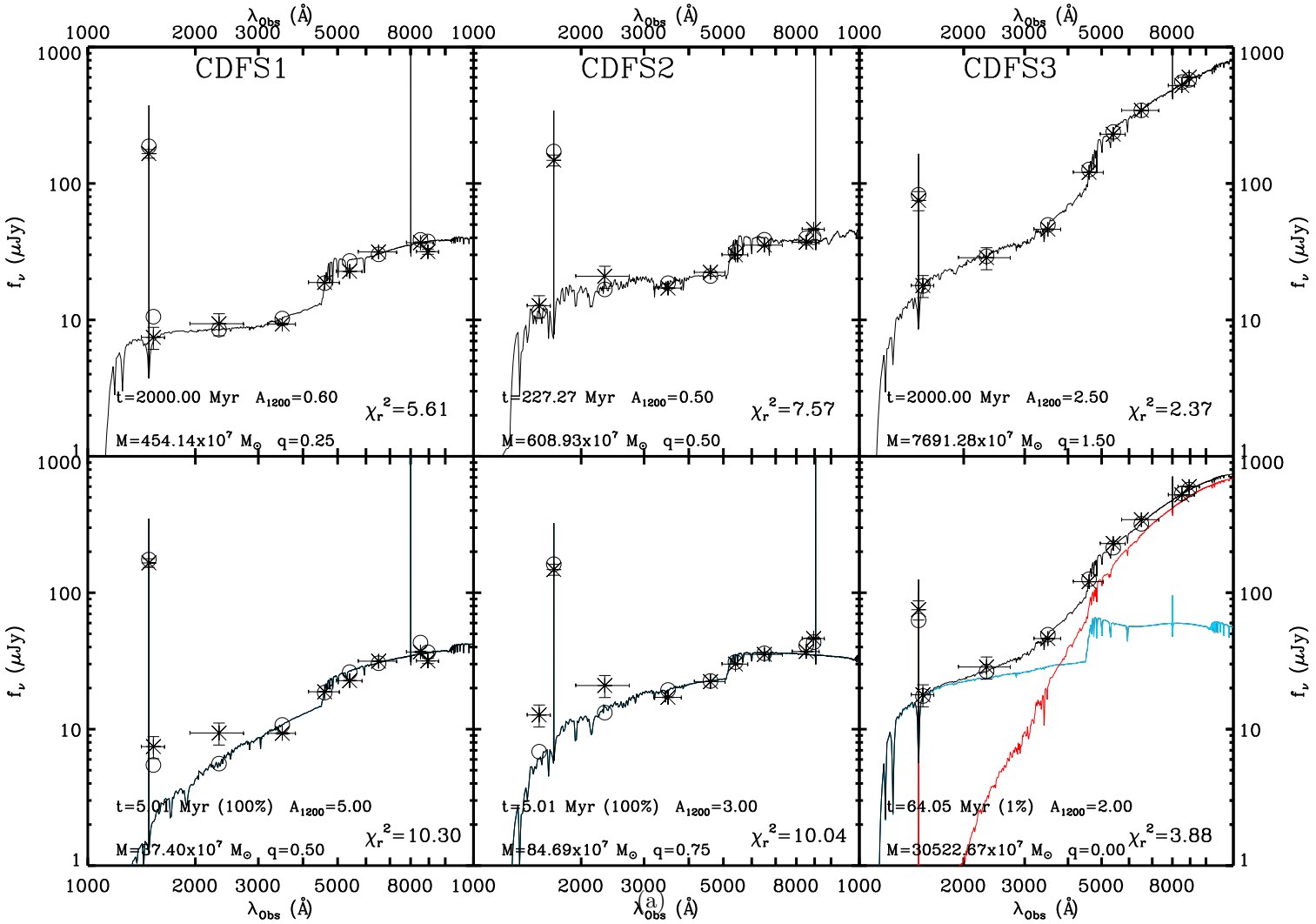

(a)

FIG. 25.—(a) The top row contains the best-fit single population models to the z ∼ 0.3 LAEs, with their observed SEDs over-plotted. The open circles represent the bandpass-averaged fluxes of the models. The second row plots the best-fit two-burst models to our objects. Objects with no mass in old stars can still have a worse fit than those in the top row, as they are forced to have a burst SFH.

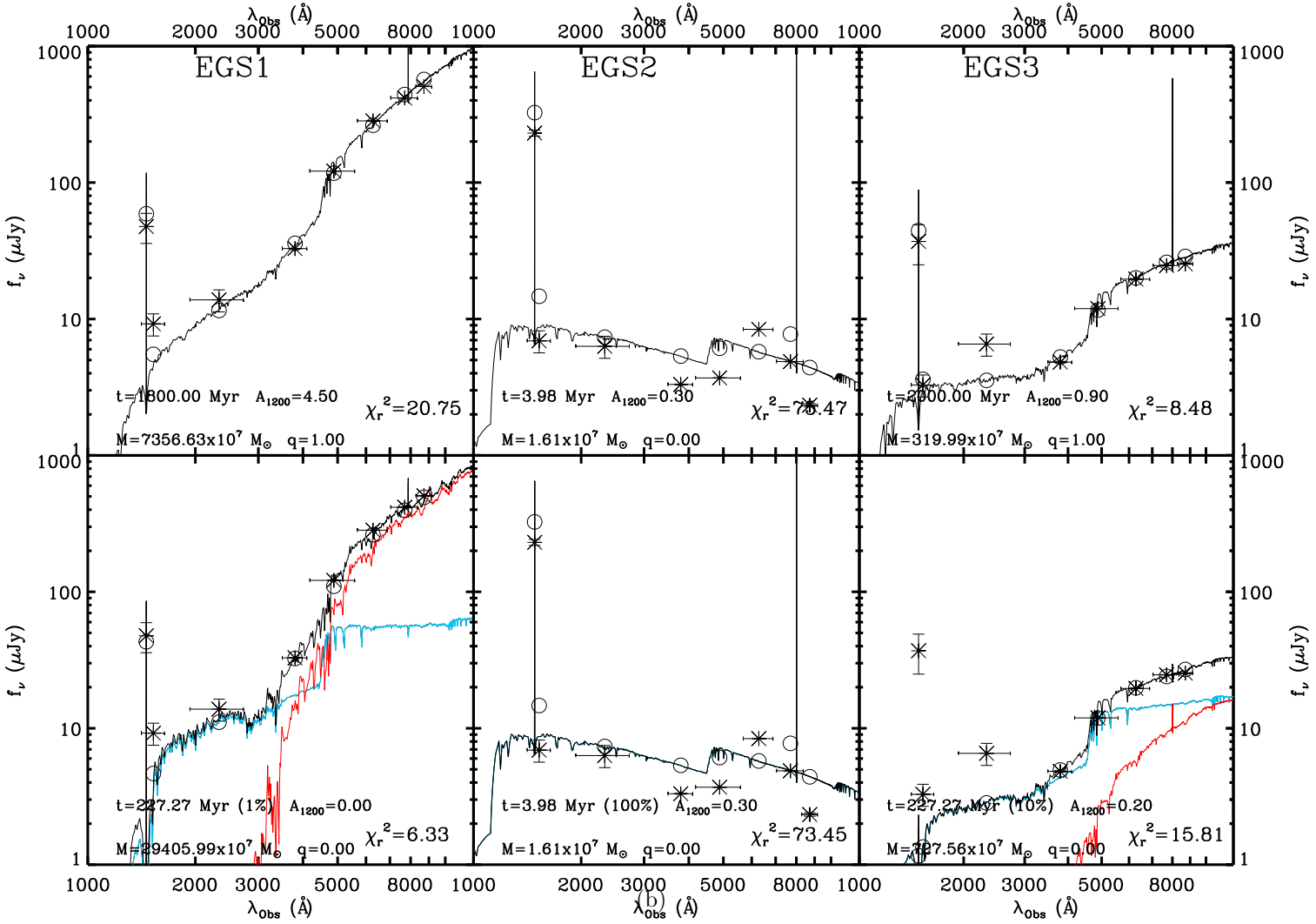

(b)

FIG. 25.—(b) Continued.

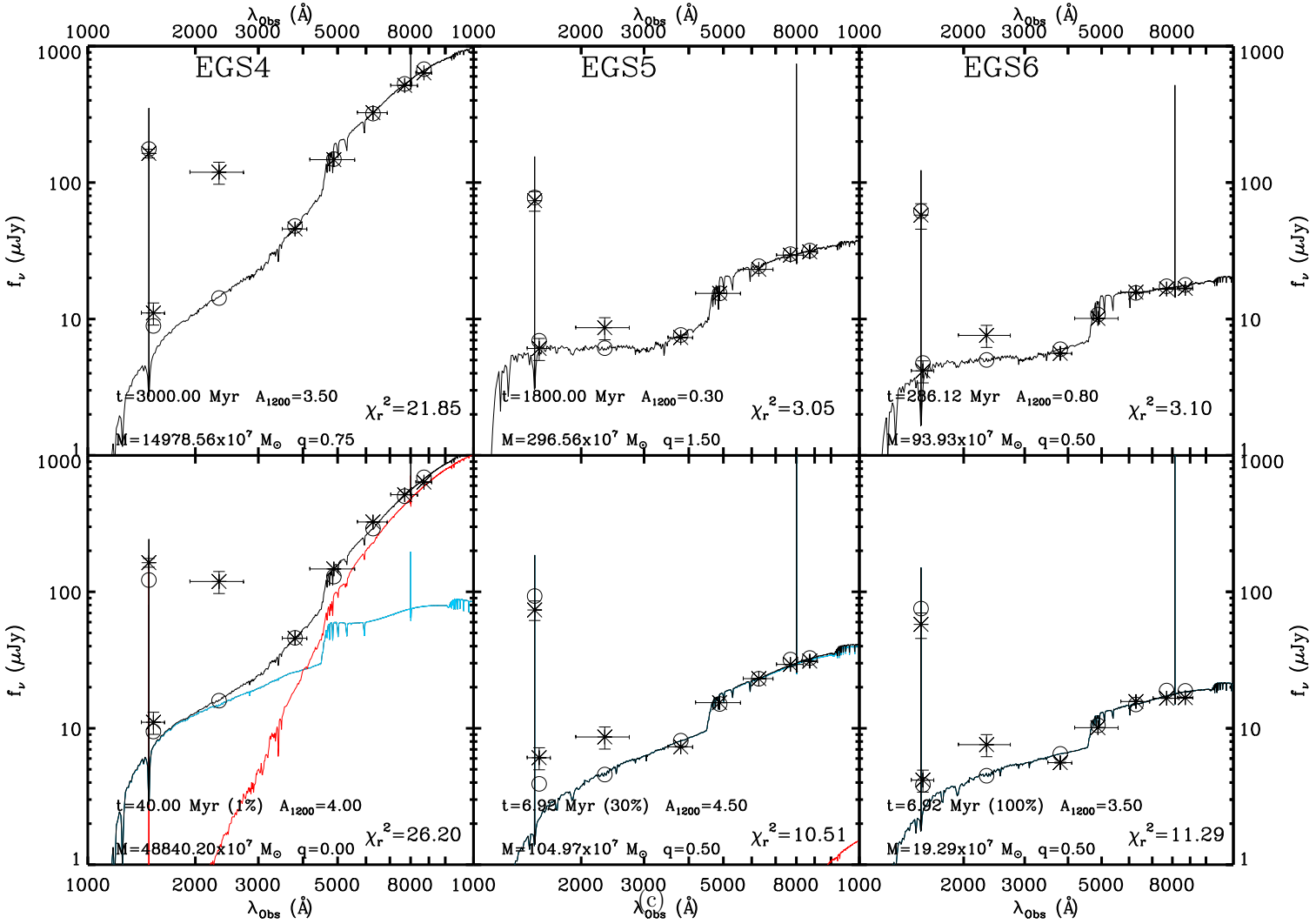

(c)

FIG. 25.—(c) Continued.

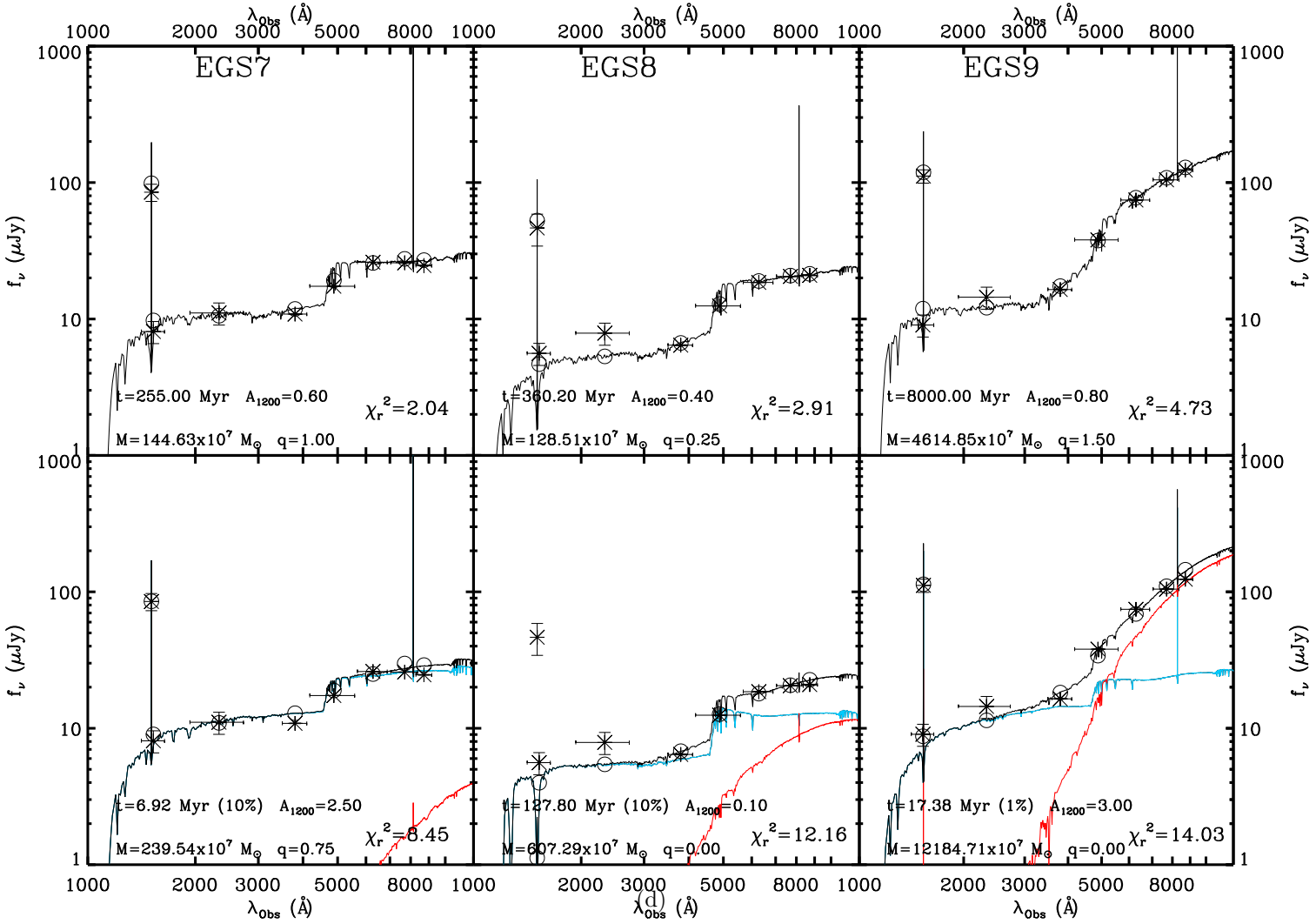

(d)

FIG. 25.—(d) Continued.

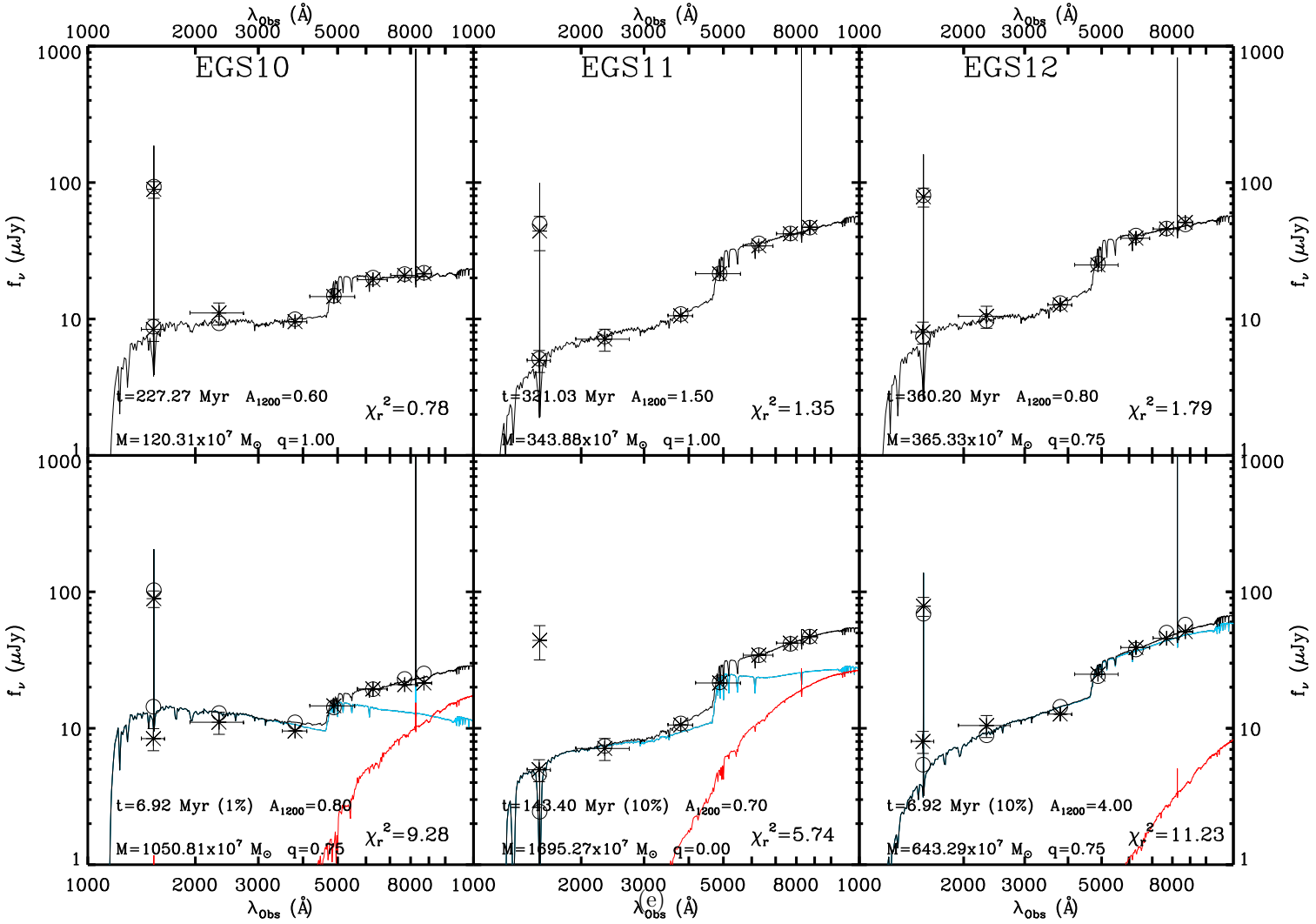

(e)

FIG. 25.—(e) Continued.

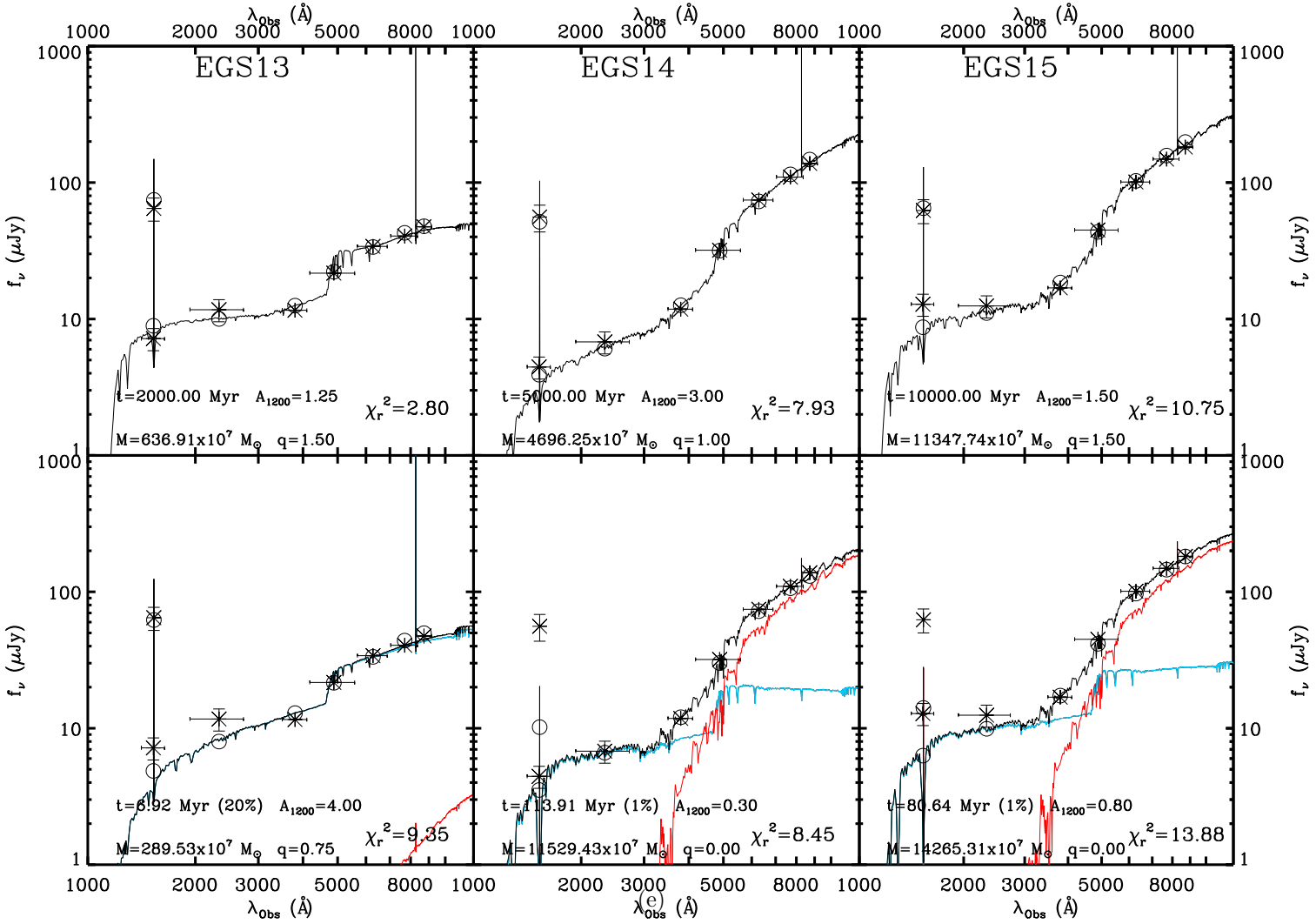

(e)

FIG. 25.—(f) Continued.

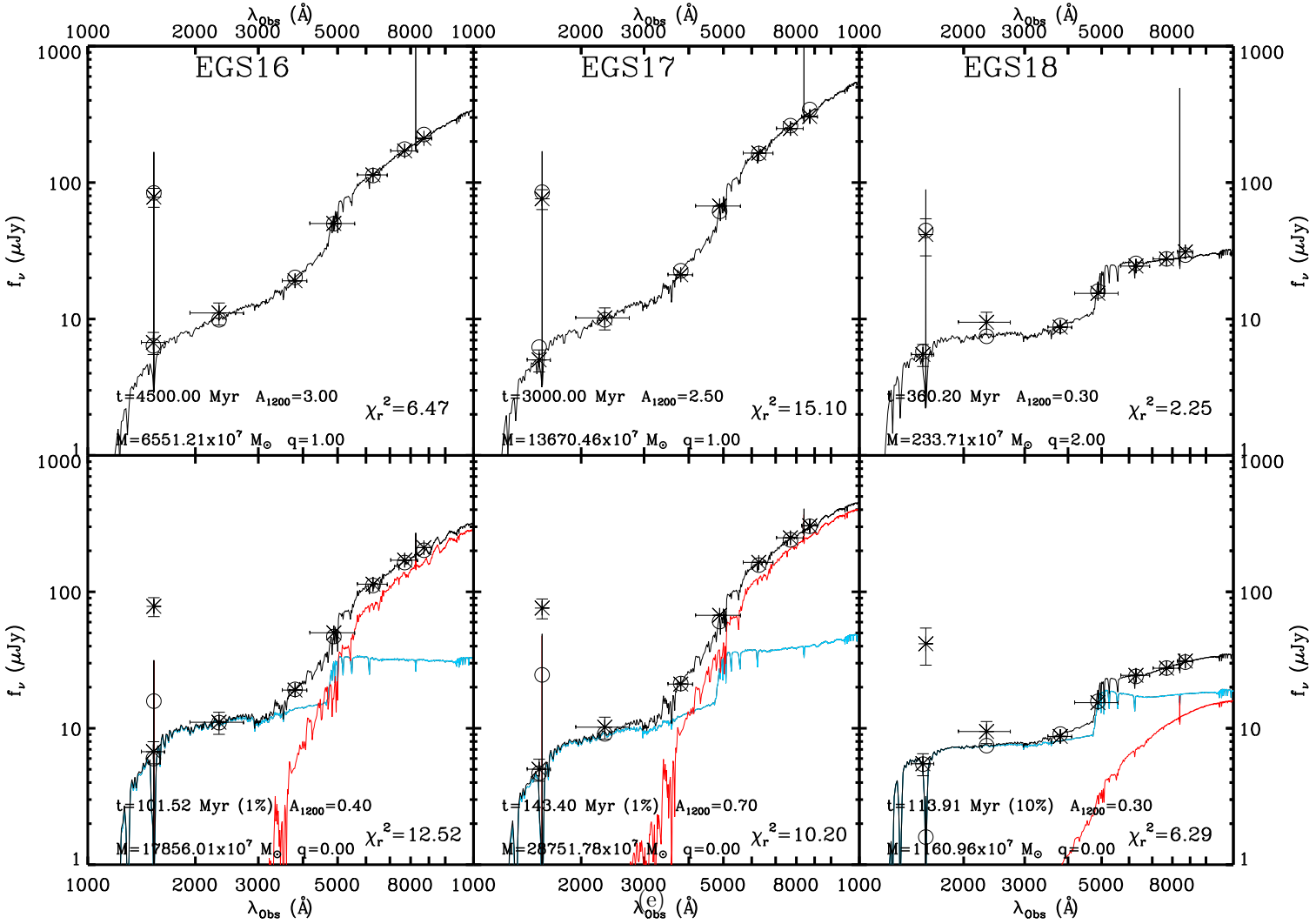

(e)

FIG. 25.—(g) Continued.

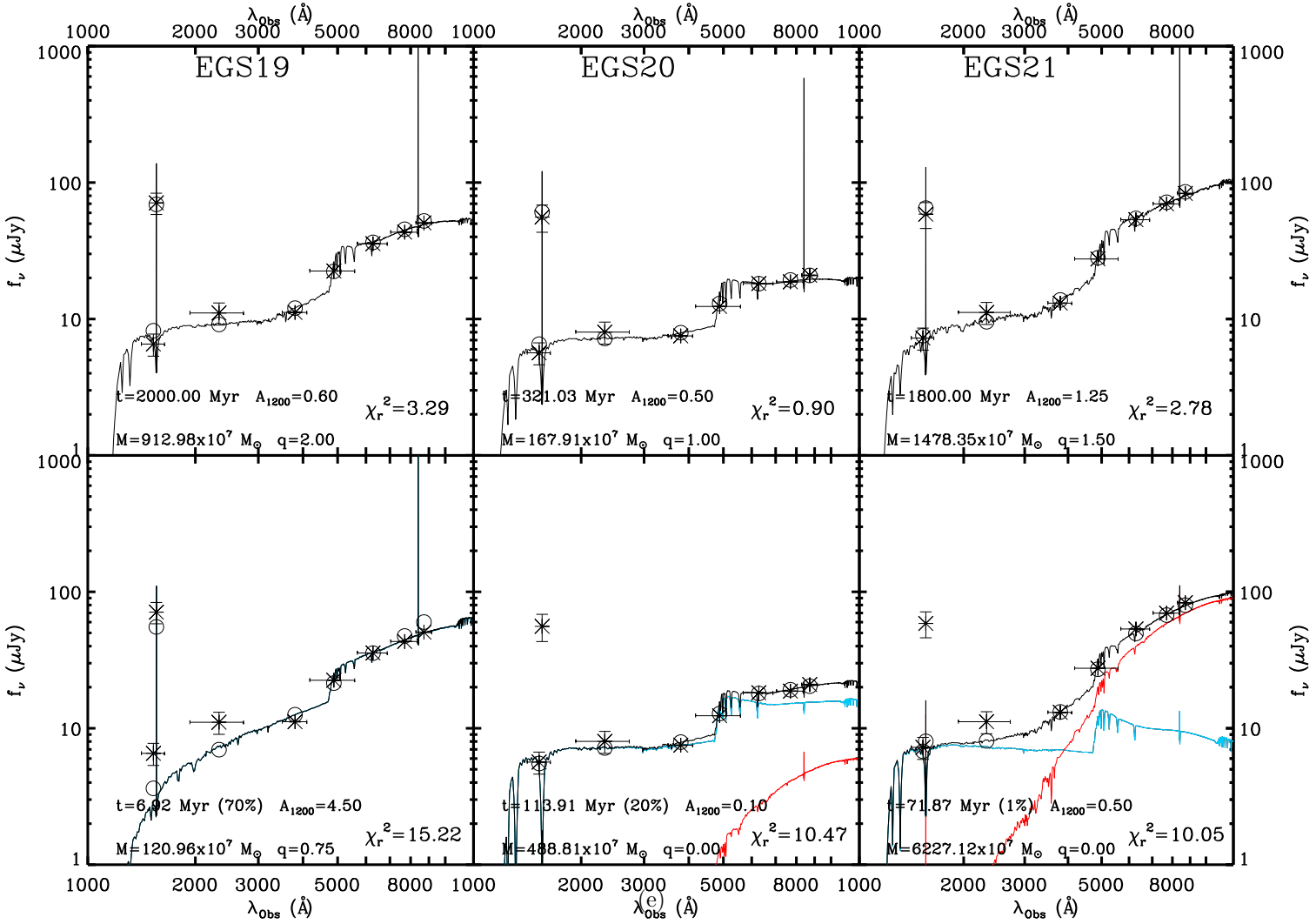

(e)

FIG. 25.—(h) Continued.

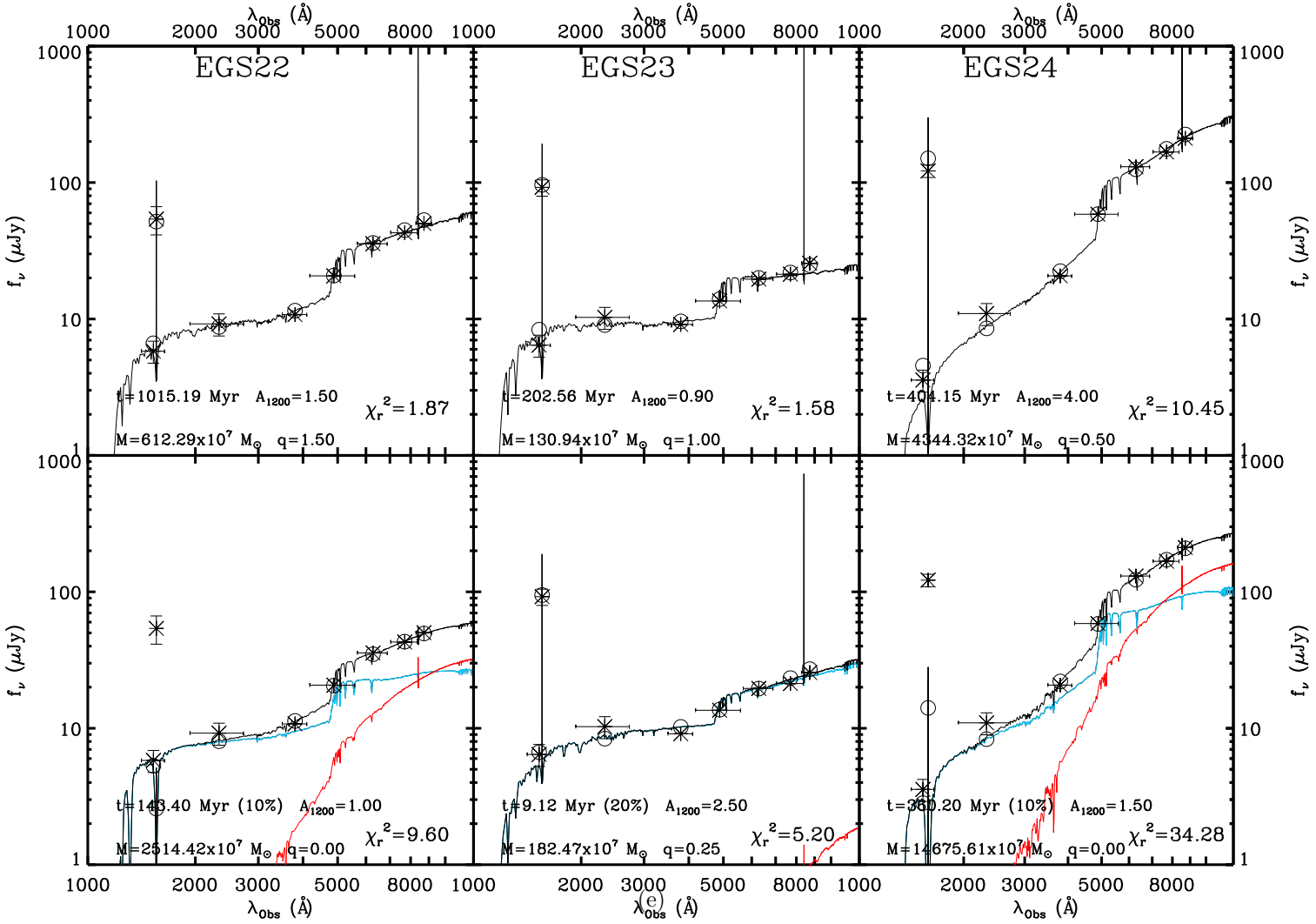

(e)

FIG. 25.—(i) Continued.

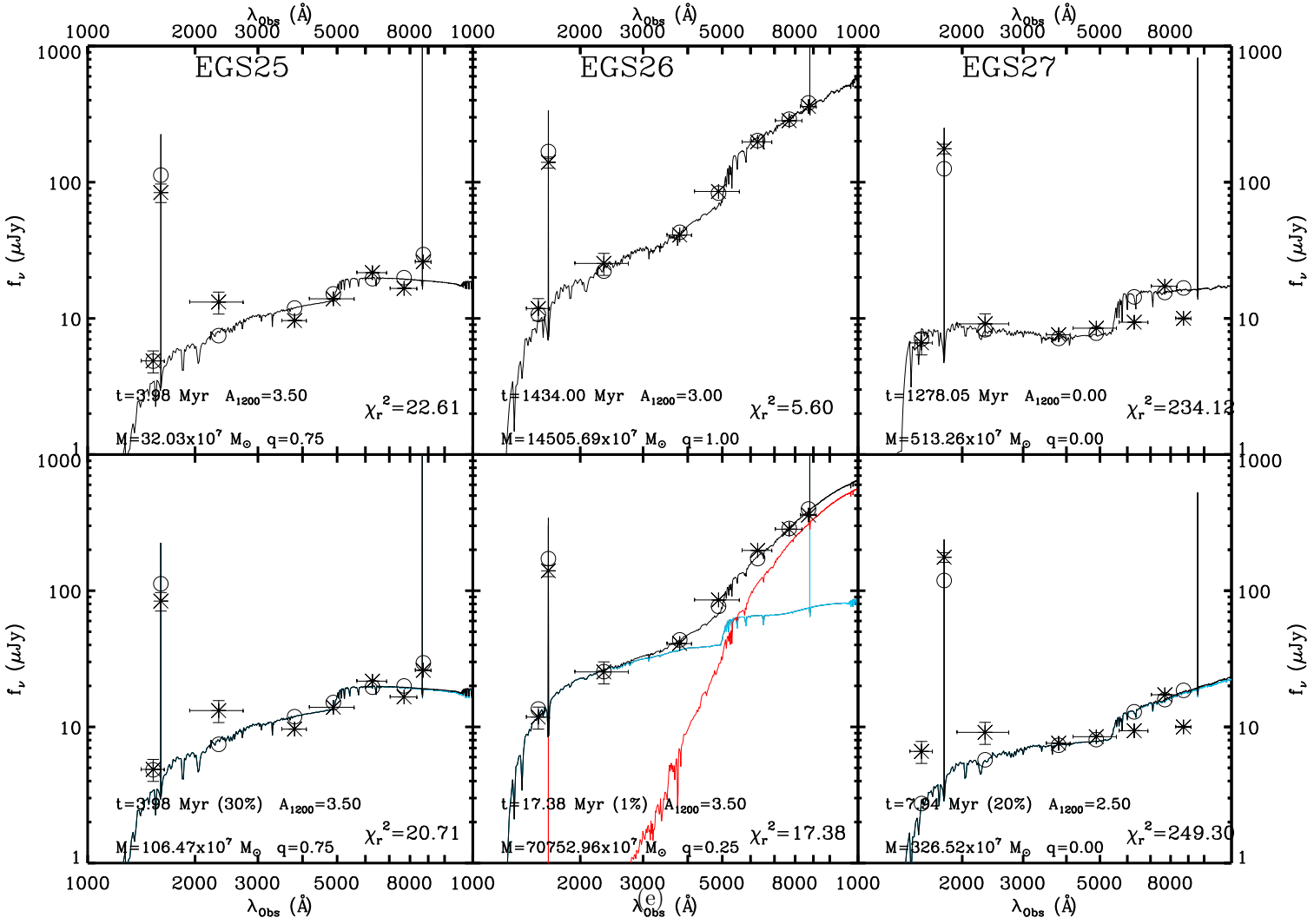

FIG. 25.—(j) Continued.

In Chapter 4 we fit stellar populations to 15 z $\sim$ 4.5 LAEs, finding an age and mass range of 3 – 500 Myr and 1.6 $\times$ 10^8 – 5.0 $\times$ 10^{10} $M_\odot$, respectively. The lower end of these new results is consistent with Chapter 4, while the upper end represents much more evolved objects, with masses three times greater. The median stellar mass at z $\sim$ 0.3 is $\sim$ 6.5 times greater than the median mass we measured at z $\sim$ 4.5. As for age, in Chapter 4, the median age was 10 Myr (with the oldest stellar population age of 500 Myr), while at z $\sim$ 0.3, over half of the objects are older than 1 Gyr.

In order to see how the observational errors would affect our results, we performed 3000 Monte Carlo simulations for each object, allowing the flux to vary by an amount proportional to the flux errors in each simulation. In Figure 26, we show the results of these simulations, plotting the average age distribution for the whole sample. We find that an average LAE at z $\sim$ 0.3 will have an age $>$ 100 Myr, with the greatest probability of being either $\sim$ 350 Myr or $>$ 1 Gyr. The gap in ages does appear to be real, as model ages in that gap are allowed (as shown by the dashed line); albeit a slightly smaller number of models exist in that bin than the two to either side. As shown in Figure 27, the distribution of derived masses follows the ages in that they are greater than what is seen at high redshift, with most objects having masses $>$ 10^9 $M_\odot$. Both the global age and mass distributions follow the individual results, in that low-redshift LAEs appear to be globally older and more massive than their high-redshift brethren.

6.4.2. *Metallicity, Dust and ISM Clumpiness*

The model grid consisted of six allowed values of metallicity: 0.005, 0.02, 0.2, 0.4, 1.0 and 2.5 $Z_{\odot}$. Only one object (CDFS1) out of the 22 with acceptable fits was best fit with the lowest value of metallicity, with only three more being best fit with Z = 0.02 $Z_{\odot}$. The majority of objects (14) were best fit with Z = 0.2 $Z_{\odot}$. In Chapter 4 we found that 53% of our objects were fit with metallicities of 0.02 $Z_{\odot}$ or less, thus showing possible evidence of metallicity evolution with redshift. This evolution does not show up in the dust content, as the mean extinction at z $\sim$ 0.3 is $A_{1200} \simeq 1.2$ mag, while at z $\sim$ 4.5 it was $A_{1200} \simeq 2.5$ mag. However, the ISM clumpiness (q) spans a much tighter range at low redshift, of q $\simeq$ 0.25 – 2.0. At z $\sim$ 4.5, the clumpiness parameter spanned q $\simeq$ 0 – 5, with over 50% of the objects having q $\leq$ 1. At z $\sim$ 0.3, only five objects have dust enhancement of the Lyα EW occurring with q $<$ 1, but dust is not extinguishing the EWs of these objects much either, as 20/22 objects have q $\leq$ 1.5.

These differences in metallicity and ISM properties at different redshifts may give us insight into the evolution of these objects. We would expect the average stellar population to become more enriched with time, and we believe that is what we are seeing with the metallicity differences between z $\sim$ 4.5 and 0.3. The fact that objects at z $\sim$ 4.5 have more dust extinction on average is interesting, although it may just be a selection effect. The z $\sim$ 0.3 LAEs were selected via spectroscopy, thus they were more sensitive to low EW objects. However, at z $\sim$ 4.5, we required a significantly strong narrowband excess in order to select an object as an LAE, which biases

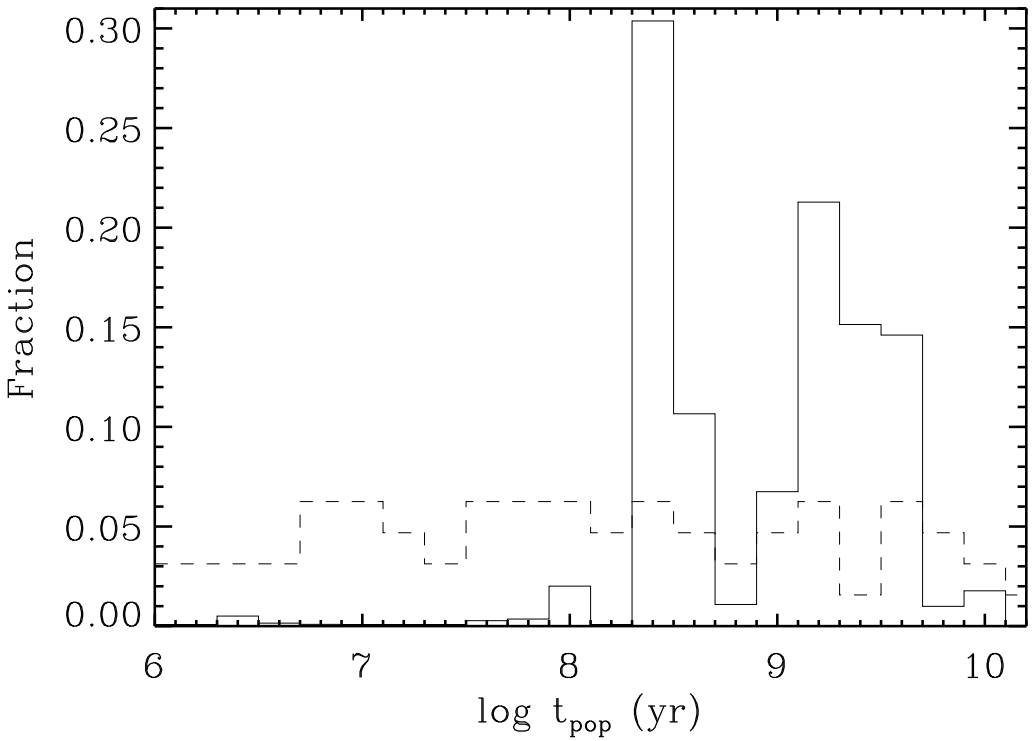

FIG. 26.—The distribution of ages from the Monte Carlo simulations averaged over all 30 objects. The dashed line overplots the available model ages using the same binning. The gap between $\sim$ 350 Myr and 1.5 Gyr does appear to be significant, given that there were available models in that range.

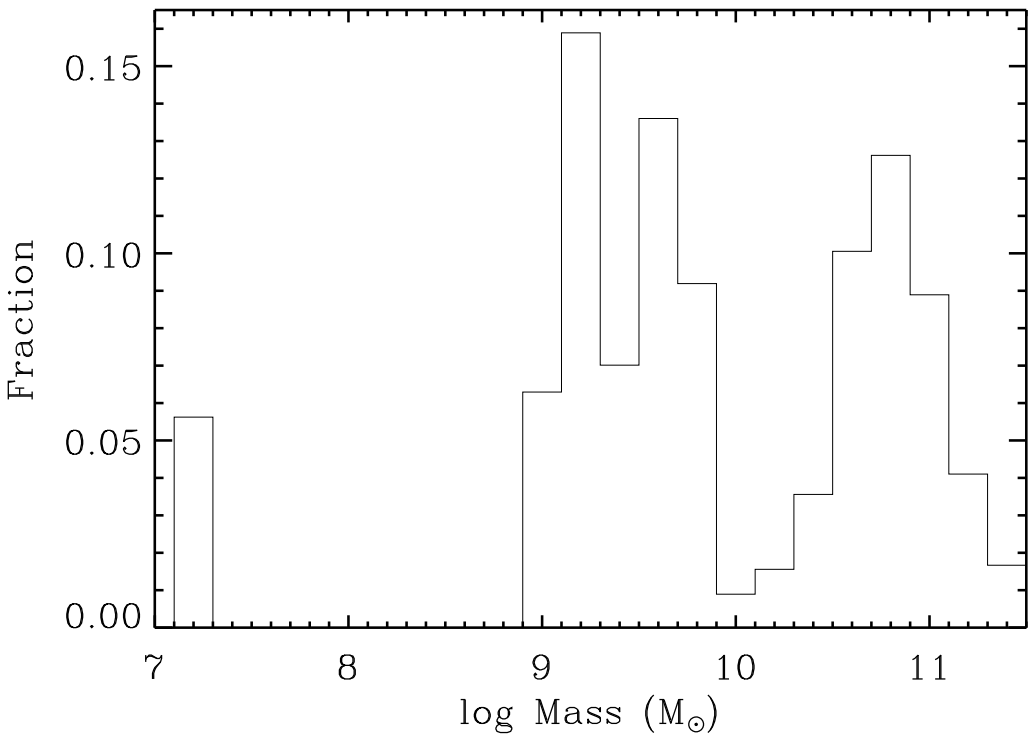

FIG. 27.—The distribution of derived masses from the Monte Carlo Simulations. The gap at 10^{10} $M_\odot$ appears to be due to the same gap in Figure 26.

us towards higher values of the Lyα EWs. As we showed in Chapter 4, a large portion of our sample had high EWs due to clumpy dust enhancement, thus we were then biased towards dusty objects as well. According to our models, only 40% of our CDF–S LAEs had EW $<$ 120 Å, whereas as z $\sim$ 0.3, over 70% of our LAEs had EWs $<$ 120 Å. In fact, for z $\sim$ 0.3, the measured EWs from D08 may be more accurate as they come from spectroscopy. Using these numbers, all 30 z $\sim$ 0.3 LAEs have EWs $<$ 120 Å, with a median value of 31 Å, and a minimum of 11.8 Å.

One may then ask, why do we not also see the high EW, dust enhanced LAEs at low redshift? There are a few, as discussed in the above paragraphs, but the numbers are significantly smaller than those at high redshift. This may indicate an evolution in the dust geometry in LAEs, and/or galaxies in general. Over time, a galaxy will accumulate more and more dust as stars continue to grow old and die. Isolated regions may become clumpy due to buoyancy and turbulence in H II regions among other things. In the high-redshift LAEs, which may be intrinsically smaller, these local events may be enough to change the ISM on a galaxy wide scale, allowing for the large range in q we found. However, at z $\sim$ 0.3, these objects may be larger in size, thus might be harder for a whole galaxy to have an entirely clumpy or entirely homogeneous ISM, which may be responsible for the fact that most z $\sim$ 0.3 LAEs have q near 1 – 1.5. In addition, external events, such as galaxy mergers, can severely disrupt the ISM. Ryan *et al.* (2008) show that the major merger fraction peaks at z $\sim$ 1.3. If the time since their last merger is large, this will also allow low-redshift LAEs to have more settled ISMs.

Although not much work has been done on LAEs at low redshift, a recent study has been published studying the role of dust in local Lyα emitting galaxies (Atek *et al.* 2008). Specifically, their plots of Lyα EW vs. dust extinction allow an opportunity to check if clumpy dust is affecting the EW, and by how much. In Figure 3 of their paper, they show this plot for Haro 11. The emission component of this plot shows significant scatter at low E(B-V), however, it approaches a constant value of $\sim$ 20 Å from E(B - V) = 0.5 – 1.0. In order for the Lyα EW to stay constant with increasing dust content, q must equal 1, which is the most likely value we found for q at z $\sim$ 0.3. This same effect is seen in their plots of IRAS 08339+6517, and also in NGC 6090, albeit less significantly. We believe that this confirms our prediction that the ISM of lower-redshift LAEs are neither extremely clumpy nor entirely homogeneous.

6.4.3. *Stellar Evolution Uncertainties*

While the BC03 models are very widely used across extragalactic astrophysics, recent insights into the contributions of post main-sequence evolution to the overall SED of a galaxy has called these models into question. The BC03 models do include all phases of stellar evolution from the zero-age main-sequence until the stellar remnant stage, including the thermally-pulsating asymptotic giant branch (TP–AGB) phase. However, Maraston et al. (2005, 2006) have recently shown that BC03 models underestimate the level at which TP-AGB stars can dominate the rest-frame near-IR. This does not affect our earlier chapters, as the rest-frame NIR ($\sim$ 1 μm) is observed at $\sim$ 5.5 μm, where we do not have detections. In addition, this evolutionary phase is

most important from 0.2 - 2 Gyr, and most of our z $\sim$ 4.5 LAEs appear to be much younger.

However, even prior to our model fitting, we would expect these z $\sim$ 0.3 LAEs to be older, possibly in the range where TP–AGB stars can dominate their NIR. But even at this lower redshift, we are not quite fitting rest-frame 1 μm. Our reddest band (z') corresponds to rest-frame $\sim$ 7000 Å, thus we would not expect a different treatment of TP–AGB stars to significantly alter our results. However, Charlot & Bruzual (2008 in prep) have devised new models, including the Maraston et al. treatment of TP–AGB stars, which will be released in the near future. Future studies at redder wavelengths will need to use these, or similar, models to more accurately fit their objects.

6.5. Conclusions

We have performed stellar population model fitting on a sample of 30 z $\sim$ 0.3 Lyα emitting galaxies, first discovered via *GALEX* spectroscopy by Deharveng *et al.* (2008). We measured the stellar population ages and masses, as well as metallicities, dust extinction, and ISM geometry. The age and mass results imply that low-redshift LAEs are both older and more massive than their high-redshift counterparts, with the youngest low-redshift LAE having a best-fit age of $\sim$ 200 Myr, much older than the average age at high redshift. We also found that the metallicity in LAEs is higher at low redshift, showing evolution in the mean metallicity of the stars inside these galaxies, as would be expected over a period of $\sim$ 9 Gyr of cosmic time.

Perhaps most interesting, we found that the ISM at low redshift appears to be very stable, in a quasi-clumpy state. At high redshift, we found that LAEs ran the

whole range from extremely clumpy to very homogeneous. At z $\sim$ 0.3, we found that while a few galaxies were fairly clumpy, most resided in the regime of q $\sim$ 1, where dust will not affect the Lyα EW. This result is confirmed by the study of local LAE analogs by Atek et al (2008). Our results show that LAEs at z $\sim$ 0.3 show significant differences from their high-redshift cousins, although further study of a larger sample will help confirm this. Although low-redshift LAE studies are difficult as they need to be done from space, help should be on the way with the near-UV sensitive Wide Field Camera 3 (WFC3) due to be installed on the *Hubble Space Telescope*.

7. CONCLUSIONS

This dissertation presents the results of five related studies, each trying to better understand the true nature of Lyman alpha galaxies. Specifically, we have performed our analyses with the overall goal of understanding the cause behind the large Lyα EWs which have been seen at high redshift.

In Chapter 2, we took our first stab at this problem by observing a field known to contain many LAEs at z $\sim$ 4.5 (LALA Cetus Field) with the ground-based MMT 6.5m telescope. The goal was to detect a large number of these objects in the broad-band, and then use this information to fit stellar population models to these objects. However, we underestimated the difficulty of detecting these objects from the ground, as only 22% (21/97) of the known LAEs in that field were detected (2 σ detections in two bands). The detections were then stacked, and we learned about the average properties of LAEs. The derived age scaled with EW, as the highest EW objects had the youngest age, and correspondingly small masses. Even though dust was unable to be constrained in this study, this was a necessary step, as we worked out the stellar population modeling process as well as the inclusion of the dust enhancement scenario into the models.

Based on our previous work, the photometry could be improved by using space-based broadband data. New narrowband data was thus needed in a field covered deeply by the *Hubble Space Telescope* (*HST*). We obtained an image in the NB656 filter from CTIO in the CDF–S, which is covered extensively by both *HST* and *Spitzer*. Although this image was relatively shallow ($\sim$ 3 hr), utilizing PSF fitting routines, we were able to discover four new LAEs at z $\sim$ 4.4. These objects had high S/N detections in the *HST* ACS data, and they were all detected in at least one *Spitzer*

IRAC band. These objects are discussed in Chapter 3, where we also go through the details of the clumpy dust enhancement scenario. The model EWs (with and without dust) were found to be consistent with earlier studies. Models were fit to the objects, and three of the four objects were consistent with Chapter 2, in that they were very young (3 – 5 Myr) and low mass ($\sim 10^8$ – 10^9 $M_\odot$), although they did show significant amounts of dust, indicating that they may not be primitive objects. The fourth object was fit by a vastly different population, with an age of 800 Myr and a mass of $\sim 7 \times 10^9$ $M_\odot$. A typical galaxy this evolved would not show strong Lyα emission. However, this object was fit with 0.4 mag of dust extinction and a clumpiness value of q = 0, indicating that the ISM is actually enhancing the EW by 50%. This object showed us that the clumpy dust scenario can explain the SEDs of some objects, although more data was needed to be sure.

Using the results of Chapter 3, we applied for telescope time to obtain more narrowband data to detect a larger sample of LAEs. The proposal was successful, and 11 new LAEs were discovered in the CDF-S, which are discussed in Chapter 4. A similar stellar population modeling analysis was performed. A few new features were added to the models, such as a two-burst star formation history, and a varying metallicity (as new constraints were added in the form of NIR upper limits), thus the four objects from Chapter 3 were also refit, for a total of 15 LAEs. The results were consistent with those found in Chapter 3. Out of 15 objects, 13 were fit by young ($\leq$ 15 Myr) stellar populations, with dust extinction in every object (A_{1200}= 0.5 – 4.5 mag). Moreover, out of these 13 objects, eight of them had q $<$ 1, indicating that

this dust is responsible for enhancing their EWs. The other two objects appear to be evolved populations (age $\geq$ 450 Myr), with clumpy dust responsible for enhancing their EWs. The detection of dust in each and every object is the strongest proof to date that LAEs are not the primitive objects they were once thought to be. In order to investigate the interesting bimodality in age, Monte Carlo simulations were run, examining the age distribution from the simulations averaged over the whole sample. The age distribution showed two peaks, at $\sim$ 4 and 400 Myr, confirming the initial suggestion of a bimodal age distribution. This is interesting, as it implies that some mechanism is hindering us from finding LAEs between 15 and 450 Myr. This could possibly be dust, as after a few 10's of Myr, enough stars will have died to possibly further saturate the ISM with dust. Over time, the stars could begin to punch holes in this dust, causing the enhanced EWs in the evolved LAEs. However, 15 objects is too small to know if this age gap is significant, thus a determination will have to wait for a larger sample.

The dust extinction found in Chapter 4 was derived by stellar population model fitting, and thus the amount of dust can be degenerate with other parameters that result in redder SEDs, such as age or metallicity. Objects which truly have this much dust should be detectable in their rest-frame FIR, which is where the peak of the dust emission occurs. At z $\sim$ 4.5, this is $\sim$ 600 μm, which has been difficult to observe deeply from the ground. In Chapter 5 we discuss the possibility that future instruments, such as ALMA, could detect this dust emission. We utilize a relation which allows one to derive the FIR flux of an object given its UV spectral slope. This

relation was used to compute the observed sub-mm fluxes of our 15 LAEs, as well as 9 LAEs from Pirzkal *et al.* (2007). A surprisingly large fraction of LAEs (42 $\pm$ 21 %) should be detectable with ALMA. These results were compared with a sample of LBGs, and it was found that even more of them would be detected, at $\sim$ 60%. This work shows that ALMA will be a crucial and efficient tool to determine if our derived dust extinction values are accurate.

In the last study, we examined a sample of 30 LAEs at z $\sim$ 0.3, in order to see if their average physical properties differed substantially from their high-redshift counterparts. These objects were discovered with the UV telescope *GALEX*, as at such a low redshift, Lyα emission cannot be observed from the ground. The advantage to this is that they are so (relatively) nearby, that their signal-to-noise is high. Corresponding optical broadband data for these objects was taken from the MUSYC and CFHTLS surveys, and then we fit stellar population models similar to Chapters 3 & 4. These objects were found to be more evolved than (the majority of) high-redshift LAEs, with ages and masses from 200 Myr – 8 Gyr and $\sim 10^9$ – 10^{11} $M_\odot$, respectively (for objects with $\chi^2_r < 10$). These objects also appear to be more metal enriched, as their derived metallicities were higher than those at high redshift. One interesting result is that their ISM geometry appears to lie in a tight range, from q = 0.25 – 2.0, with 20/30 objects having $1 \leq q \leq 2$. This could be due to the larger sizes of galaxies at lower redshift, in that it could be harder for an entire object's ISM to be uniformly clumpy or homogeneous. Nonetheless, these results match up well with

predictions of galaxy evolution, as these objects are older, more massive, and more metal enriched.

These five studies together, while finding their own unique results, each add an answer to the overall question of the physical properties of Lyα galaxies. We find that at high redshift, the majority of these galaxies are young and low mass, with significant amounts of dust, frequently enhancing their Lyα EWs. We also find that a non-negligible percentage of high-redshift LAEs are in fact evolved objects, exhibiting strong EWs due to dust enhancement. At low redshift, we find that LAEs are much more evolved, with older ages, higher metallicities, with a small range of ISM geometries across the sample. Observing LAEs in their rest-frame FIR will help confirm these model fits, as if the amount of dust we find at high redshift is true, nearly half of our LAEs will be detectable with ALMA. These combined results have added crucial knowledge to the community about our understanding of not only LAEs in general, but also the effect dust and dust geometry have on the Lyα EW. They have opened the door for future studies, as for every question we have answered, we have created many more.

During my postdoctoral studies, I plan to continue to pursue research on Lyα emitters, broadening my horizons to encompass a wider range of topics, with an emphasis on lower redshift science. As I said above, the main contribution of this thesis is that we show that the SEDs of LAEs can be fit by models with clumpy interstellar media. This brings up an important point, in that of the multiple groups which fit stellar population models to LAEs, the treatment of the Lyα line is different in

many cases. We have shown that allowing the ISM to affect the Lyα line in different ways can definitely affect your results. Pirzkal *et al.* (2007) do not include the band which encompasses the Lyα emission in their fits, thereby avoiding any uncertainty, while Lai *et al.* (2007) include this band, but add in a 30% flux error to compensate for the line. Nilsson *et al.* (2007) strategically chose a narrowband such that the line falls between broadband filters, so that they also do not have to deal with any uncertainty from the Lyα emission. One of my main concerns is that the differing treatment in the Lyα line can affect the stellar population results that the various groups are getting. I think that one way to resolve this is to form a collaboration between the various groups, exchange object fluxes, and have each group fit all other groups objects. We can then compare the results, and gain a real sense of how dependent the results are on the modeling technique. I have already begun talks with a few people, and I think that this could be a real possibility in the next few years.

One of my main interests for the future deals with LAEs at lower redshifts. Not only are you dealing with higher signal-to-noise, this regime, especially at $z < 3$, has not been well probed. We currently have two studies probing lower redshift LAEs. The first is at $z \sim 3.1$. During my graduate studies, I obtained 13 nights of telescope time on the Steward Observatory Bok 90" telescope, with the 90Prime square degree camera. We obtained [O III] narrowband data covering eight square degrees over three different fields. We plan to use these data to investigate the clustering properties of LAEs, and, with the addition of deeper data to come in the future, we should have the largest single sample of LAEs to date.

We have currently been awarded time at the Kitt Peak 4m Blanco telescope to perform narrowband imaging with the [O II] filter, which we will use to select LAEs at z $\sim$ 2.1. Lyα luminosity functions have been computed at z $\sim$ 3.1 (Gronwall *et al.* 2007) and 0.3 (Deharveng *et al.* 2008). A comparison shows striking differences between the luminosity functions, specifically showing that LAEs are much more common at z $\sim$ 3.1. By obtaining data an an intermediate redshift, we will be able to better tell at what redshift the number density of LAEs begins to fall. We will also perform stellar population model fitting of these LAEs, where the lower redshift and high signal-to-noise of the data should result in higher fidelity results.

Lastly, I would like to continue to study the population of LAEs at z $\sim$ 0.3 discussed in Chapter 6. One alternative idea for preferential Lyα escape from galaxies involves an outflowing ISM (e.g., Kunth *et al.* 1998). In this scenario, Lyα photons originally headed away from us could backscatter off of the far side of the expanding shell, thus when they try to head out of the near side of the galaxy, they are redshifted with respect to the atoms in the ISM, thus they would no longer be resonantly scattered. Shapley *et al.* (2003) find an average redshift for Lyα of 360 km s^{-1} with respect to the systemic redshift of the galaxy, showing evidence that this scenario may exist at high redshift. To look for this in a sample of LAEs, we would like to measure interstellar absorption lines spectroscopically to see if they appear blueshifted, indicating the leading edge of an outflow. While ideally we would like to study this at z $\sim$ 4.5, we would not be able to get the necessary spectroscopic

signal-to-noise necessary to measure the ISM absorption lines. However, we can do this for the z $\sim$ 0.3 LAEs, and this is one of my top priorities in the coming year.

If we find evidence for outflows, and I think that we will given the results of Tremonti *et al.* (2007) for z $\sim$ 0.6 post-starburst galaxies and Weiner *et al.* (2008) for z $\sim$ 1.4 starburst galaxies, then it remains to be determined whether outflows, clumpy ISMs, or other scenarios dominate the escape of Lyα photons. Currently Hansen & Oh (2006) have predictions about what the Lyα line profiles show look like given various ISM geometries. Also, Verhamme *et al.* (2008) have recently published a similar study, only this time looking at line profiles with outflows, albeit with a homogeneous ISM. In reality, these objects probably have outflows and inhomogeneous ISMs, thus if we knew what such an object should look like (i.e. line profiles), it could help us to better understand our observations.

The future holds many different avenues for research, and it is exciting that we have the opportunity to answer some of the many important questions in astrophysics. The advent of new instrumentation, such as WFC3 for *HST*, and new observatories, such as *JWST* and ALMA, ensure that we will continue to probe astrophysical frontiers for generations to come.

REFERENCES

Ajiki, M. *et al.* 2004, PASJ, 56, 597

Arnouts, S. *et al.* 2001, A&A, 379, 740

Atek, H. *et al.*, Accepted to A&A, astroph/0805.3501

Baker, A. J. *et al.* 2006, A&A, 372, L37

Beckwith, S. V. W. *et al.* 2006, AJ, 132, 1729

Bendo, G. J. *et al.* 2006, ApJ, 652, 283

Bertin, E. 2006, SExtractor v2.5 Manual, http://terapix.iap.fr

Bertin, E. & Arnouts, S. 1996, A&AS, 117, 393

Bertoldi, F. *et al.* 2003, A&A, 409, L47

Bruzual, G. & Charlot, S. 1993, ApJ, 405, 538

Bruzual, G. & Charlot, S. 2003, MNRAS, 344, 1000

Calzetti, D., Kinney, A. L. & Storchi-Bergmann, T. 1994, ApJ, 429, 582

Capak, P. *et al.* 2008, ApJ, 681, L53

Cedres, B., Cepa, J. & Tomita, A. 2005, ApJ, 634, 1043

Chapman, S. C., Smail, I., Windhorst, R., Muxlow, T. & Ivison, R. J. 2004, ApJ, 611, 732

Chapman, S. C., Blain, A. W., Smail, I. & Ivison, R. J. 2005, ApJ, 622, 772

Charlot, S. & Bruzual, G. 2008, in prep

Charlot, S. & Fall, S. M. 1993, ApJ, 415, 580

Chary, R.-R., Stern, D. & Eisenhardt, P. 2005, ApJ, 635, L5

Cowie, L. L., & Hu, E. M. 1998, AJ, 115, 1319

Dale, D. A. *et al.* 2001, ApJ, 549, 215

Dale, D. A. & Helou, G. 2002, ApJ, 576, 159

Davis, M. *et al.* 2007, ApJ, 660, L1

Dawson, S., Rhoads, J. E., Malhotra, S., Stern, D., Dey, A., Spinrad, H., Jannuzi, B. T., Wang, J. X. & Landes, E. 2004, ApJ, 617, 707

Dawson, S., Rhoads, J. E., Malhotra, S., Stern, D., Wang, J. X., Dey, A., Spinrad, H. & Jannuzi, B. T. 2007, ApJ, 671, 1227

Deharveng, J.-M. *et al.* 2008, ApJ, 680, 1072

De Propris, R. *et al.* 1993, AJ, 105, 1243

Djorgovski, S. & Thompson, D. J. 1992, IAUS, 149, 337

Draine, B. T. 2004, in The Cold Universe, Saas Fee Advanced Course 32, ed. D. Pfenniger & Y. Revaz (Berlin: Springer-Verlag), 213

Eggen, O. J., Lynden-Bell, D. & Sandage, A. R. 1962, ApJ, 136, 748

Ellis, R., Santos, M. R., Kneib, J.-P. & Kuijken, K. 2001, ApJ, 560, L119

Fazio, G. G. *et al.* 2004, ApJS, 154, 10

Finkelstein, S. L., Rhoads, J. E., Malhotra, S., Pirzkal, N. & Wang, J. X. 2007, ApJ, 660, 1023

Finkelstein, S. L., Rhoads, J. E., Malhotra, S., Grogin, N. & Wang, J. X. 2008a, ApJ, 678, 655

Finkelstein, S. L., Rhoads, J. E., Malhotra, S. & Grogin, N. A. 2008b, ApJ submitted, astroph/0806.3269

Fischer, P. & Kochanski, G. P. 1994, AJ, 107, 802

Ford, H. *et al.* 1998, Proc. SPIE Vol. 3356, 234

Fujita, S. S. *et al.* 2003, ApJ, 586, L115

Fukugita, M., Ichikawa, T., Gunn, J. E., Doi, M., Shimasaku, K. & Schneider, D. P. 1996, AJ, 111, 1748

Fynbo, J. U., Möller, P. & Thomsen, B. 2001, A&A, 374, 443

Gao, Y. 2008, Nature, 452, 417

Gawiser, E. *et al.* 2006a, ApJ, 642, L13

Gawiser, E. *et al.* 2006b, ApJS, 162, 1

Giacconi, R. *et al.* 2001, ApJ, 551, 624

Giavalisco, M. *et al.* 2008, in prep

Giavalisco, M., Koratkar, A. & Calzetti, D. 1996, ApJ, 466, 831

Giavalisco, M. *et al.* 2004, ApJ, 600, 93

Grazian, A. *et al.* 2006, A&A, 449, 951

Gronwall, C. *et al.* 2007, ApJ, 667, 79

Haiman, Z. & Spaans, M. 1999, ApJ, 518, 138

Hansen, M. & Oh, S. P. 2006, MNRAS, 367, 979

Hathi, N. P., Malhotra, S. & Rhoads, J. E. 2008, ApJ, 673, 686

Hu, E. M., Cowie, L. L. & McMahon, R. G. 1998, ApJ, 502, L99

Hu, E. M., Cowie, L. L., McMahon, R. G., Capak, P., Iwamuro, F., Kneib, J.-P., Maihara, T. & Motohara, K. 2002, ApJ, 568, L75

Hu, E. M., Cowie, L. L., Capak, P., McMahon, R. G., Hayashino, T. & Komiyama, Y. 2004, AJ, 127, 563

Hubble, E. P. 1936, The Realm of Nebulae, Yale University Press, New Haven, CT

Jannuzi, B. T., Dey, A. 1999, in ASP Conf. Ser. 191, Photometric Redshifts and High Redshift Galaxies, ed. R. J. Weymann, L. J. Storrie-Lombardi, M. Sawicki, & R. J. Brunner (San Francisco: ASP), 111

Kauffmann, G. & White, S. D. M. 1993, MNRAS, 261, 921

Kauffmann, G., White, S. D. M. & Guiderdoni, B. 1993, MNRAS, 264, 201

Kennicutt, R. C. Jr. 1983, ApJ, 272, 54

Kodaira, K. *et al.* 2003, PASJ, 55, L17

Koo, D. C. & Kron, R. T. 1980, PASP, 92, 537

Kudritzki, R.-P. *et al.* 2000, ApJ, 536, 19

Kunth, D. et al. 1998, A&A, 334, 11

Lai, K. *et al.* 2007, ApJ, 655, 704

Lai, K. *et al.* 2008, ApJ, 674, 70

Laidler, V. G. *et al.* 2007, PASP, 119, 1325

Landolt, A. U. 1992, AJ, 104, 340

Larson, R. B. & Tinsley, B. M. 1978, ApJ, 219, 46

Le Fevre, O. *et al.*, A&A, 428, 1043

Leitherer, C. & Heckman, T. M. 1995, ApJS, 96, 9

Leitherer, C. *et al.* 1993, ApJS, 123, 3

Madau, P. 1995, ApJ, 441, 18

Malhotra, S. & Rhoads, J. E. 2002, ApJ, 565, L71

Malhotra, S., Wang, J.X., Rhoads, J. E., Heckman, T. M. & Norman, C. A. 2003, ApJ, 585, L25

Malhotra, S. & Rhoads, J. E. 2004, ApJ, 617, L5

Malhotra, S. *et al.* 2005, ApJ, 626, 666

Maraston, C. 2005, MNRAS, 362, 799

Martin, C. *et al.* 2006, ApJ, 652, 85

Martin, C. L. *et al.* 2008, ApJ, 679, 942

McLeod, B. M., Caldwell, N., Williams, G. & Conroy, M. 2006, Megacam Observers Manual, http://grb.mmto.arizona.edu/∼ggwilli/mmt/docs/megacam/megacam_manual.html

McLeod, B. A., Gauron, T. M., Geary, J. C., Ordway, M. P. & Roll, J. B. 1998, SPIE, 3355, 477

McLinden, E., Finkelstein, S. L., Rhoads, J. & Malhotra, S. 2008, in prep

Meier, D. L. & Terlevich, R. 1981, ApJ, 246, L109

Meurer, G. R., Heckman, T. M., Lehnert, M. D., Leitherer, C. & Lowenthal, J. 1997, AJ, 112, 54 (M97)

Meurer, G. R., Heckman, T. M. & Calzetti, D. 1999, ApJ, 521, 64

Nagao, T. *et al.* 2008, ApJ, 680, 100

Neufeld, D. A. 1991, ApJ, 370, L85

Nilsson, K. K. *et al.* 2007, A&A, 471, 71

Oke, J. B. & Gunn, J. E. 1983, ApJ, 266, 713

Ouchi, M. *et al.* 2001, ApJ, 558, 83

Ouchi, M. *et al.* 2003, ApJ, 582, 60

Ouchi, M. *et al.* 2004, ApJ, 611, 685

Ouchi, M. *et al.* 2008, ApJS, 176, 301

Papovich, C., Dickinson, M. & Ferguson, H. C. 2001, ApJ, 559, 620

Partridge, R. B. & Peebles, P. J. E. 1967, ApJ, 147, 868

Pascarelle, S. M. *et al.* 1996a, ApJ, 456, 21

Pascarelle, S. M. *et al.* 1996b, Nature, 383, 45

Pentericci, L. *et al.* 2000, A&A, 361, 25

Pentericci, L. *et al.* 2002, AJ, 123, 2151

Pentericci, L. *et al.* 2007, A&A, 471, 433

Penton, S. V., Shull, J. M. & Stocke, J. T. 2000, ApJ, 544, 150

Pirzkal, N. *et al.* 2004, ApJS, 154, 501

Pirzkal, N. *et al.* 2007, ApJ, 667, 49

Reddy, N. A. & Steidel, C. C. 2004, ApJ, 603, L13

Reddy, N. A. *et al.* 2006, ApJ, 644, 792

Rhoads, J. E. 2000, PASP, 112, 771, 703

Rhoads, J. E., Malhotra, S., Dey, A., Stern, D., Spinrad, H. & Jannuzi, B. T. 2000, ApJ, 545, L85

Rhoads, J. E. & Malhotra, S. 2001, ApJ 563, L5

Rhoads, J. E., Dey, A., Malhotra, S., Stern, D., Spinrad, H., Jannuzi, B. T., Dawson, S., Brown, M. J. I. & Landes, E. 2003, AJ, 125, 1006

Rhoads, J. E., Xu, C., Dawson, S., Dey, A., Malhotra, S., Wang, J. X., Jannuzi, B. T., Spinrad, H., & Stern, D. 2004, ApJ, 611, 59

Rhoads *et al.* 2008, Submitted to ApJ, astroph/0805.1056

Ryan, R. E., Jr. *et al.* 2008, ApJ, 678, 751

Salpeter E. E. 1955, ApJ, 121, 161

Scannapieco, E., Schneider, R. & Ferrara, A. 2003, ApJ, 589, 35

Schaerer, D. 2002, A&A, 382, 28

Schlegel, D., Finkbeiner, D. P. & Davis, M. 1998, ApJ, 500, 525

Schneider, R. *et al.* 2006, MNRAS, 369, 825

Seibert, M., Heckman, T. M. & Meurer, G. R. 2002, AJ, 124, 46

Shapley, A. E., Steidel, C. C., Adelberger, K. L., Dickinson, M., Giavalisco, M. & Pettini, M. 2001, ApJ, 562 ,95

Shapley, A. E., Steidel, C. C., Pettini, M. & Adelberger, K. L. 2003, ApJ, 588, 65

Shimasaku, K. *et al.* 2003, ApJ, 586, L111

Shimasaku, K. *et al.* 2006, PASJ, 58, 313

Spergel, D. N. *et al.* 2007, ApJS, 170, 377

Steidel, C. C., Giavalisco, M., Pettini, M., Dickinson, M. & Adelberger, K. L. 1996, ApJ, 462, L17

Stetson, P. B. 1987, PASP, 99, 191

Stiavelli, M., Scarlata, C., Panagia, N., Treu, T., Bertin, G. & Bertola, F. 2001, ApJ, 561, L37

Strömgren, B. 1939, ApJ, 89, 526

Szokoly, G. P. *et al.* 2004, ApJS, 155, 271

Taniguchi, Y. *et al.* 2005, PASJ, 57, 165

Teplitz, H. I. *et al.* 2006, AJ, 132, 853

Tody, D. 1986, SPIX, 627, 733

Tody, D. 1993, ASPC, 52, 173

Tremonti, C. A. *et al.* 2004, ApJ, 613, 898

Tremonti, C. A., Moustakas, J. & Diamond-Stanic 2007, ApJ, 663, L77

Tumlinson, J. & Shull, J. M. 2000, ApJ, 528, L65

Tumlinson, J., Giroux, M. L. & Shull, J. M. 2001, ApJ, 550, L1

Valdes, F. G. 1998, ASPC, 145, 53

Valdes, F. G. & Tody, D. 1998, SPIE, 3355, 497

van Breukelen, C., Jarvis, M. J. & Venemans, B. P. 2005, MNRAS, 359, 895

Vanzella, E. *et al.* 2006, astroph/0612182

Vanzella, E. *et al.* 2008, A&A, 478, 83

Venemans, B. P. *et al.* 2002, ApJ, 569, L11

Venemans, B. P. *et al.* 2004, A&A, 424, L17

Venemans, B. P. *et al.* 2005, A&A, 431, 793

Venkatesan, A., Tumlinson, J. & Shull, J. M. 2003, ApJ, 584, 621

Verhamme, A. *et al.* 2008, Accepted to A&A

Wang, J. X., Rhoads, J. E., Malhotra, S., Dawson, S., Stern, D., Dey, A., Heckman, T. M., Norman, C. A. & Spinrad, H. 2004, ApJ, 608, L21

Wang, J. X., Malhotra, S. & Rhoads, J. E. 2005, ApJ, 622, L77

Wang, J. X. *et al.* 2007, in preparation

Weiner, B. J. *et al.* 2008, ApJ Submitted

Wilson, T. L. 2007, Astrophys Space Sci, Springer, 10.1007

Wuyts, S. *et al.* 2008, astroph/0804.0615

Xu, C. *et al.* 2007, AJ, 134, 169